UNIVERSIDAD DE VALENCIA

Doctorado en Nanociencias y Nanotecnología

Exploiting the Potential of New Coordination Frameworks for Technological Applications

–

from Temperature Sensing to Magnetic Storage

PhD Thesis of Noemi Monni

Supervisors:
Prof. Maria Laura Mercuri
Prof. Enzo Cadoni
Prof. Miguel Clemente-León

Coordinator:
Prof. Eugenio Coronado

February 2022

UNIVERSITÀ DEGLI STUDI DI SASSARI

FACOLTÀ DI SCIENZE

Dottorato di Ricerca in Scienze e Tecnologie Chimiche

XXXIV Ciclo

Exploiting the Potential of New Coordination Frameworks for Technological Applications

–

from Temperature Sensing to Magnetic Storage

PhD Thesis of Noemi Monni

Supervisors:
Prof. Maria Laura Mercuri
Prof. Enzo Cadoni
Prof. Miguel Clemente-León

Coordinator:
Prof. Carla Cannas

February 2022

This work has been performed in the framework of a Co-joint PhD thesis between the University of Sassari (Italy) and University of Valencia (Spain), with the research activities performed at the Chemical and Geological Sciences Department, University of Cagliari (Italy) and at the Institute of Molecular Science, University of Valencia (Spain).

Dedicated to my parents.

ABSTRACT

This PhD work reports on the design, synthesis and characterization of novel Coordination Frameworks (CFs), either porous or not, showing magnetic and/or optical properties, to exploit their potential in various technological applications. The design of such materials requires a particular attention in the selection of the molecular building blocks, organic linkers and metal nodes. To construct CFs with different physical properties, carboxylate and anilate derivatives have been chosen. Particularly, among the carboxylates, the 1,3,5-benzentricarboxylic acid (H_3BTC, trimesic acid), a biofriendly linker which allows to build robust 3D metal-organic frameworks while within the anilates, the 3,6-ditriazolyl-2,5-dihydroxybenzoquinone was chosen for its potential capability to build 3D supramolecular architectures due to the triazolyl pendant arms at the 3, 6 positions of the benzoquinone moiety, which are electron-donor substituents as well; these substituents in fact may affect the physical properties and the related technological applications. By playing with these two promising linkers in a wise combination with selected *d*- and *f*- transition metals, new systems, suitable for a wide range of applications, were obtained.

In **Chapter 1**, the synthesis of two N-heterocycles substituted anilate derivatives, 3,6-N-ditriazolyl-2,5-dihydroxy-1,4-benzoquinone and 3,6-N-(dipyrazolyl-4-carboxylic acid)-2,5-dihydroxy-1,4-benzoquinone, is reported. Both ligands were characterized by spectroscopic (Raman, FT-IR, UV-Vis and Fluorescence) and electrochemical (Cyclic Voltammetry) techniques.

Chapter 2 reports on the synthesis of new magnetic and redox-active anilate-based 3D MOFs, obtained by combining the 3,6-N-ditriazolyl-2,5-dihydroxy-1,4-benzoquinone, hereafter 3,6-N-ditriazolyl-Anilato, linker with M^{II}= Co, Cu, Mn, Ni and Fe d-transition metal ions. Structural, Spectroscopic, Magnetic and Electrochemical Characterization is reported for all the obtained materials.

In **Chapter 3**, the Co^{II}-3,6-N-ditriazolyl-Anilato 3D MOF was studied as potential system for CO_2 uptake and separation. The static and dynamic adsorption studies revealed that this MOF present a remarkable CO_2 adsorption and separation capability from gas mixtures, due to its 3D ultramicroporous structure, with voids

where the N2 atoms of the triazolyl groups show a significant affinity for CO_2 molecules and channels that enable the high selective entrance of CO_2.

Chapter 4 reports on the synthesis of novel flexible 3D Er-based MOF with the 3,6-N-ditriazolyl-Anilato linker, showing luminescent and SIM properties. These materials have been structurally, magnetically and optically characterized. Furthermore, one of them shows a reversible structural flexibility of the 3D framework that allows a challenging tuning of its physical properties.

In **Chapter 5**, the potential of 3,6-N-ditriazolyl-2,5-dihydroxy-1,4-benzoquinone as organic linker for Ln^{III} ions was exploited by combining it with Dy^{III}, Tb^{III} and Ho^{III} ions, which are generally employed as building units for Single Ion Magnets (SIMs). As in the previous Chapter, two series with all the Ln^{III} ions were obtained and further characterized, both structurally and magnetically.

Finally, **Chapter 6** reports on the preparation through a solvent-free synthesis of Yb^{III}/Nd^{III} mixed CFs, in different stoichiometric ratios, by using 1,3,5-benzentricarboxylic acid (H_3BTC) as biofriendly organic linker, for biomedical applications as ratiometric thermometers in the physiological temperature range (298-313 k). The materials were structurally and morphologically characterized through XRD and SEM, while their photophysics was studied at room temperature and at variable temperature, in the 10-300 K range, to test their best performances as thermometers.

The present Work is organized as follows:

- ***Part I*** contains a general Introduction on CFs, including design guidelines, synthetic methodologies and technological applications, followed by the Aim of the Work.
- ***Part II*** consists of six different Chapters containing the results (*vide supra*).
- ***Part III*** contains a Summary and Outlook.
- ***Part IV*** contains the Supporting Material *i.e.* Crystallographic Data, FT-IR and Raman Spectra, Dynamic Absorption Breakthrough measurements, Magnetic and Photoluminescence measurements.

ACKNOWLEDGMENTS

Firstly, I would like to express my sincere gratitude to my supervisors: Prof. Maria Laura Mercuri, that has always supported and guided me since the very beginning of my research experience, Prof. Miguel Clemente-León, that has kindly and constantly support me during my stay in Valencia, and Prof. Enzo Cadoni, that has always supported and helped me with fruitful discussion in Organic Chemistry. Their guidance helped me all the time of research and writing of this thesis. Prof. Eugenio Coronado is acknowledged for giving me the opportunity to work in his laboratory at the Instituto de Ciencia Molécular (ICMol), Valencia University, for this co-joint thesis.

I would like to thank Dr. Suchithra Ashoka Sahadevan and Dr. Mariangela Oggianu for the fruitful discussion and their support. I thank also Dr. Rosita Cappai and Dr. Marco Fornasier for all the memorable and funny moments we share in our office, the *Studio Bellissimo.*

I wish to thank Prof. Carla Cannas and Dr. Valentina Mameli (Chemical and Geological Science Department, Cagliari University) for helpful collaboration and discussions in PXRD and SEM-EDX measurements for NIR thermometers, a work that would never have been possible without the fundamental help of Prof. Norberto Masciocchi (Insubria University) in solving the crystal structures from PXRD patterns.

I would also like to acknowledge all the members from RTMM group at ICMol, particularly Prof. Guillermo Mínguez Espallargas, Dr. Mónica Giménez-Marqués, Dr. Eduardo Andres-Garcia and Katia Caamaño for the complete Static and Dynamic Adsorption studies and discussion of the results. Dr. José Baldoví is kindly acknowledged for his precious support performing Theoretical Calculations of Lanthanide based SIMs. Prof Juan Modesto Clemente-Juan is acknowledged for the theoretical fittings of the magnetic measurements of *3d* metal ions based CFs. I also thank Dr. Jorge Romero for performing electrochemical measurements and Dr. Mario Palacios Corella for his help and advices in lab during my stay in Valencia. A special thanks are deserved to Víctor García-López for his constant and kind help and also for all fruitful discussions we had. I also wish to warmly acknowledge Dr. Eleni Mazarakioti for the support and the nice time we have shared in Valencia.

Dr. Bruno J. C. Vieira and Prof. João C. Waerenborgh (Universidade de Lisboa) are

acknowledged for Mossbauer measurements. Prof. Francesco Quochi (Physics Department, Cagliari University), Prof Adolfo Speghini (Verona University), Dr. Manuel Souto, Dr. Carlos Brites and Dr. Miguel Rodriguez (Aveiro University) are greatly acknowledged for luminescent measurements and their contribution to the discussion.

I also kindly acknowledge CeSAR (Centro Servizi d'Ateneo per la Ricerca) *core* facility of Cagliari University for the use of NMR and SEM-EDX equipments, as well as the SCSIE (Servicio Central de Apoyo a la Investigación Experimental) *core* facility of Valencia University for the use of NMR, Mass Spectrometry, SEM-EDX, variable temperature PXRD equipments. Furthermore, J.M. Martínez-Agudo and G. Agustí (ICMol) are acknowledged for performing all magnetic, EPR and MicroRaman measurements, while Alicia Mestre (SCSIE) is acknowledged for performing variable temperature PXRDs.

This work would not have been possible without the financial support from the Italian Ministero dell'Istruzione e della Ricerca (MIUR), which has financed my PhD grant, Sassari and Valencia Universities, INSTM Consortium and COST Action MOLSPIN. I also wish to thank all people from the Chemical and Geological Science Department and the ICMol for the great time spent during these years.

LIST OF ACRONYMS

A

AC	Alternate current
An	Anilate

B

BET	Brunauer–Emmett–Teller
BTC^{3-}	1,3,5-benzentricarboxylate

C

CF	Coordination Framework
CP	Coordination Polymer
Cp_2Co	Cobaltocene
CV	Cyclic Voltammetry
CW	Continuous Wave

D

DC	Direct Current
DDBQ	2,5-Dibromo-3,6-diethoxy-1,4-benzoquinone
DHBQ	2,5-dihydroxy-1,4-benzoquinone
DLS	Dynamic Light Scattering
DR	Diffuse Reflectance

E

EPR	Electron Paramagnetic Resonance
Et	Ethyl

F

F_4BDC^{2-}	Tetrafluoroterephthalate
FT-IR	Fourier Transform-InfraRed

G

H

H_2Br_2An	Bromanilic acid
H_3BTC	1,3,5-benzentricarboxylic acid
H_2Cl_2An	Chloranilic acid
H_2F_4BDC	Tetrafluoroterephthalic Acid

H_2trz_2An	3,6-ditriazolyl-2,5-dihydroxybenzoquinone
HT	High-throughput

I

IS	Isomer Shift

L

LIBs	Lithium Ion Batteries
Ln	Lanthanide

M

Me	Methyl
MIL	Materials Institute Lavoisier
MOF	Metal-Organic Framework

N

NIR	Near Infrared
NEt_4	Tetraethylammonium

P

PL	Photoluminesce
PXRD	Powder X-Ray Diffraction

Q

QS	Quadrupole Splitting

R

REC	Radial Effective Charge
RT	Room Temperature

S

SBU	Secondary Building Unit
SC-XRD	Single Crystal X-Ray Diffraction
SEM	Scanning Electron Microscope
SIM	Single Ion Magnet
SMM	Single Molecule Magnet

T

TGA	Thermogravimetric Analysis
Trz	Triazolyl

U

UV-Vis	Ultraviolet-Visible

X

XRD	X-Ray Diffraction

Z

ZIF	Zeolitic Imidazolate Frameworks
1D	One-dimensional
2D	Two-dimensional
3D	Three-dimensional

Table of Contents

Part I - General Introduction

Part II - Results and Discussion

PART I

General Introduction

1. Molecular Materials

Molecular materials, conventionally described as *materials built by molecules, namely building blocks, able to provide specific functionalities*, are excellent candidates for a wide range of technological applications.[1–4] Molecular materials are commonly classified on the basis of their physical properties, such as magnetic, optical, or electrical ones, which can be originated from the specific nature of the single molecular entity (single-molecule property) or from the interactions that may occur between different molecules (cooperative property). A further classification as *functional or multifunctional molecular materials*[5] takes into account if one or more physical properties are combined and/or in interplay in the same crystal lattice, respectively. The possibility to tailor molecular building blocks and hence the physical properties of the resulting material, is one of the most intriguing potentialities of molecular materials. A fine tuning of molecular systems can be achieved by using the conventional methods of organic chemistry, coordination chemistry and supramolecular chemistry, that give access to a large variety of molecular architectures, ranging from homoleptic or heteroleptic transition metals or lanthanide-based complexes, to coordination polymers, including metal-organic frameworks or supramolecular architectures with various dimensionalities (1D, 2D or 3D). The different molecular architectures are responsible for many intriguing physical properties (**Scheme 1)**, such as Switchable Spin-Crossover Systems, with spin-crossover transitions induced by external stimuli,[6–8] Ferri-/Ferromagnets[9–11] which can show additional conductivity,[12,13] Metals and Semi-/Superconductors,[14,15] Single-Molecule Magnets[16–18] and Luminescent Materials.[19–21]

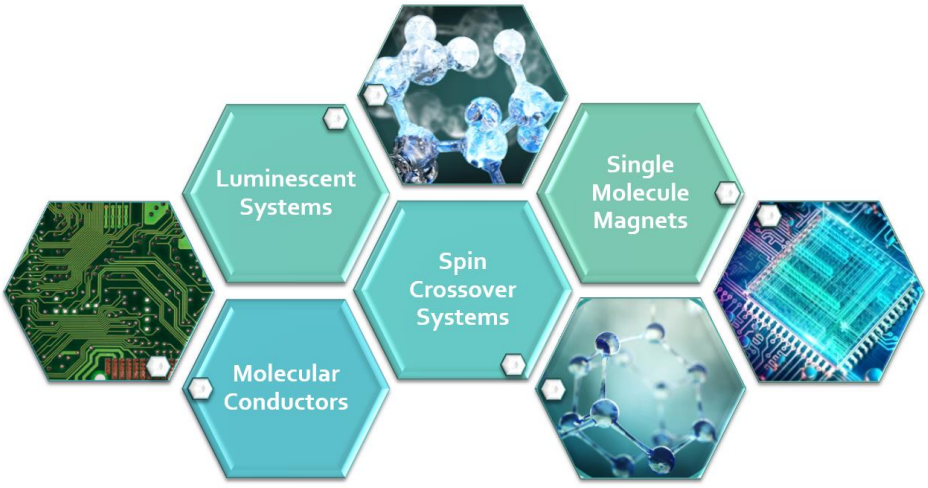

Scheme 1. Selected Molecule-based Materials.

1.1 Coordination Frameworks

Among the large variety of molecular materials, the emerging class of Coordination Frameworks (CFs), has received ever-growing attention, due to the possibility to include porosity to the aforementioned properties, , other than for their thermal and chemical stability, *etc*.[22] CFs are formed by the self-assembly of two main building blocks: the *nodes* (metal ions) and the *linkers* (organic molecules which act as ligands), as represented in **Scheme 2**, connected through coordination bonds. Because of the repetition in one, two or three dimensions of the space, these coordination compounds are called Coordination Polymers (CPs), defined by IUPAC[23] as *"Coordination compounds with repeating coordination entities extending in 1, 2, or 3 dimensions*;
Comment*: Coordination polymers do not need to be crystalline; therefore, the more appropriate terms (for crystalline states) 1-periodic, 2-periodic, and 3-periodic cannot be used throughout. These compounds may even be regarded as salts in some cases, such as those mainly formed by carboxylates. The prefix 1D-, 2D-, or 3D- is acceptable for indicating the degree of extension of the coordination polymer"*.

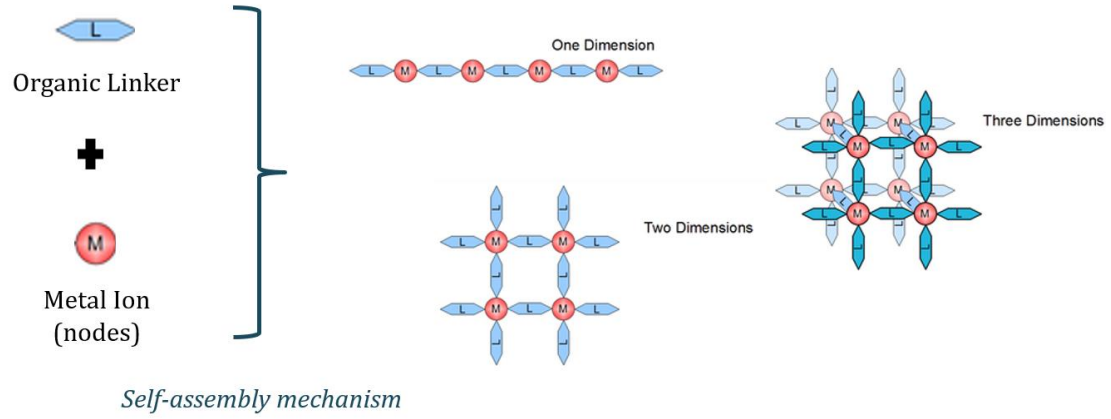

Scheme 2. Schematic representation of building blocks self-assembly mechanism leading to different dimensionalities.

Depending on the way metal ions and linkers are assembled, CPs can show potential voids leading to porous structures able to host molecules, such solvents or gases. In this case, the systems are called Metal-Organic Frameworks (MOFs), defined by IUPAC as "*Coordination Polymers with an open framework containing potential voids*.
Comment: *this wording accounts for the fact that many systems are dynamic and changes in structure and thus corresponding changes in potential porosity or solvent and/or guest filled voids may occur depending on temperature, pressure, or other external stimuli. For*

these reasons it is also not required that a MOF is crystalline. Arguments based on both theory and experiment can be used, suggesting that some of these coordination polymers (i.e., those that can be described as salts) with direct anion-cation binding are more prone to form structures with open frameworks exhibiting permanent porosity than those forming positively charged networks. However, the grey zone between these extremes is large and increasing a definition based on such a charge distinction would be too restrictive." Despite no BET measurements are required to define a material as MOF, as long as it contains potential voids, when the MOF shows a permanent porosity, retaining its porous structure upon insertion/extraction of small molecules, it is much more intriguing than a wonderful supramolecular architecture. After the first example of Metal-Organic Framework reported by Omar Yaghi and coworkers in 1995,[24] in which Copper ions were linked through nitrate ions and bipyridine, a *plethora* of MOFs were reported, making this emerging class of porous materials a challenging platform for relevant technological applications (*vide infra*, Paragraph 4). Due to their surface area with values ranging from 1000 and 10,000 m^2/g,[25] MOFs are employed in several fields, spanning from gas storage and separations, catalysis, to sensing and biomedicine.[26–30] The functional properties of these CFs, engineered for technological applications, can be finely controlled by *i)* the accurate choice of the molecular building blocks and *ii)* the synthetic routes. A rational design of a CF required a proper selection of metal nodes and organic linkers, taking into account *i)* the coordination numbers of metal ions that may give rise to a wide range of different geometries; and *ii)* the coordination modes of organic linkers that can generate different topologies.[31] Generally, mild reaction conditions are used for the synthesis of CFs, in order to control the nucleation and growth of crystals and the most used synthetic routes are hydro/solvothermal methods,[32–34] one-pot reactions,[35,36] slow diffusion techniques,[37,38] microwave[39] and sonochemical methods.[40] The design and synthesis of CFs will be discussed in detail in Paragraph 2 and 3, respectively.

2. Design of Coordination Frameworks

The understanding of the paradigm synthesis-structure-properties-performance[41] is of paramount importance to achieve new systems with specific functionalities of technological interest. Thus, to design a CP with the desired physical properties, the first step relies in the accurate selection of both organic linkers and metal nodes, followed by the development of suitable synthetic protocols. Organic linkers should be generally functionalized with binding groups as carboxylates, catecholates, phosphates, N-heterocycles, *etc*., able to provide extended frameworks through the bonding with the inorganic nodes, metal ions or clusters, commonly called secondary building units (SBUs).[42] In the choice of both organic and inorganic units, some fundamental prerequisites have to be considered. First, the coordination geometry of the organic linker should be accurately preserved during the CFs synthetic process, so that the type of interactions involved in the bonding and the directionality given by those interactions, can introduce a degree of predictability about the formation of the resulting structure. In addition, a basic knowledge of the metal ions coordination chemistry, such as their typical coordination number and/or geometry, is crucial for engineering a specific supramolecular architecture. Furthermore, the synthetic conditions play a role, allowing for the formation of an ordered crystalline material, self-assembled by the default structures of the building blocks. The structure formation is guided by the building blocks inherent directionality and rigidity, hence no structure directing agent has to be added.[42] All the above mentioned prerequisites represent powerful tools for the *a priori* design of CFs with targeted structures, always considering that the control of the spatial arrangement of linkers and the geometry around the metal ions is an ongoing challenge.

2.1 Organic Linkers

The organic linkers, with their geometry and connectivity, in terms of basic geometries and extension points (given by the term topicity, *vide infra*, Figure 2) are responsible of templating the structure of the resulting CFs. Furthermore, they could also provide physical properties to the CF, *i.e.* luminescence[43] and redox activity,[44] for example, the linkers may induce magnetic cooperativity through magnetic exchange[45] or may play the role of organic spacers, inducing Single Molecule Magnets behaviour.[46] Organic linkers could be able to exceptionally enhance the light absorption and consequent emission, *via antenna effect*, of lanthanide metal nodes.[47] Interestingly the linkers can be neutral or charged donors. Neutral donor linkers, *i.e.* bipyridines and nitriles, were firstly used in

the CFs preparation, but the obtained frameworks generally showed chemical and structural instability, with the structure collapsing upon removal of the guest molecules from the pores.[48] To overcome those drawbacks and to obtain more robust frameworks, charged chelating linkers were used afterwards, especially carboxylates which afford more robust structures and favour the formation of polynuclear clusters (SBUs) with a fixed coordination geometry and connectivity.[42,49] More in general, charged linkers allow for the formation of neutral CFs, making unnecessary the use of counter ions, due to the neutralization of the positive charges given by the metal nodes. Furthermore, the bond energy of a charged linker-metal ion bonds is in the 200-400 kJmol^{-1} range, being higher than the energy of neutral linker-metal ion ones (100-200 kJmol^{-1}) and thus providing improved thermal, mechanical and chemical stability.[42] A view of the different bond strength and interactions involved in crystalline extended structures is reported in **Figure 1**.

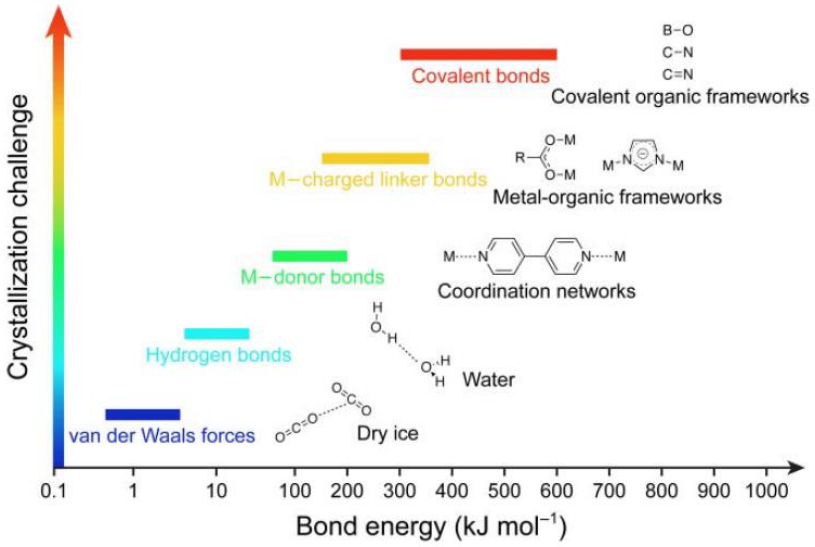

Figure 1. Overview of the different types of bonds and interactions with their energies. (Reprinted from ref [42] *© 2019 Wiley-VCH Verlag GmbH & Co. KGaA*).

On the other hand, organic linker lengths and geometries may afford frameworks characterized by different topologies, always considering that organic chemistry is based on carbon, thus angular constraints allow some geometry being easier to access. The variety of linkers geometry is wide, but in the building frameworks context it is more useful to classify linkers according to the numbers of connections it can make to adjacent SBUs within a framework structure, namely point of extension.

The organic linkers connecting the SBUs, typically have a numbers of points of extension ranging from two to twelve and they are described as ditopic, tritopic, tetratopic, *etc*.[42,50]

In **Figure 2** the most common geometry of linkers with different numbers of point of extension are reported.

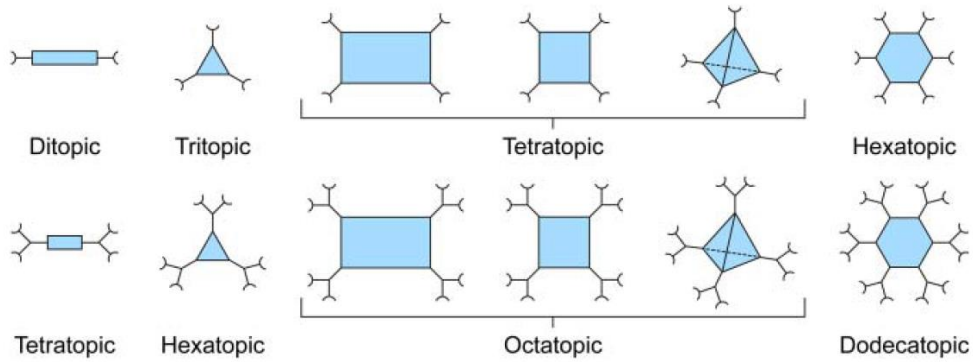

Figure 2. Basic geometries and extension points (given by the term topicity) of organic linkers used in the synthesis of CFs (ranging from 2 to 12 points of extension). (Reprinted from ref [42] *© 2019 Wiley-VCH Verlag GmbH & Co. KGaA*).

Organic linkers can be considered as assembled in three main components, as reported in **Figure 3** for selected examples. The first one is the *core unit* of the linker, which can usually defines the geometry of the backbone (an example is given by tribromobenzene units that template the threefold symmetry), which can be retained or modified by a wise choice of the other fragments, responsible of the length of the linker, called *extending units*. These units can be of different types, classified as follow: *(i)* linear units which provide an extension of the linker without changing its overall geometry and connectivity, *(ii)* angled units that change the overall symmetry but not the connectivity, and *(iii)* branched units that affect both the geometry and the connectivity of the initial *core* unit. Tuning the size of the organic linkers through different extending units, while the geometry/symmetry remains unchanged, afford CFs, particularly MOFs, with related topologies, but showing an expansion of pore sizes and volumes.[51] Furthermore, the *binding groups* are the functional chelating groups such as carboxylates, catecholates, phosphates, N-heterocycles, *etc.*, which bind the linkers to SBUs.

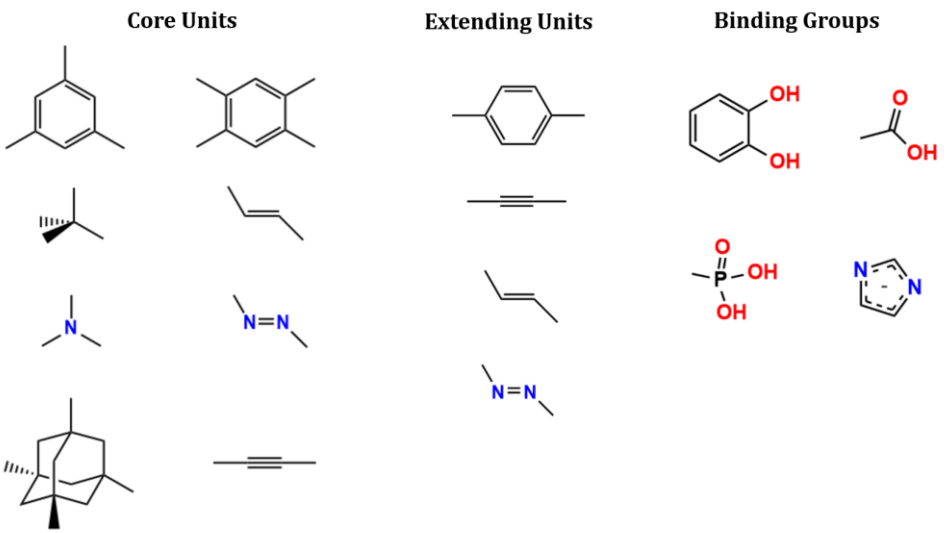

Figure 3. Organic units, used for extending, core units and functional binding groups, mostly employed in the construction of organic linkers.

The majority of organic linkers employed in CFs synthesis are built from rigid unsaturated hydrocarbon *core* and *extending units*, hence they can afford a chemically and mechanically stable framework. After careful selection of both components (*core* and *extending units*), different synthetic methodologies can be used to prepare the desired organic linkers with rigid backbones. Coupling reactions, as carbon–carbon, carbon–heteroatom, or heteroatom–heteroatom couplings, are the most employed. Then, the *binding groups* are introduced during last steps of the synthesis, often along with an *extending unit*, through different routes ranging from coupling reactions to nucleophilic substitutions. Most of the synthetic procedures for these reactions are well established, affording different protocols to synthetize organic linkers in high purity and yields. Nonetheless, the search for improved synthetic protocols and new synthetic paths that lead to the construction of novel designed linkers, with suitable properties and capable to template the desired CFs structures and functionalities, is a continue challenge.[42,50]

2.2 Metal Ions and SBUs

The choice of the metal ion is a crucial step in the design of a CFs is designed, since the metal ions themselves can bring functionalities to the crystal lattice. An interesting example is given by redox active metal ions such as copper or iron, which can either confer redox activity to the CFs to work as cathode material[52,53] or a mixed-valence character which allow for a semiconducting behaviour.[54,55] Another intriguing choice is the selection of lanthanide ions, showing magnetic and/or luminescent properties.[47,56,57]

Depending on the target application of the CFs, *i.e.* biomedical or environmental, metal ions showing biocompatibility or low-toxicity are desirable building blocks, since it might happened that CFs undergo degradation or decomposition, releasing metal ions into the environment.[58,59] Of course, when a metal node has to be chosen, a balance between different factors it is always required. For example, lanthanide based CFs are typically employed in sensing applications,[60,61] despite the toxicity issues of the metals, they remain still the best choice because of the balance between the low amount used in the CFs sensors and the advantages as high sensitivity, robustness and thermal stability of the sensing material. An overview of the most used metal nodes for CFs construction is reported in **Figure 4**.

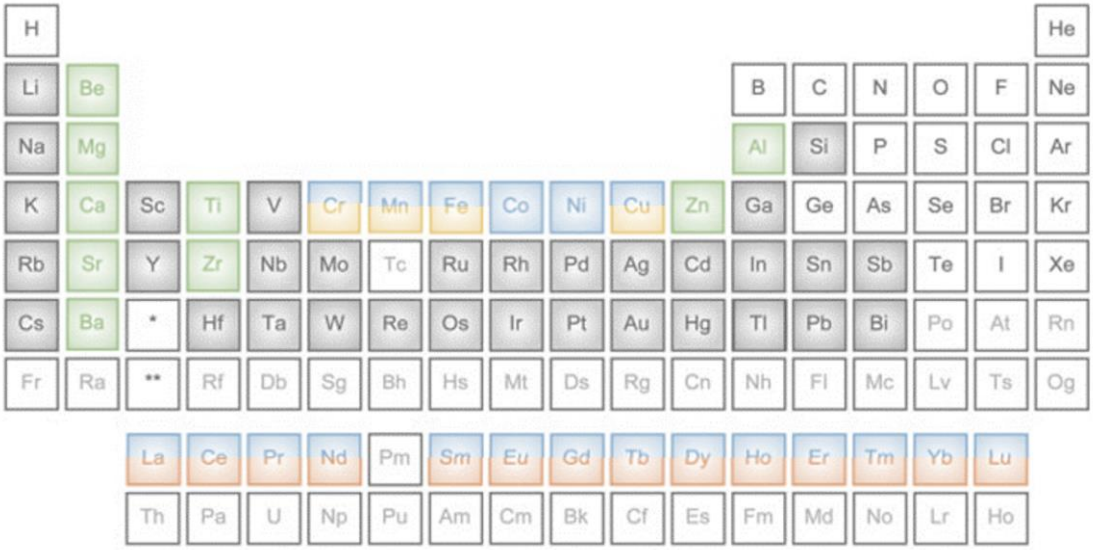

Figure 4. Periodic table with the metals used as nodes in CFs structures. The most employed to display in the final systems low toxicity, magnetism, luminescence and mixed valence behaviors are highlighted in green, blue, orange and yellow, respectively (Modified from ref [42] *© 2019 Wiley-VCH Verlag GmbH & Co. KGaA*).

The metal precursors also need to be chosen carefully, taking into account the synthetic methodology used for CFs. On a large scale synthesis, metal nitrates and perchlorates have risks of explosion, while chloride may induce corrosion,[58,62] hence metal oxides and hydroxides could be used, despite their low solubility/reactivity,[63] or electrochemical methods can be employed (*vide infra*).[62] A further strategy to avoid difficulties with the anions of the metal salts may be the use of zero-valence metal precursors.[34]

The metal nodes can be either single metal ions or polynuclear metal ions clusters (SBUs), connected by the linkers, bearing polydentate binding groups, which are part of these units as well. SBUs formation usually occurs *in situ* through a slow and reversible self-

assembly, affording highly crystalline products.[42] The possible various combinations between metal ions and organic linkers to form SBUs lead to the formation of hundreds SBUs, characterized by different geometries and by a number of points of extension, *i.e.* the numbers of connections they can make to adjacent linkers within a frameworks, ranging from 3 to 12, which confers a wide range of connectivity.[64] Hence, SBUs are excellent building units that permit the construction of a large variety of framework structures. In **Figure 5**, examples of different SBUs with points of extension in the 3-12 range are reported.

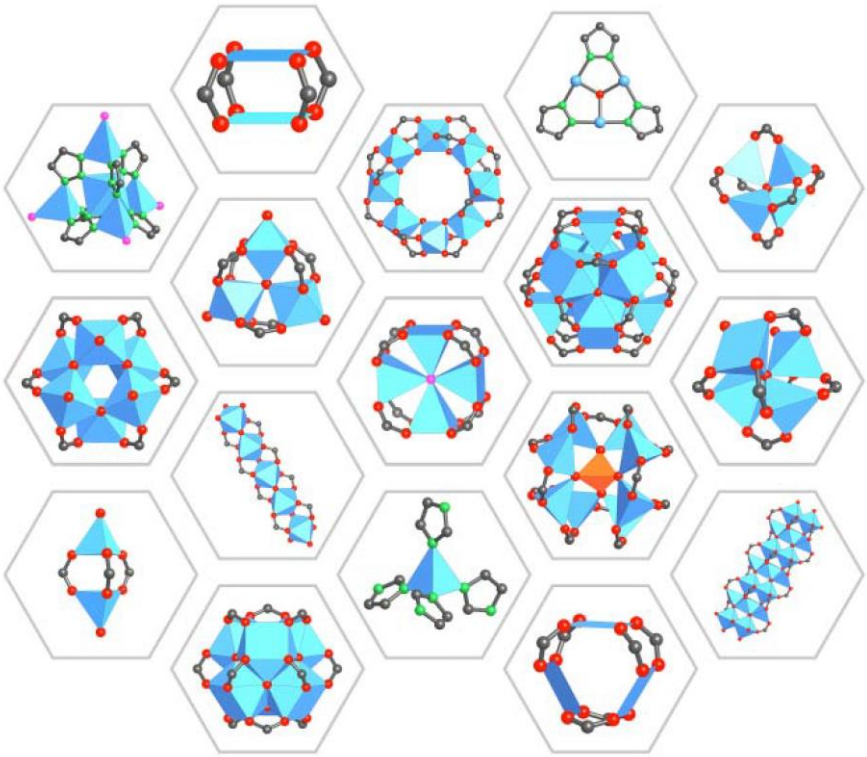

Figure 5. Examples of different SBUs having points of extension in the 3-12 range. (Reprinted from ref [42] *© 2019 Wiley-VCH Verlag GmbH & Co. KGaA*).

3. Synthetic Routes to prepare Coordination Frameworks

The CFs synthesis requires a synergistic effort among organic chemistry, coordination and material chemistry. Organic chemistry provides the synthetic control of the molecules, tailoring substituents with different functionalities, while coordination chemistry is fundamental for the understanding of the geometries variety that can be obtained by the interaction between molecules and metal ions. Finally, material chemistry aims to design and fabricate systems with interesting physical properties, potentially

useful in technological applications. The combination of the basic knowledge of these areas is mandatory in the rational design, synthesis and characterization of CFs.

There are several routes to prepare CFs, ranging from conventional one-pot synthesis, hydro/solvothermal methods, to unconventional use of microwave, sonochemistry, *etc*.[62] An overview of the different synthetic routes is reported in **Scheme 4**.

Scheme 4. Overview of the synthetic routes of CFs.

A well-known methodology, which is also one of the most used, is the solvothermal method, where the metal precursors and organic linkers, both dissolved in a solvent, are usually placed in closed vessels, such as a Teflon vial, inside an autoclave, generating autogenous pressure.[32–34] The commonly used solvents are N,N-dimethylformamide (DMF), Dimethyl sulfoxide (DMSO), N,N-diethylformamide (DEF), acetonitrile, *etc*.[65] If water is used as solvent, the method is called hydrothermal. The temperature and crystallization time varies from room temperature to high temperature, usually above the boiling point of the solvent, followed by cooling, from several hours to days.[62] In order to remarkably reduce the time synthesis and increase the yield, it is possible to couple solvothermal method with microwave. By heating the reaction mixture through a microwave synthesizer it allows to reduce the synthesis time from hours/days to minutes.[39]

Another conventional method for preparing CFs is the one-pot synthesis. The metal ions and organic linkers are dissolved in suitable solvents, under stirring and/or heating, and the powder/crystals are formed *in-situ* by self-assembly.[35,36] This method allow to obtain a large quantity of compounds, but with a less control of nucleation and growth, generally

leading to the formation of a microcrystalline powder instead of single crystals, typically obtained by using solvothermal methods. There are many factors affecting the formation of CFs, such as molar ratios of precursors, pH, solvent, reaction time and temperature, *etc*.[66,67] Hence, it is a very challenging and cumbersome process to optimise the conditions. Remarkably, High-throughput (HT) methods are thus used to systematically investigate several synthetic conditions in parallel, both at room temperature (one-pot synthesis) and using solvothermal reactions.[62,68] HT methods consists of a HT reactor block, which can contains several vials (mainly Teflon vials when the HT method involves solvothermal reactions) with variable volumes, ranging from a few microliters to a few millilitres (**Scheme 5**). Hence, a wide set of reaction parameters can be tested in parallel and in a short time, allowing for a systematic optimisation of reaction conditions.[68]

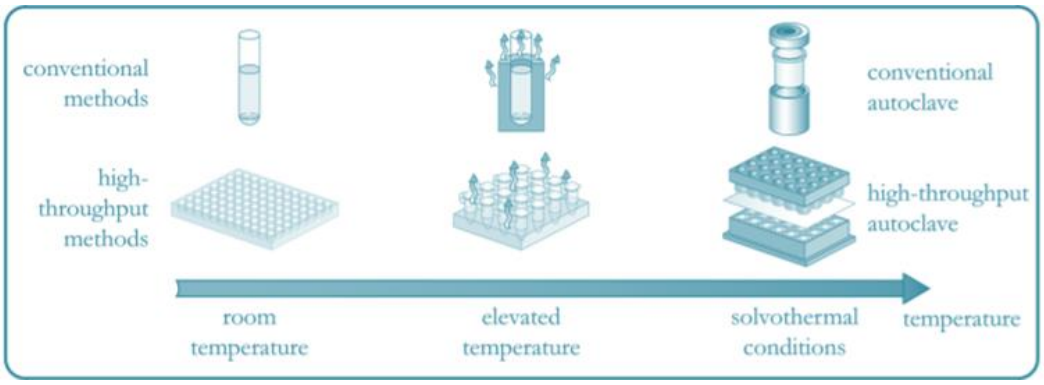

Scheme 5. Schematic representation of conventional and high-throughput methods. (Modified with permission from ref [62] *Copyright © 2012, American Chemical Society*).

A further method based on mild conditions reactions, is the layering technique, which consists in the crystallization by slow diffusion of reactants into each other, leading to concentration gradients of the precursors. Herein, metal precursors, ligands and counterions are dissolved in different miscible solvents with different density, then the solutions are layered on top in a thin test tube. Usually, the crystals are formed at the interface through the slow diffusion over several days/weeks.[37,38]

Recently, new synthetic routes to prepare CFs have been exploited, using a different source of energy instead of heat, such as microwave irradiation, mechanical energy, ultrasounds or the application of an electric potential.[62] The use of microwave irradiation to synthetize CFs consist in the interaction of electromagnetic waves with mobile electric charges, generally given by ions from the precursors in solution or electrons/ions in a solid. A particular attention is needed when solvent and selective energy input are chosen,

since starting materials could interact with the microwaves. Generally the synthesis are carried out at temperature above 100°C, with reaction times ranging from minutes to hours, affording crystalline materials faster and in the nanoscale size range.[69,70] Mechanical energy can be also used to obtain microcrystalline powder CFs, under solvent-free conditions, being an environmental friendly synthetic route, since the use of organic solvents is avoided.[71] Generally these syntheses can be performed at room temperature or with the further use of a thermal treatment, with reaction times in the range of hours/days.[72] A less explored route than the others, is the sonochemical synthesis,[40] where high-energy ultrasounds are applied to reaction mixtures, creating some bubbles in the reaction mixture, where the observed rapid release of energy, lead to temperatures of ~5000 K and pressures of ~1000 bar. A large number of parameters influence the formation of the bubbles and the energy released in it, like the acoustic frequency and intensity, the choice of solvent taking into account its vapor pressure, viscosity and chemical reactivity, the temperature, *etc*.[62]

Finally, CFs can be obtained in form of microcrystalline powders and thin films by using electrochemical methods, as firstly reported in 2005 by researchers at BASF company.[73] They developed an electrochemical method that allow the exclusion of anions, such as nitrate, perchlorate, or chloride, which are not easy to handle when large-scale production processes are required.[62] Hence, instead of using metal salts as precursors, metal ions are provided by using a selected anode which can furnish a continuous anodic dissolution of the ions into the reaction mixture, where an organic linkers, *i.e.* 1,3,5-benzentricarboxylic acid (H_3BTC),[73] and a conducting salt, *i.e* salts whose anion components can be monosulfonate, disulfonate and so on,[74] are also present. The electrochemical methodologies allow to run continuous processes and to obtain higher yields than conventional batch reactions, which are both fundamental requirements for industrial processes. The production of CFs, especially MOFs, in large scale for commercial use, is certainly challenging even though many scientific efforts still have to be done in order to provide accessible, rapid, cost-effective and commercially viable routes, taking into account several parameters, such as availability and cost of starting materials, synthetic conditions, high yields, low percentage of impurities, *etc*. The current research is addressed to the large-scale production of these materials and the scale-up of some well-known MOFs, *i.e.* Fe-MIL-100 and MOF-5, has been recently reported.[65,73]

4. Applications of Coordination Frameworks

Among CFs materials, MOFs are the most studied for technological applications in many relevant fields, involving society challenges, from environment to biomedicine, due to their exceptional surface areas, wide structural diversity and tailorable pore sizes,[75] thus overcoming traditional porous materials. Due to these features, MOFs show relevant properties such as ultrahigh gas storage capacities, high selectivity in gas separations, a unique capability to harvest water from air, *etc.*.[76–79] Furthermore, by a fine tuning of the pore functionalities, it is possible to insert active sites (*i.e.* metals or functional groups) that can act as catalytic centers, favoring selectively reactions of organic molecules.[80,81] By tailoring the pore functionalities it is also possible to tune the electrical properties of the MOFs, affording the formation of porous conductive frameworks.[82] Regarding the CPs, their lack of permanent porosity does not interfere with their use in technological applications, conversely they can also be employed in different fields,[83] including catalysis, sensing and biomedicine.[84–86] An overview of selected CFs technological applications is reported in **Scheme 6**.

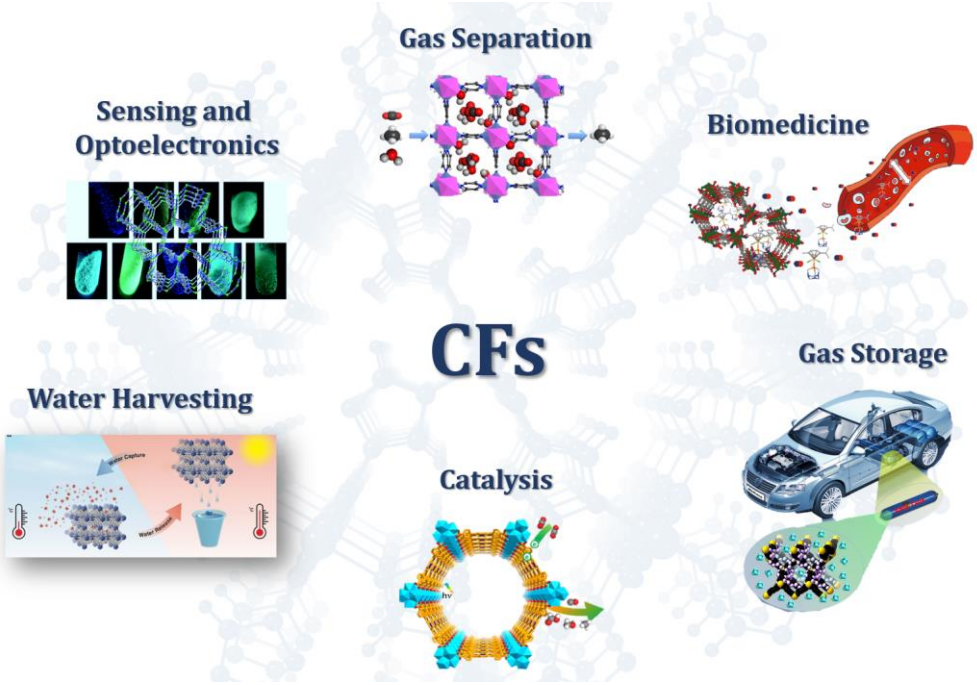

Scheme 6. Overview of selected CFs technological applications.

Among the huge variety of organic linkers (*vide supra*),two main classes *i.e.* carboxylates and anilates derivatives, are gaining ever-growing attention. The carboxylate class, containing at least one aromatic ring as *core unit*, is the most used for its ability to construct thermally and chemically robust 2D and 3D frameworks, through various

coordination modes, excellent candidates for gas storage and separation, catalysis, *etc.*[87]. Recently, the anilato family has been extensively used, in particular for *i)* their *inherent* redox-activity, *i.e.* two-electron reversible reduction to form aromatic hydroquinone/catechol *via* semiquinone radical formation, which leads to a *non-innocent* behavior, with two or more accessible oxidation states of the linker depending on the chelation to metal ion; *ii)* their six-membered ring, easy to functionalize with various substituents/functional groups in order to tune its redox potential, solubility, and the electrochemical response; *iii)* the influence of the steric and electronic nature of substituents of the benzoquinone ring, to modulate the electronic properties of the linker and thus influence the reactivity and physical properties of the resulting materials; *iv)* their excellent ability to construct 2D extended networks. Anilic acids, formulated as $H_2X_2C_6O_4$ (H_2X_2An), where X and C_6O_4 indicate substituents and anilate moiety (An), respectively, are derivatives of 2,5-dihydroxy-1,4-benzoquinone (DHBQ), obtained by replacing the hydrogen at the 3 and 6 position of the quinone ring with different functional groups.

In the present work, the following linkers (**Scheme 7**) belonging to these two classes, have been selected to construct new CFs in order to exploit their physical properties and potential applications (*Part II*). Hence, some recent examples of both carboxylate-based and anilate-based CFs employed in selected cutting-edge application fields, are herein reported.

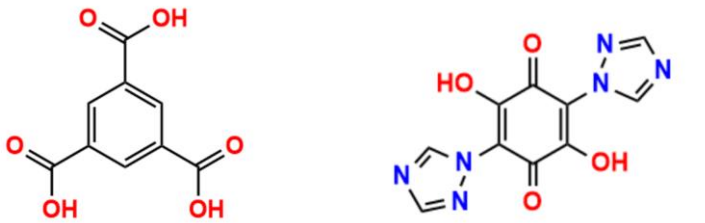

Scheme 7. Organic molecules selected as linkers for the construction of new CFs.

4.1 Carboxylate-based CFs

Carboxylate-based linkers represent the most used family of molecules employed as organic linkers for building CFs. In fact, they are able to strongly chelate metal ions, leading to formation of chemically and thermally robust frameworks, often neutral, since their charged nature neutralizes the positive charges of the metal nodes, avoiding the need

for counter ions. Carboxylate-based linkers also favor the formation of polynuclear clusters (SBUs) with a fixed overall coordination geometry and connectivity, giving precise directionality to the CFs. Some of the most used carboxylate-based linkers, which can also be further functionalized, are reported in **Chart 1**.

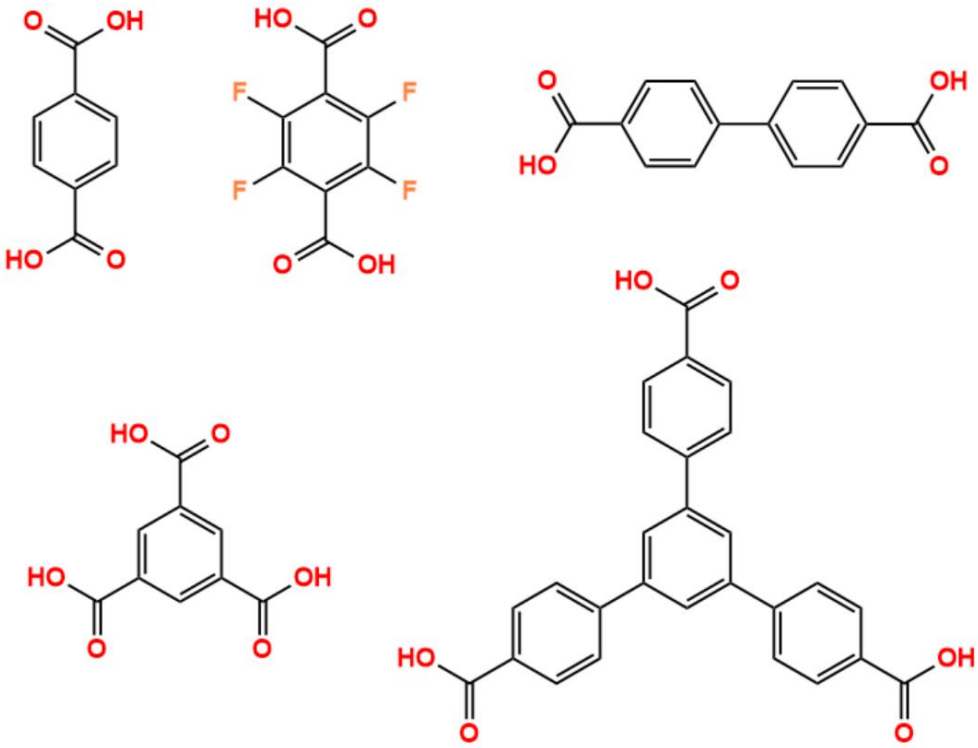

Chart 1. Some of the most used carboxylate linkers.

The linkers belonging to carboxylate family show the further advantage of being biocompatible, hence are the perfect candidates to construct CFs for biomedical applications.[88,89] One of the most extensively used carboxylate linkers is the 1,3,5-benzentricarboxylic acid (BTC), known as trimesic acid, which is one of the building blocks of several MOFs belonging to MIL (Materials of Institute Lavoisier) class; the MOF with Fe^{III} as metal node is one of the most commonly used in biomedicine, spanning from drug delivery and nanothermometry, to biosensing, bioimaging and magnetic resonance imaging (MRI).[28] Among these applications, nanothermometry is receiving great attention in recent years, since the detection of the local temperature of nanostructured biosystems, with sub-micrometric spatial resolution, endows a full understanding of their dynamics, as for example the temperature-dependent cell division rate,[92] and their physical properties which can be influenced by temperature changes, as it occurs in protein denaturation processes.[90,91] More importantly, the temperature sensing of biological tissues at the nanoscale allows for an early diagnosis and treatment of

numerous diseases, including cancer, because major pathological cells show a higher temperature than normal surrounding tissues.[92,93]

MOFs are challenging and versatile platforms for designing luminescence properties, as luminescence can be originated from all their building blocks: metal ions, linkers, and guest ions/molecules. In lanthanide-containing MOFs (LnMOFs), the organic ligands can effectively act as light-harvesting antennas towards the lanthanide ions and sensitize their visible (Vis) or near-infrared (NIR) luminescence via resonance energy transfer (RET) from the lowest triplet state upon intersystem crossing.[94] A thermometer based on lanthanide metal–organic frameworks (LnMOFs) allows to determine absolute temperature, by measuring the intensities of two transitions deriving from distinct emitting centers (linker/Ln(III) ion, dye-hosted in the MOF nanorodes/Ln(III) and Ln(III)-Ln(III)).[95] Recently, a new methodology for luminescent thermometers has been developed based on mixed-lanthanide MOFs (Ln'Ln''MOFs). Mixed Ln'Ln''MOFs thermometers use the intensity ratio of two emissions from different lanthanide ions, commonly Tb(III) and Eu(III), as the thermometric parameter and does not require any additional calibration of luminescence intensity, thus overcoming the main drawbacks of most luminescent thermometers, such as the temperature-dependent intensity of one transition, whose accuracy can be affected by the concentration and inhomogeneity of luminescence centers as well as the optoelectronic drifts of the excitation source and detectors. Both ions are excited to the singlet state of the ligand, which transfers energy into both lanthanide ions. Alternatively, the triplet state of the ligand can be excited from the singlet state, and then it becomes the donor state in the energy transfer process populating Eu^{III} and Tb^{III}. The ligand-to-lanthanide energy transfer is non-resonant and, being phonon assisted, it depends on temperature. Such new luminescent thermometers have distinct advantages over other conventional thermometers because of their high sensitivity, fast response, non-invasive operation, and inertness to strong electric or magnetic fields. Other than sensitivity, other properties such as high thermal stability and luminescence detectable over a wide temperature range are fundamental prerequisites to design highly efficient mixed lanthanide ratiometric thermometers.[95]

In 2016, Rocha *et al.* reported on a microporous MOFs, based on the Eu^{III}-to-Tb^{III} emission ratio Tb^{III}-MIL-103 doped with Eu^{III}, formulated as $[(Tb_{0.95}Eu_{0.05})(btb)(H_2O)]\cdot(solv)_x$ [solv = H_2O, CH_3OH], by using 1,3,5-tris(4-carboxyphenyl)benzene (H_3btb) as organic linker and. This material proved to be a good platform for luminescent ratiometric thermometry, giving its best performances

especially in the cryogenic range (<100 K).[96] Generally, Ln'Ln''MOFs are prepared by using solvothermal synthesis, which affords crystals in the micron-range. Interestingly, they can be also prepared through a solvent-free method by using mechanical energy, provided by grinding the precursors, followed by a thermal treatment. A new family of Ln'Ln''MOFs, Eu^{III} and Dy^{III} co-doped Y-MOFs, showing the MIL-78 topology and the characteristic lanthanide luminescence in the visible range, has been obtained (**Figure 6**).[72] This material can be used as ratiometric thermometer due to the temperature dependence of its blue/red characteristic emissions.

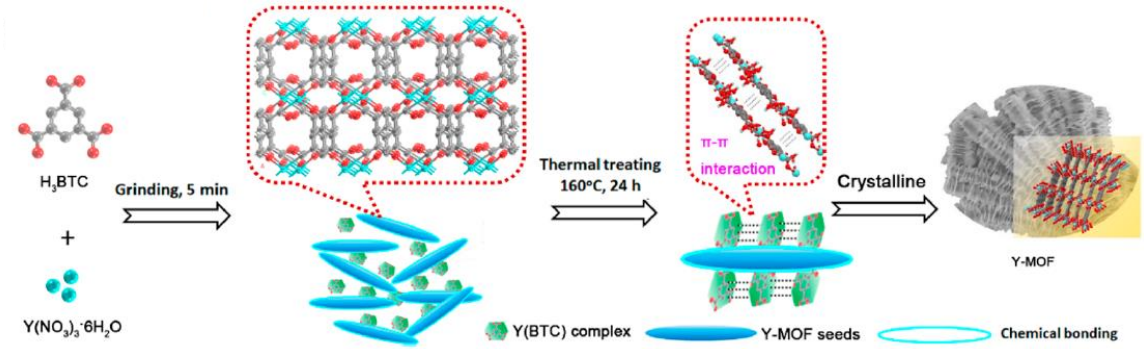

Figure 6. Schematic representation of the synthetic methodology affording Y-MOF crystalline phase. Reprinted with permission from Reference[72] Copyright © 2019, American Chemical Society.

A major drawback of these materials is that the excitation is mainly performed in the ultraviolet (UV) region, thus limiting their use as efficient optical ratiometric thermometers in tissue biological thermometry. Hence, Zaręba *et al.* reported for the first time the multi-photon absorption as a general strategy for performing NIR-to-VIS remote temperature sensing, by shifting the excitation of Eu^{III}, Tb^{III}-CFs wavelength through a nonlinear optical process.[97] NIR instead of UV or visible light should be used as excitation source and the linkers (first and ancillary ligands) should not contain C–H, N–H, and O–H vibrational quenchers of the NIR emission. A novel thermosensitive mixed Ln'Ln''MOFs $(Nd_{0.577}Yb_{0.423})_2(BDC\text{-}F_4)_3\text{-}(DMF)(H_2O)xDMF$ ($H_2BDC\text{-}F_4$ = 2,3,5,6-tetrafluoro-1,4-benzenedicarboxylate), has been recently prepared as a luminescent ratiometric thermometer, showing excellent temperature dependent photoluminescence properties in the physiological 293–313 K temperature range.[98] In this case, $H_2BDC\text{-}F_4$ has been selected as first linker because its triplet energy level is much higher than the accepted level of lanthanide ions (**Scheme 8**), so that the energy transfer or interaction between the linker and the lanthanide ions are prevented. Furthermore, the absence of

some high energy chemical bonds, such as C–H, N–H, and O–H, avoid quenching of lanthanide NIR emission.[98]

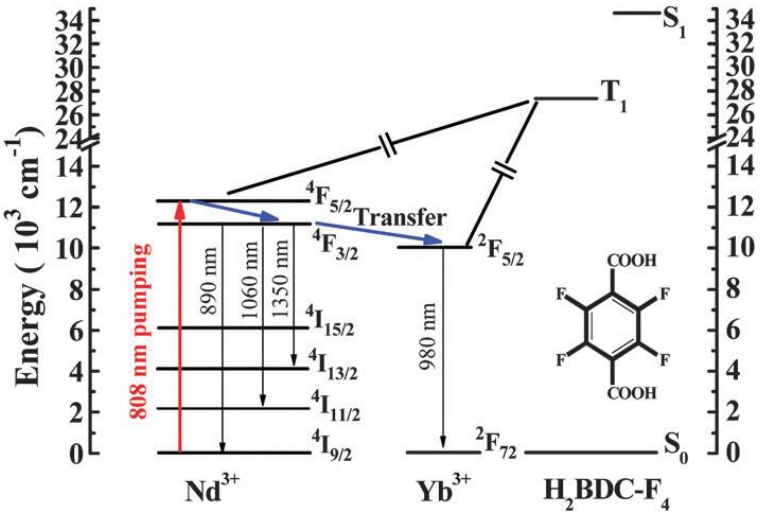

Scheme 8. Schematic representation of energy processes in NIR mixed lanthanide-based MOFs. Reprinted with permission from [98]. Copyright © 2015, The Royal Society of Chemistry.

To improve the thermometric performance of Nd^{III}/Yb^{III} mixed Ln'Ln''MOFs, 1,3,5-benzene-tris-benzoic acid (H_3BTB) has been used as organic linker in the new thermosensitive NIR mixed $Nd_{0.866}Yb_{0.134}BTB$. The H_3BTB linker favors the Ln^{III} sensitization process through the triplet energy level and additionally, the trigonal-planar geometry confers rigidity and robustness to the MOF. This MOF shows excellent temperature dependence of the photoluminescence properties in the physiological range (303 - 333 K), along with low cytotoxicity and good biocompatibility with biological cells.[99] These type of nanothermometers with NIR excitation and NIR luminescence, are harmless for biological tissue, and the resolution is accurate (up to 0.0096 K in some CFs[99]) for measuring the temperature difference in major pathological cells, such as brain tumor cells, which shows a temperature increase in the 0.5–3.3 K range than normal surrounding tissues, thus indicating that these materials can be potentially applied as a luminescent thermometers for biological thermal sensing.[95]

4.2 Anilate-based CFs

Anilate ligands are promising candidates to construct novel Functional and Multifunctional Frameworks (*vide supra*), due to the presence of the benzoquinone ring as *core unit*, easy to functionalize with different substituents at the 3,6 positions, capability to mediate magnetic superexchange interactions between *d*-transition metal

ions,[100] to act as suitable *antennae* towards NIR-emitting lanthanide ions[38,101] and/or to isolate lanthanide ions magnetically, favoring the formation of SIMs/SMMs,[56] and last but not least, their inherent redox activity (*vide supra*)[102] which allows for a significant enhancement of the magnetic ordering temperature and electrical conductivity of the material. Furthermore, anilates are 1,2 bidentate chelating linkers, due to the presence of hydroxy group in 2,5 positions, which can be deprotonated, forming two symmetric chelating groups through the oxygen atoms from carbonyl and hydroxide groups in 1,4 and 2,5 position, respectively. In **Chart 2** some of the most interesting anilates are reported.

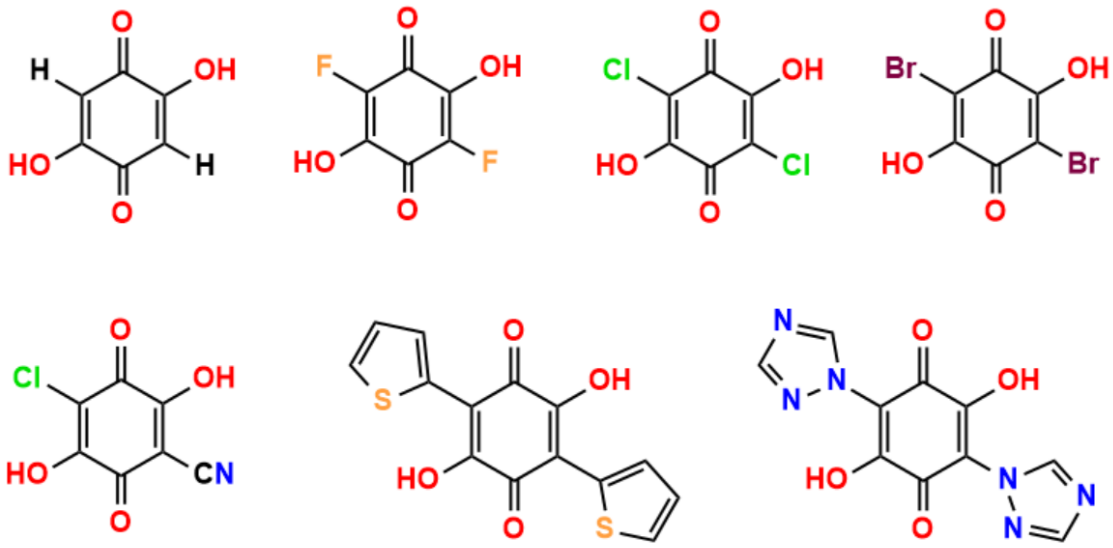

Chart 2. Selected anilate linkers with different substituents.

Generally anilates afford 2D CFs, which show the classical honeycomb packing pattern, where six metal ions are coordinate by anilate ligands forming a hexagonal motif, in which every ion is trischelated, surrounded by six oxygen atoms in an octahedral geometry. By using one-pot reaction, in 2011 Nikitina *et al.* reported on the first example of bimetallic 2D anilate based CFs, where chloranilate linker (Cl_2An^{2-}) coordinates Fe^{III} and Mn^{II}.[103] Anilate-based 2D materials showing peculiar conducting and/or magnetic or luminescent properties have been also reported recently by Mercuri, Avarvari *et al.*[38,104–106] Noteworthy, 2D CPs formed by NIR-emitting lanthanides (Ln^{III} = Er, Nd and Yb) and chlorocianoanilate ($ClCNAn^{2-}$), the first example of heterosubstituted anilate in the family, can be exfoliated, by a top-down approach, to fabricate ultrathin robust and crystalline nanosheets. Since the discovery of graphene, the demand for nanosheets has been of ever-growing interest, as they are powerful platforms with potential applications

in various fields ranging from sensing, biomedicine to electronic devices, despite the research is still at the very early stage. Furthermore, anilate derivative linkers can also afford magnetic lanthanide based-2D CPs. In 2019, Sahadevan *et al.* reported of a new series of four 2D layered CPs based on $ClCNAn^{2-}$ and Dy^{III}, formulated as $[Dy_2(ClCNAn)_3(DMSO)_6]_n$ (two polymorphs), $[Dy_2(ClCNAn)_3(DMF)_6]n\cdot(DCM)_2$ and $[(Me_2NH_2)_2[Dy_2(ClCNAn)_4(H_2O)_2]n\cdot(DMF)$. The materials show a variety of topologies, ranging from (6,3)- to (4,4)-, evidencing the versatility of $ClCNAn^{2-}$ in constructing different 2D frameworks and its capability to mediate anti-ferromagnetic interactions between Dy^{III} ions.[107] Dy-based 2D CPs can also show a slow magnetic relaxation, as reported in 2020 by Benmansour *et al.* They prepared a series of multifunctional 2D CFs based on bromanilate linker (Br_2An^{2-}) and Dy^{III} ions, formulated as $[Dy_2(Br_2An)_3(G)_n]\cdot nG$ (with G = H_2O, dimethylformamide (DMF) and dimethylsulfoxide (DMSO)), shown in **Figure 7**.[108] These CFs are able to reversibly exchange the coordinated and non-coordinated solvent molecules and prove their multifunctionality showing field-induced slow relaxation of the magnetization and luminescence, which can be influenced by solvent exchange.

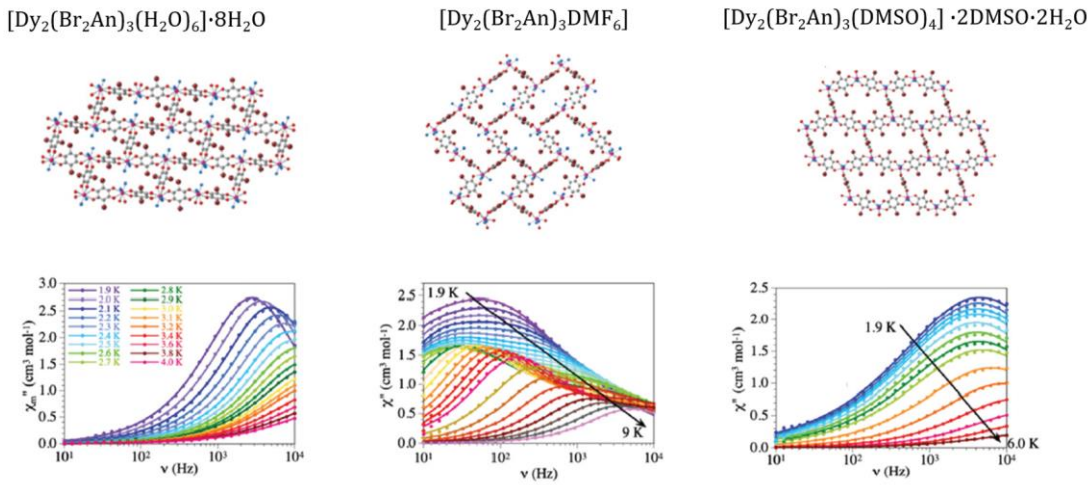

Figure 7. Layered structures of the different Br_2An based CFs along with their frequency dependence of χ_m'' at different temperature (dc field of 1000 Oe). Reprinted with permission from Reference[108] Copyright © 2019, The Royal Society of Chemistry.

Furthermore, they capability to undergo one-electron reduction to form the semiquinone, starting from the benzoquinone moiety, aroused an ever-growing interest in using them as building blocks of CFs with improved physical properties.[109–112] One of these interesting examples was reported by Harris and co-workers in 2015,[102,111] which

prepared a porous semiquinoid magnet (**Figure 8**), formulated as $(Me_2NH_2)_2[Fe_2(Cl_2An)_3]\cdot 2H_2O\cdot 6DMF$, with a BET surface area of 885(105) m^2g^{-1}.
In this CF, iron metal ions are present in a mixed valence state Fe^{II}/Fe^{III}, as well as the chloranilate bridging ligand which is simultaneously present in its benzoquinoid and semiquinoid form, generated *in situ*,[102] and leading to a porous antiferromagnet, with a spontaneous magnetization below 80 K. Due to its delocalized nature, this CF shows also conductivity values of $\sigma = 1.4(7) \times 10^{-2}$ S cm^{-1} (E_a = 0.26(1) eV), being a porous multi-functional framework with the coexistence of magnetism and conductivity. Furthermore, by soaking this material in a cobaltocene (Cp_2Co) solution for 48 hours, a new compound, formulated as $(Cp_2Co)_{1.43}(Me_2NH_2)_{1.57}[Fe_2L_3]\cdot 4.9DMF$, was obtained. The significant increase of semiquinones in the CF leads to stronger magnetic exchange interactions between metal ions, causing an increase of the magnetic ordering temperature up to 105 K, which is a remarkable value for a metal-organic solid and one of the highest values for a semiquinone-based framework,[111] of considerable interest for spintronics applications, in next-generation data processing and storage.

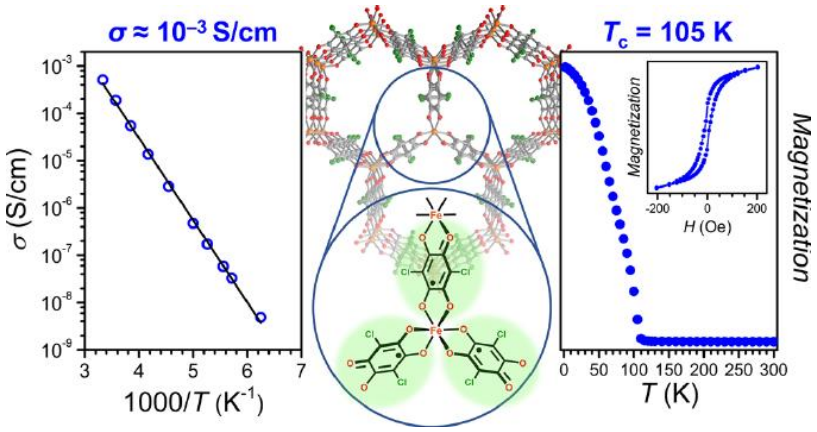

Figure 8. Plot of conductivity properties (left) and variable-temperature field-cooled magnetization recorded under an applied dc field of 10 Oe (right) for $(Me_2NH_2)_2[Fe_2(Cl_2An)_3]\cdot 2H_2O\cdot 6DMF$. Perspective view of crystal structure of $(Me_2NH_2)_2[Fe_2(Cl_2An)_3]\cdot 2H_2O\cdot 6DMF$ along the *c* axis, having the typical honeycomb motif, shown in the middle. Reprinted with permission from Reference[111] Copyright © 2015, American Chemical Society.

The versatility of anilates in the construction of CFs with applications in different fields, such as gas sorption, it has been recently further explored by Abrahams *et al.* Interestingly they reported on a 1D CFs of Mg^{II} or Zn^{II} metal ions, linked through hydranilate (H_2An^{2-}) formed *in situ*, formulated as $M^{II}(H_2An)(H_2O)_2\cdot 2H_2O\cdot xROH$, (M = Mg or Zn). These 1D CFs were able to uptake significant amounts of H_2, CO_2 and CH_4 at low pressures, upon dehydration that afford microporous material.[113] Noteworthy they also reported on

the synthesis of novel anilate-based CFs, formulated as $(NEt_4)_2[Zn_2(Cl_2An)_3]$ and $(NEt_4)_2[Zn_2(F_2An)_3]$, with a layered cationic/anionic structure of (6,3)-topology, where the NEt_4^+ cations template the anionic layers in an eclipsed way to form large cavities. This porous MOFs shows almost 40% of void volume and it is capable to capture significant amounts of CO_2. Furthermore, Abrahams and co-workers reported on a CF with layered anionic square-grid structure with interleaved layers of counter-cations, formulated as $(NEt_4)[Y(Cl_2An)_2]$, that show high sorption enthalpies for H_2, N_2, CO_2 and, particularly, CH_4.[37,114] Finally, selected examples of different anilato-based CFs structures are reported in **Scheme 9**.

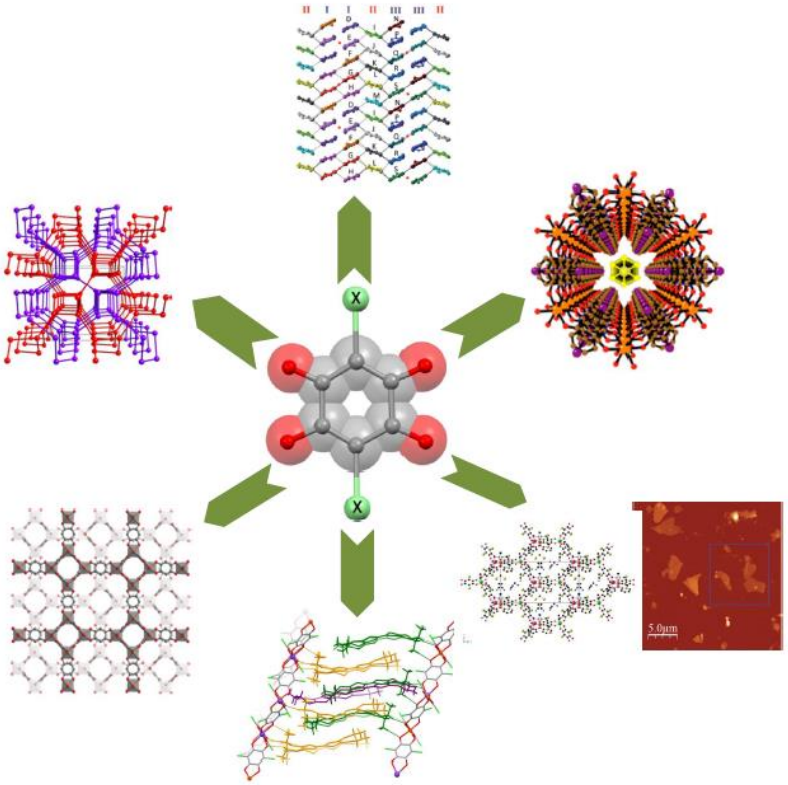

Scheme 9. Overview of different anilato-based CFs structures.

5. Aim of the Work

The present Work aims to develop novel CFs with magnetic and/or optical properties, to exploit their potential in specific technological applications, from temperature sensing to gas separation. To achieve this goal, two different linkers has been selected: the 1,3,5-benzentricarboxylic acid (trimesic acid), a biofriendly tritopic linker, which possess an aromatic ring as *core unit* and an unexplored anilate tetratopic linker, bearing two triazolyl groups at the 3,6 positions of the benzoquinone ring, which allow the construction of 3D frameworks, when compared to the ditopic conventional anilates. As metal nodes, a wide variety of *d*-(M^{II}=Co, Cu, Ni, Mn and Fe) and *f*-(Ln^{III}=Nd, Er, Yb, Dy, Tb, Ho) transition metal ions has been selected in order to engineer CFs with magnetic and/or luminescent properties. The characterization of the obtained materials has been performed through a Multi-Technique Approach involving X-Ray Diffraction on single crystals and powders (SC-XRD and PXRD), Magnetometry (SQUID and PPMS), Spectroscopic Techniques (FT-IR, Raman, Photoluminescence) and Thermogravimetric Analysis (TGA). The experimental magnetic and luminescent measurements are supported by theoretical calculations, by using Radial Effective Charge (REC) Model.

The Research Activity has been carried out as follow:

- Synthesis and Characterization of the tetratopic 3,6-ditriazolyl-anilate and the novel 3,6-N-(dipyrazolyl-4-carboxylic acid) anilate (Chapter 1).
- Design, Synthesis, Structural and Physical Characterization of the new class of magnetic and redox-active *3d*-transition metal ions/3,6-ditriazolyl-anilate MOFs (Chapter 2).
- Static and Dynamic Adsorption Studies on Co-triazolyl-anilato-based ultramicroporous MOF, as showing high selectivity, high adsorption capacity and high regenerability for CO_2 absorption and separation from CO_2/CH_4 mixtures, other than a scalable synthetic protocol, thus an optimal candidate in separation technology industry (Chapter 3).
- Design, Synthesis, Structural and Physical Characterization of the new class of lanthanide metal ions/3,6-ditriazolyil-anilate CPs/MOFs, with a particular emphasis on their structural flexibility which has been proven to be, in the case of the Er^{III}-based multifunctional MOF, a challenging strategy to tune Luminescent and Single Ion Magnet properties (Chapter 4 and 5).

- ❖ Design, Synthesis, Structural and Physical Characterization of CPs based on NIR-emitting lanthanide ions (Yb^{III} and Nd^{III}) and 1,3,5-benzentricarboxylic acid, as suitable ratiometric mixed Lanthanide thermometers for biological applications (Chapter 6).

References

1 S. Roth, M. Burghard and G. Leising, *Curr. Opin. Solid State Mater. Sci.*, 1998, **3**, 209–215.

2 D. L. Ma, H. Z. He, K. H. Leung, D. S. H. Chan and C. H. Leung, *Angew. Chem. - Int. Ed.*, 2013, **52**, 7666–7682.

3 R. Thomas, S. P. Thomas, H. Lakhotiya, A. H. Mamakhel, M. Bondesgaard, V. Birkedal and B. B. Iversen, *Chem. Sci.*, 2021, **12**, 12391–12399.

4 X.-L. Chen, X.-D. Tao, Z. Wei, L. Meng, F.-L. Lin, D.-H. Zhang, Y.-Y. Jing and C.-Z. Lu, *ACS Appl. Mater. Interfaces*, 2021, **13**, 46909–46918.

5 M. Atzori and F. Artizzu, *Functional Molecular Materials: An Introductory Textbook*, Pan Stanford Publishing Pte. Ltd., 2018.

6 C. P. Kohler, R. Jakobi, E. Meissner, L. Wiehl, H. Spiering and P. Gutlich, *J. Phys. Chem. Solids*, 1990, **51**, 239–247.

7 P. Gutlich, V. Ksenofontov and A. B. Gaspar, *Coord. Chem. Rev.*, 2005, **249**, 1811–1829.

8 S. Ohkoshi, K. Imoto, Y. Tsunobuchi, S. Takano and H. Tokoro, *Nat. Chem.*, 2011, **3**, 564–569.

9 J. S. Miller, A. J. Epstein and W. M. Reiff, *Science*, 1988, **240**, 40–47.

10 S. A. Chavan, J. V Yakhmi and I. K. Gopalakrishnan, *Mater. Sci. Eng. C*, 1995, **3**, 175–179.

11 S. Konar, P. S. Mukherjee, E. Zangrando, F. Lloret and N. R. Chaudhuri, *Angew. Chemie*, 2002, **114**, 1631–1633.

12 E. Coronado, J. R. Galán-Mascarós, C. J. Gómez-García and V. Laukhin, *Nature*, 2000, **408**, 447–449.

13 E. Coronado and P. Day, *Chem. Rev.*, 2004, **104**, 5419–5448.

14 J. Ferraris, D. O. Cowan, V. Walatka and J. H. Perlstein, *J. Am. Chem. Soc.*, 1973, **95**, 948–949.

15 R. P. Shibaeva and E. B. Yagubskii, *Chem. Rev.*, 2004, **104**, 5347–5378.

16 G. Cosquer, Y. Shen, M. Almeida and M. Yamashita, *Dalt. Trans.*, 2018, **47**, 7616–7627.

17 A. Zabala-Lekuona, J. M. Seco and E. Colacio, *Coord. Chem. Rev.*, 2021, **441**, 213984.

18 R. Sessoli, D. Gatteschi, A. Caneschi and M. A. Novakt, *Nature*, 1993, **365**, 141–143.

19 D. S. Chemla and J. Zyss, *Nonlinear Optical Properties of Organic Molecules and Crystal*, Academic Press, New York, 1987, vol. 1.

20 R. J. Curry and W. P. Gillin, *Appl. Phys. Lett.*, 1999, **75**, 1380–1382.

21 F. Artizzu, L. Marchiò, M. L. Mercuri, L. Pilia, A. Serpe, F. Quochi, R. Orrù, F. Cordella, M. Saba, A. Mura, G. Bongiovanni and P. Deplano, *Adv. Funct. Mater.*, 2007, **17**, 2365–2376.

22 O. M. Yaghi, *J. Am. Chem. Soc.*, 2016, **138**, 15507–15509.

23 S. R. Batten, N. R. Champness, X.-M. Chen, J. Garcia-Martinez, S. Kitagawa, L. Öhrström, M. O'keeffe, M. P. Suh and J. Reedijk, *Pure Appl. Chem*, 2013, **85**, 1715–1724.

24 O. M. Yaghi and H. Li, *J. Am. Chem. Soc.*, 1995, **117**, 10401–10402.

25 H. Furukawa, K. E. Cordova, M. O'Keeffe and O. M. Yaghi, *Science*, 2013, **341**, 1230444.

26 M. Eddaoudi, J. Kim, N. Rosi, D. Vodak, J. Wachter, M. O. Keeffe and O. M. Yaghi, *Science*, 2002, **295**, 469–472.

27 V. Pascanu, G. González Miera, A. K. Inge and B. Martín-Matute, *J. Am. Chem. Soc.*, 2019, **141**, 7223–7234.

28 M. Oggianu, N. Monni, V. Mameli, C. Cannas, S. A. Sahadevan and M. L. Mercuri, *Magnetochemistry*, 2020, **6**, 1–14.

29 Z. Hu, B. J. Deibert and J. Li, *Chem. Soc. Rev.*, 2014, 43, 5815–5840.

30 M. J. Uddin, R. E. Ampiaw and W. Lee, *Chemosphere*, 2021, **284**, 131314.

31 S. Kitagawa, R. Kitaura and S. Noro, *Angew. Chemie Int. Ed.*, 2004, **43**, 2334–2375.

32 M. Bosch, X. Sun, S. Yuan, Y.-P. Chen, Q. Wang, X. Wang and H.-C. Zhou, *Eur. J. Inorg. Chem.*, 2016, **2016**, 4368–4372.

33 S. Nayak, H. P. Nayek, C. Pietzonka, G. Novitchi and S. Dehnen, *J. Mol. Struct.*, 2011, **1004**, 82–87.

34 M. Faustini, J. Kim, G. Jeong, J. Y. Kim, H. R. Moon, W. Ahn and D. Kim, *J. Am. Chem. Soc.*, 2013, **135**, 14619–14626.

35 W. Lou, J. Yang, L. Li and J. Li, *J. Solid State Chem.*, 2014, **213**, 224–228.

36 J. Soo Seo, D. Whang, H. Lee, S. Im Jun, J. Oh, Y. Jin and K. Kim, *Nature*, 2000, **404**, 982–986.

37 C. J. Kingsbury, B. F. Abrahams, J. E. Auckett, H. Chevreau, A. D. Dharma, S. Duyker, Q. He, C. Hua, T. A. Hudson, K. S. Murray, W. Phonsri, V. K. Peterson and R. Robson, *Chem. Eur. J.*, 2019, **25**, 5222–5234.

38 S. Ashoka Sahadevan, N. Monni, A. Abhervé, D. Marongiu, V. Sarritzu, N. Sestu, M. Saba, A. Mura, G. Bongiovanni, C. Cannas, F. Quochi, N. Avarvari, M. L. Mercuri, A. Abherve, D. Marongiu, V. Sarritzu, N. Sestu, M. Saba, A. Mura, G. Bongiovanni, C. Cannas, F.

Quochi, N. Avarvari and M. L. Mercuri, *Chem. Mater.*, 2018, **30**, 6575–6586.

39 Z. Ni and R. I. Masel, *J. Am. Chem. Soc.*, 2006, **128**, 12394–12395.

40 W.-J. Son, J. Kim, J. Kim and W.-S. Ahn, *Chem. Commun. (Camb).*, 2008, 6336–6338.

41 G. B. Olson, *Science*, 1997, **277**, 1237–1242.

42 O. M. Yaghi, M. J. Kalmutzki and C. S. Diercks, *Introduction to Reticular Chemistry*, Wiley - VCH, 2019.

43 P. Samanta, S. Let, W. Mandal, S. Dutta and S. K. Ghosh, *Inorg. Chem. Front.*, 2020, **7**, 1801–1821.

44 J. Calbo, M. J. Golomb and A. Walsh, *J. Mater. Chem. A*, 2019, **7**, 16571–16597.

45 G. Mínguez Espallargas and E. Coronado, *Chem. Soc. Rev.*, 2018, **47**, 533–557.

46 G. Brunet, D. A. Safin, J. Jover, E. Ruiz and M. Murugesu, *J. Mater. Chem. C*, 2017, **5**, 835–841.

47 S. Ashoka Sahadevan, N. Monni, A. Abhervé, D. Marongiu, V. Sarritzu, N. Sestu, M. Saba, A. Mura, G. Bongiovanni, C. Cannas, F. Quochi, N. Avarvari and M. L. Mercuri, *Chem. Mater.*, 2018, **30**, 6575–6586.

48 S. Subramanian and M. J. Zaworotko, *Angew. Chem. Int. Ed. Engl.*, 1995, **34**, 2127–2129.

49 O. M. Yaghi, G. Li and Li Hailian, *Nature*, 1995, **378**, 703–706.

50 W. Lu, Z. Wei, Z. Y. Gu, T. F. Liu, J. Park, J. Park, J. Tian, M. Zhang, Q. Zhang, T. Gentle, M. Bosch and H. C. Zhou, *Chem. Soc. Rev.*, 2014, 43, 5561–5593.

51 G. E. M. Schukraft, S. Ayala, B. L. Dick and S. M. Cohen, *Chem. Commun.*, 2017, **53**, 10684–10687.

52 Z. Zhang, H. Yoshikawa and K. Awaga, *J. Am. Chem. Soc.*, 2014, **136**, 16112–16115.

53 Q. Jiang, P. Xiong, J. Liu, Z. Xie, Q. Wang, X. Q. Yang, E. Hu, Y. Cao, J. Sun, Y. Xu and L. Chen, *Angew. Chemie - Int. Ed.*, 2020, **59**, 5273–5277.

54 S. A. Sahadevan, A. Abhervé, N. Monni, C. Sáenz De Pipaón, J. R. Galán-Mascarós, J. C. Waerenborgh, B. J. C. Vieira, P. Auban-Senzier, S. Pillet, E.-E. Bendeif, P. Alemany, E. Canadell, M. L. Mercuri and N. Avarvari, *J. Am. Chem. Soc.*, 2018, **140**, 12611–12621.

55 S. Benmansour, A. Abhervé, P. Gómez-Claramunt, C. Vallés-García and C. J. Gómez-García, *ACS Appl. Mater. Interfaces*, 2017, **9**, 26210–26218.

56 S. Benmansour and C. J. Gómez-García, *Magnetochemistry*, 2020, **6**, 1–44.

57 T. N. Nguyen, S. V. Eliseeva, A. Gładysiak, S. Petoud and K. C. Stylianou, *J. Mater. Chem. A*, 2020, **8**, 10188–10192.

58 P. Rocío-Bautista, I. Taima-Mancera, J. Pasán and V. Pino, *Separations*, 2019, **6**, 1–21.

59 Y. Bai, Y. Dou, L. H. Xie, W. Rutledge, J. R. Li and H. C. Zhou, *Chem. Soc. Rev.*, 2016, **45**, 2327–2367.

60 S. Ashoka Sahadevan, N. Monni, M. Oggianu, A. Abhervé;, D. Marongiu, M. Saba, A. Mura, G. Bongiovanni, V. Mameli, C. Cannas, N. Avarvari, F. Quochi and M. L. Mercuri, *ACS Appl. Nano Mater.*, 2020, **3**, 94–104.

61 S. M. Sheta, S. M. El-Sheikh and M. M. Abd-Elzaher, *Anal. Bioanal. Chem.*, 2019, **411**, 1339–1349.

62 N. Stock and S. Biswas, *Chem. Rev.*, 2012, **112**, 933–969.

63 M. Gaab, N. Trukhan, S. Maurer, R. Gummaraju and U. Müller, *Microporous Mesoporous Mater.*, 2012, **157**, 131–136.

64 D. J. Tranchemontagne, J. L. Tranchemontagne, M. O'keeffe and O. M. Yaghi, *Chem. Soc. Rev.*, 2009, **38**, 1257–1283.

65 A. U. Czaja, N. Trukhan and U. Müller, *Chem. Soc. Rev.*, 2009, **38**, 1284–1293.

66 D. Sud and G. Kaur, *Polyhedron*, 2021, **193**, 114897.

67 Q. Xia, H. Wang, B. Huang, X. Yuan, J. Zhang, J. Zhang, L. Jiang, T. Xiong and G. Zeng, *Small*, 2019, **15**, 1–25.

68 R. Banerjee, A. Phan, B. Wang, C. Knobler, H. Furukawa, M. O'Keeffe and O. M. Yaghi, *Science*, 2008, **319**, 939–943.

69 P. Horcajada, T. Chalati, C. Serre, B. Gillet, C. Sebrie, T. Baati, J. F. Eubank, D. Heurtaux, P. Clayette, C. Kreuz, J. S. Chang, Y. K. Hwang, V. Marsaud, P. N. Bories, L. Cynober, S. Gil, G. Férey, P. Couvreur and R. Gref, *Nat. Mater.*, 2010, **9**, 172–178.

70 S. H. Jhung, J. H. Lee, J. W. Yoon, C. Serre, G. Férey and J. S. Chang, *Adv. Mater.*, 2007, **19**, 121–124.

71 A. Pichon, A. Lazuen-Garay and S. L. James, *CrystEngComm*, 2006, **8**, 211–214.

72 J. Liu, L. Pei, Z. Xia and Y. Xu, *Cryst. Growth Des.*, 2019, **19**, 6586–6591.

73 U. Mueller, M. Schubert, F. Teich, H. Puetter, K. Schierle-Arndt and J. Pastré, *J. Mater. Chem.*, 2006, **16**, 626–636.

74 Mueller, U.; Puetter, H.; Hesse, M.; Wessel, H. WO 2005/049892

75 H. Furukawa, N. Ko, Y. B. Go, N. Aratani, S. B. Choi, E. Choi, A. Ö. Yazaydin, R. Q. Snurr, M. O'Keeffe, J. Kim and O. M. Yaghi, *Science (80-.).*, 2010, **329**, 424–428.

76 A. M. Fracaroli, H. Furukawa, M. Suzuki, M. Dodd, S. Okajima, F. Gandara, J. A. Reimer and O. M. Yaghi, *J. Am. Chem. Soc.*, 2014, **136**, 8863–8866.

77 P. Nugent, E. G. Giannopoulou, S. D. Burd, O. Elemento, E. G. Giannopoulou, K. Forrest, T. Pham, S. Ma, B. Space, L. Wojtas, M. Eddaoudi and M. J. Zaworotko, *Nature*, 2013, **495**, 80–84.

78 J. Canivet, A. Fateeva, Y. Guo, B. Coasne and D. Farrusseng, *Chem. Soc. Rev.*, 2014, **43**, 5594–5617.

79 H. Kim, S. Yang, S. R. Rao, S. Narayanan, E. A. Kapustin, H. Furukawa, A. S. Umans, O. M. Yaghi and E. N. Wang, *Science*, 2017, **358**, 1–10.

80 K. Manna, P. Ji, Z. Lin, F. X. Greene, A. Urban, N. C. Thacker and W. Lin, *Nat. Commun.*, 2016, **7**, 1–11.

81 J. E. Mondloch, M. J. Katz, W. C. Isley, P. Ghosh, P. Liao, W. Bury, G. W. Wagner, M. G. Hall, J. B. Decoste, G. W. Peterson, R. Q. Snurr, C. J. Cramer, J. T. Hupp and O. K. Farha, *Nat. Mater.*, 2015, **14**, 512–516.

82 L. Sun, C. H. Hendon, M. A. Minier, A. Walsh and M. Dincə, *J. Am. Chem. Soc.*, 2015, **137**, 6164–6167.

83 A. Morsali and L. Hashemi, in *Main Group Metal Coordination Polymers: Structures and Nanostructures*, John Wiley & Sons, Inc., 2017, pp. 17–30.

84 R. F. Mendes, M. M. Antunes, P. Silva, P. Barbosa, F. Figueiredo, A. Linden, J. Rocha, A. A. Valente and F. A. Almeida Paz, *Chem. - A Eur. J.*, 2016, **22**, 13136–13146.

85 X. Liu, L. Cui, K. Yu, J. Lv, Y. Liu, Y. Ma and B. Zhou, *Inorg. Chem.*, 2021, **60**, 14072–14082.

86 J. L. Wang, X. Y. Wang, Y. H. Wang, X. Y. Hu, J. R. Lian, Y. L. Guan, H. Y. Chen, Y. J. He and H. S. Wang, *Coord. Chem. Rev.*, 2020, **411**, 213256.

87 M. Safaei, M. M. Foroughi, N. Ebrahimpoor, S. Jahani, A. Omidi and M. Khatami, *Trends Anal. Chem.*, 2019, **118**, 401–425.

88 S. Rojas, T. Devic and P. Horcajada, *J. Mater. Chem. B*, 2017, **5**, 2560–2573.

89 T. Hidalgo, M. Alonso-Nocelo, B. L. Bouzo, S. Reimondez-Troitiño, C. Abuin-Redondo, M. De La Fuente and P. Horcajada, *Nanoscale*, 2020, **12**, 4839–4845.

90 F. Tardieu, M. Reymond, P. Hamard, C. Granier and B. Muller, *J. Exp. Bot.*, 2000, **51**, 1505–1514.

91 G. N. Somero, *Annu. Rev. Physiol.*, 1995, **57**, 43–68.

92 A. M. Stark and S. Way, *Cancer*, 1975, **33**, 1664–1670.

93 T. B. Huff, L. Tong, Y. Zhao, M. N. Hansen, J.-X. Cheng and A. Wei, *Nanomedicine*, 2007, **2**, 125–132.

94 W. P. Lustig, S. Mukherjee, N. D. Rudd, A. V. Desai, J. Li and S. K. Ghosh, *Chem. Soc. Rev.*, 2017, **46**, 3242–3285.

95 J. Rocha, C. D. S. Brites and L. D. Carlos, *Chem. Eur. J.*, 2016, **22**, 14782–14795.

96 D. Ananias, C. D. S. Brites, L. D. Carlos and J. Rocha, *Eur. J. Inorg. Chem.*, 2016, **2016**, 1967–1971.

97 J. K. Zareba, M. Nyk, J. Janczak and M. Samoć, *ACS Appl. Mater. Interfaces*, 2019, **11**, 10435–10441.

98 X. Lian, D. Zhao, Y. Cui, Y. Yang and G. Qian, *Chem. Commun.*, 2015, **51**, 17676–17679.

99 D. Zhao, J. Zhang, D. Yue, X. Lian, Y. Cui, Y. Yang and G. Qian, *Chem. Commun.*, 2016, **52**, 8259–8262.

100 M. Atzori, S. Benmansour, G. Mínguez Espallargas, M. Clemente-León, A. Abhervé, P. Gómez-Claramunt, E. Coronado, F. Artizzu, E. Sessini, P. Deplano, A. Serpe, M. L. Mercuri and C. J. Gómez García, *Inorg. Chem.*, 2013, **52**, 10031–10040.

101 S. Ashoka Sahadevan, N. Monni, M. Oggianu, A. Abhervé, D. Marongiu, M. Saba, A. Mura, G. Bongiovanni, V. Mameli, C. Cannas, N. Avarvari, F. Quochi and M. L. Mercuri, *ACS Appl. Nano Mater.*, 2020, **3**, 1, 94-104

102 I. R. Jeon, B. Negru, R. P. Van Duyne and T. D. Harris, *J. Am. Chem. Soc.*, 2015, **137**, 15699–15702.

103 Z. K. Nikitina, N. S. Ovanesyan, V. D. Makhaev, G. V. Shilov and S. M. Aldoshin, *Dokl. Chem.*, 2011, **437**, 129–132.

104 M. L. Mercuri, F. Congiu, G. Concas and S. Ashoka Sahadevan, *Magnetochemistry*, 2017, **3**, 17.

105 S. Ashoka Sahadevan, N. Monni, A. Abhervé, P. Auban-Senzier, E. Canadell, M. L. Mercuri and N. Avarvari, *Inorg. Chem.*, 2017, **56**, 20, 12564–12571

106 S. A. Sahadevan, A. Abhervé, N. Monni, C. Sáenz de Pipaón, J. R. Galán-Mascarós, J. C. Waerenborgh, B. J. C. Vieira, P. Auban-Senzier, S. Pillet, E.-E. Bendeif, P. Alemany, E. Canadell, M. L. Mercuri and N. Avarvari, *J. Am. Chem. Soc.*, 2018, **140**, 12611–12621.

107 S. A. Sahadevan, N. Monni, A. Abhervé, G. Cosquer, M. Oggianu, G. Ennas, M. Yamashita, N. Avarvari and M. L. Mercuri, *Inorg. Chem.*, 2019, **58**, 20, 13988–13998

108 S. Benmansour, A. Hernández-Paredes, A. Mondal, G. López Martínez, J. Canet-Ferrer, S. Konar and C. J. Gómez-García, *Chem. Commun.*, 2020, **56**, 9862–9865.

109 L. E. Darago, M. L. Aubrey, C. J. Yu, M. I. Gonzalez and J. R. Long, *J. Am. Chem. Soc.*, 2015, **137**, 15703–15711.

110 L. Liu, J. A. Degayner, L. Sun, D. Z. Zee and T. D. Harris, *Chem. Sci.*, 2019, **10**, 4652–4661.

111 J. A. DeGayner, I. R. Jeon, L. Sun, M. Dincă and T. D. Harris, *J. Am. Chem. Soc.*, 2017, **139**, 4175–4184.

112 M. P. Van Koeverden, B. F. Abrahams, D. M. D'Alessandro, P. W. Doheny, C. Hua, T. A. Hudson, G. N. L. Jameson, K. S. Murray, W. Phonsri, R. Robson and A. L. Sutton, *Chem. Mater.*, 2020, **32**, 7551–7563.

113 B. F. Abrahams, A. D. Dharma, B. Dyett, T. A. Hudson, H. Maynard-Casely, C. J. Kingsbury, L. J. McCormick, R. Robson, A. L. Sutton and K. F. White, *Dalt. Trans.*, 2016, **45**, 1339–1344.

114 C. J. Kingsbury, B. F. Abrahams, D. M. D'Alessandro, T. A. Hudson, R. Murase, R. Robson and K. F. White, *Cryst. Growth Des.*, 2017, **17**, 1465–1470.

PART II

Results and Discussion

Chapter 1

Synthesis and Characterization of new Potential Building Blocks for Extended CFs: N-heterocycles Anilate Derivatives

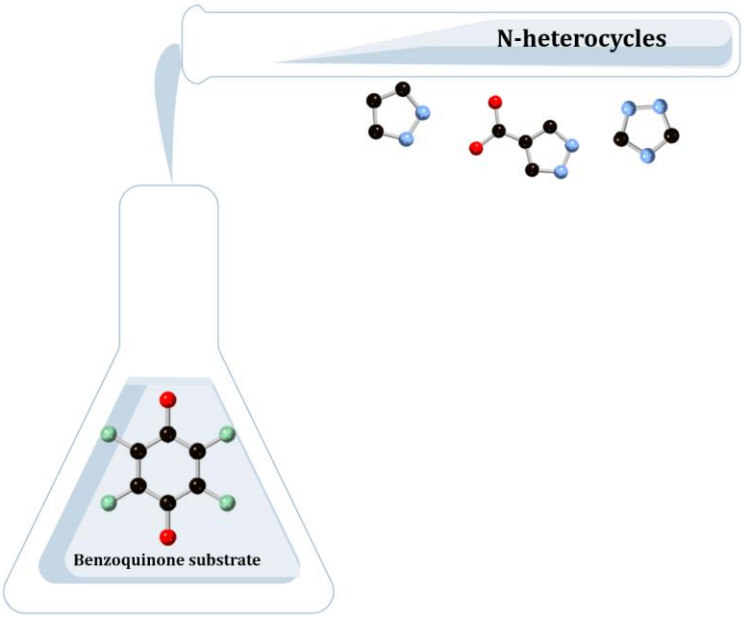

Abstract

The search for new *molecular building blocks* is a challenge in the design and preparation of new extended CFs with functional properties. Among the *plethora* of organic molecules which can act as valuable linkers, the 3,6-disubstituted-2,5-dihydroxy-1,4-benzoquinones, namely anilates, formulated as $H_4C_6O_4$ (C_6O_4 indicating the anilate moiety An), are very promising molecular building blocks due to their promising features, summarized as follows: *i)* different coordination modes leading to structures with a various dimensionality; *ii)* capability to mediate magnetic interactions between d- transition metal ions and to magnetically isolate lanthanide ions and *iii)* capability to undergo one or two-electrons reduction, showing a *non-innocent* behavior. In the present Chapter, the synthesis of two N-heterocycles substituted anilate derivatives, where triazole and 4-ethylpyrazole carboxylate were selected as substituents at the 3, 6 positions of the anilate ring, is reported. The obtained linkers have been characterized basically by Elemental Analysis, NMR and Mass Spectrometry.by Raman, FT-IR, UV-Vis and Fluorescence, while their redox behaviour was studied by Cyclic Voltammetry.

1. Introduction

Since the outstanding growth of reticular chemistry, defined by Omar Yaghi as the area of chemistry where molecular building blocks, *i.e.* organic *linkers* and/or metal *nodes*, are strongly bonded to afford CFs, including CPs, MOFs and Covalent-Organic Frameworks (COFs), the design and synthesis of new organic linkers has become one of the current major challenges in this area. In order to construct such supramolecular architectures with desired physical properties for a specific application, prerequisites as the molecular structure, coordination modes and presence of substituents, which can give different functionalities, need to be fulfill in the selection of an organic linker.[1,2] Among the countless organic molecules which can be chosen as organic linkers, a promising family of multi-acting linkers is represented by the quinones and their derivatives. Quinones are naturally occurring organic molecules forming conjugated six-membered cyclic diketones in *ortho* or positions, namely *o*-quinones and *p*-quinones, respectively. Their chemistry have been explored for many decades because of their presence as natural products with relevant biological activities as anticoagulant,[3] anticancer,[4] antioxidative,[5] antidiabetic,[6] *etc*. Recently, this class of molecules has received ever-growing attention in material chemistry due to their inherent redox activity,[7] which lead to a *non-innocent* behaviour, making them promising candidates for electrochemical applications, such as purely organic electrodes for Lithium Ion Batteries (LIBs).[8–10] Interestingly, when *p*-benzoquinone is substituted with hydroxy groups in 2,5 positions, the 2,5-dihydroxy-1,4-benzoquinone, formulated as $H_4C_6O_4$ (H_4An), with C_6O_4 indicating the anilate moiety (An),[11,12] is the precursor of a wide variety of functionalized anilate derivatives. Different synthetic paths can be used for the substitution of the hydrogens at the 3,6 positions with other functional groups, such as halogen groups,[13–15] cyano group,[16–18] heterocycles,[19,20] *etc*. Linkers belonging to the anilate family can coordinate metal ions through different coordination modes, as reported in **Scheme 1.1**, and among them, the bis-1,2-bidentate mode (II in **Scheme 1.1**) is one of the most interesting since allows to construct a diverse range of novel supramolecular frameworks of different dimensionality.[12,21]

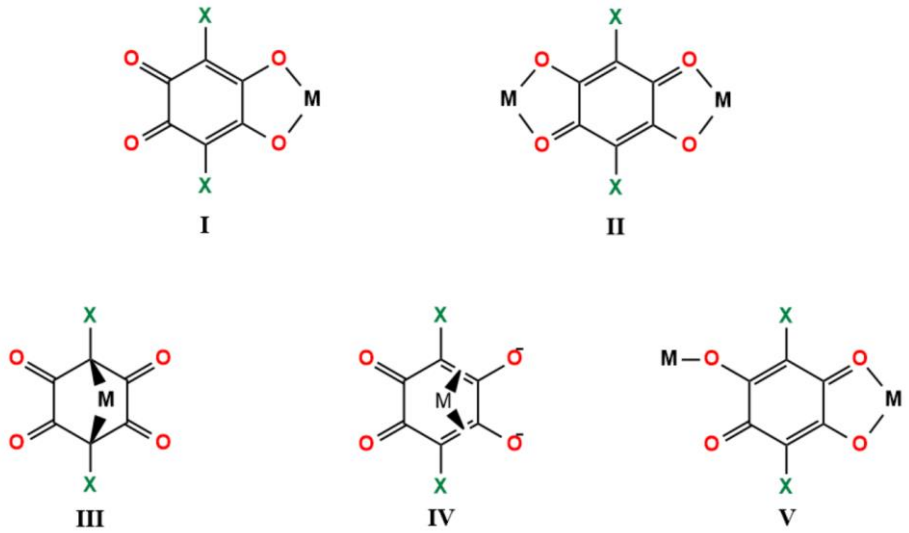

Scheme 1.1. Differen coordination modes of anilate dianions: 1,2-bidentate (**I**), bis-1,2-bidentate (**II**), 1,4-bidentate (**III**), p-bonding (**IV**), 1,2-bidentate/monodentate (**V**).

Generally, anilates with non-coordinating substituents group in 3,6 positions act as linkers between metal ions, affording mainly 1D chains[22–24] and 2D frameworks,[25–28] while 3D ones are more rares.[22,29] A valuable strategy to improve the anilates capability to obtain 3D frameworks is the replacement of non-coordinating substituents with coordinating ones, *i.e.* N-heterocycles which can provide a further coordination site with nitrogen atoms present in the pendant ring. Furthermore, the insertion of N-heterocycles as substituents in the anilate ring might improve either their capability of magnetically coupling the metal ions or their tendence to be reduced by one or two electrons to their semiquinone or hydroquinone forms, respectively. In this context, we have selected two different N-heterocycles, triazole and 4-ethylpyrazole carboxylate, as substituents in the anilate ring to design the 3,6-N-ditriazolyl-2,5-dihydroxy-1,4-benzoquinone and the novel 3,6-N-(dipyrazolyl-4-carboxylic acid)-2,5-dihydroxy-1,4-benzoquinone organic linkers. The N-heterocycles anilate derivatives here in prepared were characterized basically by Elemental Analysis, Mass Spectrometry and NMR Spectroscopy and then by Raman, FT-IR, UV-Vis and Fluorescence Spectroscopies and by Cyclic Voltammetry, for investigating their optical and electrochemical properties.

2. Experimental Section

2.1 General Remarks

Reagents of analytical grade were purchased from Zentek (TCI) and Sigma Aldrich and used without further purification. Synthesis of compounds **1-3** was modified from literature[30] while 2,5-Dibromo-3,6-diethoxy-1,4-benzoquinone (called hereafter DDBQ) was prepare according the procedure already reported.[19] NMR spectra were recorded on a Bruker Avance III HD 600 spectrometer (600 MHz for 1H). Chemical shifts are expressed in parts per million (ppm, δ), downfield from TMS as an external reference. The following abbreviations are used: singlet (s), doublet (d), triplet (t), quartet (q). MS (MALDI-TOF) spectra were recorded on a high resolution Sciex TRIPLETOFT5600. Elemental analyses (C, H, and N) were performed with a CE Instruments EA 1110 CHNS.

2.2 Synthesis

2,3,5,6-N-tetratriazolyl-1,4-benzoquinone (1). 1,2,4-triazole (6.9 g, 0.1 mol) and Bromanile (5.3 g, 0.0125 mol) were dissolved in 25 mL of DMSO, then the reaction mixture was heated till 50°C for 6 h. The orange solid formed was filtered, washed with fresh DMSO and dried in air overnight. The solid was characterized in without further purification. ^{1}H NMR (600 MHz, DMSO-d_6): δ = 8.69 (d), 8.05 (d) MS (MALDI-TOF): m/z calcd for $C_{14}H_8N_{12}O_2$: 377.09; found 377.1

3,6-N-ditriazolyl-2,5-dihydroxy-1,4-benzoquinone (2). 1 g (2.6 mmol) of **1** was dissolved in 10 mL of water with $NaHCO_3$ (0.53 g 6.3 mmol). After 15 min stirring a dark red precipitate appears, this was filtered and redissolved in 50 mL of water. Upon adding H_2SO_4 96% to reach pH ~ 3 compound **3** start to precipitate as a brown powder. (Yield 84%) ^{1}H NMR (600 MHz, DMSO-d_6): δ = 8.40 (s), 8.05 (s) MS (MALDI-TOF): m/z calcd for $C_{10}H_6N_6O_4$: 275.05; found 275.05 Elemental analysis calcd (%) for $C_{10}H_6N_6O_4$: C 36.59, H 3.69, N 25.60; found: C 36.55, H 3.24, N 26.50.

3,6-N-(dipyrazolyl-4-carboxylicacid)-2,5-diethoxy-1,4-benzoquinone (3). 4-ethylpyrazole carboxylate (314 mg, 2.24 mmol), DDBQ (200 mg, 0.56 mmol) and K_2CO_3 (309 mg, 2.24 mg) were dissolved in DMF and heated at 70°C for 48 h, giving a brownish solid which was filtered and let it dry standing at air overnight. The solid was characterized without further purification. ^{1}H NMR (600 MHz, DMSO-d_6): δ = 7.79 (d),

7.74 (d), 4.22 (q), 1.27 (m) MS (MALDI-TOF): m/z calcd for $C_{18}H_{16}N_4O_8$: 417.10; found 417.11.

3,6-N-(dipyrazolyl-4-carboxylic acid)-2,5-dihydroxy-1,4-benzoquinone (4). 200 mg (0.48 mmol) of **4** were dissolved in 20 mL of Acetonitrile and mixed with a water solution of NaOH (60 mg, 1.5 mmol). The solution was stirred and heated at reflux temperature for 2 h. When cooled to room temperature, 3 mL of HCl 37% were added and the solution let at 4°C, overnight. Then, 5 precipitate as an orange powder, filtered from the mother liquor and dried in air (Yield 23%) ^{1}H NMR (600 MHz, DMSO-d_6): δ = 8.06 (d), 7.89 (d), 3.55 (s) MS (MALDI-TOF): m/z calcd for $C_{14}H_8N_4O_8$: 361.04; found 361.04 Elemental analysis calcd (%) for $C_{14}H_8N_4O_8$: C 44.46, H 2.66, N 14.81; found: C 45.01, H 2.60, N 14.78.

2.3 Physical Measurements

Spectroscopic Measurements. FT-IR spectra were collected using a Bruker Equinox 55 Spectrometer, on KBr pellets. Raman spectra were performed on a powder sample by a LabRAM-HR Evolution confocal Raman Microscope (Horiba). The measurements were conducted with an excitation wavelength of λ_{ex}= 532 nm. The laser was focused using a 100× objective (0.8 NA), thus leading to a laser spot with a diameter of ca. 1 μm. A CCD camera was employed to collect the backscattered light that was dispersed by an 1800 grooves per mm grating providing a spectral resolution of ~ 1 cm^{-1}.

UV-Vis absorption spectra (800–200 nm) were recorded on a Varian Cary 5 Spectrophotometer. Solutions for UV-Vis spectra were prepared by using water as a solvent and NaOH in stoichiometric quantity to favor the dissolution of the ligands.

Photoluminescence (PL) Spectroscopy. PL emission spectra (300-600 nm) were collected in H_2O solutions, with a Horiba-Jobin Yvon Fluoromax-4 Fluorimeter, using a DC Xenon lamp. Bandpass was set as 5 nm slit width for each measurement.

Electrochemical Measurements. Cyclic Voltammetry was carried out with a Gamry electrochemical workstation (Gamry 1000E potentiostat/galvanostat), using a three-electrode cell equipped with a Glassy carbon working electrode, a Ag/AgCl (in KCl 3 M) reference and a platinum-wire as counter electrode. The experiments were performed at room temperature (25 °C), in dry and Argon-degassed CH_3CN solution containing 0.1 M $[(n\text{-}Bu)_4N]PF_6$ as supporting electrolyte, at 100, 50, 20, 10 and 5 mV/s

scan rates. Ferrocene was added as an internal standard upon completion of each experiment.

3. Results and Discussion

3.1 Synthesis

The reactions to functionalize benzoquinone ring, at the 3,6 positions, with N-heterocycles were first reported by Gauß *et al.*,[20] which obtained different tetrasubstituted benzoquinones starting from Chloranile as substrate. To improve some of these reactions it is possible to use as substrate Bromanile, which favors the nucleophilic substitution due to the presence of a better leaving group as bromine instead of chlorine. When Bromanile is added to a DMSO solution prepared with a large excess of Triazole, after several hours of stirring at mild conditions, the tetra-N-triazolyl-benzoquinone is obtained as an orange powder. To obtain the derivative 3,6-N-ditriazolyl-2,5-dihydroxy-1,4-benzoquinone (**2**), it is possible to hydrolize **1** in an aqueous solution of sodium hydrogencarbonate, forming the sodium salt of the hydrolized product which can be further acidified with concentrated sulfuric acid. This procedure, reported by Gauß *et al.*,[20] lead to the formation of **2** as a brownish precipitate (**Scheme 1.2**).

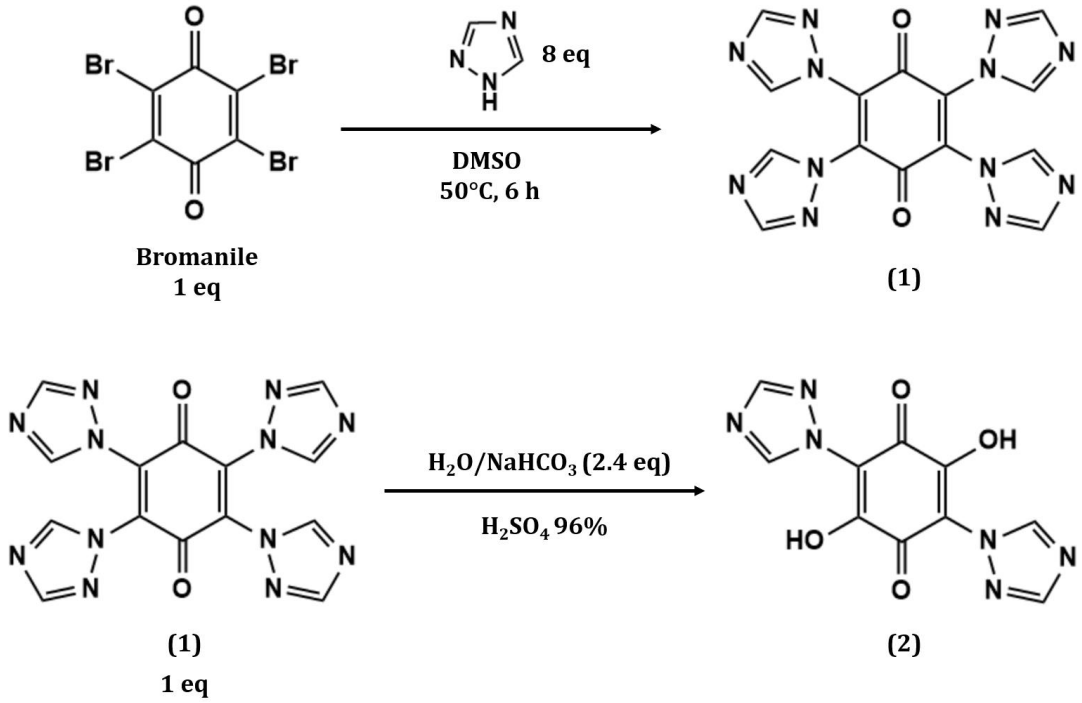

Scheme 1.2. Synthetic path for the preparation of **2**.

To tailor the benzoquinone ring with N-heterocycles containing functional groups, such as carboxylate, the new synthetic path has been developed, as shown in **Scheme 1.3.** When 2,5-dibromo-3,6-diethoxy-1,4-benzoquinone (DDBQ)[19] is added to a DMF solution of 4-ethylpyrazole carboxylate and the weak base potassium carbonate, 3,6-N-(dipyrazolyl-4-carboxylic acid)-2,5-diethoxy-1,4-benzoquinone (**3**) is formed as a brownish precipitate, after stirring 48h at 70°C. The treatment of **3** with a solution of sodium hydroxide lead to the complete hydrolysis of ethoxy groups, forming the new benzoquinone derivative 3,6-N-(dipyrazolyl-4-carboxylic acid)-2,5-dihydroxy-1,4-benzoquinone (**4**), belonging to anilates family.

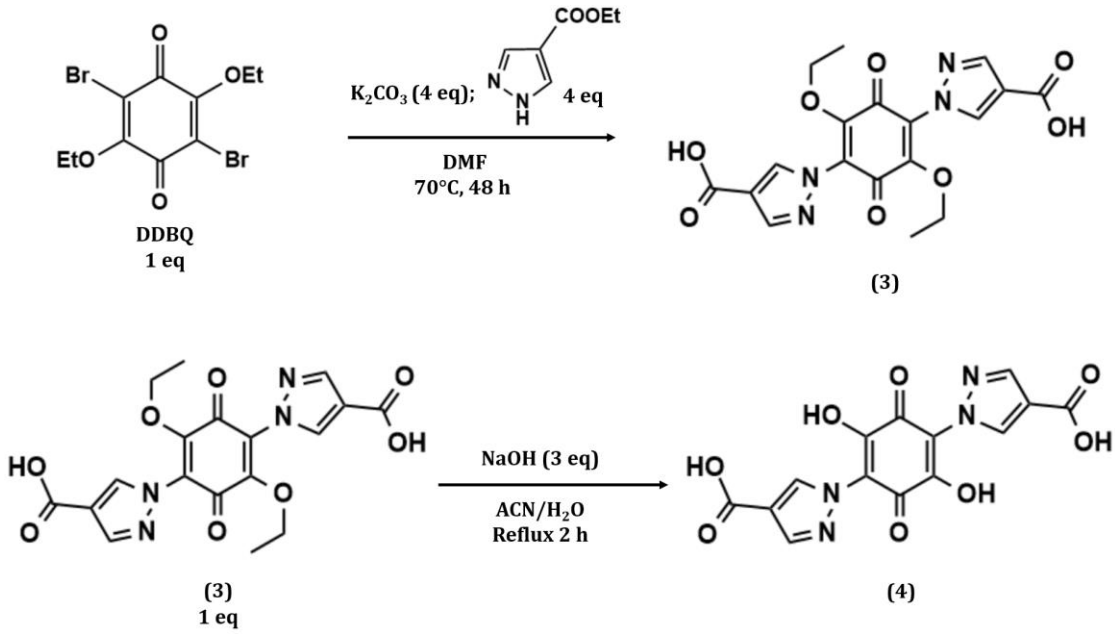

Scheme 1.3. Synthetic path for the preparation of **4**.

The N-heterocycles anilate derivatives are generally luminescent and redox-active organic linkers which can be synthetized through accessible reaction paths. **2** and **4** are promising candidates as molecular building blocks for CFs, thanks to the anilate moiety which enables the coordination to the metal node in a bis-1,2-bidentate mode. Hence, a spectroscopical and electrochemical characterization of **2** and **4** is herein reported.

3.2 FT-IR and Raman Spectroscopies

The spectroscopical characterization of **1-4** is reported in **Figures 1.1-1.4**, showing the FT-IR and Raman spectra for the benzoquinone derivatives.

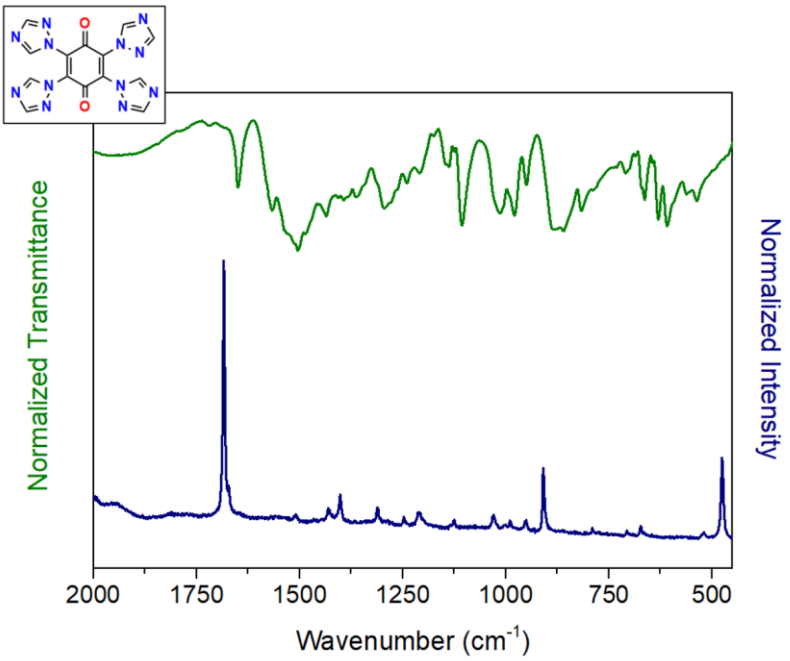

Figure 1.1. Raman spectrum (blue) in 2000-400 cm^{-1} range and FT-IR spectrum (green) in 1800-400 cm^{-1} range of **1** (without purification).

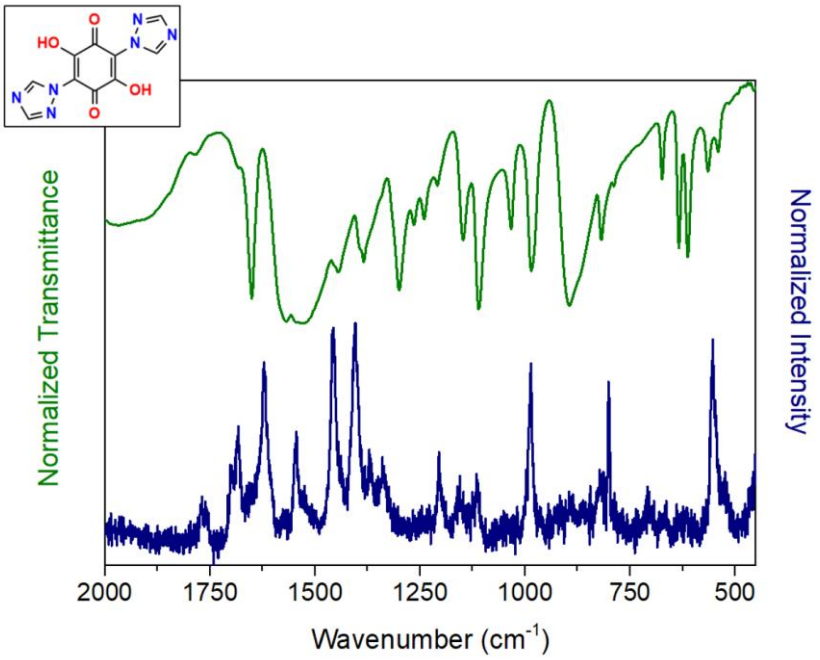

Figure 1.2. Raman spectrum (blue) in 2000-400 cm^{-1} range and FT-IR spectrum (green) in 1800-400 cm^{-1} range of **2**.

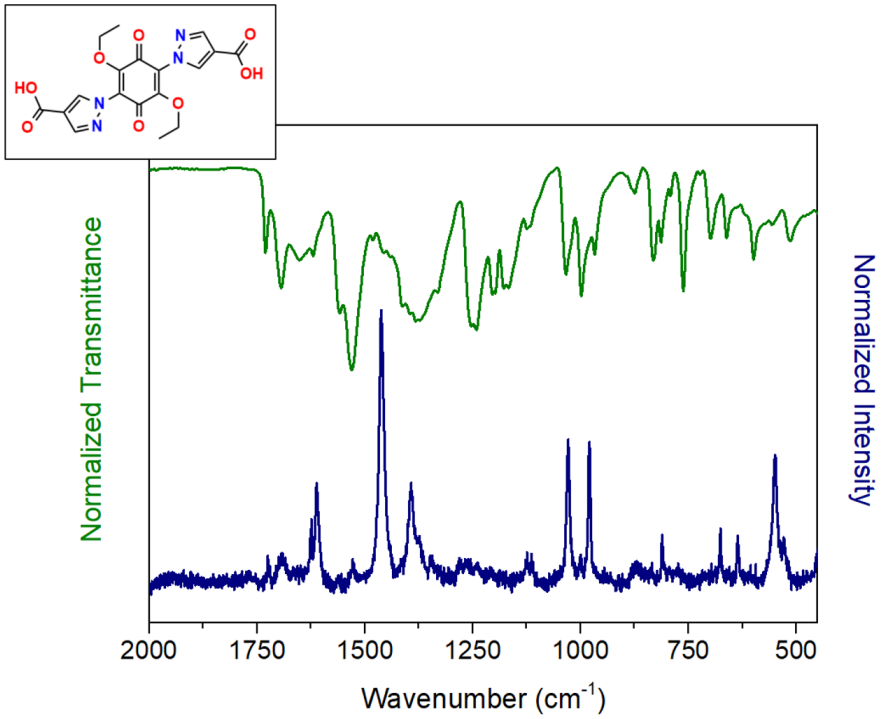

Figure 1.3. Raman spectrum (blue) in 2000-400 cm^{-1} range and FT-IR spectrum (green) in 1800-400 cm^{-1} range of **3** (without purification).

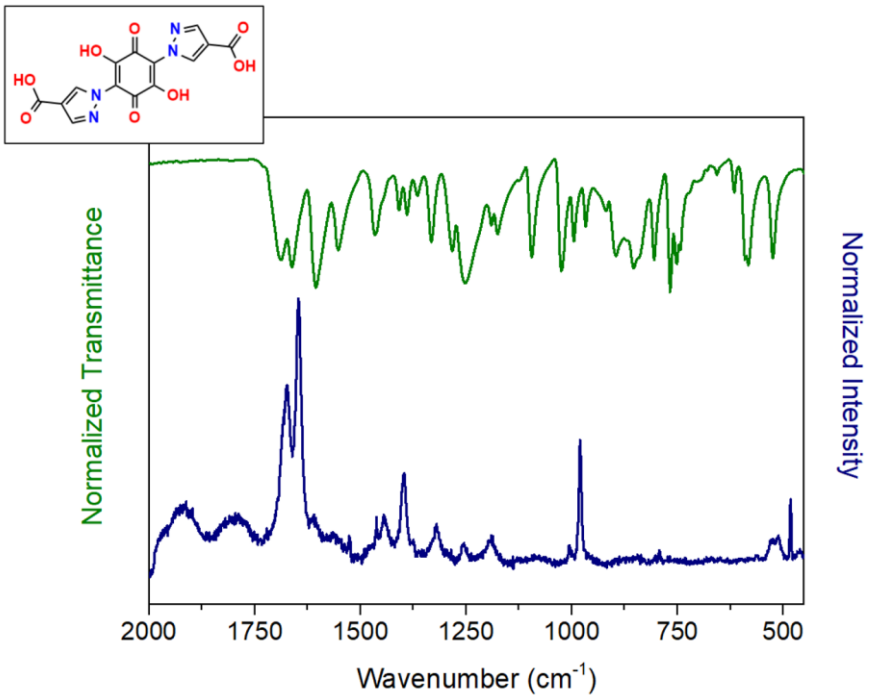

Figure 1.4. Raman spectrum (blue) in 2000-400 cm^{-1} range and FT-IR spectrum (green) in 1800-400 cm^{-1} range of **4**.

FT-IR spectra of **1-4** show the typical bands in 1540-1480 cm^{-1} region, attributable to the νC-O stretching of the benzoquinone ring.[31,32] Furthermore, in all the spectra it is possible to identify the band related to νN=N stretching in the 1560-1540 cm^{-1} region.[33,34] Spectra of **3** and **4** further display the bands typical of the carboxylic group in the 1700-1600 cm^{-1} region. In FT-IR spectra of **1-4** it is observed the presence, in 1250-1020 cm^{-1} range, of a new νC-N stretching band in addition to the others typical of free pyrazole and triazole, indicating the substitution of benzoquinone ring with N-heterocycles.[34,35]

Raman spectra of all compounds further confirm the dianionic benzoquinone form of **1-4**, with the band at ~ 1680 cm^{-1} related with νC=O stretching.[36,37] Furthermore, all spectra display bands attributable to the presence of N-heterocycles in the 1300-900 cm^{-1}region. In **2-4** spectra the band at 1396 cm^{-1} is also observed and may be due to the bending of OH groups present in the organic molecules,[32] considering also that this band does not appear in spectra of **1**, which have not OH groups in its molecular structure. Raman spectroscopy is also a probe to confirm the hydrolysis of ethoxy groups to hydroxy groups in **4**. In fact, **3** shows the band attributable to the stretching of C-O-C bonds in the ethoxy groups at 1029 cm^{-1} which disappears in **4**, as result of

complete hydrolysis reaction.[32,38] In **Table 1.1** are listed the characteristic bands of both FT-IR and Raman for **1-4**, with their assignments.

Table 1.1. Assignments of characteristic Infrared (IR) and Raman (R) bands for compounds **1-4** (all frequencies are in cm^{-1}).[32–35,38]

	1		**2**		**3**		**4**	
	IR	**R**	**IR**	**R**	**IR**	**R**	**IR**	**R**
νC-C/C=C		475		553		548		529
νC-N	1014		1033		1033		1025	
	1142		1147		1167		1175	
	1208		1209		1204		1189	
	1240		1240		1253		1253	
νC_{BQ}-N	1105		1110		1119		1095	
νC-O-C						1029		
δ O-H			1384	1396	1414	1396	1389	1414
νN=N	1537		1533		1558		1552	
νC=C				1622		1623		1646
νC=C/νC-O	1648		1648		1655		1661	
νC=O	1564	1684	1567	1684	1620	1684	1605	1675
					1692		1686	

3.3 UV-Vis Absorption and Emission Properties

The UV-Vis absorption spectra of **2** and **4**, reported in **Figure 1.5**, show two main absorption bands in the 200-800 nm region. Both spectra were recorded in H_2O solution in the stoichiometric presence of NaOH to allow the complete deprotonation of both anilate derivatives and consequent dissolution, which was not otherwise possible neither in other solvents. The absorption spectrum of **2** shows two bands in the UV region, the first one is centered at λ_{max} = 264 nm, attributable to the triazole ring,[39,40] while the other one is the convolution of two bands centered at λ_{max} ~ 306 nm and 316 nm, respectively, which is typically observed for the anilate moiety.[18] All the bands present high extinction coefficients ε = 29107 $dm^3\ mol^{-1}\ cm^{-1}$, 16846 $dm^3\ mol^{-1}\ cm^{-1}$ and 16409 $dm^3\ mol^{-1}\ cm^{-1}$, respectively. A similar absorption spectrum is observed for **4**, showing a band at λ_{max} = 264 nm (ε = 33880 $dm^3\ mol^{-1}\ cm^{-1}$) and another one, not resolved, centered at λ_{max} = 313 nm (ε = 15152 $dm^3\ mol^{-1}\ cm^{-1}$).

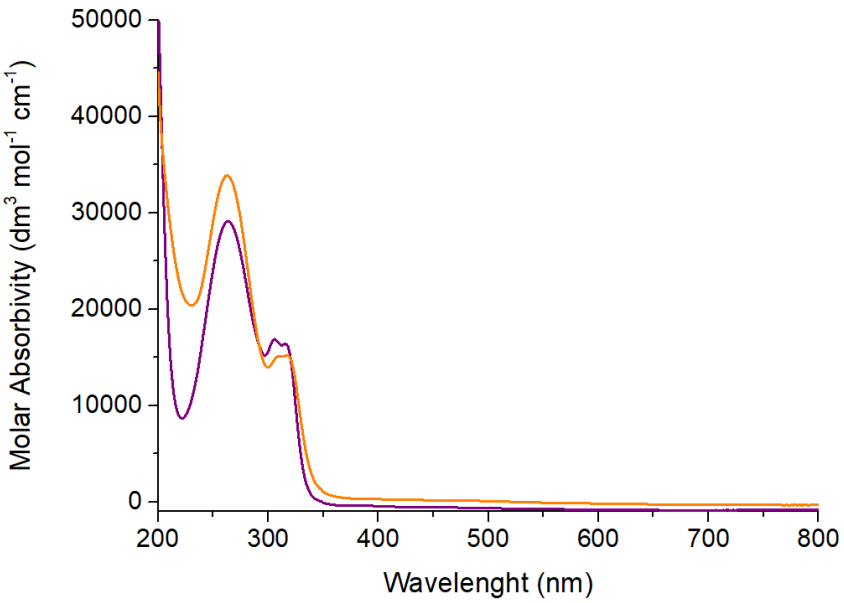

Figure 1.5. UV-Vis spectra (200–800 nm) for **2** (purple line) and **4** (orange line) in H_2O solution in their dianionic form.

Considering the observed absorption bands, **2** and **4** were thus excited at two different wavelength, λ_{exc} = 270 nm and 320 nm. Both compounds shows similar photoluminescence (PL) spectra, herein reported, along with their absorption spectra, in **Figures 1.6** and **1.7**. When the anilate derivatives are excited ad 270 nm, an intense emission band centered at λ_{max} = 406 nm and a lower intense emission band centered in the range 400-500 nm are observed. The band at 406 nm is attributable to the presence of the aromatic N-heterocycles,[40] which have an higher electronic delocalization that confers good emission properties to the molecules. When the anilate derivatives are excited at 320 nm two different emission bands, attributable to the benzoquinone ring, appear at 490 nm and 400 nm for **2** and **4**, respectively.[18]

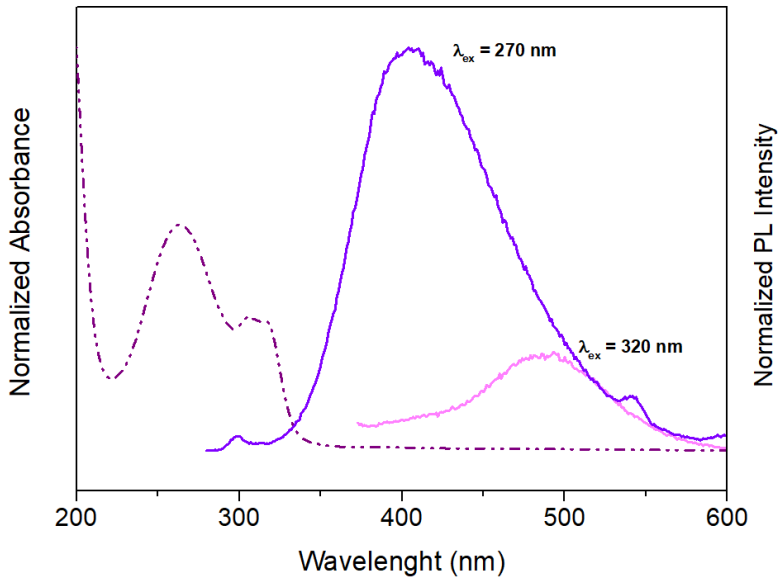

Figure 1.6. UV-Vis (dashed lines) and PL (solid lines) spectra (200–600 nm) for **2** in in H_2O solution in its dianionic form, with λ_{ex} = 270 nm (purple line) and λ_{ex} = 320 (magenta line).

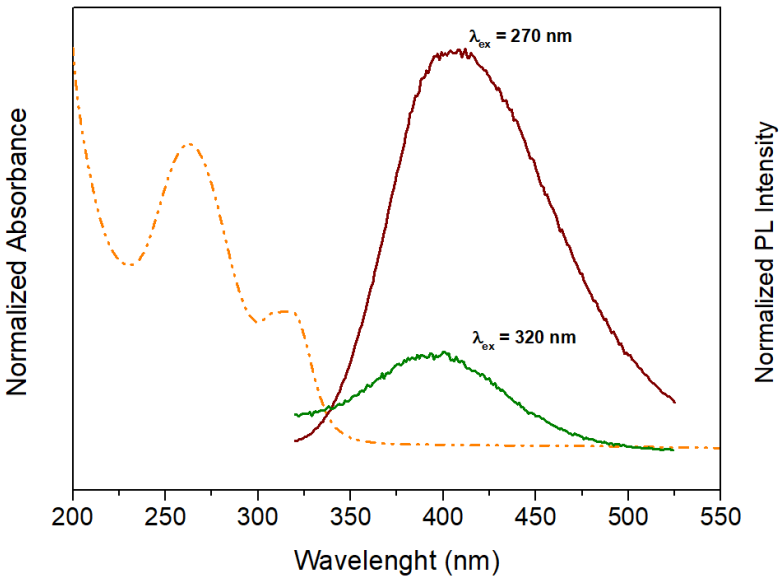

Figure 1.7. UV-Vis (dashed lines) and PL (solid lines) spectra (200–550 nm) for **4** in in H_2O solution in its dianionic form, with λ_{ex} = 270 nm (brown line) and λ_{ex} = 320 (green line).

3.4 Electrochemical Studies

Anilate derivatives, due to the benzoquinone moiety, can undergo a reduction process where the benzoquinone ring can be reduced to its corresponding semiquinone and/or hydroquinone form (**Scheme 1.3**).

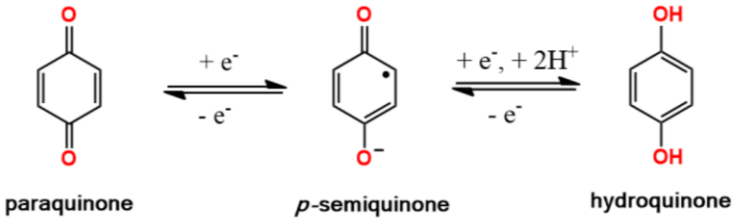

Scheme 1.3. Reversible redox reactions for the *p*-quinone/hydroquinone couple.

Cyclic voltammetry was performed on **2** and **4**, in order to get insight on their electrochemical properties. Cyclic voltammogram of **2**, reported in **Figure 1.8**, shows one broad irreversible reduction peak centered at - 1.24 V vs. Ag/AgCl. Although the reduction peak is at very lower potential values, it can be due to the reduction of the benzoquinone moiety, which in this case is irreversible, since the reduction peak of triazole is generally at even lower values.[41] **2** was measured at different scan rates (100, 50, 20, 10 and 5 mV/s), but only slow scan rates allowed to obtain the voltammogram reported in **Figure 1.8**.

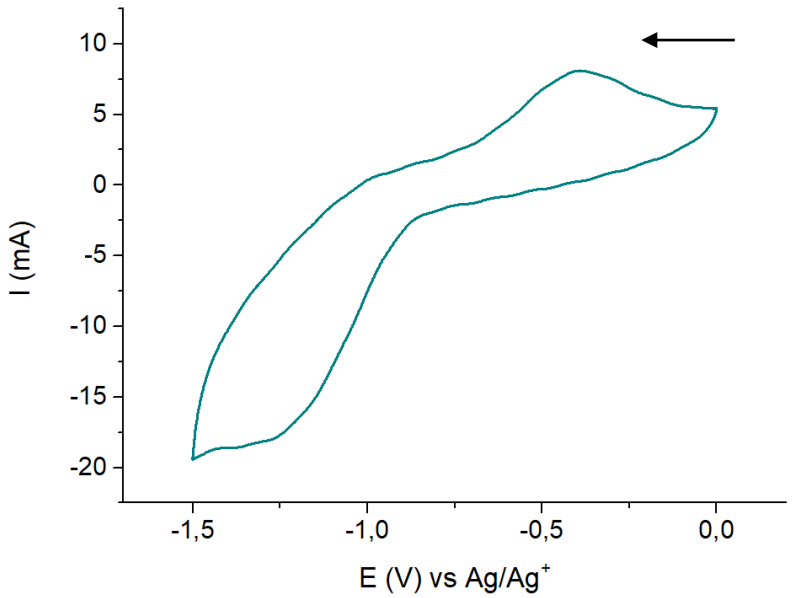

Figure 1.8. Cyclic voltammogram (-2 − 0.5 V) of **2**, in a CH_3CN solution with $[NBu_4][PF_6]$ (0.1 M) as electrolyte (Scan rate = 5 mV/s).

Cyclic voltammogram of **4** was performed in a wider potential range (-2,0 − 2,0 V) at different scan rates:100, 50, 20, 10 and 5 mV/s, showing same electrochemical behavior. In **Figure 1.9**, the initial potential is 0 V vs. Ag/AgCl. An arrow has been added to the figure to indicate that the potential was first reduced to -2 V vs. Ag/AgCl and then increased to 2 V vs. Ag/AgCl. The experiment was cycled 10 times and the first two cycles were discarded. Similar quasi-reversible peak at -0,62 V vs. Ag/AgCl is obtained if the voltammogram is measured in the 0, -2 V vs. Ag/AgCl range, due to the reduction of the benzoquinone ring to semiquinone, as previously reported in thiophene substituted anilate.[19]. On the other hand, an irreversible peak at 1.17 V vs. Ag/AgCl is obtained if the cyclic voltammogram is measured in the 0, 2 V vs. Ag/AgCl range, which may be reasonably attributable to the oxidation of pyrazole derivative moiety. Similar results were obtained by differential pulse voltammetry (DPV)**.**

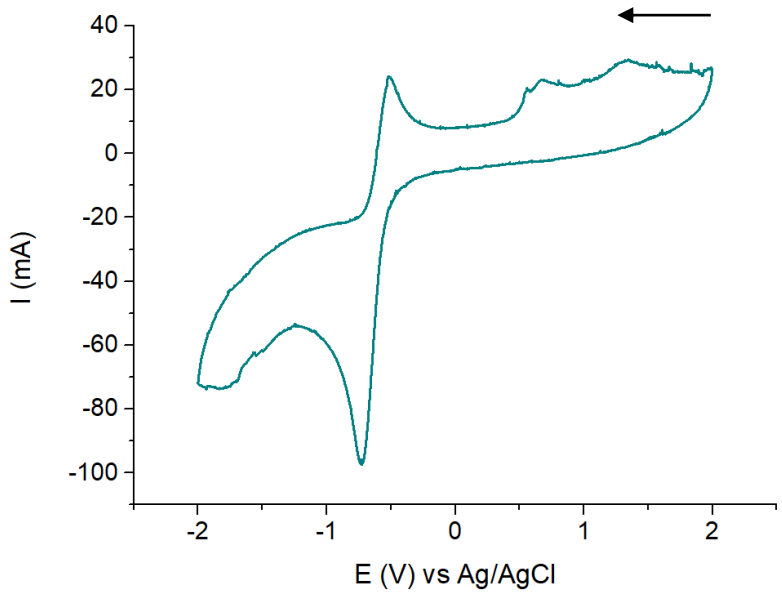

Figure 1.9. Cyclic Voltammogram (-2.5 − 2.5 V) of **4**, in a CH_3CN solution with $[NBu_4][PF_6]$ (0.1 M) as electrolyte (Scan rate = 100 mV/s).

4. Conclusions

The attainable synthetic protocols of two N-heterocycles anilate derivatives, functionalized with triazole and 4-ethylpyrazole carboxylate respectively, through nucleophilic substitution of the benzoquinone ring, have been reported. The obtained

anilate derivatives, 3,6-N-ditriazolyl-2,5-dihydroxy-1,4-benzoquinone (**2**) and 3,6-N-(dipyrazolyl-4-carboxylic acid)-2,5-dihydroxy-1,4-benzoquinone (**4**), have been characterized spectroscopically (Raman, FT-IR, UV-Vis and Fluorescence) and electrochemically (Cyclic Voltammetry). FT-IR and Raman spectroscopies were used as probes to further confirm both the substitution of the N-heterocycle and their benzoquinoid dianionic form. Absorption and emission properties of the two anilate derivatives are influenced by the presence of the triazole and 4-ethylpyrazole carboxylate respectively, which give rise to an intense emission band in the blue region, centered at ~ 400 nm, when excited at 270 nm. When the excitation wavelength is at 320 nm, an emission band in the 400-500 nm region, resulted from the benzoquinone moiety is observed,. Furthermore, cyclic voltammetry was performed on the two anilate derivatives, showing an irreversible reduction peak at E_c = -1.24 V for **2** and a quasi-reversible reduction peak at $E_{1/2}$ =-0.51 V for **4**, due to the capability of benzoquinone moiety to undergo a one or two-electrons reduction process, typical of the *non-innocent* behavior of benzoquinone moiety. Considering their properties along with the presence of coordinating substituents at the 3,6 positions of the benzoquinone ring, these anilate derivatives are interesting potential candidates as molecular building blocks for the construction of new 3D CFs with functional properties.

References

1 S. Ali Akbar Razavi and A. Morsali, *Coord. Chem. Rev.*, 2019, **399**, 213023.

2 W. Lu, Z. Wei, Z. Y. Gu, T. F. Liu, J. Park, J. Park, J. Tian, M. Zhang, Q. Zhang, T. Gentle, M. Bosch and H. C. Zhou, *Chem. Soc. Rev.*, 2014, 43, 5561–5593.

3 J. M. Khanna, M. H. Malone, K. L. Euler and L. R. Brady, *J. Pharm. Sci.*, 1965, **54**, 1016–1020.

4 M. Saibu, S. Sagar, I. Green, F. Ameer and M. Meyer, *Anticancer Res.*, 2014, **34**, 4077–4086.

5 S. Tsukamoto, A. D. Macabalang, T. Abe, H. Hirota and T. Ohta, *Tetrahedron*, 2002, **58**, 1103–1105.

6 B. Zhang, G. Salituro, D. Szalkowski, Z. Li, Y. Zhang, I. Royo, D. Vilella, M. T. Díez, F. Pelaez, C. Ruby, R. L. Kendall, X. Mao, P. Griffin, J. Calaycay, J. R. Zierath, J. V. Heck,

R. G. Smith and D. E. Moller, *Science*, 1999, **284**, 974–977.

7 O. Müller and J. P. Baumberger, *Trans. Electrochem. Soc.*, 1937, **71**, 181–194.

8 Q. Yu, Z. Yao, J. Shi, W. Tang, C. Wang, D. Li and C. Fan, *Org. Electron.*, 2021, **89**, 106057.

9 Y. Misaki, S. Noda, M. Kato, T. Yamauchi, T. Oshima, A. Yoshimura, T. Shirahata and M. Yao, *ChemSusChem*, 2020, **13**, 2312–2320.

10 M. Nisula and M. Karppinen, *J. Mater. Chem. A*, 2018, **6**, 7027–7033.

11 M. L. Mercuri, F. Congiu, G. Concas and S. Ashoka Sahadevan, *Magnetochemistry*, 2017, **3**, 17.

12 S. Kitagawa and S. Kawata, *Coord. Chem. Rev.*, 2002, **224**, 11–34.

13 K. Wallenfels and K. Friedrich, *Chem. Ber.*, 1960, **93**, 3070–3082.

14 J. Stenhouse, *J. Chem. Soc.*, 1868, **23**, 6–14.

15 H. A. Torrey and W. H. Hunter, *J. Am. Chem. Soc.*, 1912, **34**, 702–716.

16 K. Wallenfels, G. Bachmann, D. Hofmann and R. Kern, *Tetrahedron*, 1965, **21**, 2239–2256.

17 B. Zaman, Y. Morita, J. Toyoda, H. Yamochi, S. Sekizaki and K. Nakasuji, *Mol. Cryst. Liq. Cryst. Sci. Technol.*, 1996, **287**, 247–254.

18 M. Atzori, F. Artizzu, L. Marchiò, D. Loche, A. Caneschi, A. Serpe, P. Deplano, N. Avarvari and M. L. Mercuri, *Dalton Trans.*, 2015, **44**, 15786–15802.

19 M. Atzori, F. Pop, T. Cauchy, M. L. Mercuri and N. Avarvari, *Org. Biomol. Chem.*, 2014, **12**, 8752–8763.

20 W. Gauβ, H. Heitzer and S. Petersen, *Justus Liebigs Ann. Chem.*, 1973, **764**, 131–144.

21 S. Benmansour and C. J. Gómez-García, *Magnetochemistry*, 2020, **6**, 1–44.

22 B. F. Abrahams, J. Coleiro, K. Ha, B. F. Hoskins, S. D. Orchard and R. Robson, *J. Chem. Soc. Dalt. Trans.*, 2002, **2**, 1586.

23 S. Kawata, S. Kitagawa, H. Kumagai, C. Kudo, H. Kamesaki, T. Ishiyama, R. Suzuki, M. Kondo and M. Katada, *Inorg. Chem.*, 1996, **35**, 4449–4461.

24 S. Kawata, S. Kitagawa, H. Kumagai, T. Ishiyama, K. Honda, H. Tobita, I. Keiichi Adachi and M. Katada, *Chem. Mater.*, 1998, **10**, 3902–3912.

25 M. Atzori, S. Benmansour, G. Mínguez Espallargas, M. Clemente-León, A. Abhervé, P.

Gómez-Claramunt, E. Coronado, F. Artizzu, E. Sessini, P. Deplano, A. Serpe, M. L. Mercuri and C. J. Gómez García, *Inorg. Chem.*, 2013, **52**, 10031–10040.

26 S. A. Sahadevan, A. Abhervé, N. Monni, C. Sáenz de Pipaón, J. R. Galán-Mascarós, J. C. Waerenborgh, B. J. C. Vieira, P. Auban-Senzier, S. Pillet, E.-E. Bendeif, P. Alemany, E. Canadell, M. L. Mercuri and N. Avarvari, *J. Am. Chem. Soc.*, 2018, **140**, 12611–12621.

27 S. Benmansour, A. Hernández-Paredes, A. Mondal, G. López Martínez, J. Canet-Ferrer, S. Konar and C. J. Gómez-García, *Chem. Commun.*, 2020, **56**, 9862–9865.

28 L. Liu, J. A. Degayner, L. Sun, D. Z. Zee and T. D. Harris, *Chem. Sci.*, 2019, **10**, 4652–4661.

29 L. E. Darago, M. L. Aubrey, C. J. Yu, M. I. Gonzalez and J. R. Long, *J. Am. Chem. Soc.*, 2015, **137**, 15703–15711.

30 J.-H. Lee, J.-T. Jang, J.-S. Choi, S. H. Moon, S.-H. Noh, J.-W. Kim, J.-G. Kim, I.-S. Kim, K. I. Park and J. Cheon, *Nat. Nanotechnol.*, 2011, **6**, 418–22.

31 M. E. Ziebel, L. E. Darago and J. R. Long, *J. Am. Chem. Soc.*, 2018, **140**, 3040–3051.

32 A. Pawlukojć, G. Bator, L. Sobczyk, E. Grech and J. Nowicka-Scheibe, *J. Phys. Org. Chem.*, 2003, **16**, 709–714.

33 M. K. Trivedi, R. M. Tallapragada, A. Branton, D. Trivedi, G. Nayak, R. K. Mishra and S. Jana, *J. Mol. Pharm. Org. Process Res.*, 2015, **03**, 1–6.

34 V. Krishnakumar, N. Jayamani and R. Mathammal, *Spectrochim. Acta - Part A Mol. Biomol. Spectrosc.*, 2011, **79**, 1959–1968.

35 F. Billes, I. Ziegler and H. Mikosch, *Spectrochim. Acta - Part A Mol. Biomol. Spectrosc.*, 2016, **153**, 349–362.

36 I. R. Jeon, B. Negru, R. P. Van Duyne and T. D. Harris, *J. Am. Chem. Soc.*, 2015, **137**, 15699–15702.

37 J. A. DeGayner, I. R. Jeon, L. Sun, M. Dincă and T. D. Harris, *J. Am. Chem. Soc.*, 2017, **139**, 4175–4184.

38 X. Zhao and T. Kitagawa, *J. Raman Spectrosc.*, 1998, **29**, 773–780.

39 M. R. Atkinson, E. A. Parkes and J. B. Polya, *J. Chem. Soc.*, 1954, 4256–4262.

40 J. Huo, Z. Hu, D. Chen, S. Luo, Z. Wang, Y. Gao, M. Zhang and H. Chen, *ACS Omega*, 2017, **2**, 5557–5564.

41 S. V. Lokesh, A. K. Satpati and B. S. Sherigara, *Open Electrochem. J.*, 2010, **2**, 15–21.

Chapter 2

A New Family of Magnetic and Redox Active Metal-Organic Frameworks based on 3,6-ditriazolyl-2,5-dihydroxy-1,4-benzoquinone

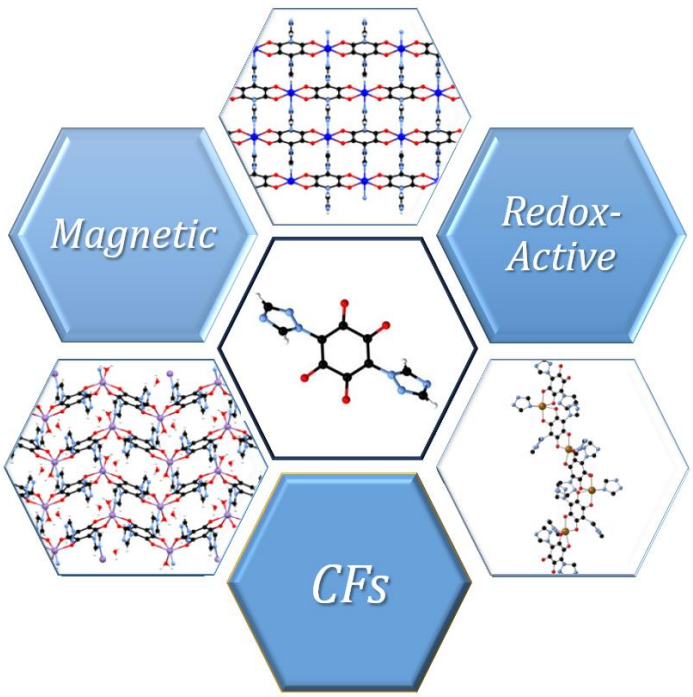

Abstract

The synthesis and characterization of novel magnetic and redox-active CFs based on *3d* transition metal ions and 3,6-ditriazolyl-2,5-dihydroxybenzoquinone (H_2trz_2An) is therein reported. By combining H_2trz_2An with M^{II} ions *via* hydrothermal method, two phases, formulated as $[M_2(trz_2An)_2]_n3H_2O$ (M = Co^{II} (**1**), Cu^{II} (**2**) and Ni^{II} (**3**)) and $[Mn(trz_2An)(H_2O)]_n \cdot 2H_2O$ (**4**) were obtained, whereas the use of one-pot strategy led to the formation of a further phase formulated as $[M(trz_2An)]_n \cdot 2H_2O$ (M = Fe^{II}/Fe^{III} (**5**), Co^{II} (**6**)). All the compounds crystallize as neutral polymeric 3D frameworks, in which the metal ions are coordinated through the oxygen atoms of the anilate linkers forming either straight (**1-3**) or *zig-zag* (**4-6**) 1D chains. These chains are connected through the nitrogen atom in 4 position of the triazolyl group, which completes the coordination sphere of each metal ion, affording a 3D structure. **1-3** frameworks contain a void volume of 23% and 1D channels which can be useful for sorption of small molecules. All compounds show antiferromagnetic interactions along the chains, except **5** which is characterized by weak ferromagnetic interactions. Interestingly, all **1-6** series show a redox behavior due to the presence of the anilate linker, being reduced electrochemically in the -0.7 – - 0.9 V range, due to the benzoquinone-semiquinone one electron reduction.

1. Introduction

Metal-Organic Frameworks (MOFs) are a fascinating class of crystalline molecular materials obtained by the self-assembly of metal nodes and organic linkers. These molecular building blocks can be organized in frameworks with different dimensionality (1D, 2D or 3D) which are characterized by potential voids.[1] The possibility to combine the different metal ions with an enormous number of organic linkers allows an incredible chemical and structural control of the final material.[2,3] By a rational design, intriguing physical properties such as magnetic, conducting and/or luminescence and porosity, can be tailored in the MOFs for a wide range of applications, such as gas storage and separation,[4–7] catalysis,[8–10] asymmetric synthesis,[11,12] energy storage,[13,14] biomedicine,[15,16] sensing,[17–19] *etc*.[20–22] The aforementioned properties which allow MOFs to be employed in such diverse application fields, derived out of the various structures and depend on the molecular building blocks. The metal node is generally a transition metal or lanthanide ion and can give magnetic and/or luminescence properties.[23–25] The organic linker is typically a molecule which must contain coordinating functional groups (carboxylate, imidazolate, phosphonates, *etc.*)[26–28] in order to build different porous and stable structures. Nevertheless, the linker could also provide and/or improve the already existent physical properties. In this context, redox active linkers are becoming very popular in the recent years since the modulation of their redox states is a current and emerging strategy to enhance physical properties of the MOFs, such as magnetism and/or conductivity.[29] Among the redox active organic linkers, the quinone derivatives are widely used and especially the 2,5-dihydroxy-1,4-benzoquinone derivatives, which have proved to be excellent candidates to construct MOFs in which magnetic and conducting properties are simultaneously tuned through the redox activity of the linker.[30–34] Recently, it has been reported by Harris *et al.*[30] an example of permanently porous 2D-MOF incorporating the 3,6-dichloro-2,5-dihydroxy-1,4-benzoquinone linker (namely chloranilic acid, H_2Cl_2An) in its semiquinoid form as a results from a spontaneous electron transfer from Fe^{II}, chosen as metal node, to Cl_2An^{2-}. Hence iron metal ions are present in a mixed valence state Fe^{II}/Fe^{III}, as well as the chloranilate linker which is simultaneously present in its benzoquinoid and semiquinoid form, generated *in situ*. The resulting MOF is a porous semiconducting antiferromagnet, showing a spontaneous magnetization below 80 K and conductivity values of $\sigma = 1.4(7) \times 10^{-2}$ S cm^{-1}, due the mixed valence given by both Fe^{II}/Fe^{III} and benzoquinoid/semiquinoid couples. In order to fully reduce the Cl_2An linker, the obtained MOF was then soaked in a Cobaltocene

solution for 48 h, allowing the complete reduction of the benzoquinone-semiquinone couple to the semiquinone Cl_2An^{3-} form. Through this post-synthetic approach, the complete reduction of Cl_2An in its semiquinoid form led to a further improvement of the physical properties, with an increase of the magnetic ordering temperature up to 105 K, one of the highest values for a semiquinone-based framework.[31]

In this context, to enlarge the study of CFs based on new redox-active anilates, the anilate derivative functionalized with 1,2,4-triazolyl groups at the 3 and 6 positions of the benzoquinone ring, 3,6-N-ditriazolyl-2,5-dihydroxy-1,4-benzoquinone, namely H_2trz_2An, (see *Chapter 1*) was selected as organic linker for constructing a new series of MOFs based on transition metal ions. In fact, the presence of the nitrogen (N4) of the triazole provide a further coordination site (see **Scheme 2.1**), leading to the formation of new 3D extended frameworks. Hence, the synthesis of new anilate-based MOFs formulated respectively as $[M_2(trz_2An)_2]_n3H_2O$ (M = Co^{II} (**1**), Cu^{II} (**2**) and Ni^{II} (**3**)), $[Mn(trz_2An)(H_2O)]_n\cdot 2H_2O$ (**4**) and $[M(trz_2An)]_n\cdot 2H_2O$ (M = Fe^{II}/Fe^{III} (**5**), Co^{II} (**6**)), is reported in the present work. The structural, spectroscopic, magnetic and electrochemical characterization of all compounds has been reported therein.

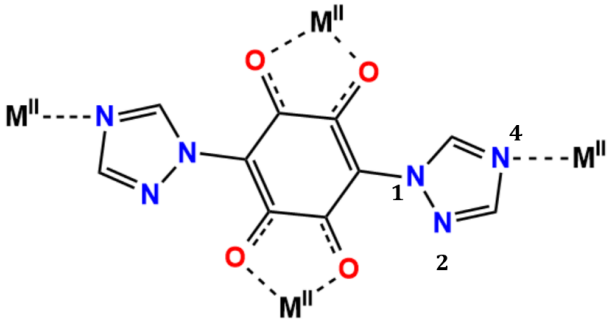

Scheme 2.1. Coordination sites of trz_2An, highlighting the terminal nitrogen (N4) of the triazolyl group as further coordinative atom.

2. Experimental Section

2.1 General Remarks

Reagents of analytical grade were purchased from Zentek (TCI) and Sigma Aldrich and used without further purification. Synthesis of ligand H_2trz_2An was modified from literature[35] as reported in *Chapter 1*. Elemental analyses (C, H, and N) were performed with a CE Instruments EA 1110 CHNS.

2.2 Synthesis

$[M(trz_2An)]_n \cdot 3H_2O$ (M = Co^{II} (1), Cu^{II} (2) and Ni^{II} (3)). A 5 mL Teflon vial with a mixture of MCl_2 (0.05 mmol, 11.9 mg (**1**), 9.8 mg (**2**), 8.3 mg (**3**)), H_2trz_2An (0.05 mmol, 13.7 mg), NaOH (0.1 mmol, 4 mg) and water (5 mL) was heated at 130°C for 2 days. After being cooled to room temperature, rectangular brown (**1**) and yellowish (**2**) crystals suitable for XRD were obtained, while **3** precipitate as orange powder analyzed by powder XRD. It was possible to obtain a large quantity of **1**, performing the synthesis in a stainless steel autoclave of 80 mL volume, with a scale up of the reaction mixture of 8 times, by using 0.4 mmol of H_2trz_2An, 0.8 mmol of NaOH and 0.4 mmol of $CoCl_2 \cdot 6H_2O$ in 40 mL of water.

$[Mn(trz_2An)(H_2O)]_n \cdot 2.5H_2O$ (4). Synthetic procedure was the same used for **1-3**, with $MnCl_2$ (0.05 mmol, 8.1 mg) as a precursor of Mn^{II} ions. When cooled to room temperature suitable XRD crystals of **4** were obtained, which appear as purple needle-like crystals.

$[M(trz_2An)]_n \cdot nH_2O$ (M = Fe^{II}/Fe^{III}, n = 9 (5), Co^{II}, n = 8 (6)). A solution of $Fe(ClO_4)_2 \cdot xH2O$ (0.83 mmol, 211 mg) in acetone (10 mL) was added dropwise, under stirring, to an aqueous solution (10 mL) of H_2trz_2An (0.17 mmol, 47 mg) and NaOH (0.34 mmol, 14 mg) showing an instantaneous precipitation of a black microcrystalline powder (**5**). When $CoCl_2$ is used as a precursor in the same stoichiometric ratio, **6** precipitate as a dark red microcrystalline powder. Both samples were analyzed by powder XRD showing isostructural phases. In order to obtain a single crystal suitable for XRD, an aqueous solution (1 mL) of H_2trz_2An (0.017 mmol, 4.7 mg) and NaOH (0.034 mmol, 1.4 mg) was placed in the bottom of a thin test tube, above was carefully layered a blank solution of water and acetone in 1:1 ratio, in the middle, and then a solution of $Fe(ClO_4)_2 \cdot xH_2O$ (0.083 mmol, 21.1 mg) in acetone (1 mL) on top. After three weeks black rectangular crystals of **5**, suitable for XRD measurement, appear at the interface.

Table 2.1. Elemental analysis for **1-6**.

		Calculated			Found		
		%C	**%H**	**%N**	**%C**	**%H**	**%N**
1	$C_{10}H_{10}N_6O_7Co$	31.18	2.62	21.82	31.12	2.45	22.00
2	$C_{10}H_{10}N_6O_7Cu$	30.82	2.59	21.56	30.80	2.47	21.19
3	$C_{10}H_{10}N_6O_7Ni$	31.20	2.62	21.83	29.14	2.74	22.23
4	$C_{10}H_{11}N_6O_{7.5}Mn$	30.78	2.84	21.54	30.99	2.46	21.50
5	$C_{10}H_{22}N_6O_{13}Fe$	24.50	4.52	17.15	24.66	2.90	17.80
6	$C_{10}H_{20}N_6O_{12}Co$	25.27	4.24	17.68	25.82	3.70	17.53

2.3 Physical Measurements

X-Ray Diffraction (Single Crystal and Powder). Single crystals of **1**, **2**, **4** and **5** were mounted on a glass fiber using a viscous hydrocarbon oil to coat the crystal and then transferred directly to the cold nitrogen stream for data collection. X-ray data of **1-2** and **4-5** were collected at 120 K on a Supernova diffractometer equipped with a graphite-monochromated Enhance (Mo) X-ray Source ($\lambda = 0.710\ 73$ Å). The program CrysAlisPro, Oxford Diffraction Ltd., was used for unit cell determinations and data reduction. Empirical absorption correction was performed using spherical harmonics, implemented in the SCALE3 ABSPACK scaling algorithm. The structures were solved with the ShelXT structure solution program[36] and refined with the SHELXL-2013 program,[37] using Olex2.[38] Non-hydrogen atoms were refined anisotropically, and hydrogen atoms were placed in calculated positions refined using idealized geometries (riding model) and assigned fixed isotropic displacement parameters. The crystallographic data for **1**, **2** and **4** are reported in **Table 2.2**, while crystallographic data of **5** are not included due to the low quality of the data.

Table 2.2. Crystallographic data for **1**, **2** and **4**.

	1	**2**	**4**
Empirical formula	$C_{20}\ H_8\ N_{12}\ O_{10}\ Co_2$	$C_{10}\ H_4\ N_6\ O_4\ Cu$	$C_{20}\ H_{16}\ N_{12}\ O_{13}\ Mn_2$
Fw	694.24	335.73	742.33
Crystal color	brown	Light brown	purple
Crystal size (mm^3)	0.05 x 0.04 x 0.01	0.16 x 0.03 x 0.03	0.12 × 0.05 × 0.04
Temperature (K)	120	120	120
Wavelength (Å)	0.71073	0.71073	0.71073
Crystal system, Z	Orthorhombic	Orthorhombic	Orthorhombic
Space group	*Pnnm*	*Pnnm*	*Fdd2*

a (Å)	9.529(2)	9.4714(7)	26.4194(9)
b (Å)	10.157(2)	9.8698(8)	21.4757(8)
c (Å)	7.903(2)	8.0219(12)	9.3762(4)
α (°)	90	90	90
β (°)	90	90	90
γ (°)	90	90	90
V (Å^3)	764.9(3)	749.89(14)	5319.8(4)
ρ_{calc} (g.cm^{-3})	1.438	1.487	1.854
μ(MoKα) (mm^{-1})	1.144	1.479	1.043
2θ range (°)	6.532 to 52.934	5.962 to 57.462	6.624 to 56.074
Index ranges	-11 ≤ h ≤ 11, -12 ≤ k ≤ 12, -9 ≤ l ≤ 9	-8 ≤ h ≤ 12, -13≤ k ≤ 7, -8 ≤ l ≤ 10	-21 ≤ h ≤ 34, -28 ≤ k ≤ 27, -11 ≤ l ≤ 12
Reflections collected	7555	1921	7731
Independent reflections	800 [R_{int} = 0.1290, R_{sigma} = 0.0857]	917 [R_{int} = 0.0934, R_{sigma} = 0.1585]	2720 [R_{int} = 0.0628, R_{sigma} = 0.0907]
Data/restraints/parameters	800/1/59	917/0/59	2720/1/217
Goodness-of-fit on F2	1.123	1.013	1.042
Final R indexes [I>=2σ (I)]	R_1 = 0.1076, wR_2 = 0.2829	R_1 = 0.0738, wR_2 = 0.1500	R_1 = 0.0488 wR_2 = 0.0929
Final R indexes [all data]	R_1 = 0.1315, wR_2 = 0.2939	R_1 = 0.1322, wR_2 = 0.1751	R_1 = 0.0647 wR_2 = 0.1024

Powder X-ray diffraction (PXRD) pattern was performed using a 0.7 mm glass capillary filled with polycrystalline samples of the compounds and mounted and aligned on an Empyrean PANalytical powder diffractometer, using Cu Kα radiation (λ = 1.541 77 Å). A total of three scans were collected for each compound at room temperature in the 2θ range of 10−40°.

Magnetic Measurements. Magnetic measurements were performed with a Quantum Design MPMS-XL-5 SQUID magnetometer in the 2−300 K temperature range with an applied magnetic field of 0.1 T at a scan rate of 2 K min^{-1}.

Electrochemical Measurements. The electrochemical experiments were performed using a Gamry electrochemical workstation (Gamry 1010E potentiostat/galvanostat). The powdered materials (2 mg) were mixed in 2 mL of Nafion-5% and ethanol (1:10) and deposited on a 3 mm diameter glassy carbon disc working electrode, which was polished sequentially with 0.3, 0.1 and 0.05 μm alumina powders and washed with deionized water before each experiment. A typical three-electrode experimental cell equipped with a platinum wire as the counter electrode and a Metrohm Ag/AgCl electrode as a reference electrode was used for the electrochemical characterization of the working electrodes. All measurements were carried out after nitrogen bubbling. The electrochemical properties

were studied measuring CVs at different scan rates (from 100 to 5 mV/s) in CH3CN solution of TEA-BF4 0.1M.

Spectroscopic Measurements. FT-IR spectra were collected using a Bruker Equinox 55 spectrometer, preparing the samples as KBr pellets. Raman spectroscopic characterization was carried out on a LabRAM-HR Evolution confocal Raman microscope (Horiba). The measurements were conducted with an excitation wavelength of λ_{ex}= 532 nm. The laser was focused using a 100× objective (0.8 NA), thus leading to a laser spot with a diameter of ca. 1 μm. A CCD camera was employed to collect the backscattered light that was dispersed by an 1800 grooves per mm grating providing a spectral resolution of ~ 1 cm^{-1}. The corresponding Raman spectra were then constructed by processing the data using Lab Spec 5 software.

Mössbauer spectra were collected between 295 and 4 K in transmission mode using a conventional constant-acceleration spectrometer and a 25 mCi ^{57}Co source in a Rh matrix. The velocity scale was calibrated using α-Fe foil. Isomer shifts, IS, are given relative to this standard at room temperature. The absorber was obtained by gently packing the sample into a perspex holder. Absorber thickness was calculated on the basis of the corresponding electronic mass-absorption coefficients for the 14.4 keV radiation, according to Long *et al*.[39] Low-temperature measurements were performed in a bath cryostat with the sample immersed in He exchange gas. The spectra were fitted to Lorentzian lines using a non-linear least-squares method.[40]

EPR measurements were recorded in a Bruker ELEXYS E580 spectrometer under X-band irradiation (~ 9.4 GHz).

TGA was performed in alumina crucibles with the instrument STA-6000 under nitrogen flux (40 mL/min), in the 25-800°C temperature range at 10°C/min.

3. Results and Discussion

3.1 Synthesis

When the organic ligand H_2trz_2An is combined with metal ion precursors *via* hydrothermal method, using a 1:1 stoichiometric ratio, two new phases formulated as $[M(trz_2An)]_n3{\cdot}H_2O$ (M = Co^{II} (**1**), Cu^{II} (**2**) and Ni^{II} (**3**)) and $[Mn(trz_2An)(H_2O)]_n{\cdot}3.5H_2O$ (**4**) are obtained, respectively, as shown in **Scheme 2.2**. Remarkably the synthesis of **1** has been optimized and it can be scaled up to 8 times in a proper autoclave, as reported in experimental section.

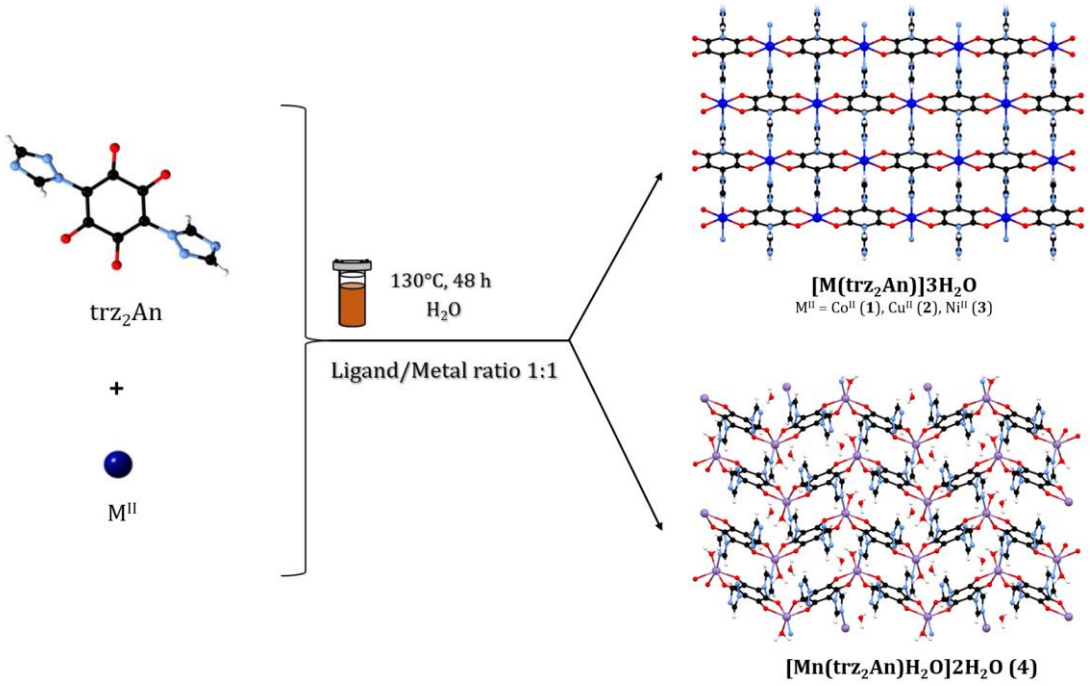

Scheme 2.2. Synthetic procedure for **1-4**.

Due to the great affinity of the H_2trz_2An organic ligand for transition metal ions, when the metal salt solution is added dropwise to the ligand solution, another phase formulated as **$[M(trz_2An)]_n{\cdot}nH_2O$** (M = Fe^{II}/Fe^{III}, n = 9 (**5**), Co^{II}, n = 8 (**6**)), is obtained as a microcrystalline powder. Single crystals of **5** were obtained by *layering* technique and an acetone solution of $Fe(ClO_4)_2 \cdot xH_2O$ was carefully layered on top of an aqueous solution of H_2trz_2An, with an intermediate blank solution of water and acetone in 1:1 ratio, which lead to the formation of black rectangular crystals at the interphase, after three weeks (**Scheme 2.3**). Same method did not allow the formation of single crystals of **6**.

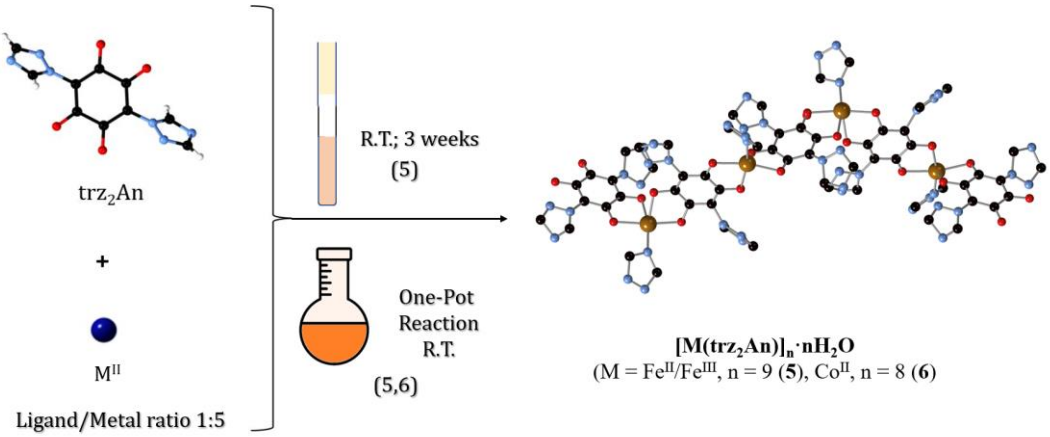

Scheme 2.3. Synthetic procedure for **5-6**.

1-6 frameworks show great thermal stability, with a first weightloss due to uncoordinated water molecules and the complete decomposition of the framework up to 400°C, as reported by thermogravimetric analysis (see *Chapter 3* and Supporting Material, *Part IV*, *Chapter 2*).

3.2 Crystal Structure

1-6 crystallize as 3D neutral extended frameworks of the trz_2An ligand bridging the M^{II} ions, with different coordination geometry which lead to different crystal structures.

3.2.1 Structure of 1- 3.

The structure of **1** and **2** was solved from single-crystal X-ray diffraction data, while **3** was found to be isostructural to **1** and **2** by PXRD (see below). **1** and **2** crystallize in the orthorhombic *Pnnm* space group and its asymmetric unit is formed by one M^{II} (Co^{II} or Cu^{II}) ion with an occupancy of 0.25 and one quarter of trz_2An ligand plus disordered water molecules. M^{II} ions are equatorially coordinated to four oxygen atoms of two bis(bidentate) trz_2An ligands leading to $[M(trz_2An)]_n$ chains running along the *c* axis (see **Figure 2.1a**). The distorted octahedral coordination sphere of M^{II} ions is completed with two nitrogen atoms from N4 atoms of the 1,2,4-triazole substituted pendant rings of trz_2An ligands from two neighbouring chains. In addition, the bis(bidentate) trz_2An ligands of each chain are linked to other two neighbouring chains through N4 atoms of the 1,2,4-triazole substituted pendant rings (**Figure 2.1b**), leading to a 3D neutral polymeric framework. The space between four interconnected chains contains pockets, which could be suitable for the sorption of small molecules as CO_2 (**Figure 2.1c**), making the **1-3** MOFs promising materials for gas uptake and separation (see *Chapter 3*).

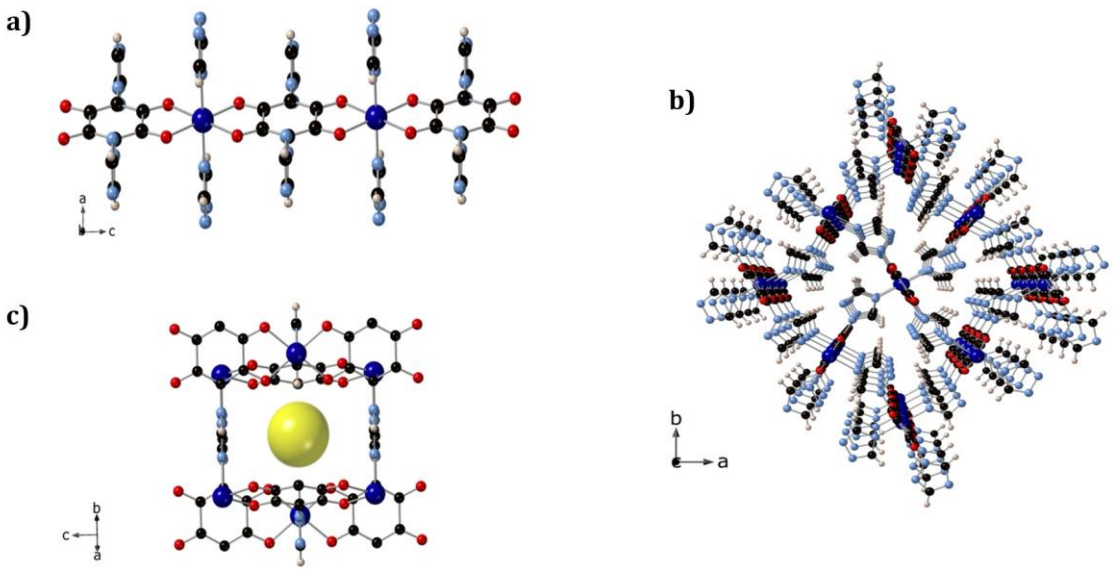

Figure 2.1. Crystal structure of **1-3** showing (a) the anilato-based chains, (b) the microporous channels parallel to the *c*-axis and (c) orthogonal to the *c*-axis with a yellow ball of 4 Å diameter representing the 23.5 % void volume. The black, pink, blue, red, and dark blue spheres represent the C, H, N, O, and M^{II} atoms, respectively.

The distances between triazolyl groups of neighbouring chains, which define the walls of the channels running along the *c* axis, are 3.27 Å for **1** and 3.06 Å for **2** (N2-N2 distance) (**Figure 2.2a**). On the other hand, the distances between the centroids of parallel triazole rings in the channels perpendicular to the *c*-axis are 7.9 Å in **1** and 8.0 Å in **2** (**Figure 2.2b**). The shortest M^{II} intrachain and interchain distances are 7.906 and 8.007 Å for **1** and 8.022 and 7.929 Å, for **2**, respectively. The distances between two M^{II} ions from neighbouring chains ions, linked through the triazolyl groups, are 13.297 Å in **1** and 13.679 Å in **2**.

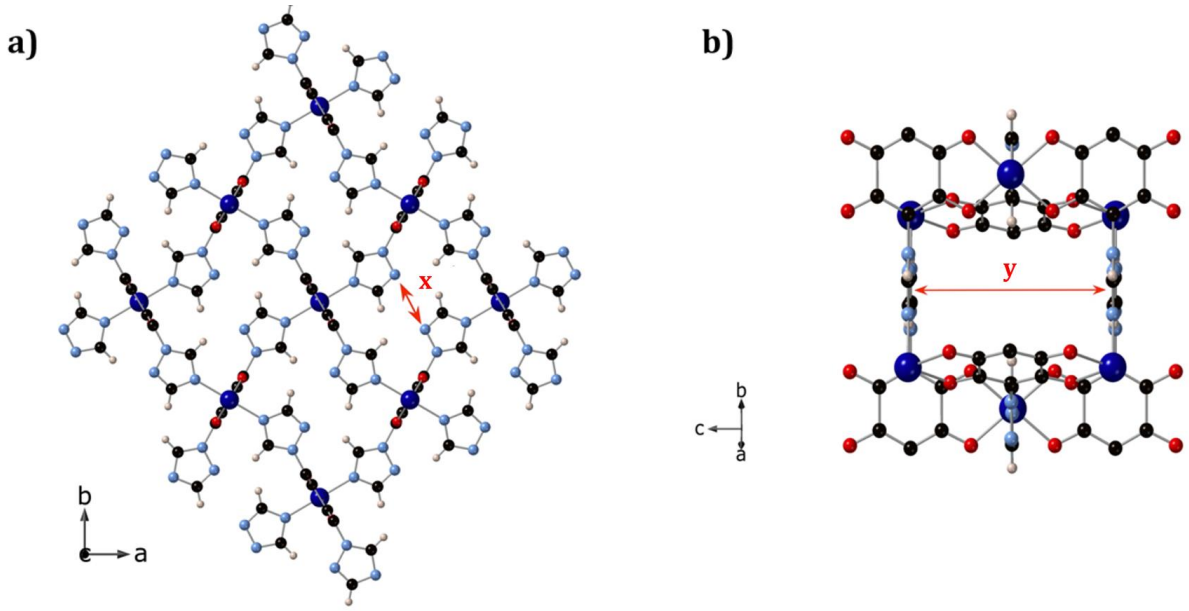

Figure 2.2. View of (a) the structure of **1** and **2** in the *ab* plane with N2-N2 distance (x = 3.27 Å for **1** and 3.06 Å for **2**) and (b) of the microporous channels orthogonal to the *c*-axis, with distance between the centroids of the parallel triazole rings placed at the walls of these channels (y = 7.9 Å for **1** and 8.0 Å for **2**). The black, pink, blue, red, and dark blue spheres represent the C, H, N, O, and M^{II} atoms, respectively.

The four equatorial Co-O and the two axial Co-N bond lengths in **1** are quite similar (2.087(5) and 2.094(8) Å, respectively). In contrast to this, the four equatorial Cu^{II}-O distances of **2** (2.158(5) Å) are longer than the two apical Cu^{II}-N ones (1.972(7) Å). These distances are similar in **1** to those found in 1D chains of formula $[Co(Cl_2An)(H_2O)_2]\cdot G$ (Cl_2An = chloranilic acid; G = H_2O and phenazine) with Co^{II} in the high spin state.[9] On the other hand, they are different to those found in the 1D chains connected through pyrazine ligands of formula $[Cu(Cl_2An)(C_4H_4N_2)]$, which shows two different Cu-O distances (1.955(2) and 2.290(2) Å) and one intermediate Cu-N distance (2.091(2) Å).[41] The C-O distances of 1.257(8) (**1**) and 1.271(9) Å (**2**) in the anilate ligand, the two C-C distances of 1.360(8) and 1.559(15) Å (**1**) and 1.378(8) and 1.523(13) Å (**2**), all together confirm that the anilato linkers is present in its dianionic benzoquinone form (L^{2-} oxidation state).[10] One molecule of water was found to be disordered over several positions and it could not be modelled satisfactorily. It was removed from the electron density map using the OLEX solvent mask command.[8] Two voids of 90.4 $Å^3$ (**1**) and 111.8 $Å^3$ (**2**) were found in the unit cell of the filtered crystals giving a void volume of 23.5% (**1**) and 29.8 % (**2**), which can be occupied by uncoordinated water molecules, as confirmed by thermogravimetric analysis (TGA) which evidences the presence of water molecules in the channels (see *Chapter 3*). PXRD patterns of the polycrystalline sample

of **1-3** are perfectly consistent with the calculated pattern (**Figure 2.3**) confirming the homogeneity and purity of the bulk samples.

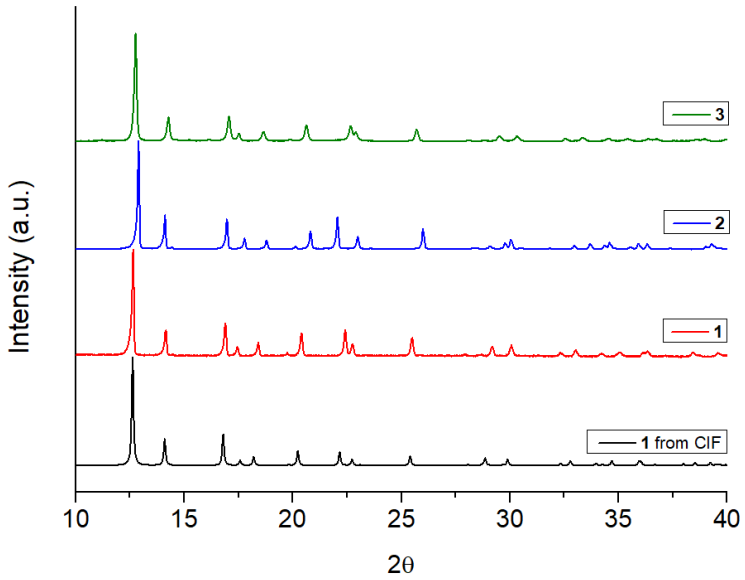

Figure 2.3. Experimental PXRD of **1-3** compared with the calculated from CIF of **1** in the 10-40° range.

3.2.2 Structure of 4.

When trz_2An ligand is combined with Mn^{II} ions by using the same synthetic hydrothermal method, a different phase is obtained (**4**), which crystallize as orthorhombic *Fdd2* space group. The asymmetric unit is composed by one Mn^{II} ion, one trz_2An ligand, one coordinating water molecule and two solvated water molecules, one of them with an occupancy of 0.5, giving rise to the formula $[Mn(trz_2An)(H_2O)]_n \cdot 1.5H_2O$. Elemental analysis is more consistent with the formula $[Mn(trz_2An)(H_2O)]_n \cdot 2.5H_2O$, which may be an indication of the hygroscopicity of **4**. Each Mn^{II} ion has a distorted *cis*-octahedral coordination geometry, where one trz_2An linker coordinating with N4, one water molecule and four oxygen atoms of two trz_2An in *cis* create an octahedral environment around the metal ion. Here, if compared to **1-3**, one nitrogen of the coordination sphere is replaced by one water molecule, changing the coordination geometry. Mn^{II} ions are linked by trz_2An ligands along *a* axis, giving rise to a zigzag 1D chains in which the shortest intrachain Mn···Mn distance is 8.231 Å. Each chain is linked through trz_2An ligands to other two neighbouring chains through N4 atoms of the 1,2,4-triazolyl substituted pendant rings, in which the shortest interchain Mn···Mn distance is 5.961 Å. These interconnected chains through the trz_2An ligands give rise to the 3D neutral polymeric framework, as shown in **Figure 2.4**.

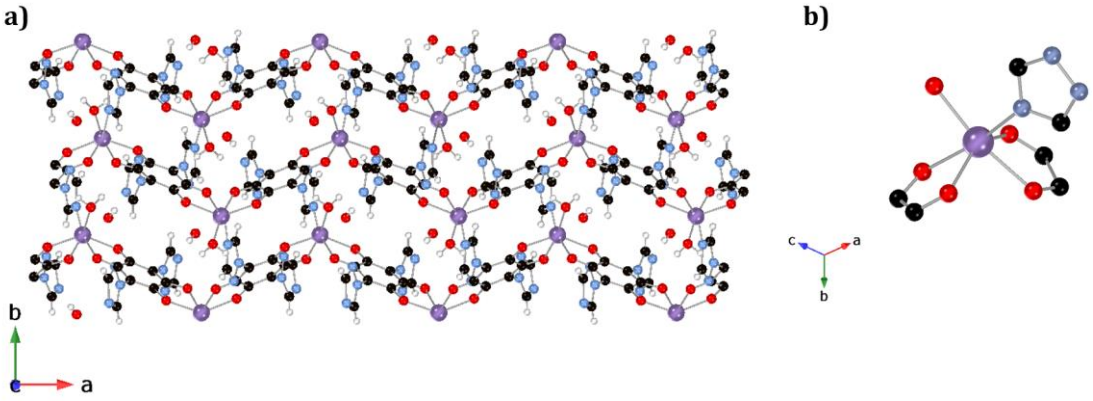

Figure 2.4. View (a) along c axis of **4** and (b) the distorted octahedral coordination sphere of Mn^{II}. The black, white, blue, red, and purple spheres represent the C, H, N, O, and Mn atoms, respectively.

There is another phase with Mn^{II} and trz_2An ligand, which was deposited in the CCDC by Robson *et al.* in 2017,[42] without synthetic details. This compound is formulated as $[Mn_2(trz_2An)_2]_n \cdot CH_3OH]$ and crystallizes in the monoclinic $P2_1/c$ space group, having Mn^{II} in a slight distorted octahedral coordination sphere formed by four oxygen atoms of two trz_2An and two nitrogen atoms of two trz_2An. Hence, the coordination sphere is more similar to that of **1-3**, but here nitrogen atoms occupy one an axial position and one an equatorial position instead of the two axial positions, as in **1-3**. $[[Mn_2(trz_2An)_2]_n \cdot CH_3OH]$ shows straight 1D chains along *a* axis, Also in this case, the presence of triazolyl as substituent, afford a 3D structure, with the 1D chains interconnected by N4 atoms of the 1,2,4-triazolyl pendant arms. Due to the larger ionic radius of the Mn^{II} ion, the mean Mn-O distance of **4** (2.202 Å (4)) and of $[[Mn_2(trz_2An)_2]_n \cdot CH_3OH]$ (2.202 Å (2)) is longer than that one observed in **1** (2.090 Å (6)) and **2** (2.160 Å (5)).

Eight voids of 43.4 $Å^3$ were found in the unit cell of the filtered crystals of **4**, giving a total void volume of 6.5%, showing a more compact structure than $[[Mn_2(trz_2An)_2]_n \cdot CH_3OH]$, which instead owns 31% of void volume. Polycrystalline sample of **4** is completely pure and homogeneous, as confirmed by PXRD pattern which is perfectly consistent with the calculated from the CIF (**Figure 2.5**).

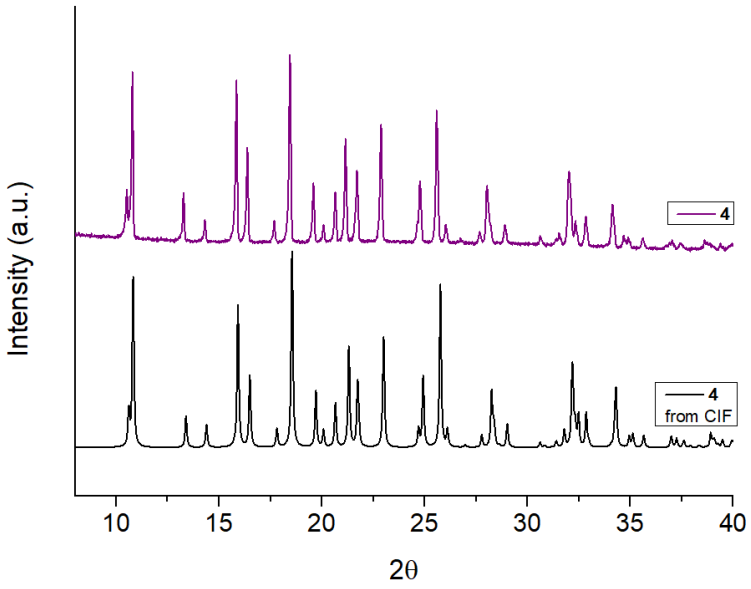

Figure 2.5. Experimental PXRD of **4** compared with the calculated from CIF of **4** in the range 10-40°.

3.2.3 Structure of 5-6.

The single crystal structure of **5** could not be solved properly due to severe disorder problems affecting the trz_2An linker, the metal and the solvent molecules. Four crystals from different syntheses were measured leading to similar results. The best solution was found with a tetragonal $P4_3$ space group. The unit cell is composed by one Fe ion atom and one trz_2An linker plus disordered solvent molecules. The two 1,2,4-triazolyl substituted pendant rings present a disorder, which was solved with two possible configurations fixing the geometry using ShelX constraints. Each Fe ion is coordinated to four oxygens of two bis(bidentate) trz_2An linkers in *cis*. This leads to zig-zag helical chains running parallel to the *c* axis. The coordination geometry of iron is completed with the N4 atom from the triazolyl pendant group of a neighboring chain. Unfortunately, the severe disorder of the triazole rings does not allow to estimate if all the possible configurations of the triazole rings are coordinating to Fe ions. The best solution indicates that at least one of the two 1,2,4-triazolyl substituted pendant rings of each trz_2An linker is coordinating to Fe ions from neighbouring chains but these results have to be taken with caution due to the low quality of the structure. These results suggest the presence of hexa, penta- and/or tetra-coordinated Fe ions and they could explain the presence of three different iron sites in oxidation states II and III observed by Mössbauer Spectroscopy (*vide infra*). The presence of Fe^{III} could cause the partial reduction of the trz_2An linker to its semiquinone form, $trz_2An^{\bullet -}$, due to a spontaneous electron transfer from Fe^{II} to the linker. In agreement with this, preliminary conductivity measurements on a pressed pellet

formed by **5** crystals performed by four probe method show a conductivity of 10^{-10} S/cm, which is three orders of magnitude higher than that of **2** (conductivity of 10^{-13} S/cm). Finally, the packing of these chains leads to voids running parallel to *a*, *b* and *c* axes, which are occupied by disordered solvent molecules.

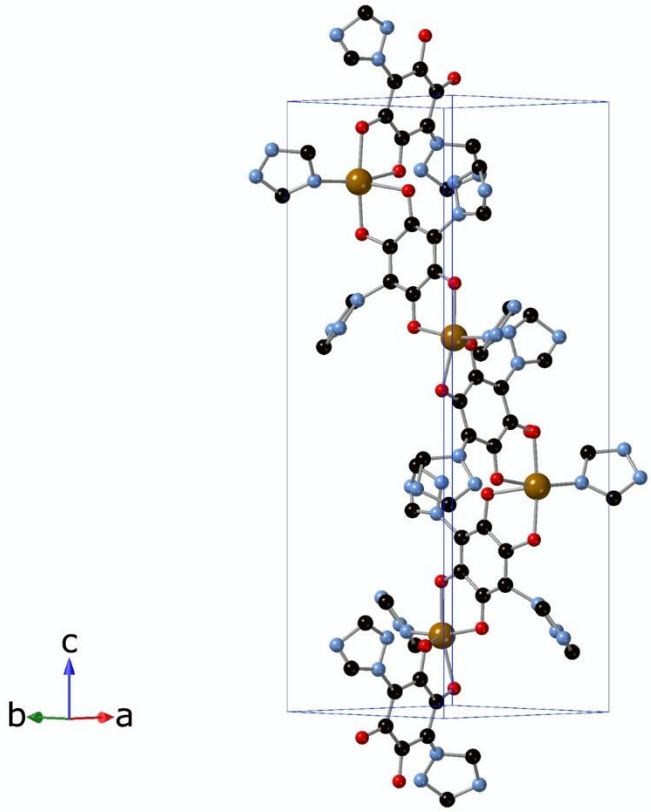

Figure 2.6. View of the helical chains running parallel to the *c* axis in 5. The black, blue, red, and brown spheres represent the C, N, O, and Fe atoms, respectively.

Polycrystalline sample of **5** can be obtained by one-pot reaction, leading to a completely homogeneous powder isostructural to the crystals of **5** obtained by layering technique. Furthermore, by one-pot reaction it is possible to obtain a pure and homogeneous polycrystalline sample Co^{II}-based, showing same crystal structure of **5**, as confirmed by PXRD patterns which are perfectly consistent with each other (**Figure 2.7**).

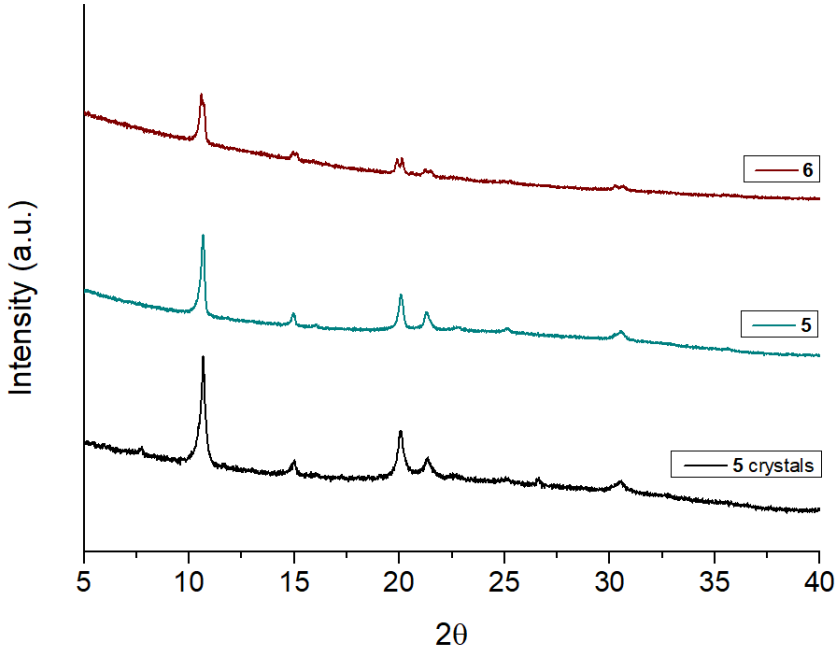

Figure 2.7. Experimental PXRD of **5**, both synthetized *via* layering (black line) and *via* one pot (cyano line), and polycrystalline sample of **6** (brown line) in the range 10-40°.

3.3 FT-IR Spectroscopy

Figures 2.8 and **2.9** report the FT-IR spectra of **1-6** compared with the H_2trz_2An spectrum. According to Pawlukojć *et al.*,[43] the band centered at 1650 cm^{-1} is assigned to the νCO stretching vibrational mode for the uncoordinated C=O groups of the free ligand. In all FT-IR spectra of **1-6**, this band is downshifted compared to the free ligand and it can be attributed to a weakened double bond character of the terminal C=O groups when coordinating the metal ion. In 1550-1450 cm^{-1} range a downshifted broad band is observed for **1-6**, which can be assigned to a νC=C + νC=O combination band, where again the downshift observed is attributable to the metal-ligand coordination. Furthermore, in this range, a further band at ~ 1520 cm^{-1} is attributable to νN=N stretching mode.[44] The bands present in the 1400-1100 cm^{-1} region are assigned to the vibrational stretching of the triazolyl aromatic rings and to the νC-N vibration, both of the C-N of the triazolyl groups and of the C-N bond between benzoquinone and triazolyl ring.[44,45] Finally, also the bands attributable to νM-N and νM-O vibrations can be observed in the 480-430 cm^{-1} range.[46]

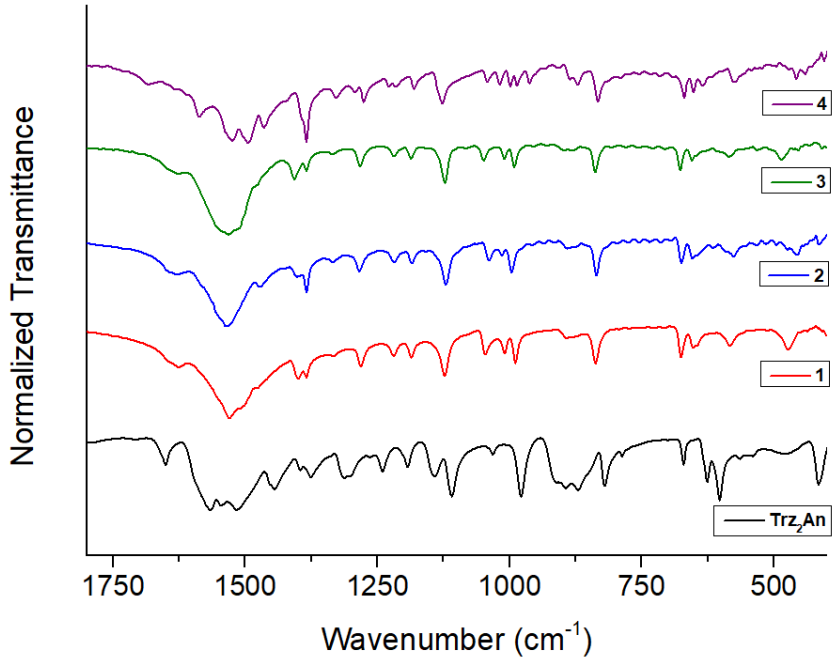

Figure 2.8. FT-IR spectra of H_2trz_2An free ligand and **1-4** in the 1800-400 cm^{-1} range.

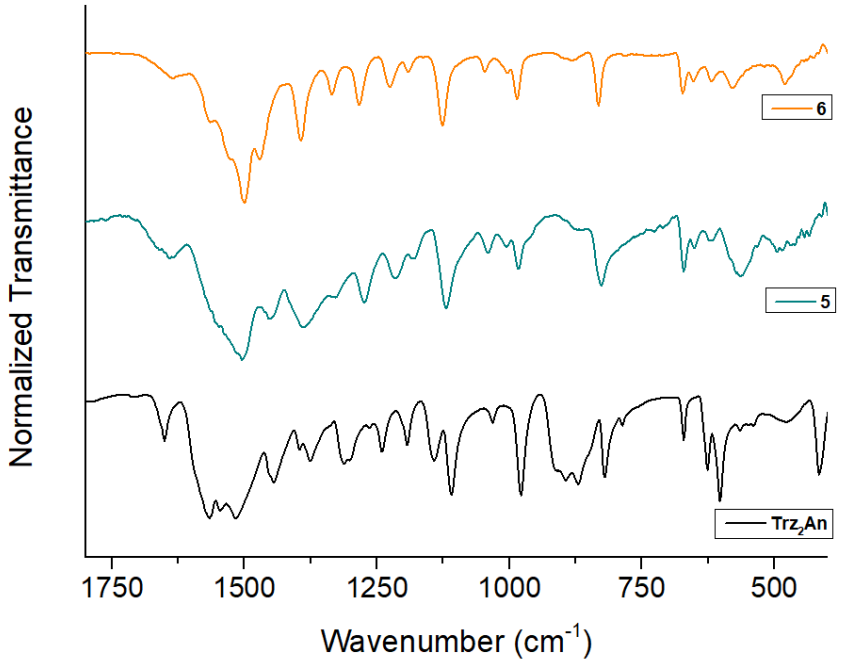

Figure 2.9. FT-IR spectra of H_2trz_2An free ligand and **5-6** in the 1800-400 cm^{-1} range.

The characteristic vibrational bands of **1-6**, along with their assignments, are shown in the following **Table 2.3**.

Table 2.3. Assignments of characteristic bands for **1-6**, all the frequencies are in cm^{-1}.[46–50]

Vibrational Modes	1	2	3	4	5	6
ν C=O	1625	1629	1629	1585	1640	1634
ν N=N	1529	1536	1533	1523	1546	1525
νC=O+νC=C	1508	1473	1479	1494	1504	15000
ν ar. ring	1400 1384	1403 1382	1405 1384	1382	1389	1393
ν C-N	1280 1124	1284 1120	1282 1122	1276 1126	1274 1119	1282 1126
δ C=C	846	835	838	833	825	831
νM-O; νM-N	472	455	485	457 441	487 467	480

3.4 Mossbauer Spectroscopy

The Mössbauer spectra of **5** (**Figure 2.10**) above 25 K may be fitted with three quadrupole doublets and at 4 K with two magnetic sextets and one doublet. At 25 K the onset of strong magnetic correlations is observed. Above 25 K the isomer shift, IS, and QS (**Table 2.4**) of the doublet with relative area I~16% is typical of high spin Fe^{II} S=2.[51,52] The magnetic hyperfine field B_{hf} of the corresponding sextet at 4 K is also consistent with this assignment. The doublet with the smallest splitting and I~47% above 25 K, gives rise at 4 K to a sextet with B_{hf} consistent with Fe^{III} S=5/2. At 25 K part of the Fe^{III} is already observed as an incipient sextet denoting the onset of slow relaxation of the direction of the Fe^{III} magnetic moments. In contrast to the Fe^{III} S=5/2 and Fe^{II} S=2 cations, the doublet with QS~1.6 mm/s and I~35% shows no magnetic correlations down to 4 K which may be explained if it is attributed to low spin Fe^{II} (S=0).

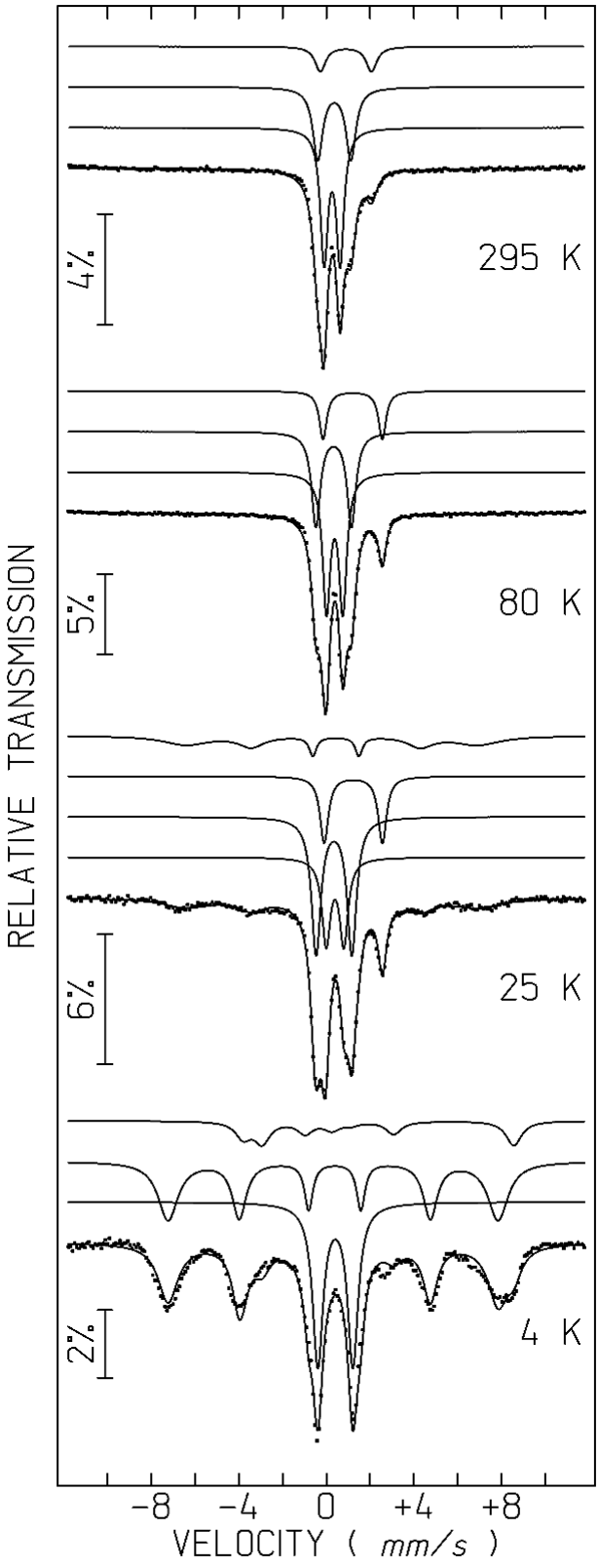

Figure 2.10. Mössbauer spectra of **5** taken at different temperatures.

Table 2.4. Estimated parameters from the Mössbauer spectra of **5** taken at different temperatures (T)

T	IS	QS, ε	B_{hf}	I	Fe spin
295 K	0.36	0.73		49%	Fe^{3+} S=5/2
	0.42	1.51		35%	Fe^{2+} S=0
	1.04	2.17		16%	Fe^{2+} S=2
130 K	0.47	0.73		46%	Fe^{3+} S=5/2
	0.43	1.60		37%	Fe^{2+} S=0
	1.28	2.68		16%	Fe^{2+} S=2
80 K	0.49	0.74		47%	Fe^{3+} S=5/2
	0.45	1.62		37%	Fe^{2+} S=0
	1.31	2.71		16%	Fe^{2+} S=2
25 K	0.51	0.80	-	21%	Fe^{3+} S=5/2
	0.45	-0.19	41.3	24%	Fe^{3+} S=5/2
	0.46	1.63	-	38%	Fe^{2+} S=0
	1.34	2.66	-	17%	Fe^{2+} S=2
4 K	0.46	-0.09	46.7	49%	Fe^{3+} S=5/2
	0.52	1.60	-	35%	Fe^{2+} S=0
	1.34	3.53	34.0	16%	Fe^{2+} S=2

IS (mm/s) isomer shift relative to metallic α-Fe at 295 K; QS (mm/s) quadrupole splitting and ε (mm/s) quadrupole shift estimated for quadrupole doublets and magnetic sextets, respectively. B_{hf} (tesla) magnetic hyperfine field; I relative area. Estimated errors ≤ 0.03 mm/s for IS, QS, ε, < 0.3 T for B_{hf} and <2% for I.

3.5 Magnetic Properties

The thermal dependence of χT product *vs* temperature of **1-4** are reported in **Figure 2.11**. At 300 K, values of 2.9, 0.4, 1.4 and 4.4 emu·K·mol^{-1}, are observed respectively for **1-4**. When the temperature decreases, χT product of **1-4** decreases as well, indicating an antiferromagnetic exchange coupling between the metal ion centers. This behavior is typical for single chains of transition metal ions connected through anilate ligands, like $[(M)(Cl_2An)(H_2O)_2]_n$ and $[(M)(Cl_2An)(H_2O)_2(phz)]_n$ (M = Fe^{II}, Co^{II}, Mn^{II}; phz = phenazine) previously reported by Kawata *et al*.[53,54] The value of χT for **1** is higher than the spin-only value for a high-spin Co^{II} (d^7) due to considerable orbital momentum contribution to the magnetic moment. Upon cooling, χT decreases continuously with a very abrupt decrease below 100 K to reach a value of 0.4 emu·K·mol^{-1} at 2 K. This is indicative of antiferromagnetic interactions between Co^{II} centers as observed in 1D compounds $[Co(Cl_2An)(H_2O)_2]\cdot G$, containing chloranilato ligand.[53] Indeed, low-temperature data below 50 K can be fitted using the zero-field susceptibility derived by

Fisher for the spin-1/2 Ising chain.[55] The best set of parameters are: J = –2.55 cm^{-1} (for –2J Hamiltonian formalism), g_z = 7.8 and TIP = 6.5x10^{-3} (**Figure 2.12**).

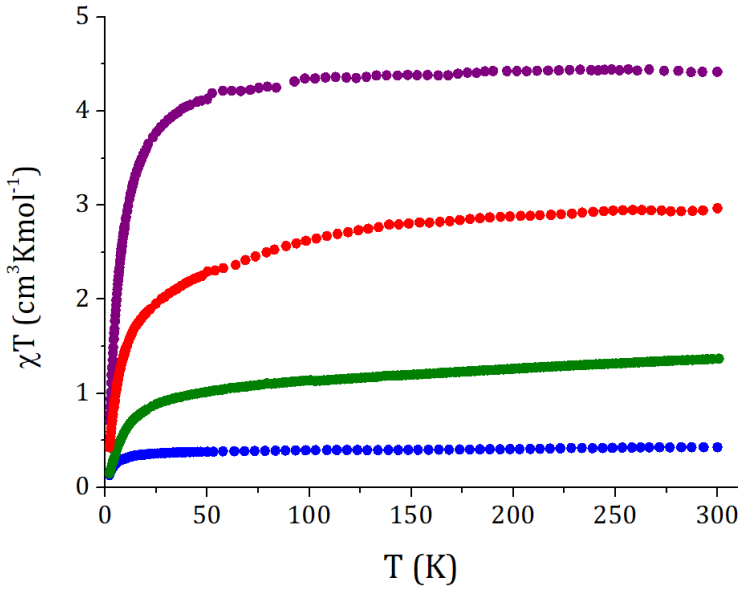

Figure 2.11. Temperature dependence of χ_mT of **1** (red)**, 2** (blue), **3** (green) and **4** (purple) under an applied field of 0.1 T.

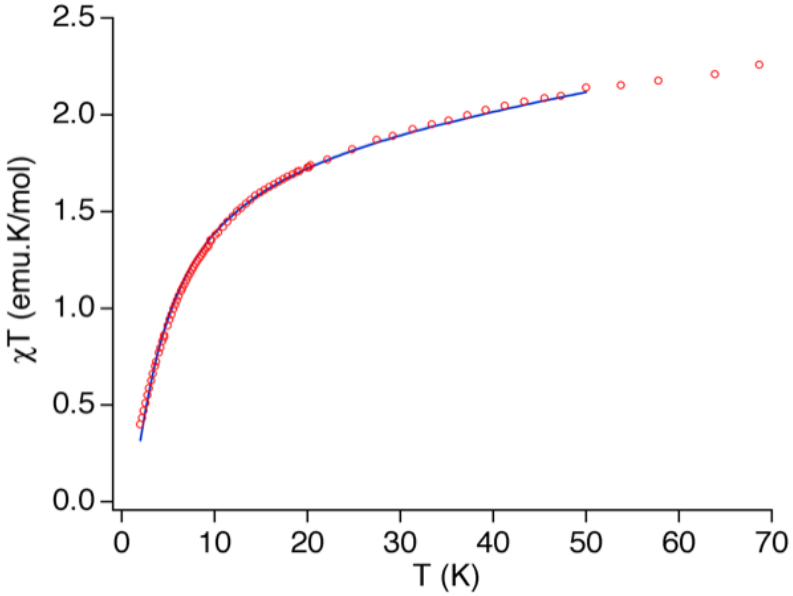

Figure 2.12. Low temperature thermal dependence of χ_mT of **1** (red empty spheres) and best fit of experimental data using the zero-field susceptibility derived by Fisher for the spin-1/2 Ising chain (solid line).

χ_MT product for Mn^{II} chain has a value of 4.4 emu K mol^{-1} at room temperature. This value is very close to the expected value for an isolated S=5/2 associated to on Mn^{II} ion.

This value decreases continuously on cooling showing the presence of antiferromagnetic interactions. When χ_M is represented versus temperature, a continuous increasing is observed when temperature decreases till a maximum at 3.5 K with a value of 0.388 emu mol^{-1}. Similar experimental behavior is observed for Ni^{II} and Cu^{II} chain with $\chi_M T$ product at room temperature 1.05 and 0.386 emu K mol^{-1}, respectively. These values are expected for isolated spins of each ion, S=2 and S=1/2. When the thermal variation of susceptibility is represented in both cases, a maximum is not clearly observed.

The magnetic data have been analyzed using an isotropic model for a chain of interacting effective spins. We can calculate the magnetic susceptibility of this Heisenberg chain using a closed chain computational procedure with increasing number of centers (N). We assumed that the N = 16 calculation is close to the exact solution for Cu^{2+} chain in the full experimental temperature range. This limit is N=10 for Ni^{2+} chain and N = 6 for Mn^{2+} chain. Calculations were performed with the magnetism package MAGPACK.[56] This model very satisfactorily reproduces the magnetic data in the whole temperature range using the following parameters: J = –1.29 cm^{-1}, g = 2.03 and a paramagnetic impurity 4% for **2**, J = –1.52 cm^{-1}, g = 2.07 and a paramagnetic impurity 6% for **3** and J = –0.249 cm^{-1} and g = 2.00 for **4**. The values of the exchange parameters(J) herein used are within the normal range observed for this kind of compounds. (**Figure .2.13-2.15**)

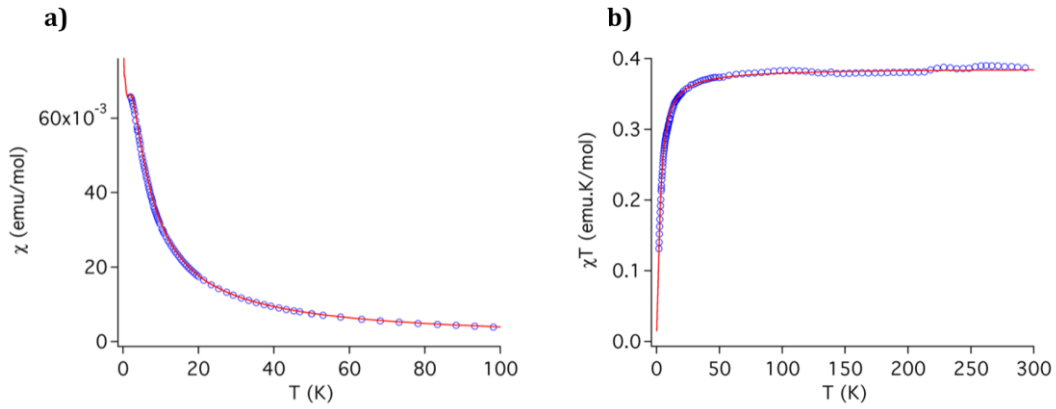

Figure 2.13. Thermal dependence of χ (a) and $\chi_m T$ (b) of **2** (red empty spheres) and best fit of experimental data using the zero-field susceptibility derived by Fisher for the spin-1/2 Ising chain (solid line).

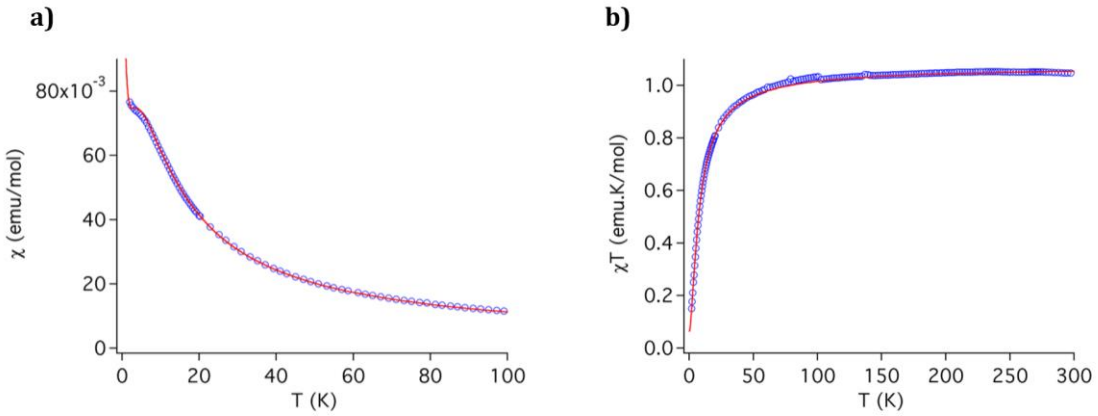

Figure 2.14. Thermal dependence of χ (a) and $\chi_m T$ (b) of **3** (red empty spheres) and best fit of experimental data using the zero-field susceptibility derived by Fisher for the spin-1/2 Ising chain (solid line).

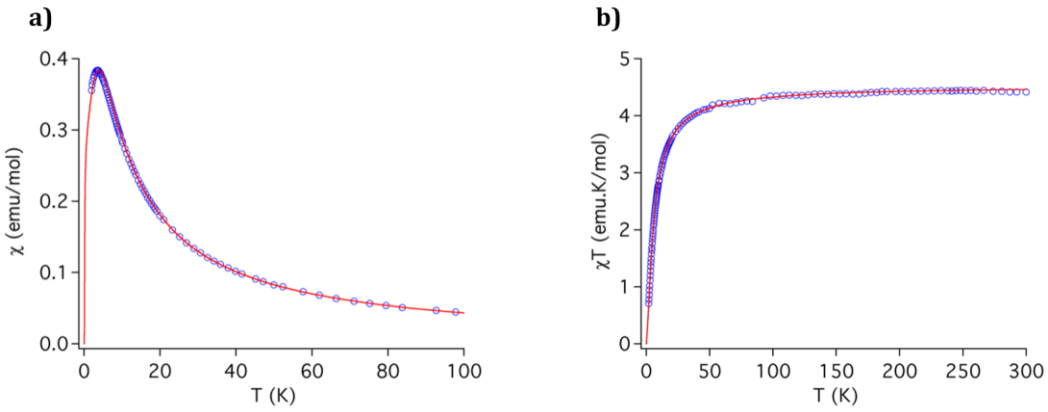

Figure 2.15. Thermal dependence of χ (a) and $\chi_m T$ (b) of **4** (red empty spheres) and best fit of experimental data using the zero-field susceptibility derived by Fisher for the spin-1/2 Ising chain (solid line).

The isothermal field (H) dependence of the magnetization (M) was measured up to 5 T at 2 K (**Figure 2.16**) for all **1-4** compounds and it shows a linear increase at lower magnetic fields as expected for an antiferromagnetic behavior.

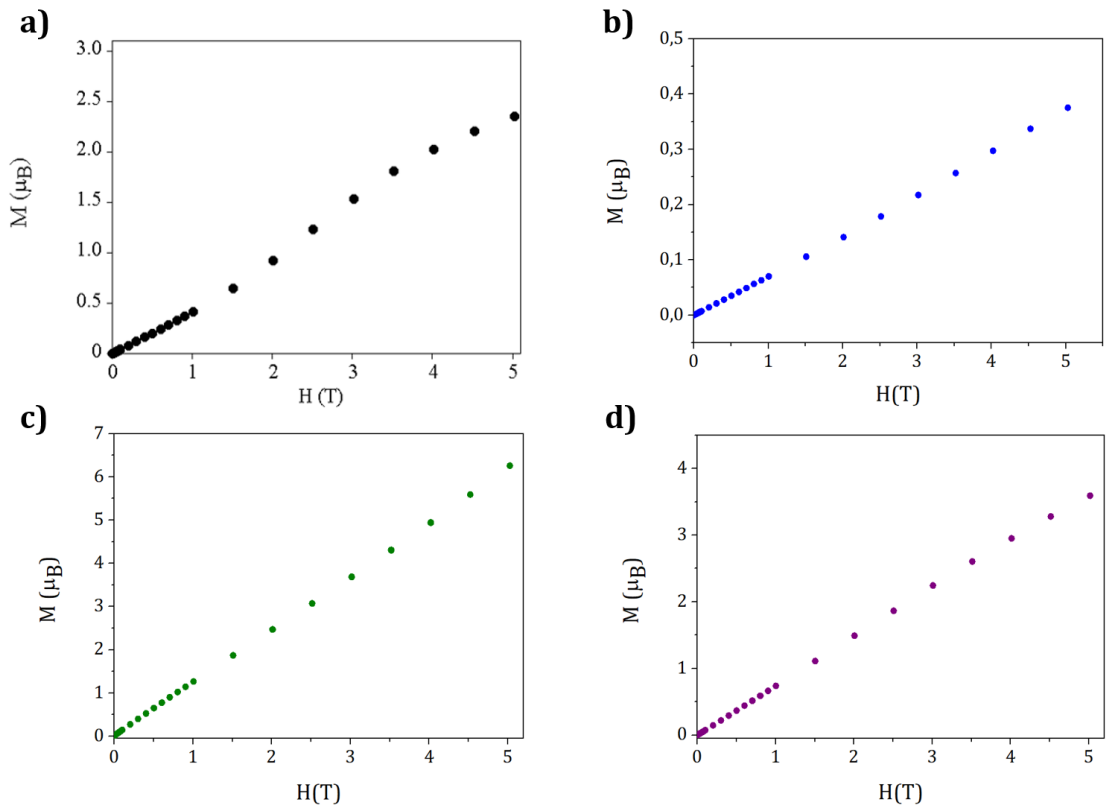

Figure 2.16. Field dependence of the Magnetization (M-H) measured at 2 K for **1-4**, panel *a*, *b*, *c* and *d* respectively.

The thermal variation of χT product of **5** at 0.1 T is reported in **Figure 2.17**. A value of 3.2 emu·K·mol^{-1} is observed, which is higher than that expected for 50 % of high-spin Fe^{III} and 16 % of high-spin Fe^{II} found by Mössbauer spectroscopy (2.7 emu·K·mol^{-1} considering spin-only value of 4.375 emu·K·mol^{-1} for high-spin Fe^{III} and a typical value of 3.5 emu·K·mol^{-1} for high-spin Fe^{II}). This can be due to the contribution of unpaired electrons from the reduced anilate ligands, which could not be confirmed by EPR measurements (*vide infra*), or to a ferromagnetic coupling. In agreement with this, there is a continuous increase of χT on lowering the temperature to a maximum of 4.3 emu·K·mol^{-1} at 15 K. At lower temperatures, χT decreases to reach 2.2 emu·K·mol^{-1} at 2 K. Isothermal magnetizations at 2 and 5 K show a gradual increase without reaching saturation at 5 T to values of 2.9 and 2.8 Bohr magneton, respectively (**Figure 2.18**). These results suggest a complicate exchange interaction whose interpretation is not possible without a proper structural model. If we compare the χT *vs.* T curves of **5** with those of pure Fe^{II} cis- chains linked through chloranilate ligands,[53] the curves resemble with a less marked increase of χT for the chloranilate compound (from 3.5 emu·K·mol^{-1} at 300 K to 3.7 emu·K·mol^{-1} at 10 K). Finally, in order to confirm the magnetic ordering

found by Mössbauer measurements (*vide supra*), variable-frequency AC magnetic measurements have been performed. **5** shows a small AC signal below 3 K, Thus, the out-of-phase (χ'') molar magnetic susceptibility becomes nonzero below 3K, while the in-phase (χ') molar magnetic susceptibility exhibits a maximum at ca. 2.3 K, which is only observed at the maximum frequency of 10000 Hz. These measurements do not clarify if the sextuplet observed in Mössbauer measurements is related to slow relaxation of the magnetization of part of the iron centers or to magnetic ordering. Magnetic measurements at lower temperature are needed to clarify this point since a shift of these peaks to higher temperatures by applying DC magnetic fields was not achieved.

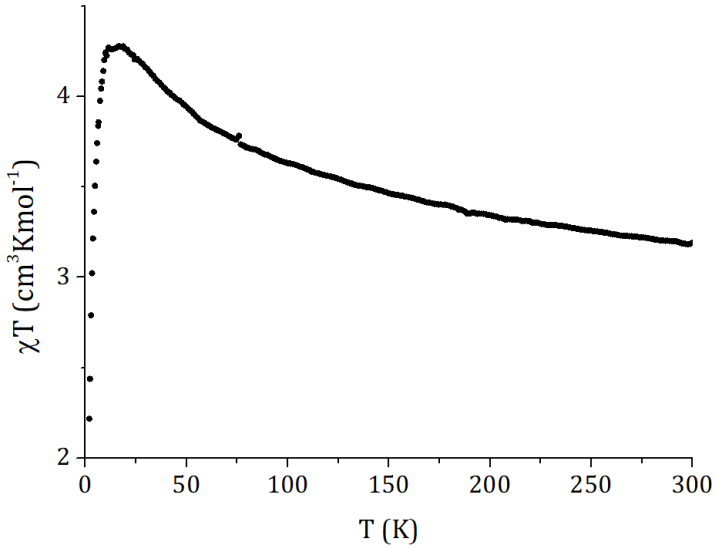

Figure 2.17. Temperature dependence of $\chi_m T$ of **5** under an applied field of 0.1 T.

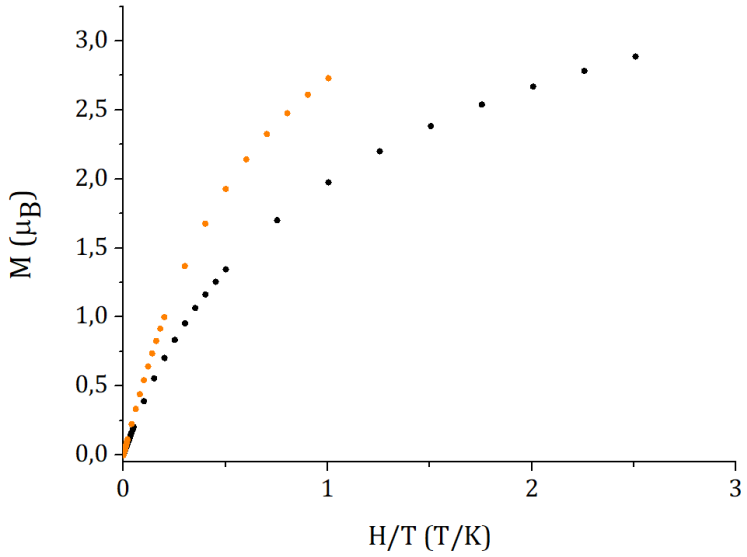

Figure 2.18. Magnetization vs H/T measured at 2 K (black line) and 5 K (orange line) for **5**, up to H =5T.

6 presents a χT value of 2.5 emu·K·mol^{-1} at 300 K (**Figure 2.19**), which decreases on lowering the temperature. Upon cooling, χT decreases continuously with a very abrupt decrease below 100 K to reach a value of 0.4 emu·K·mol^{-1} at 2 K. This is indicative of antiferromagnetic interactions between Co^{II} centers as observed in **1**. The fitting of this data to zero-field susceptibility derived by Fisher for the spin-1/2 Ising chain used for **1** is in progress.

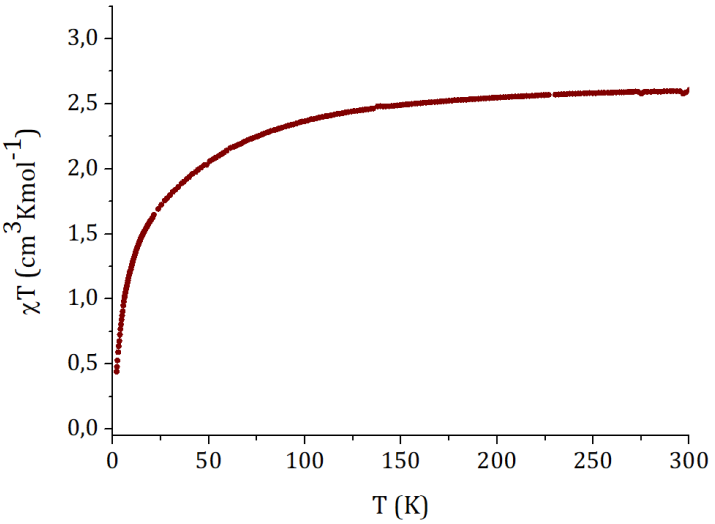

Figure 2.19. Temperature dependence of $\chi_m T$ of **6** under an applied field of 0.1 T.

The isothermal field (H) dependence of the magnetization of **6** was measured up to 8 T at 2 K (**Figure 2.20**). Until 4 T, it shows a linear increase at lower magnetic fields, typical of the antiferromagnetic behavior. The magnetization at 8 T (2.8 B. M) is significantly lower than the expected saturation for a system with (S = 3/2 and g > 2).

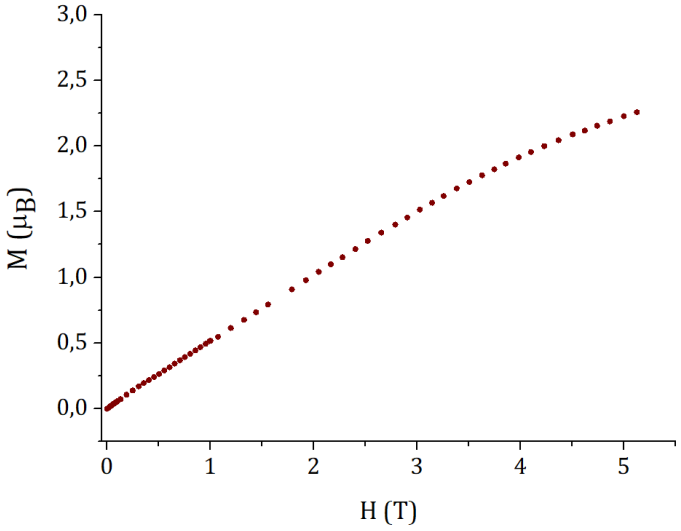

Figure 2.20. Field dependence of the Magnetization (M-H) measured at 2 K for **6**.

3.6 EPR Spectroscopy

EPR Spectroscopy was performed on **5** to verify the presence of $trz_2An^{\bullet -}$ semiquinone linker, eventually formed by the spontaneous oxidation process $Fe^{II} \rightarrow Fe^{III}$.The X-band EPR spectrum of **5** at 4 K displays two broad bands (**Figure 2.21**), an intense band centered at g = 4.2 and a weaker band centered at g = 2.1. It does not show an obvious underlying component attributed to the organic radical as observed by Van Koeverden *et al.* in the 2D compound (PhenQ)$[Fe_2(Cl_2An)_3]\cdot$nDMF, which displays a broad signal at room temperature.[34] The strong feature at g_{eff} = 4.3 in a X-band spectrum arises in a completely rhombic system (E/D = 1/3) for D > 0.05 cm^{-1} (but a similar resonance occurs in an axial system when D is large (on the order of 1 cm^{-1})).[57]

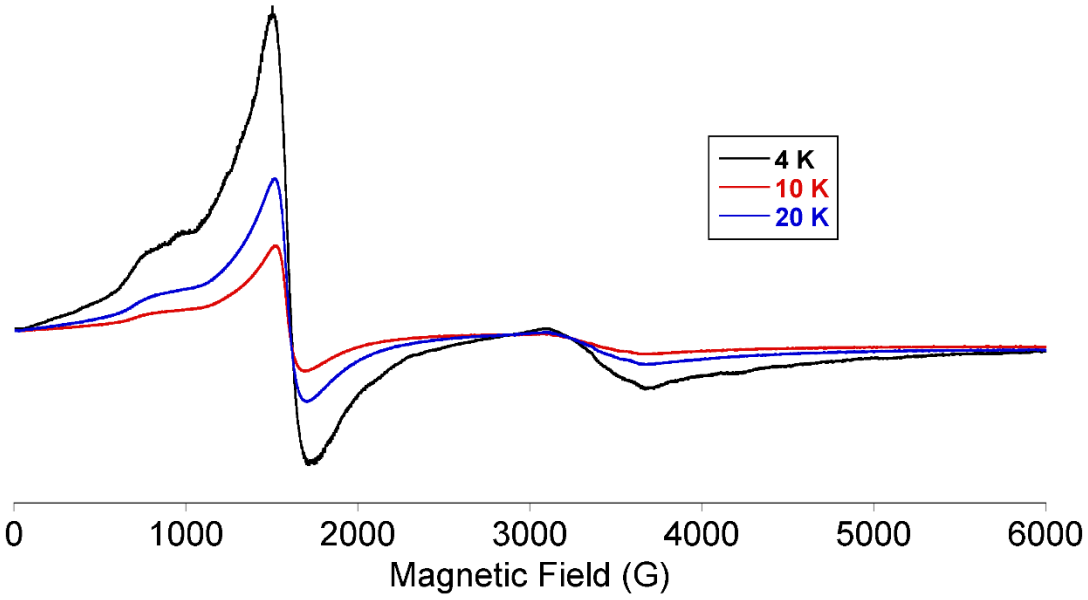

Figure 2.21. EPR spectra of **5** at 4 (black line), 10 (red line) and 20 K (blue line).

3.7 Electrochemical Properties

Considering the redox activity of anilate based materials, due to the presence of benzoquinone ring, solid state Cyclic Voltammetry was performed on **1**-**6** to explore their electrochemical behavior. Cyclic Voltammogram of **1**, measured in -2.5− 1.0 V (vs. Ag/AgCl) potential range and reported in **Figure 2.22**, shows two irreversible reduction peaks at -0.72 V and -2.10 V. The first one is due to the one-electron reduction which lead to formation of the semiquinoid form of the anilate linker,[58] while the second one is

the peak attributed to the complete reduction to hydroquinone. Since the oxidation potential of Co^{II}/Co^{III} couple is generally above 1 V, depending on the ligand which coordinate the metal ion,[59] no oxidation peaks are herein observed.

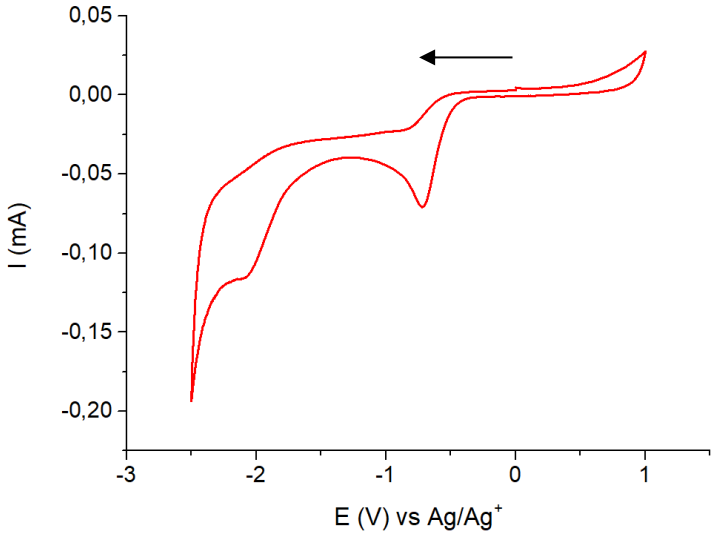

Figure 2.22. Cyclic voltammogram of **1** recorded at a scan rate of 50 mV/s , on a 3 mm GC electrode, in contact with 2 mL of Nafion-5% and ethanol (1:10).

Cyclic Voltammogram of **2** was recorded in -1.5 − 1.0 V (vs. Ag/AgCl) potential range and it shows one irreversible reduction peaks at -0.95 V, as reported in **Figure 2.23**, due to the one-electron reduction of the benzoquinone moiety typical of the anilate linker. When **2** is measured in the - 0.1 − 0.5 V potential range, the reduction peak associated to the Cu^{II}/Cu^{I} couple is clearly observed at E_c = 0.34 V,[60] as shown in the Inset of the **Figure 2.23**.

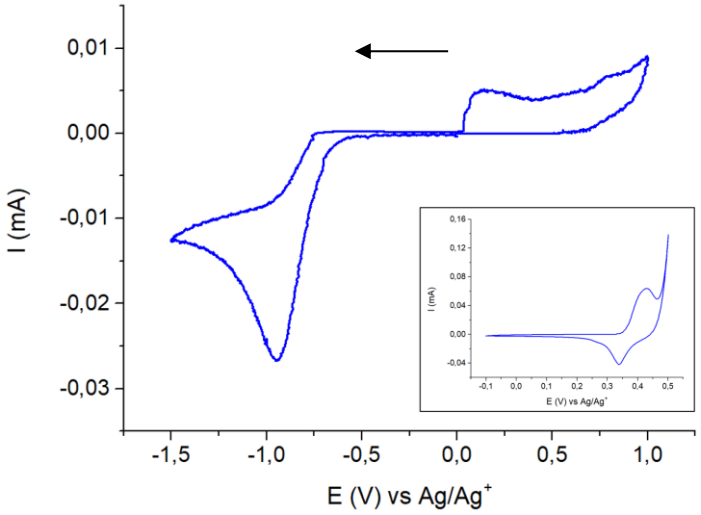

Figure 2.23. Cyclic voltammogram of **2** recorded at a scan rate of 25 mV/s , on a 3 mm GC electrode, in contact with 2 mL of Nafion-5% and ethanol (1:10).

Compound **3** was studied in the -2.0 − 0.0 V (vs. Ag/AgCl) potential range and it shows instead only the reversible one-electron reduction to the semiquinoid form of the anilate at E_c=- 0.86 V. (**Figure 2.24**).

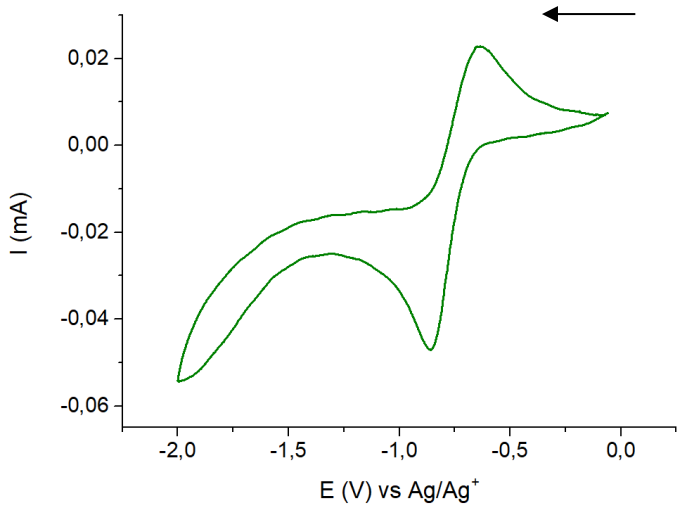

Figure 2.24. Cyclic voltammogram of **3** recorded at a scan rate of 50 mV/s , on a 3 mm GC electrode, in contact with 2 mL of Nafion-5% and ethanol (1:10).

Reduction of the quinone ligand is quasi reversible for **1**, **2** and **3**. No clear differences in this peak attributable to the effect of the reduction of Cu^{II} to Cu^{I} are observed, but further experiments at different scan rates to confirm these findings are in progress.

A similar behavior is shown in **4**, measured in the same potential range of **3**, where the reversible one-electron reduction peak at - 0.89 V, due to the semiquinoid form, is observed (**Figure 2.25**).

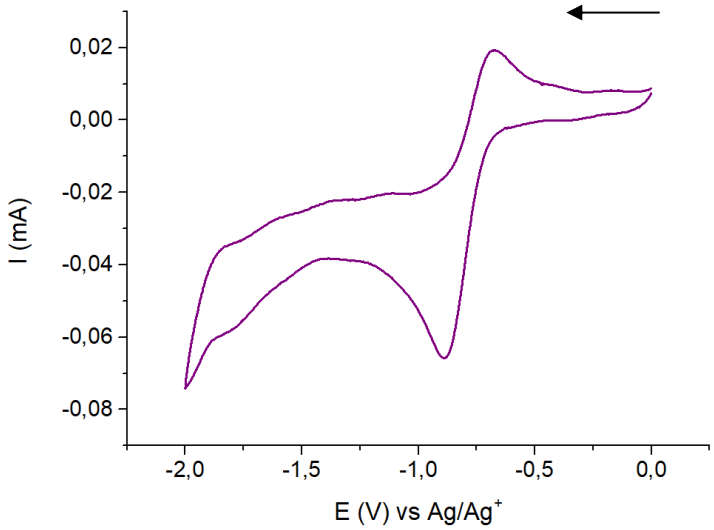

Figure 2.25. Cyclic voltammogram of **4** recorded at a scan rate of 100 mV/s , on a 3 mm GC electrode, in contact with 2 mL of Nafion-5% and ethanol (1:10).

Compound **5** and **6** were measured in the potential range of **3** and **4**, showing to be less stable than **1-4** (**Figure 2.26**). Herein is reported only the voltammogram of **5,**showing the first reversible reduction peak at E_c = - 0.77 V.

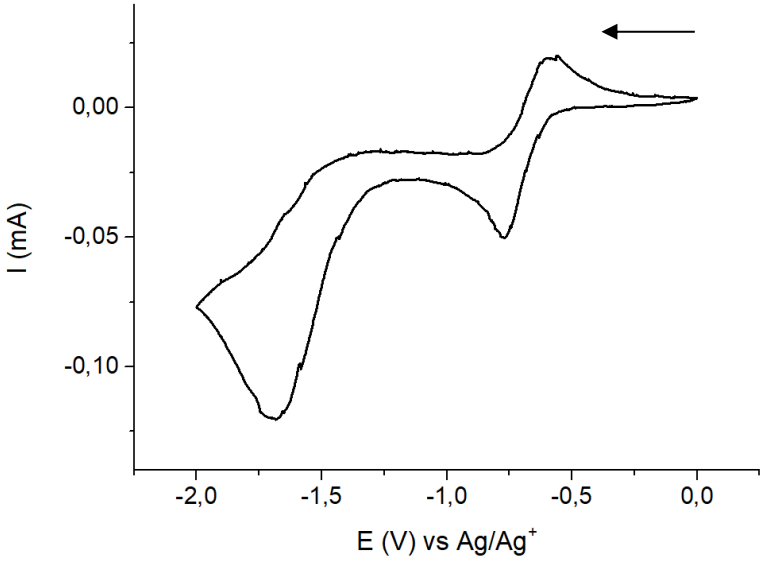

Figure 2.26. Cyclic voltammogram of **5** recorded at a scan rate of 50 mV/s , on a 3 mm GC electrode, in contact with 2 mL of Nafion-5% and ethanol (1:10).

4. Conclusions

A series of 3D CFs based on *3d* metal transition ions and 3,6-N-ditriazolyl-2,5-dihydroxy-1,4-benzoquinone (H_2trz_2An) was synthetized, by using different synthetic strategies such as conventional one-pot reactions, layering and hydrothermal methods. Noteworthy, the presence of triazolyl group in the anilate ring afford different polymeric 3D frameworks, formulated as $[M_2(trz_2An)_2]_n3H_2O$ (M = Co^{II} (**1**), Cu^{II} (**2**) and Ni^{II} (**3**)), $[Mn(trz_2An)(H_2O)]n\cdot 2H_2O$ (**4**) and $[M(trz_2An)]n\cdot 2H_2O$ (M = Fe^{II}/Fe^{III} (**5**), Co^{II} (**6**)). In **1-3**, M^{II} ions are equatorially coordinated to four oxygen atoms of two bis(bidentate) trz_2An ligands, leading to 1D straight chains running along the *c* axis. The coordination sphere of M^{II} ions is completed with two nitrogen atoms from N4 atoms of the 1,2,4-triazolyl substituted pendant rings of anilate linkers from two neighboring chains. The bis(bidentate) trz_2An linkers of each chain are bonded to other two neighboring chains through N4 atoms of the 1,2,4-triazole substituted pendant rings, leading to a 3D neutral polymeric framework, containing 1D channels suitable for sorption of small molecules.

When H_2trz_2An is combined with Mn^{II} ions, by using the same synthetic procedure, a different phase is obtained. In this case, the coordination geometry of Mn^{II} ion is distorted cis-octahedral and the ions are linked by trz_2An ligands along *a* axis, giving rise to zigzag 1D chains. As in **1-3**, those chains are connected through the N4 of the triazolyl group in trz_2An. In **5-6**, each M^{II} ion is coordinated to four oxygens of two bis(bidentate) trz_2An linkers in *cis*, forming 1D *zig-zag* helical chains running parallel to the *c* axis. Again, the coordination geometry of M^{II} is completed with the N4 atom from the triazolyl pendant group of a neighboring chain, but due to the severe disorder of the triazole rings it was not possible to determine if all the possible configurations of the triazole rings are coordinating to M^{II}. Compounds **1-4** and **6** show a magnetic behavior dominated by antiferromagnetic interaction in the anilato 1D chains as previously reported by Kitagawa *et al.* with comparable *J* values.[53] Therefore, it seems that magnetic interaction through the triazolyl substituent are negligible due to the lack of electronic delocalization given by the N-bonding of triazolyl group to the benzoquinone ring. On the contrary, **5** shows a different behavior which suggests a ferromagnet coupling with possible slow relaxation of the magnetization or magnetic ordering at very low temperatures. This could be related to the partial oxidation of Fe^{II} to Fe^{III} and possible reduction of the anilate ligands to compensate the positive charge. However, a complete understanding of its magnetic properties it is not possible without a proper structural model. The optimization of the synthesis is in progress to obtain crystals of better quality enabling structural resolution. Finally, the M^{II}-trz_2An series further show a redox activity due to the presence of the benzoquinone *core*, evidenced by Cyclic Voltammetry, showing a reduction potential (E_c) in the -0.7 – -0.9 V range, attributable to the one-electron reduction benzoquinone → semiquinone, paving the way to tune magnetic and conducting properties of these MOFs by post-synthetic chemical or electrochemical reduction.

.

References

1 S. R. Batten, N. R. Champness, X. M. Chen, J. Garcia-Martinez, S. Kitagawa, L. Öhrström, M. O'Keeffe, M. P. Suh and J. Reedijk, *CrystEngComm*, 2012, **14**, 3001–3004.

2 C. Wang, D. Liu and W. Lin, *J. Am. Chem. Soc.*, 2013, **135**, 13222–13234.

3 S. Ali Akbar Razavi and A. Morsali, *Coord. Chem. Rev.*, 2019, **399**, 213023.

4 N. L. Rosi, J. Eckert, M. Eddaoudi and D. T. Vodak, 2016, **300**, 1127–1129.

5 M. Eddaoudi, J. Kim, N. Rosi, D. Vodak, J. Wachter, M. O. Keeffe and O. M. Yaghi, *Science*, 2002, **295**, 469–472.

6 E. Miguel-Casañ, E. Andres-Garcia, J. Calbo, M. Giménez-Marqués and G. Mínguez Espallargas, *Chem. - A Eur. J.*, 2021, **27**, 4653–4659.

7 J. Yu, L. H. Xie, J. R. Li, Y. Ma, J. M. Seminario and P. B. Balbuena, *Chem. Rev.*, 2017, **117**, 9674–9754.

8 N. Maksimchuk, M. Timofeeva, M. Melgunov, a Shmakov, Y. Chesalov, D. Dybtsev, V. Fedin and O. Kholdeeva, *J. Catal.*, 2008, **257**, 315–323.

9 V. Pascanu, G. González Miera, A. K. Inge and B. Martín-Matute, *J. Am. Chem. Soc.*, 2019, **141**, 7223–7234.

10 Y. Wen, M. Feng, P. Zhang, H.-C. Zhou, V. K. Sharma and X. Ma, *ACS ES&T Eng.*, 2021, **1**, 804–826.

11 X. Jing, C. He, D. Dong, L. Yang and C. Duan, *Angew. Chem. Int. Ed. Engl.*, 2012, **51**, 10127–31.

12 C. Wu, A. Hu, L. Zhang and W. Lin, *J. Am. Chem. Soc.*, 2005, **127**, 8940–8941.

13 A. E. Baumann, D. A. Burns, B. Liu and V. S. Thoi, *Commun. Chem.*, 2019, **2**, 1–14.

14 J. Calbo, M. J. Golomb and A. Walsh, *J. Mater. Chem. A*, 2019, **7**, 16571–16597.

15 M. Oggianu, N. Monni, V. Mameli, C. Cannas, S. A. Sahadevan and M. L. Mercuri, *Magnetochemistry*, 2020, **6**, 1–14.

16 X. Lian, D. Zhao, Y. Cui, Y. Yang and G. Qian, *Chem. Commun.*, 2015, **51**, 17676–17679.

17 Z. Hu, B. J. Deibert and J. Li, *Chem. Soc. Rev.*, 2014, 43, 5815–5840.

18 Q. Tang, S. Liu, Y. Liu, J. Miao, S. Li, L. Zhang, Z. Shi and Z. Zheng, *Inorg. Chem.*,

2013, **52**, 2799–2801.

19 P. Samanta, S. Let, W. Mandal, S. Dutta and S. K. Ghosh, *Inorg. Chem. Front.*, 2020, **7**, 1801–1821.

20 W.-T. Koo, J.-S. Jang and I.-D. Kim, *Chem*, 2019, **5**, 1938–1963.

21 L. H. G. Kalinke, D. Cangussu, M. Mon, R. Bruno, E. Tiburcio, F. Lloret, D. Armentano, E. Pardo and J. Ferrando-Soria, *Inorg. Chem.*, 2019, **58**, 14498–14506.

22 M. J. Uddin, R. E. Ampiaw and W. Lee, *Chemosphere*, 2021, **284**, 131314.

23 M. Usman, M. Chibuike, D. Patil, S. Rigin, S. Zhang, Y. Wu, J. Lindline and T. V. Timofeeva, *Inorg. Chem. Commun.*, 2020, **122**, 108261.

24 K. Son, R. K. Kim, S. Kim, G. Schütz, K. M. Choi and H. Oh, *Phys. Status Solidi Appl. Mater. Sci.*, 2020, **217**, 1–6.

25 S. Benmansour and C. J. Gómez-García, *Magnetochemistry*, 2020, **6**, 1–44.

26 H. Li, M. Eddaoudi, M. O'Keeffe and O. M. Yaghi, *Nature*, 1999, **402**, 276–279.

27 R. Banerjee, A. Phan, B. Wang, C. Knobler, H. Furukawa, M. O'Keeffe and O. M. Yaghi, *Science*, 2008, **319**, 939–943.

28 M. Taddei, F. Costantino and R. Vivani, *Eur. J. Inorg. Chem.*, 2016, **2016**, 4300–4309.

29 N. Monni, M. Oggianu, S. A. Sahadevan and M. L. Mercuri, *Magnetochemistry*, 2021, **7**, 1–12.

30 I. R. Jeon, B. Negru, R. P. Van Duyne and T. D. Harris, *J. Am. Chem. Soc.*, 2015, **137**, 15699–15702.

31 J. A. DeGayner, I. R. Jeon, L. Sun, M. Dincă and T. D. Harris, *J. Am. Chem. Soc.*, 2017, **139**, 4175–4184.

32 L. Liu, J. A. Degayner, L. Sun, D. Z. Zee and T. D. Harris, *Chem. Sci.*, 2019, **10**, 4652–4661.

33 R. Murase, C. J. Commons, T. A. Hudson, G. N. L. Jameson, C. D. Ling, K. S. Murray, W. Phonsri, R. Robson, Q. Xia, B. F. Abrahams and D. M. D'Alessandro, *Inorg. Chem.*, 2020, **59**, 3619–3630.

34 M. P. Van Koeverden, B. F. Abrahams, D. M. D'Alessandro, P. W. Doheny, C. Hua, T. A. Hudson, G. N. L. Jameson, K. S. Murray, W. Phonsri, R. Robson and A. L. Sutton, *Chem. Mater.*, 2020, **32**, 7551–7563.

35 J.-H. Lee, J.-T. Jang, J.-S. Choi, S. H. Moon, S.-H. Noh, J.-W. Kim, J.-G. Kim, I.-S.

Kim, K. I. Park and J. Cheon, *Nat. Nanotechnol.*, 2011, **6**, 418–22.

36 G. M. Sheldrick, *Acta Crystallogr. Sect. A Found. Crystallogr.*, 2015, **71**, 3–8.

37 G. M. Sheldrick, *Acta Crystallogr. Sect. C Struct. Chem.*, 2015, **71**, 3–8.

38 O. V. Dolomanov, L. J. Bourhis, R. J. Gildea, J. A. K. Howard and H. Puschmann, *J. Appl. Crystallogr.*, 2009, **42**, 339–341.

39 G. J. Long, T. E. Cranshaw and G. Longworth, *Mössbauer Eff. Ref. Data J.*, 1983, **6**, 42–49.

40 J. C. Waerenborgh, P. Salamakha, O. Sologub, A. P. Gonçalves, C. Cardoso, S. Sério, M. Godinho and M. Almeida, *Chem. Mater.*, 2000, **12**, 1743–1749.

41 S. Kawata, S. Kitagawa, M. Kondo, I. Furuchi and M. Munakata, *Angew. Chemie - Int. Ed.*, 1994, **33**, 1759–1761.

42 C. J. Kingsbury, B. F. Abrahams and R. Robson, *CCDC 1568063 Exp. Cryst. Struct. Determ.*

43 A. Pawlukojć, G. Bator, L. Sobczyk, E. Grech and J. Nowicka-Scheibe, *J. Phys. Org. Chem.*, 2003, **16**, 709–714.

44 F. Billes, I. Ziegler and H. Mikosch, *Spectrochim. Acta - Part A Mol. Biomol. Spectrosc.*, 2016, **153**, 349–362.

45 V. Krishnakumar, N. Jayamani and R. Mathammal, *Spectrochim. Acta - Part A Mol. Biomol. Spectrosc.*, 2011, **79**, 1959–1968.

46 M. Yadav, S. Sharma and J. Devi, *J. Chem. Sci.*, , DOI:10.1007/s12039-020-01854-6.

47 F. M. A. Kerim, H. F. Aly and A. El-Agramy, *Proc. Indian Acad. Sci. - Sect. A*, 1977, **85**, 559–566.

48 M. K. Trivedi, R. M. Tallapragada, A. Branton, D. Trivedi, G. Nayak, R. K. Mishra and S. Jana, *J. Mol. Pharm. Org. Process Res.*, 2015, **03**, 1–6.

49 O. Roubeau, B. Agricole, R. Cle and S. Ravaine, *J. Phys. Chem. B*, 2004, **108**, 15110–15116.

50 Q. Deng, C. Tian, Z. Luo, Y. Zhou, B. Gou, H. Liu, Y. Ding and R. Yang, *Chem. Commun.*, 2020, **56**, 12234–12237.

51 E. Bill, in *Practical Approaches to Biological Inorganic Chemistry*, eds. R. R. Crichton and R. O. Louro, Elsevier, 2nd edn., 2019, pp. 201–228.

52 N. N. Greenwood and T. C. Gibb, *Mössbauer Spectroscopy*, Ltd. Publishers, London,

1971.

53 S. Kawata, S. Kitagawa, H. Kumagai, T. Ishiyama, K. Honda, H. Tobita, I. Keiichi Adachi and M. Katada, *Chem. Mater.*, 1998, **10**, 3902–3912.

54 S. Kawata, S. Kitagawa, H. Kumagai, C. Kudo, H. Kamesaki, T. Ishiyama, R. Suzuki, M. Kondo and M. Katada, *Inorg. Chem.*, 1996, **35**, 4449–4461.

55 M. E. Fisher, *J. Math. Phys.*, 1963, **4**, 124–135.

56 J. J. Borrás-Almenar, J. M. Clemente-Juan, E. Coronado and B. S. Tsukerblar, *J. Comput. Chem.*, 2001, **22**, 985–991.

57 D. Collison and A. K. Powell, *Inorg. Chem.*, 1990, **29**, 4735–4746.

58 B. F. Abrahams, A. M. Bond, T. H. Le, L. J. McCormick, A. Nafady, R. Robson and N. Vo, *Chem. Commun.*, 2012, **48**, 11422–11424.

59 H. Ogino and K. Ogino, *Inorg. Chem.*, 1983, **22**, 2208–2211.

60 J. D. Cope, H. U. Valle, R. S. Hall, K. M. Riley, E. Goel, S. Biswas, M. P. Hendrich, D. O. Wipf, S. L. Stokes and J. P. Emerson, *Eur. J. Inorg. Chem.*, 2020, **2020**, 1278–1285.

Chapter 3

A thermally/chemically robust and easily regenerable anilato-based ultramicroporous 3D MOF for CO_2 uptake and separation

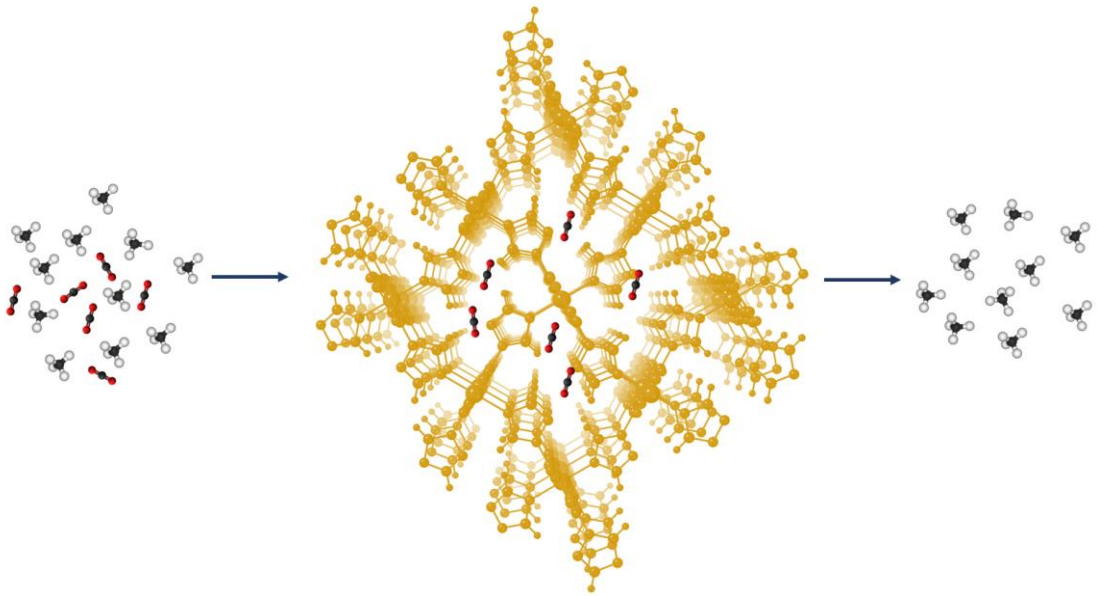

N. Monni, E. Andres-Garcia, K. Caamaño, V. García-López, J. M. Clemente-Juan, M. Giménez-Marqués, M. Oggianu, E. Cadoni, G. Mínguez Espallargas,* M. Clemente-León,* M. L. Mercuri* and E. Coronado. *J. Mater. Chem. A*, **2021**, 9, 25189-25195

Abstract

The combination of the properly designed organic linker, 3,6-N-ditriazolyl-2,5-dihydroxy-1,4-benzoquinone (H_2trz_2An), with Co^{II} ions results in a novel 3D ultramicroporous MOF with high CO_2 uptake capacity and separation efficiency, with particular attention to CO_2/N_2 and CO_2/CH_4 gas mixtures. This material consists of 1D chains of octahedrally coordinated Co^{II} ions linked through the anilato ligands in the equatorial positions and to the triazole substituents from two neighbouring chains in the two axial positions. This leads to a 3D microporous structure with voids with an affinity for CO_2 molecules and channels that enable the selective entrance of CO_2 but not of molecules with larger kinetic diameter such as N_2 or CH_4. The adsorption studies revealed that *i)* the MOF presents a remarkable carbon dioxide uptake, above 20% in weight; *ii)* CO_2 adsorptive separation is successfully performed in CO_2:N_2 and CO_2:CH_4 gas mixtures, exhibiting high selectivity in a large operation range; *iii)* regeneration is easily achieved at mild conditions.

1. Introduction

Methane (CH_4) has a widespread use as clean energy source, but current natural gas reserves are too contaminated in order to be considered economically profit-making[1] and the most important contaminants, as CO_2, need to be removed before further transport for processing.[2] Thus, among the hundreds of billions of cubic meters of natural gas produced, approximately 20% requires significant treatments in order to remove CO_2.[3] In addition, capturing CO_2 from the atmosphere represents the key challenge of this century, since CO_2 has been recognized as the primary anthropogenic greenhouse contributor to the increase of earth's average temperature.[4] This *Kyoto protocol* gas[5] has been increasing its concentration since industrial revolution, reaching the current alarming level of 415 ppm[6]. Furthermore, separation processes consume upon 70% of the energy cost in typical chemical plant[7], thus, the importance of separation techniques development research is worldwide acknowledged.[8]

Among the different types of porous materials that can be used for the aforementioned problems, Metal-Organic Frameworks (MOFs) are very versatile networks formed by organic molecules (*linkers*) and metal ions (*nodes*) which self-assemble in a large variety of porous architectures.[9,10] Because of their intrinsic porosity they have attracted ever-growing interest in several applications ranging from gas storage and separation, catalysis, chemical sensing, to biomedicine.[11–14] Noteworthy Long. *et al.* recently reported on the unprecedented adsorption behaviour shown by diamine-appended MOFs, which maintain affinity for CO_2 under moisture exposure and show excellent long-term stability, both crucial requirements for CO_2 capture.[4] Additionally decreasing pore size in ultramicroporous materials (pore size < 0.7 nm), is a remarkable strategy for highly selective sorption properties with benchmark results for CO_2:N_2 separation.[15–17] An alternative strategy consists in the construction of coordination polymers formed by discrete compartments, *i.e.* compartmentalized, featuring internal cavities where small gas molecules can diffuse onto, establishing weak interactions with the network.[18,19] Furthermore, MOFs have the potential to exhibit lower regeneration energies than traditional adsorbents or amine-based solvents. Therefore, they are considered excellent candidates for gas adsorptive separation industrial processes, with particular attention to CO_2 removal from CO_2:CH_4 mixtures, and carbon dioxide capture from air (CO_2:N_2).

Among the linkers, interest has recently been renovated[20–25] on 3,6-disubstituted (X)-2,5-dihydroxybenzoquinone derivatives (X=H, F, Cl, Br, I, CN), *i.e.* anilates, for their

ability to act as suitable building blocks of coordination polymers and MOFs, showing peculiar physical properties from layered magnets, to magnetic conductors and lanthanide-based 2D NIR-emitters.[26–29] Interestingly, Robson *et al*. have reported on the capability of 1D frameworks of Mg(II) or Zn(II) metal ions to uptake, upon dehydration, significant amounts of H_2, CO_2 and CH_4 at low pressures.[30] Significant amounts of CO_2 are also captured on $(NEt_4)_2[Zn_2(Cl_2An)_3]$ and $(NEt_4)_2[Zn_2(F_2An)_3]$ (Cl_2An = chloranilate, F_2An = fluoranilate) 2D porous compounds.[31] Very recently, uptake of proper sized guest molecules on the porous 2D square-grid framework, $(NEt_4)[Y(Cl_2An)_2]$, has been reported, showing high sorption enthalpies for H_2, N_2, CO_2 and, particularly, CH_4 that have been related to the ability of these molecules to interact simultaneously with more than one internal surface of the square channels.[32] However, selective adsorption properties have not been reported for this family of compounds until now. We herein report on the use of 3,6-N-ditriazolyl-2,5-dihydroxy-1,4-benzoquinone (H_2trz_2An),[34] shown in **Scheme 1**, bearing two triazole pendant arms at the 3,6 position of the anilato moiety instead of the much simpler substituents found in this position with a few exceptions.[35] This anilato linker has the potential to construct 3D MOFs, due to the coordinative properties of the N4 atoms of the triazole group.[36] In addition to this, the presence of not coordinated N2 atom and the fact that anilato ring is the most electron-rich among anilates, due to the strong electron-donor power of the triazole group, could enhance the sorption of CO_2 molecules.

Trz_2An

Scheme 3.1. Chemical structure of the 3,6-N-ditriazolyl-2,5-dihydroxy-1,4-benzoquinone (H_2trz_2An) ligand, indicating the numbered positions of nitrogen in triazole pendant ring.

2. Experimental Section

2.1 General Remarks

H_2trz_2An was prepared according to the literature.[33] Reagents of analytical grade were purchased from Zentek (TCI) and Sigma Aldrich and used without further purification. Elemental analyses (C, H, and N) were performed with a CE Instruments EA 1110 CHNS.

2.2 Synthesis

$[Co(trz_2An)]_n \cdot 3H_2O$ (1). A 5 mL Teflon vial with a mixture of $CoCl_2 \cdot 6H_2O$ (11.9 mg, 0.05 mmol), H_2trz_2An (13.7 mg, 0.05 mmol), NaOH (4 mg, 0.1 mmol) and water (5 mL) was heated at 130°C for 48 hours. After being cooled to room temperature, rectangular dark brown crystals, suitable for an X-ray diffraction study, were obtained. To obtain a large quantity of **1**, the synthesis was performed in a stainless steel autoclave of 80 mL volume, with a scale up of the reaction mixture of 8 times, by using 0.4 mmol of H_2trz_2An, 0.8 mmol of NaOH and 0.4 mmol of $CoCl_2 \cdot 6H_2O$ in 40 mL of water. Elemental Analysis: *Calcd %* for $C_{10}H_{10}N_6O_7Co$ (385.16): C, 31.18; H, 2.62; N, 21.82. *Found:* C, 31.12; H, 2.45; N, 22.

2.3 Physical Measurements

Powder X-Ray Diffraction (PXRD). PXRD pattern was performed using a 0.7 mm glass capillary filled with polycrystalline samples of the compounds and mounted and aligned on an Empyrean PANalytical powder diffractometer, using Cu Kα radiation (λ = 1.541 77 Å). A total of three scans were collected for each compound at room temperature in the 2θ range of 10−40°. PXRD patterns at different pH were performed using the same equipment, filling a 0.7 mm glass capillary with polycrystalline samples previously soaked in an aqueous solution, both at pH = 1 and a pH = 12. Variable temperature PXRD patterns were performed using a θ–θ Bragg–Brentano focalizing geometry Bruker D8 Avance A25 diffraction system equipped with a Cu Kα source (λ = 1.54056 Å), in the 2θ range of 2−40° and in the temperature range 25-400°C.

Magnetic Measurements. Magnetic measurements were performed with a Quantum Design MPMS-XL-5 SQUID magnetometer in the 2−300 K temperature range with an applied magnetic field of 0.1 T at a scan rate of 2 K min^{-1}.

Gas sorption. Low pressure nitrogen and carbon dioxide volumetric isotherms were carried out in a Tristar II Plus Micromeritics sorptometer, at 77 K and 273 K, respectively. Activation was set at 393 K, under vacuum, for 2 hours. High-pressure gravimetric adsorption isotherms of CO_2, CH_4 and N_2 were measured at different temperatures, ranging from 283 to 318 K, in an IGA-100 gas sorption analyser (from Hiden Isochema) using approximately 50 mg of sample. Before each adsorption experiment, the sample was outgassed at 393 K under vacuum (10^{-5} Pa) for two hours. Equilibrium conditions corresponded to 600 s interval, and 0.001 mg min^{-1} tolerance.

Dynamic Adsorptive Separation Measurements. An ABR (HIDEN Isochema) automated breakthrough analyser setup, based on a packed adsorption column, was used to determine the adsorption dynamics of gas mixtures. Pressure, temperature and inlet composition are controlled, and the outlet composition is analysed, by an integrated mass spectrometer (HPR-20 QIC). The fixed-bed column was filled with 286 mg of compound **1**. Before each measurement, the sample was regenerated at atmospheric temperature and pressure, in 40 ml min^{-1} Ar flow for 20 minutes. Operation conditions ranged 283-323 K, at 1 bar. The inlet mixture was set to a 15 ml min^{-1} flow of a dilution of carbon dioxide in N_2 or CH_4 (5%, 20%, 50%). Time zero was set with the first detection of helium, which was used as a trace (an extra 1 ml min^{-1} of He in the total feed flow of 16 ml min^{-1}).

Other measurements. Elemental analyses (C, H, and N) were performed with a CE Instruments EA 1110 CHNS.

FT-IR spectra were performed in KBr pellets in a Bruker Equinox 55 spectrophotometer.

TGA was performed in alumina crucibles with the instrument STA-6000 under nitrogen flux (40 mL/min), in the 25-800°C temperature range at 10°C/min.

3. Results and Discussion

3.1 Synthesis

By combining $CoCl_2 \cdot 6H_2O$ with H_2trz_2An, in 1:1 stoichiometric ratio, *via* hydrothermal method (**Scheme 3.2**), dark brown rectangular crystals of $[Co(trz_2An)]_n \cdot 3H_2O$ (**1**) suitable for a single crystal X-ray study, were obtained. Remarkably the synthesis of this MOF can be scaled up to 8 times in a proper autoclave (see experimental section 2.2).

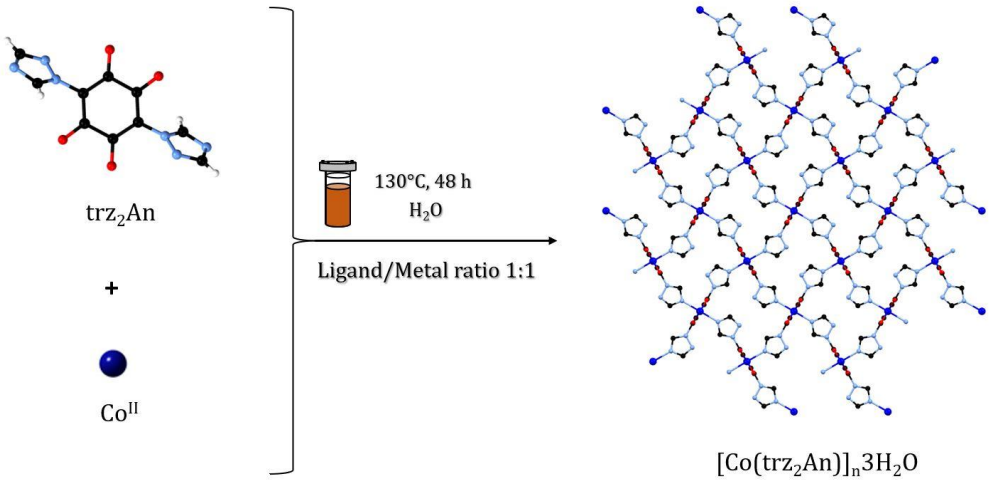

Scheme 3.1. Synthetic strategy for **1**.

3.2 Chemical and Thermal Stability

As previously discussed in *Chapter 2*, Co-based MOF **1** crystallizes in the orthorhombic *Pnnm* space group and it is a 3D framework in which the Co^{II} ions are equatorially coordinated to four oxygen atoms of two bis(bidentate) trz_2An ligands, leading to $[Co(trz_2An)]_n$ chains running along the *c* axis. The distorted octahedral coordination sphere of Co^{II} ions is completed with two nitrogen atoms from N4 atoms of the 1,2,4-triazole substituted pendant rings of trz_2An ligands from two neighbouring chains. In addition, the bis(bidentate) trz_2An ligands of each chain are linked to other two neighbouring chains through N4 atoms of the 1,2,4-triazole substituted pendant rings leading to a 3D neutral polymeric framework. Since the space between four interconnected chains contains pockets, **1** is a potential suitable material for the selective sorption of small molecules as CO_2.

Hence, to first evaluate the potential of **1** as a chemically and thermically stable MOF applicable in gas storage and separation, thermogravimetric analysis was performed, as

reported in **Figure 3.1**, to study its thermal stability and confirm water content previously observed from crystal structure data (see *Chapter 2*).

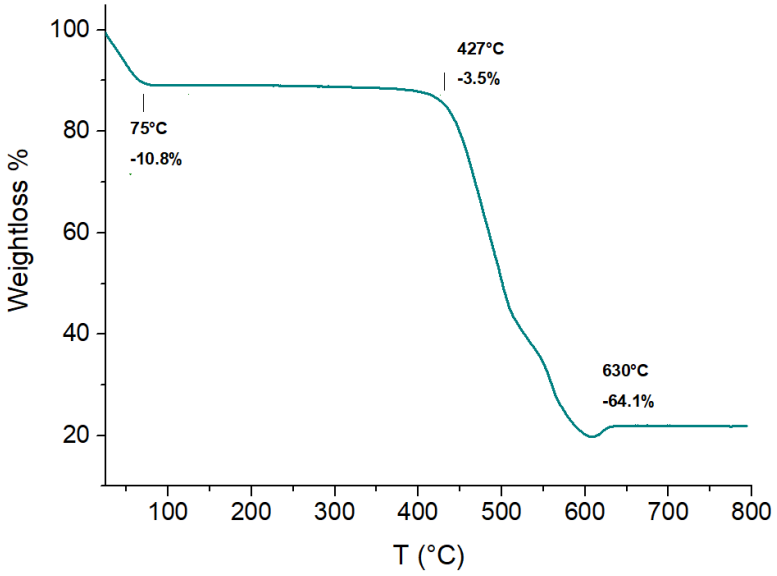

Figure 3.1. Thermogram of **1** in 25-800°C temperature range. The percentages shown in the graph are referred to the previous one weightloss.

The thermogram of **1** shows a first weight loss of 10.8% at 75°C, which is consistent with the non-coordinated water molecules found in the channels. The system shows very high thermal stability up to 400°C, starting to collapse at T > 400°C with the ligand degradation. To further investigate if the crystal structure was retained while increasing the temperature, variable PXRD patterns were collected, as shown in **Figure 3.2**.

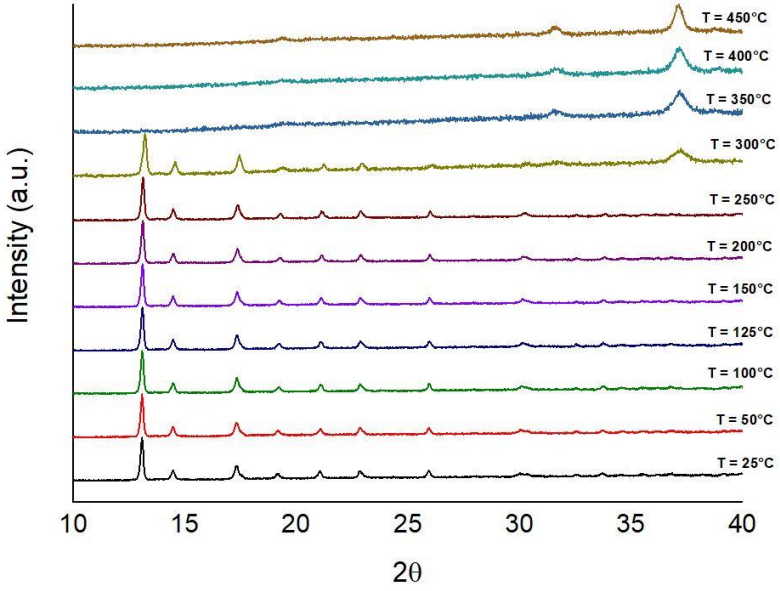

Figure 3.2. Variable temperature PXRD patterns of compound **1** in the range 10-40°.

The observed crystallinity of **1** is retained up to 300°C, while at higher temperature a new crystalline phase is observed, which could be identified as Co_3O_4 (PDF Card n° 00-042-1467). Due to its high thermal stability, the crystal structure is preserved after the activation at 150°C, which was required to perform static isothermal adsorption measurements (*vide infra*). **Figure 3.3** shows similar PXRD patterns of the as-synthesized and activated samples.

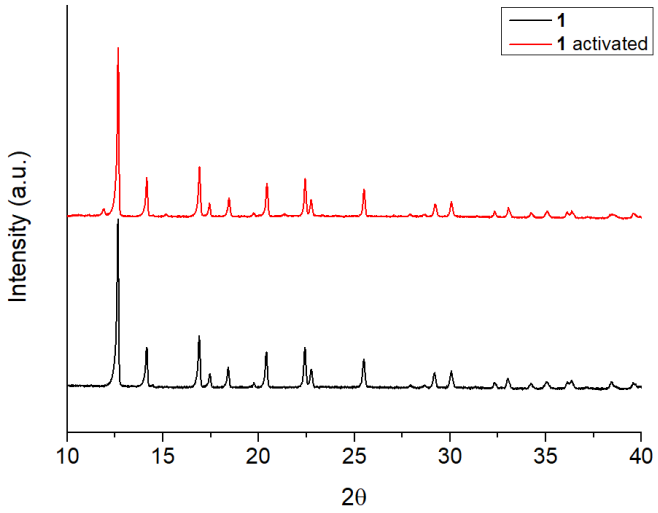

Figure 3.3. Powder XRD patterns of compound **1** at RT (red) and **1** after the activation at 150°C (black), in the range 10-40°.

Finally, by soaking **1** for 24 hours in aqueous solution at different pH values (ranging from 1 to 12) it is possible to observe its extraordinary chemical stability in retaining its crystallinity, as shown in **Figure 3.4**.

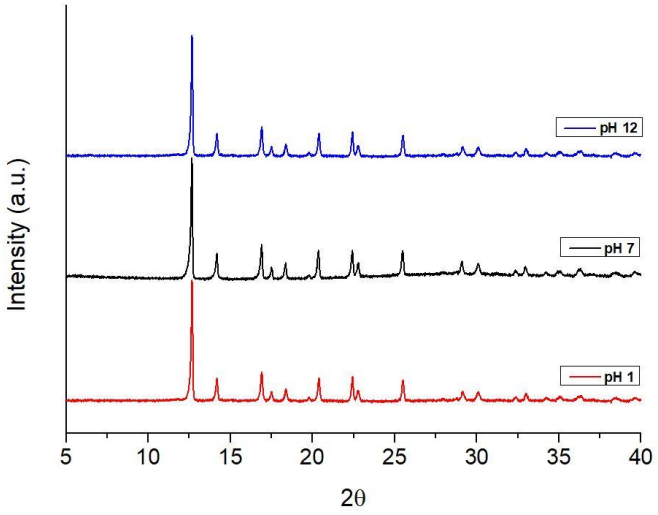

Figure 3.4. PXRD patterns of **1** after soaking for 24 hours in aqueous solutions of pH = 1, 7 and 12. Concentration: 20 mg of **1** /20 mL buffer solution.

3.3 Static Isothermal Adsorption Measurements

In order to study the textural properties of the material and its behaviour with the interest gases, low pressure nitrogen and carbon dioxide volumetric isotherms were carried out in a Tristar II Plus Micromeritics sorptometer, at 77 K and 273 K, respectively. Activation was set at 393 K, under vacuum, for 2 hours. Although single gas (low-pressure) nitrogen isotherm (77 K) is the most common and standardized adsorption textural characterization measurement, this MOF presents a negligible adsorption curve, as pores from **1** are not accessible to N_2. On the other hand, carbon dioxide isotherm presents a promising adsorption capacity at 1 bar, highlighting the potential of this novel MOF in gas separation processes. The slightly shorter CO_2 kinetic diameter enable its diffusion along the framework, reaching a competitive adsorption capacity of 88 ml CO_2 per gram of sample, and with characteristic surface area values corresponding to 431 $m^2\ g^{-1}$ (BET surface area) and 446 $m^2\ g^{-1}$ (Langmuir surface area). **Figure 3.5a** exhibits the remarkably different (high-pressure) adsorption profiles for CO_2, N_2, and CH_4. These gravimetric isotherms reveal the dominant role of kinetics, as the slightly shorter CO_2 kinetic diameter enables its diffusion along the channels of the MOF. An outstanding CO_2 adsorption capacity[35] is found for **1**, with more than 20% in weight (5.4 mmol g^{-1}, at 10 bar and 298 K), while nitrogen and methane values are negligible (even at high pressure). Variable temperature measurements show the expected increase in adsorbed CO_2 with decreasing temperature (**Figure 3.5b**), allowing the calculation of the adsorption enthalpy applying virial equations for fitting experimental data points, with a fourth-grade polynomial. In addition, heat of adsorption was calculated according to the Clausius-Clapeyron equation, through the data extracted from the experimental isotherms at different temperatures, giving the value of 21.07 kJ mol^{-1} (**Figure 3.6**), in agreement with typical interaction of CO_2 with triazole groups.[36]

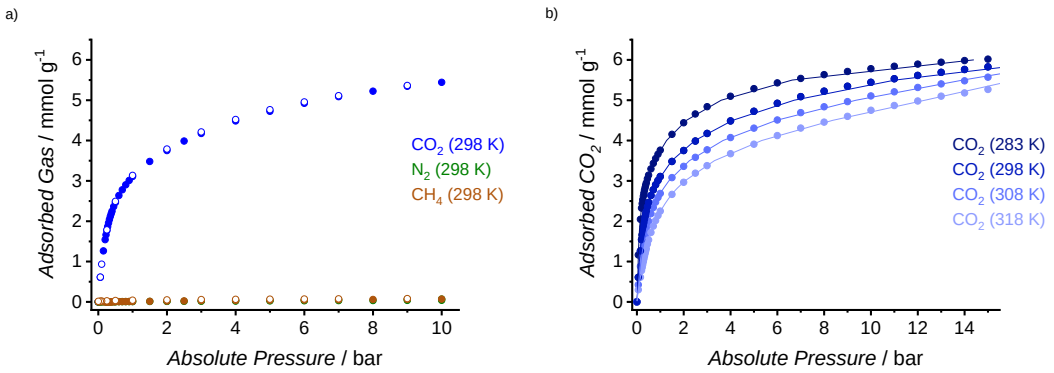

Figure 3.5. High pressure gravimetric single-gas isotherms for **1**: *a*) CO_2 (*blue*), N_2 (*green*) and CH_4 (*orange*) gas adsorption isotherms on **1**, at 298 K; *b*) CO_2 gas adsorption isotherms on **1**, at different temperatures (283 K – 318 K), including Virial fittings. Solid circles for adsorption and open ones for desorption.

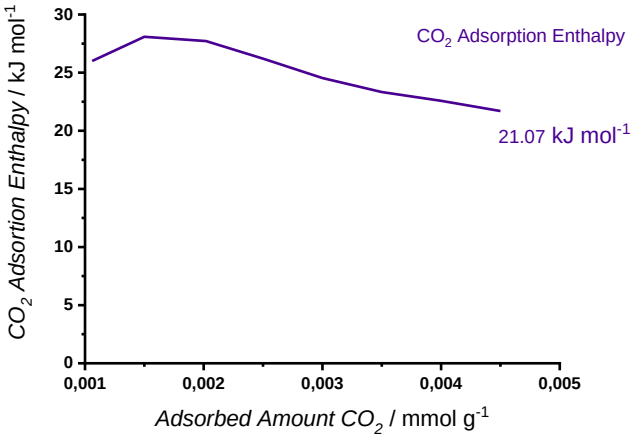

Figure 3.6. Isosteric heat of adsorption of CO_2 on **1**, according to the Clausius-Clapeyron equation.

Kinetics analysis reveals the impact of temperature in the behaviour of the gas-framework interaction. At low temperature (283-298 K) adsorption exhibits a steeper slope at the beginning of the profile (low pressure region), promoting an agile adsorption at low CO_2 concentrations (**Figure 3.7**).

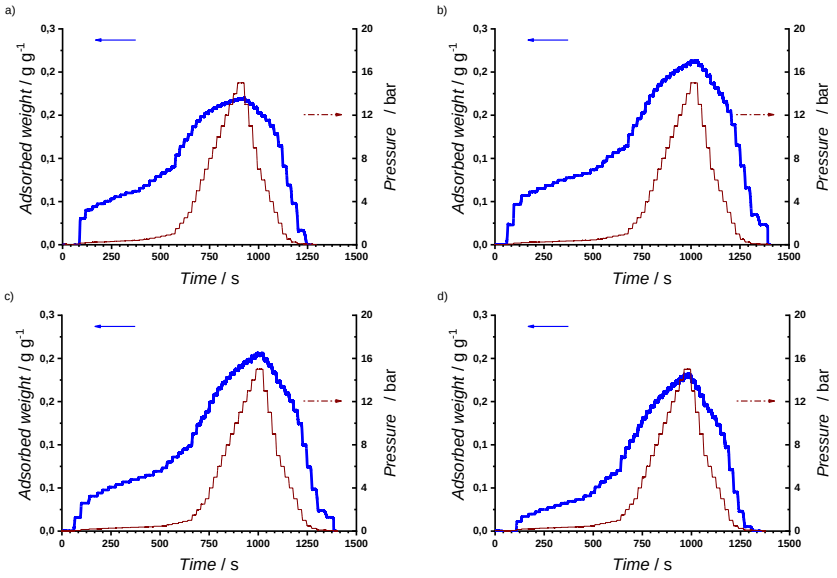

Figure 3.7. Isothermal kinetic study for CO_2 adsorption (pressure vs. time) in compound **1**, at 15 bar, at different temperatures: (*a*) 283 K, (*b*) 298 K, (*c*) 308 K, and (*d*) 318 K. Equilibrium conditions set to 600 s interval, with a tolerance of 0.001 mg min^{-1}**.**

That facility of reaching equilibrium is of outmost importance for industrial implementation, as it favours the use of the MOF in dynamic conditions.

3.4 Dynamic Adsorptive Separation Measurements

Dynamic condition measurements in a Breakthrough setup mimic the behaviour of the MOF in a real gas adsorptive separation process. In **Figure 3.8**, breakthrough profiles for separation of 1:4 (CO_2:N_2 and CO_2:CH_4) mixtures are reported (further measurements with different mixture compositions can be found in the Supporting Material, *Part IV, Chapter 3*). The outlet flow is analysed after breaking through the column, exhibiting both an outstanding adsorption region for CO_2, and an overlapping between the tracer curve and the second gas in the mixture.

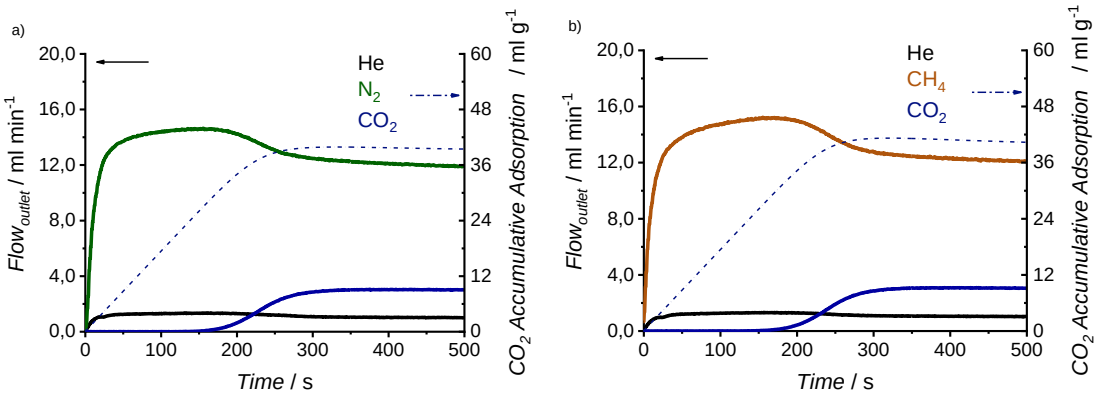

Figure 3.8. Breakthrough exit flowrates (solid line, left axis) and CO_2 accumulative adsorption (dash-dot line, right axis) vs. time at 283 K and 1 bar, on **1**. Inlet composition corresponds to a 20 % dilution of CO_2: *a*) in nitrogen, and *b*) in methane. Time zero is set with the first detection of helium (tracer). The total flow rate is 15 ml min^{-1}.

In **Figure 3.9** the experimental results from the breakthrough measurements are summarized, performed for two gas mixtures (CO_2:N_2 and CO_2:CH_4), three temperatures (283 K, 298 K and 323 K) and three CO_2 inlet concentrations (5 %, 20 % and 50 %). As adsorption is an exothermic process, it is promoted at low temperature, in concordance with the obtained results. Initial analysis of these results indicates that the adsorption capacity decrease with lowering CO_2 concentration and increasing temperature.

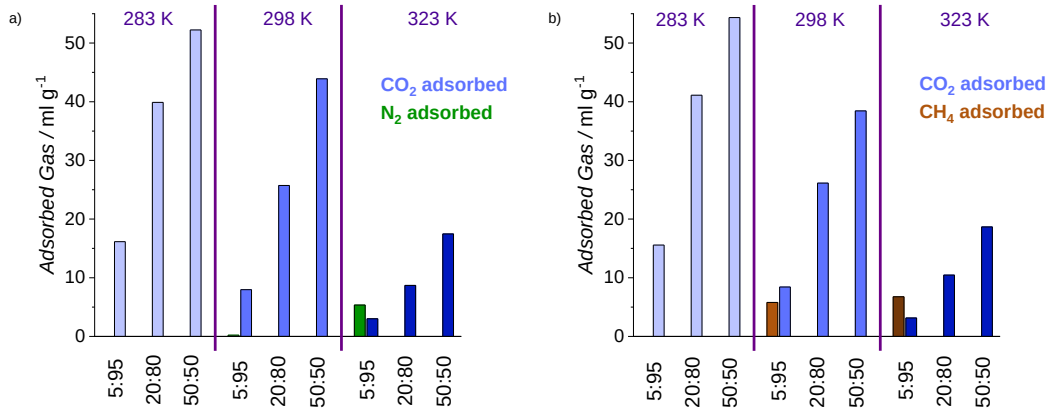

Figure 3.9. Gas adsorbed amounts on **1**, calculated from breakthrough profiles, at 1 bar (absolute pressure) for: *a*) CO_2:N_2, and *b*) CO_2:CH_4 mixtures; at different concentrations (5 %, 20 % and 50 %) and different temperatures (283 K, 298 K and 323 K). Time zero is set with the first detection of helium (tracer).

A more in-depth analysis of the capacity of the material to discriminate between the gases can be obtained by analysing the selectivity, α (**Table 3.1**). As it can be observed

in **Table 3.1**, **1** exhibits the same trends and capacities/selectivity ranges for both CO_2:N_2 and CO_2:CH_4 mixtures, with very large selectivity values (α > 1000) obtained in all the ranges of temperature and composition. In fact, even at the most critical conditions (low CO_2 concentration and high temperature), the selectivity values still are significantly large (α = 10), being among the best MOFs reported so far. At similar conditions, ZIF-95 and ZIF-100 have α values in the range 4 to 25,[37] amino-functionalized MIL-53, (NH_2)-MIL-53(Al), presents α values in the range 20 to 200,[38] the compartmentalized coordination polymer CCP-6 have α values in the range 3 to >1000 (only at most favoured conditions),[18] and a novel L-histidine-based 3D chiral MOF, Cu^{II} 2(S,S)- hismox·$5H_2O$, has also been shown to be very effective, with α values above 1000, in kinetics-controlled separation processes.[39]

Table 3.1. Experimental dynamic selectivities (α)[a] for **1**; calculated from the integration of the breakthrough curves, considering gas mixture inlet composition.

	5% CO_2 (in N_2 mixture)	20% CO_2 (in N_2 mixture)	50% CO_2 (in N_2 mixture)
283 K	>1000	>1000	>1000
298 K	>500	>1000	>1000
323 K	10	>1000	>1000
	5% CO_2 (in CH_4 mixture)	20% CO_2 (in CH_4 mixture)	50% CO_2 (in CH_4 mixture)
283 K	>1000	>1000	>1000
298 K	26	>1000	>1000
323 K	8	>1000	>1000

[a] $\alpha = [(q_{ads,1}/F_{0,1})/(q_{ads,2}/F_{0,2})]$, where $q_{ads,i}$ represents the gas adsorbed amount, and $F_{0,i}$ the inlet single-gas flow, for carbon dioxide (1) and the secondary gas (2).

In addition, a further advantage of **1** is its high capacity, which is competitive with effective CO_2 capture materials, as MOF-74(Me).[40] But more importantly, fully regeneration of **1** is achieved at atmospheric temperature and pressure, by simply flowing argon for 20 minutes (see **Figure 3.10**).

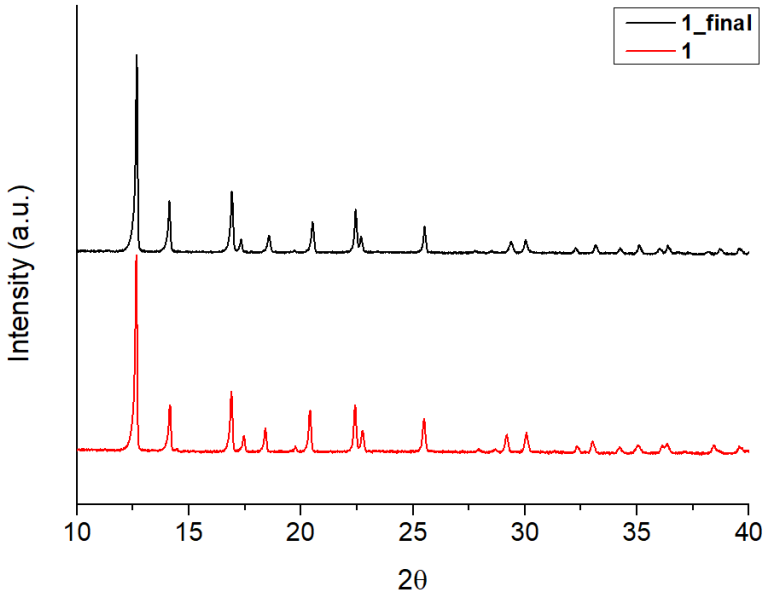

Figure 3.10. Powder XRD patterns of compound **1** before adsorption measurements (red) and compound **1** after completing adsorption study (black), in the range 10-40°.

The double replicas of all the breakthrough measurements were performed and are reported in **Tables 3.2** and **3.3**, to compare.

Table 3.2. Experimental selectivity (α) for compound **1**, calculated from the integration of the respective breakthrough curves in CO_2:N_2 adsorptive separation. (original and replica measurements).

Exp. conditions	CO_2 adsorbed (ml g^{-1})	N_2 adsorbed (ml g^{-1})	Selectivity (α)
283 K; 5% CO_2	16.1	0.0	>1000
283 K; 5% CO_2	15.1	0.0	>1000
283 K; 20% CO_2	39.9	0.0	>1000
283 K; 20% CO_2	40.1	0.0	>1000
283 K; 50% CO_2	52.2	0.0	>1000
283 K; 50% CO_2	54.6	0.0	>1000
298 K; 5% CO_2	8.0	0.2*	>500
298 K; 5% CO_2	8.0	0.9*	159
298 K; 20% CO_2	25.7	0.0	>1000
298 K; 20% CO_2	26.0	0.0	>1000
298 K; 50% CO_2	43.9	0.0	>1000
298 K; 50% CO_2	39.8	0.0	>1000
323 K; 5% CO_2	3.0	5.3	10
323 K; 5% CO_2	3.0	6.3	8
323 K; 20% CO_2	8.7	0.0	>1000
323 K; 20% CO_2	9.4	0.0	>1000
323 K; 50% CO_2	17.5	0.0	>1000
323 K; 50% CO_2	17.3	0.0	>1000

(*) negligible values

Table 3.3. Experimental selectivity (α) for compound **1**, calculated from the integration of the respective breakthrough curves in CO_2:CH_4 adsorptive separation. (original and replica measurements).

Exp. conditions	CO_2 adsorbed (ml g^{-1})	CH_4 adsorbed (ml g^{-1})	Selectivity (α)
283 K; 5% CO_2	15.6	0.0	>1000
283 K; 5% CO_2	15.8	0.0	>1000
283 K; 20% CO_2	41.1	0.0	>1000
283 K; 20% CO_2	38.8	0.0	>1000
283 K; 50% CO_2	54.3	0.0	>1000
283 K; 50% CO_2	56.4	0.0	>1000
298 K; 5% CO_2	8.4	5.8	26
298 K; 5% CO_2	8.2	4.8	30
298 K; 20% CO_2	26.1	0.0	>1000
298 K; 20% CO_2	23.9	0.0	>1000
298 K; 50% CO_2	38.4	0.0	>1000
298 K; 50% CO_2	45.7	0.0	>1000
323 K; 5% CO_2	3.1	6.8	8
323 K; 5% CO_2	3.2	9.6	6
323 K; 20% CO_2	10.5	0.0	>1000
323 K; 20% CO_2	12.5	0.0	>1000
323 K; 50% CO_2	18.7	0.0	>1000
323 K; 50% CO_2	20.2	0.0	>1000

3.5 Stability Studies

To further evaluate the robustness of **1**, gravimetric measurements of the CO_2 adsorption was performed, measuring the sample after all the gas separation studies (40 different breakthrough separation studies with regeneration) and the sample was stored in a closed vial under air atmosphere at room temperature for 3 months. The sorption capacity of the material is mostly retained (see **Table 3.4** and **Figure 3.11**).

Table 3.4. CO_2 sorption capacity at 6 bar and 283 K of the original sample before and after gas separation studies, with 3 months of storage between the measurements.

Sample	**CO_2 sorption capacity / mmol·g^{-1}**
Original Sample	5.4
Sample after 3 months	4.9

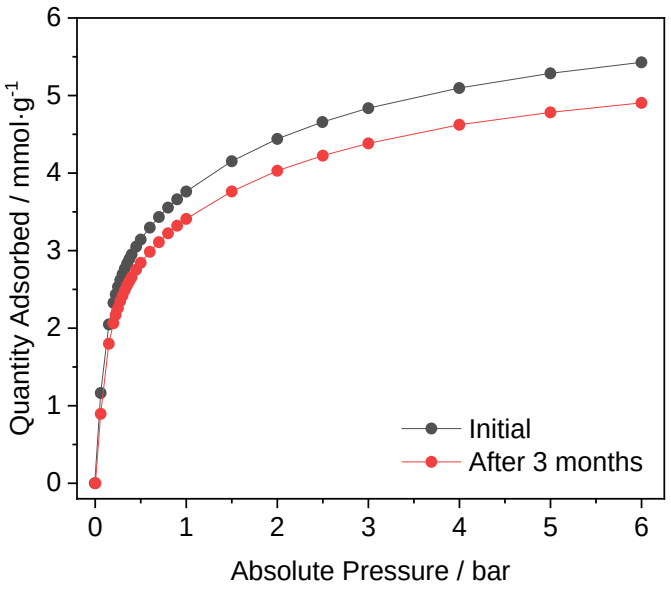

Figure 3.11. CO_2 adsorption isotherms at 283 K of the initial material and the sample after performing all the separation studies (40 different breakthrough separation studies with regeneration). Before CO_2 adsorption isotherm, samples were activated at 150 °C for 2 hours.

To evaluate the chemical stability of **1**, the product was divided in three aliquots (50 mg each) and soaked in different solutions (10 mL) with pH values adjusted at pH = 1, 7 and 12 for 3 hours. The materials were then washed three times with MeOH and collected by centrifugation (8000 rpm, 10 min at RT) and left to dry in air overnight. The porosity of the samples was evaluated by CO_2 sorption measurements after activation at 150 °C for 2h. The CO_2 sorption capacity of the material (**Figure 3.12**) is not affected after this study, as the material retains the same amount of CO_2 with minor differences in the CO_2 sorption isotherms attributed to performing different experiments. The sorption capacity for each sample is resumed in **Table 3.5**. The robustness and of the framework was assessed after the solvent treatment and gas sorption measurements, by performing PXRD measurements of the treated materials (**Figure 3.13**). The crystalline structure of the samples after the solvent treatment is retained in all the cases.

Table 3.12. CO_2 sorption capacity at 1 bar and 273 K of the pristine material and treated samples.

Sample	CO_2 sorption capacity / mmol·g^{-1}
Pristine Material	3.8
pH = 1	3.7
pH = 7	3.9
pH = 12	3.8

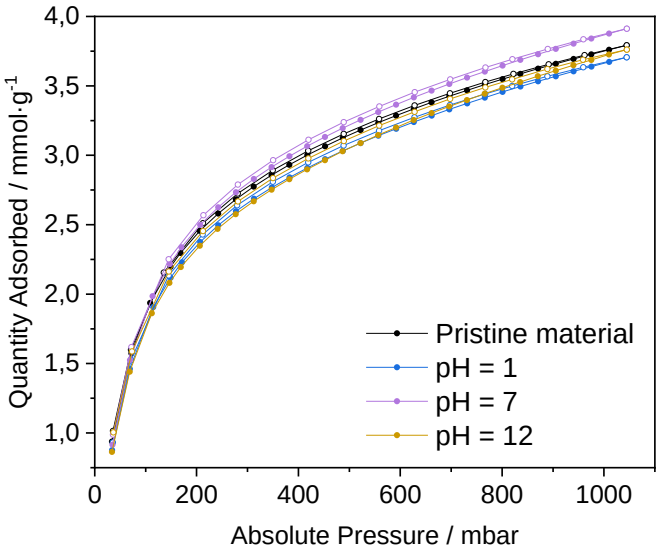

Figure 3.12. CO_2 sorption isotherms at 273 K of the pristine and treated materials at different pH activated at 150 °C for 2 hours (solid symbols for adsorption and open ones for desorption).

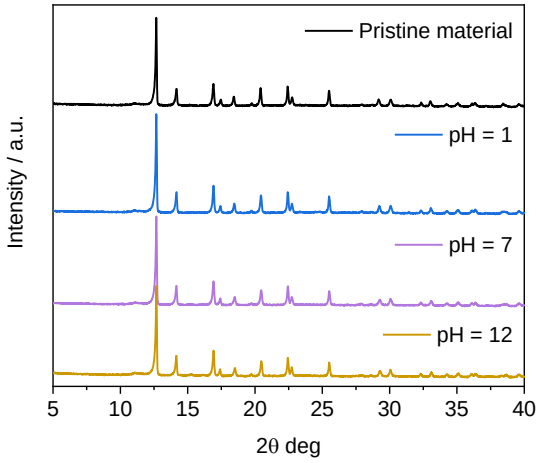

Figure 3.13. PXRD patterns of the pristine material and the treated samples at different pH after CO_2 sorption measurements

4. Conclusions

The H_2trz_2An anilate derivative, bearing a triazole pendant arm at the 3,6 position of the anilato moiety, has been used for the first time in combination with Co^{II} nodes to afford **1**, a 3D MOF formed by 1D chains of octahedrally coordinated Co^{II} ions linked through the anilato ligands. Interestingly, the two axial positions of Co^{II} in these chains are bridged by the triazole substituents from two neighbouring chains, which act as ancillary groups, instead of the solvent molecules, commonly found in similar compounds reported in the literature. This leads to a very stable and robust 3D ultramicroporous structure with channels to enable the selective entrance of CO_2, hindering the diffusion of molecules with larger kinetic diameter, such as N_2 or CH_4. The presence of triazole rings in the structural voids increases the affinity for CO_2 molecules. In order to evaluate the potential of this MOF in adsorptive separations, static and dynamic adsorption measurements were performed. MOF **1** presents not only high adsorption static capacity (above 20% in weight), but also approaching values at dynamic conditions and an outstanding selectivity in both nitrogen and methane mixtures. It should be noted that a good CO_2 sorption capacity is not enough for a material to serve for separation applications, if the CO_2 is not adsorbed selectively. MOF **1**, which shows peculiar thermal and chemical robustness, is presented as a promising alternative in CO_2 gas separation processes, since it combines the advantages from both kinetic and thermodynamic control mechanisms. Remarkably, its framework is able to sieve larger molecules, as nitrogen or methane, to reach outstanding CO_2 selectivity values (>1000), at different temperature and concentration conditions. Remarkably, the material can be regenerated at mild conditions. The favourable balance of these three characteristics *i.e.* high selectivity, high adsorption capacity and high regenerability, positions **1** as an exceptional candidate in separation technology industry.

References

1 R. van Wissen, M. Golombok and J. J. H. Brouwers, *Separation of carbon dioxide and methane in continuous countercurrent gas centrifuges*, 2005, vol. 60.

2 K. Liao, Q. Yao, X. Wu and W. Jia, *Energies*, 2012, **5**, 3892–3907.

3 R. W. Baker, *Membrane technologies and applications*, John Wiley & Sons, Ltd, 2nd editio., 2011.

4 R. Hughes, G. Kotamreddy, A. Ostace, D. Bhattacharyya, R. L. Siegelman, S. T. Parker, S. A. Didas, J. R. Long, B. Omell and M. Matuszewski, *Energy & Fuels*, 2021, **35**, 6040–6055.

5 C. Cambridge University Press UK, .

6 H. Yang, Z. Xu, M. Fan, R. Gupta, R. B. Slimane, A. E. Bland and I. Wright, *J. Environ. Sci.*, 2008, **20**, 14–27.

7 P. C. Wankat, *Separation Process Engineering: includes mass transfer analysis. (4th ed.)*, Prentice Hall, Massachusetts (USA), 2017.

8 D. S. Sholl and R. P. Lively, *Nature*, 2016, **532**, 435–437.

9 H.-C. Zhou, J. R. Long and O. M. Yaghi, *Chem. Rev.*, 2012, **112**, 673–674.

10 H.-C. J. Zhou and S. Kitagawa, *Chem. Soc. Rev.*, 2014, **43**, 5415–5418.

11 H. Li, K. Wang, Y. Sun, C. T. Lollar, J. Li and H. C. Zhou, *Mater. Today*, 2018, **21**, 108–121.

12 V. Pascanu, G. González Miera, A. K. Inge and B. Martín-Matute, *J. Am. Chem. Soc.*, 2019, **141**, 7223–7234.

13 S. A. Diamantis, A. Margariti, A. D. Pournara, G. S. Papaefstathiou, M. J. Manos and T. Lazarides, *Inorg. Chem. Front.*, 2018, **5**, 1493–1511.

14 M. Oggianu, N. Monni, V. Mameli, C. Cannas, S. A. Sahadevan and M. L. Mercuri, *Magnetochemistry*, 2020, **6**, 1–14.

15 P. M. Bhatt, Y. Belmabkhout, A. Cadiau, K. Adil, O. Shekhah, A. Shkurenko, L. J. Barbour and M. Eddaoudi, *J. Am. Chem. Soc.*, 2016, **138**, 9301–9307.

16 K. J. Chen, D. G. Madden, T. Pham, K. A. Forrest, A. Kumar, Q. Y. Yang, W. Xue, B. Space, J. J. Perry, J. P. Zhang, X. M. Chen and M. J. Zaworotko, *Angew. Chemie - Int. Ed.*, 2016, **55**, 10268–10272.

17 S. Mukherjee, S. Chen, A. A. Bezrukov, M. Mostrom, V. V. Terskikh, D. Franz, S. Q.

Wang, A. Kumar, M. Chen, B. Space, Y. Huang and M. J. Zaworotko, *Angew. Chemie - Int. Ed.*, 2020, **59**, 16188–16194.

18 G. Mínguez Espallargas, E. Miguel-Casañ, E. Andres-Garcia, J. Calbo and M. Giménez-Marqués, *Chem. Eur. J.*, 2021, **27**, 4653-4659.

19 M. Giménez-Marqués, N. Calvo Galve, M. Palomino, S. Valencia, F. Rey, G. Sastre, I. J. Vitórica-Yrezábal, M. Jiménez-Ruiz, J. A. Rodríguez-Velamazán, M. A. González, J. L. Jordá, E. Coronado and G. M. Espallargas, *Chem. Sci.*, 2017, **8**, 3109–3120.

20 L. E. Darago, M. L. Aubrey, C. J. Yu, M. I. Gonzalez and J. R. Long, *J. Am. Chem. Soc.*, 2015, **137**, 15703–15711.

21 S. A. Sahadevan, A. Abhervé, N. Monni, C. Sáenz de Pipaón, J. R. Galán-Mascarós, J. C. Waerenborgh, B. J. C. Vieira, P. Auban-Senzier, S. Pillet, E.-E. Bendeif, P. Alemany, E. Canadell, M. L. Mercuri and N. Avarvari, *J. Am. Chem. Soc.*, 2018, **140**, 12611–12621.

22 S. Ashoka Sahadevan, N. Monni, M. Oggianu, A. Abhervé;, D. Marongiu, M. Saba, A. Mura, G. Bongiovanni, V. Mameli, C. Cannas, N. Avarvari, F. Quochi and M. L. Mercuri, *ACS Appl. Nano Mater.*, 2020, **3**, 94-104.

23 J. A. DeGayner, I. R. Jeon, L. Sun, M. Dincă and T. D. Harris, *J. Am. Chem. Soc.*, 2017, **139**, 4175–4184.

24 S. Benmansour, A. Hernández-Paredes, A. Mondal, G. López Martínez, J. Canet-Ferrer, S. Konar and C. J. Gómez-García, *Chem. Commun.*, 2020, **56**, 9862–9865.

25 A. E. Thorarinsdottir and T. D. Harris, *Chem. Rev.*, 2020, **120**, 8716–8789.

26 M. L. Mercuri, F. Congiu, G. Concas and S. Ashoka Sahadevan, *Magnetochemistry*, 2017, **3**, 17.

27 M. Atzori, S. Benmansour, G. Mínguez Espallargas, M. Clemente-León, A. Abhervé, P. Gómez-Claramunt, E. Coronado, F. Artizzu, E. Sessini, P. Deplano, A. Serpe, M. L. Mercuri and C. J. Gómez García, *Inorg. Chem.*, 2013, **52**, 10031–10040.

28 S. Benmansour, A. Abhervé, P. Gómez-Claramunt, C. Vallés-García and C. J. Gómez-García, *ACS Appl. Mater. Interfaces*, 2017, **9**, 26210–26218.

29 S. Ashoka Sahadevan, N. Monni, A. Abhervé, D. Marongiu, V. Sarritzu, N. Sestu, M. Saba, A. Mura, G. Bongiovanni, C. Cannas, F. Quochi, N. Avarvari and M. L. Mercuri, *Chem. Mater.*, 2018, **30**, 6575–6586.

30 B. F. Abrahams, A. D. Dharma, B. Dyett, T. A. Hudson, H. Maynard-Casely, C. J. Kingsbury, L. J. McCormick, R. Robson, A. L. Sutton and K. F. White, *Dalt. Trans.*,

2016, **45**, 1339–1344.

31 C. J. Kingsbury, B. F. Abrahams, D. M. D'Alessandro, T. A. Hudson, R. Murase, R. Robson and K. F. White, *Cryst. Growth Des.*, 2017, **17**, 1465–1470.

32 C. J. Kingsbury, B. F. Abrahams, J. E. Auckett, H. Chevreau, A. D. Dharma, S. Duyker, Q. He, C. Hua, T. A. Hudson, K. S. Murray, W. Phonsri, V. K. Peterson and R. Robson, *Chem. Eur. J.*, 2019, **25**, 5222–5234.

33 W. Gauβ, H. Heitzer and S. Petersen, *Justus Liebigs Ann. Chem.*, 1973, **764**, 131–144.

34 M. Atzori, F. Pop, T. Cauchy, M. L. Mercuri and N. Avarvari, *Org. Biomol. Chem.*, 2014, **12**, 8752–8763.

35 R. S. Liu, X. D. Shi, C. T. Wang, Y. Z. Gao, S. Xu, G. P. Hao, S. Chen and A. H. Lu, *ChemSusChem*, 2021, **14**, 1428–1471.

36 Z. Luo, L. Liu, J. Ning, K. Lei, Y. Lu, F. Li and J. Chen, *Angew. Chemie - Int. Ed.*, 2018, **57**, 9443–9446.

37 B. Wang, A. P. Cote, H. Furukawa, M. O/'Keeffe and O. M. Yaghi, *Nature*, 2008, **453**, 207–211.

38 S. Couck, E. Gobechiya, C. E. A. Kirschhock, P. Serra-Crespo, J. Juan-Alcañiz, A. Martinez Joaristi, E. Stavitski, J. Gascon, F. Kapteijn, G. V Baron and J. F. M. Denayer, *ChemSusChem*, 2012, **5**, 740–750.

39 M. Mon, R. Bruno, E. Tiburcio, A. Grau-Atienza, A. Sepúlveda-Escribano, E. V Ramos-Fernandez, A. Fuoco, E. Esposito, M. Monteleone, J. C. Jansen, J. Cano, J. Ferrando-Soria, D. Armentano and E. Pardo, *Chem. Mater.*, , DOI:10.1021/acs.chemmater.9b01995.

40 A. C. Kizzie, A. G. Wong-Foy and A. J. Matzger, *Langmuir*, 2011, **27**, 6368–6373.

41 Z. Lu, J. Zhang, J. Duan, L. Du and C. Hang, *J. Mater. Chem. A*, 2017, **5**, 17287–17292.

42 B. Zheng, J. Bai, J. Duan, L. Wojtas and M. J. Zaworotko, *J. Am. Chem. Soc.*, 2011, **133**, 748–751.

Chapter 4

Reversible Tuning of Luminescent and SIM properties in a 3D Anilato-based Er-MOF through Structural Flexibility

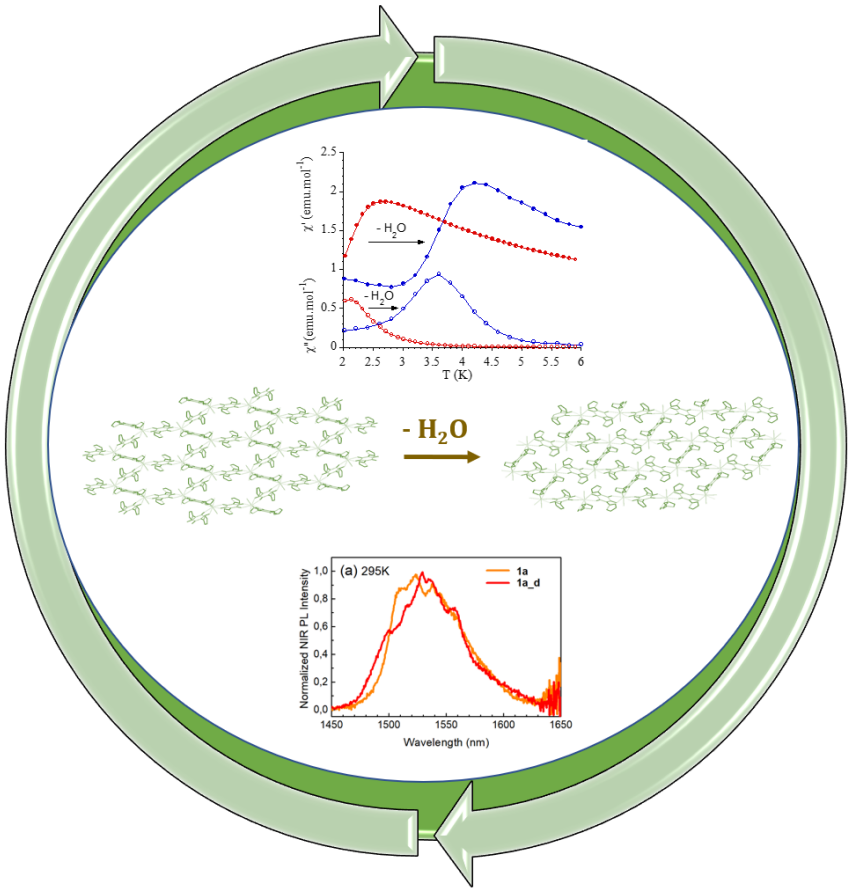

Abstract

By combining 3,6-N-ditriazolyl-2,5-dihydroxy-1,4-benzoquinone (H_2trz_2An) with NIR-emitting Er^{III} ion, two different 3D neutral polymorphic CFs (**1a** and **1b**), differing for the number of uncoordinated water molecules, formulated as $[Ln_2(trz_2An)_3(H_2O)_4]_n \cdot xH_2O$ (x = 10, phase a; x = 7, phase b), have been obtained. The structure of **1a** shows layers with (6,3) topology forming six-membered rings with distorted hexagonal cavities along the *bc* plane. These 2D layers are interconnected through the N4 atoms of the two pendant arms of the trz_2An linkers, leading to a 3D MOF, where neighboring layers are eclipsed along the *a* axis, with hexagonal channels filled with water molecules. In **1b** layers with (6,3) topology in the [101] plane are present, where each Er^{III} ion is connected to three other Er^{III} ions through bis-bidentate trz_2An ligands, forming rectangular six-membered cavities. **1a** and **1b** are multifunctional materials showing coexistence of NIR emission and field induced slow relaxation of the magnetization. Remarkably, **1a** is a flexible MOF, showing a reversible structural phase transition between a hexagonal – rectangular cavity, involving shrinkage/expansion from the distorted hexagonal 2D framework to a distorted 3,6-brickwall rectangular 3D structure of **1a_d** less porous CF, upon dehydration/hydration external stimulus, under mild conditions (vacuum/heating to 360 K). This partially dehydrated compound shows an increase in the emission intensity and an improvement of the magnetic blocking temperature with respect to the hydrated compound, mainly related to the loss of one water coordination molecule. Theoretical calculations support experimental findings evidencing that the slight improvement of SIM properties is related also to the loss of a water molecule, which promote magnetic relaxation by erasing its molecular vibrations which can couple to spin states.

..

1. Introduction

Metal-organic frameworks (MOFs), formed by organic molecules (*linkers*) and metal ions (*nodes*) are attracting considerable attention in material science thanks to their fascinating supramolecular architectures[1,2] and the richness of their chemical and physical properties. Noteworthy, some of them possess structural flexibility,[3] a unique feature which depends on the nature of metal–ligand interactions, which in turn, depends on both organic ligands and metal ions/clusters. As a direct consequence, flexible MOFs show dynamic properties such as opening/closing of pores, expansion/shrinkage of the framework and/or a reversible change of physical properties, induced by different type of stimuli such as light, electrical potential, guest inclusion or pressure.[4–6] Despite the *plethora* of MOFs reported so far, those showing structural flexibility and dynamic behaviour are rare, in spite of their great potential in several applications, from storage, to sensing and biomedicine (drug delivery). More importantly this uncommon features makes MOFs a challenging platform for designing multi-functionality with the possibility to tune the physical properties upon reversible structural changes in response to external stimuli.[7,8] Lanthanide based MOFs (Ln-MOFs) in particular, show peculiar luminescence properties, ranging from Vis to NIR range of emission.[9] By properly choosing the organic linker it is possible to exceptionally enhance the light absorption and consequent emission *via* antenna effect to the lanthanide ions, which is otherwise very weak due to the forbidden *f-f* transitions. On the other hand, Lanthanide ions possess large *inherent* anisotropy, *i.e.* large unquenched orbital angular moments, resulting from strong spin−orbit coupling and weak ligand fields, which impart strong magnetic anisotropy. Their interesting magnetic behaviour make them attractive candidates to build Single-Ion Magnets (SIMs),[10] a class of molecular materials containing a single spin center that exhibits slow magnetic relaxation, purely of a molecular origin, rather than cooperative behaviour favoured by magnetic exchange between magnetic centers mediated by a suitable organic linker in extended networks. In this second generation of single-molecule magnets, the slow relaxation of the magnetization is due to magnetic anisotropy of the single-ion, which arises from the combination of spin-orbit coupling and an adequate ligand field in those based on lanthanide ions. Controlled spatial organization of SIMs to build large-scale ordered arrays can be achieved by assembling lanthanide ions into a 3D frameworks affording the so-called SIM-MOF.[11,12] Among the organic linkers which can either act as a powerful *antenna* or isolate magnetically the metal ions, 3,6-disubstituted (X)-2,5-dihydroxybenzoquinone derivatives (X=H, F, Cl, Br, I, CN, *etc.*) *i.e.* anilates, have been recently studied as building blocks for lanthanide based

frameworks,[13–16] leading to several bi-dimensional (2D) and a few three-dimensional (3D) lattices[17–20] with interesting properties such as single-ion magnetism, luminescence, gas/solvent adsorption/absorption and solvent exchange.[21] Previous attempts to tune the magnetic and optical properties of these Ln-anilato-based frameworks are based on the exchange of coordinated and non-coordinated solvent molecules, which is not accompanied by drastic structural changes.[16] In the present work, the 3,6-N-ditriazolyl-2,5-dihydroxy-1,4-benzoquinone (H_2trz_2An) anilato derivative[22], has been used to construct 3D MOFs, thanks to the coordinative properties of the N4 atoms of the two triazole pendant arms at the 3,6 position of the anilato moiety. Indeed, it afforded Mn(II)[23] and ultramicroporous Co(II) 3D MOFs, showing same rigid scaffold as zeolites, and the latter excellent capability in CO_2 capture and separation.[24]

When Lanthanides ions are used as metal nodes, particularly the NIR emitting luminescent Er^{III} ion, two 3D Er-trz_2An-based frameworks formulated as $[Er_2(trz_2An)_3(H_2O)_4]_n \cdot 10H_2O$ (**1a**, porous) and $[Er_2(trz_2An)_3(H_2O)_4]_n \cdot 7H_2O$ (**1b**, non-porous), have been obtained. Both Polymorphs have been characterized by Single-Crystal X-Ray Diffraction (SC-XRD), Luminescence Spectroscopy and Magnetometry, which indicate that the two compounds present a field-induced slow relaxation of magnetization. Interestingly, all techniques probed a reversible structural flexibility and shrinkage/expansion dynamic behaviour of **1a** framework, that originates from a change in coordination environment of Er^{III} ions, in response to the removal of coordinative water molecules. Noteworthy, such a structural flexibility of **1a** 3D MOF induces important and reversible structural changes after partial desolvation, which allows a tuning of its SIM and luminescence properties.

2. Experimental Section

2.1. General Remarks

The lanthanides precursors, NaOH in pellets and the solvents used were purchased from AlfaAesar and Exacta Optech and used without further purification. Synthesis of ligand H_2trz_2An was performed as reported in Chapter 1, according with literature.[16] Elemental analyses (C, H, and N) were performed with a CE Instruments EA 1110 CHNS.

2.2. Synthesis

$[Er_2(trz_2An)_3(H_2O)_4]_n \cdot 10H_2O$ (1a) and $[Er_2(trz_2An)_3(H_2O)_4]_n \cdot 7H_2O$ (1b). A 5 mL Teflon vial with a mixture of $Er(NO_3)_3 \cdot 6H_2O$ (0.05 mmol; 22.2 mg), H_2trz_2An (0.05 mmol, 13.7 mg), NaOH (0.1 mmol, 4 mg) and water (5 mL) was heated at 130°C for 48 hours and then the vial was slowly cooled to room temperature. Two different types of crystals were obtained from the same batch, dark red-block crystals (**phase a**) and orange prismatic crystals (**phase b**), both of them were suitable for single crystal X-Ray Diffraction (XRD) measurements. Their density's difference was exploited to separate them, using CH_2Cl_2/CH_2Br_2 solvent mix in the ratio 0.925/0.975, for all the further measurements. Elemental analysis of **1a** and **1b** is reported below in **Table 4.1**. Both single crystals and polycrystalline powder of **1a** were placed under vacuum in a vacuum line pump and then sealed in a glove box to obtain **$[Er_2(trz_2An)_3(H_2O)_2]_n$ (1a_d)**, whereas the same attempt on **1b** produced no changes.

Table 4.1. Elemental analysis for all the compounds **1a** and **1b**.

		Calculated			Founded		
		%C	**%H**	**%N**	**%C**	**%H**	**%N**
1a	$C_{30}H_{40}N_{18}O_{26}Er_2$	25.68	2,87	17,97	25,37	2,81	17,86
1b	$C_{30}H_{34}N_{18}O_{23}Er_2$	26,71	2,54	18,69	26,70	2,24	18,57

2.3. Physical Measurements

X-Ray Crystallography. Single crystal X-Ray diffraction was performed on **1a** and **1b** crystals, which were mounted on a glass fiber using a viscous hydrocarbon oil to coat the single crystal and then transferred directly to the cold nitrogen stream for data collection. X ray data were collected at 120 K for both samples. Furthermore, a single crystal of **1a** was measured at 360 K and another one was measured at 120 K after being placed in vacuum. Measurements were performed on a Supernova diffractometer equipped with a graphite-

monochromated Enhance (Mo) X-ray Source (λ = 0.710 73 Å). The program CrysAlisPro, Oxford Diffraction Ltd., was used for unit cell determinations and data reduction. Empirical absorption correction was performed using spherical harmonics, implemented in the SCALE3 ABSPACK scaling algorithm. The structures were solved with the ShelXT structure solution program[25] and refined with the SHELXL-2013 program,[26] using Olex2.[27] Non-hydrogen atoms were refined anisotropically, and hydrogen atoms were placed in calculated positions refined using idealized geometries (riding model) and assigned fixed isotropic displacement parameters. Crystallographic data of all the compounds are summarized in **Table 4.2**. Powder X-ray diffraction patterns were performed using a 0.7 mm glass capillary filled with polycrystalline samples of the compounds and mounted and aligned on an Empyrean PANalytical powder diffractometer, using Cu Kα radiation (λ = 1.541 77 Å). A total of three scans were collected for each compound at room temperature in the 2θ range of 5−40°. Polycrystalline samples of **1a** and **1b** were further placed under vacuum in a vacuum line pump and were then opened in the glove box to be sealed in the 0.7 mm glass capillary.

Table 4.2. Crystallographic data for compound **1a**, **1a_d** and **1b**.

	1a	**1a_d (vacuum)**	**1b**
Empirical formula	$C_{30}H_{28}N_{18}O_{25}Er_2$	$C_{30}H_{14}N_{18}O_{18}Er_2$	$C_{30}H_{28}N_{18}O_{20}Er_2$
FW	1.375.22	1249.12	1295.22
Crystal color	Dark Purple	Purple	Orange
Crystal size (mm^3)	0.24 × 0.15 × 0.07	0.29 × 0.24 × 0.12	0.24 × 0.15 × 0.13
Temperature (K)	120	120	120
Wavelength (Å)	(MoKa) λ = 0.71073	(MoKa) λ = 0.71073	(MoKa) λ = 0.71073
Crystal system	triclinic	triclinic	triclinic
Space group	*P-1*	*P-1*	*P-1*
a (Å)	8.9555 (7)	9.013(3)	8.6201(3)
b (Å)	9.4191 (7)	9.200(3)	10.4220 (4)
c (Å)	15.4553 (12)	12.495(3)	11.9887(4)
a (°)	75.154 (7)	94.90(2)	80.139(3)
b (°)	77.176 (7)	98.10(2)	79.145(3)
g (°)	67.936 (7)	115.67(3)	82.373(3)
V ($Å^3$)	1156.33 (17)	912.1(5)	1036.52(7)
ρ_{calc} ($g.cm^{-3}$)	1.975	2.274	2.075
μ(MoKα) (mm^{-1})	3.712	4.681	4.126
2θ range (°)	5.59 to 55.74	6.15 to 56.152	6.584 to 56.08
Index ranges	-11 ≤ h ≤ 11, -11 ≤ k ≤ 12, -17 ≤ l ≤ 20	-11 ≤ h ≤ 11, -12 ≤ k ≤ 11, -15 ≤ l ≤ 16	-11 ≤ h ≤ 11, -13 ≤ k ≤ 12, -15 ≤ l ≤ 14
Reflections collected	7799	10668	14194
Independent reflections	4608 [R_{int} = 0.0362, R_{sigma} = 0.0667]	3881 [R_{int} = 0.1745, R_{sigma} = 0.2099]	4366 [R_{int} = 0.0203, R_{sigma} = 0.0223]
Data/restraints/parameters	4608/0/339	3881/0/282	4366/0/324
Goodness-of-fit on F2	1.046	1.083	1.055

Final R indexes [I>=2σ (I)]	R_1 = 0.0354, wR_2 = 0.0680	R_1=0.1421,wR_2=0.3156	R_1=0.0155,wR_2=0.0370
Final R indexes [all data]	R_1 = 0.0414, wR_2 = 0.0735	R_1=0.2075,wR_2=0.3765	R_1=0.0162,wR_2= 0.0373
Largest diff.peak/hole/e Å^{-3}	1.21/-1.47	3.98/-3.63	0.88/-0.93

Thermogravimetric Analysis. Thermogravimetric analysis were performed in alumina crucibles with the instrument STA-6000 under nitrogen flux (40 mL/min), in the 25-800°C temperature range at 10°C/min.

Magnetic Measurements. Magnetic measurements were performed with Quantum Design MPMS-XL-5 SQUID and PPMS-9 magnetometers on powdered polycrystalline samples measured with eicosane to avoid preferential orientations. In the case of **1a**, it was necessary to protect the sample covering it with H_2O since the vacuum of the squid chamber caused desolvation and the formation of **1a_d**.

Theoretical Calculations. For the theoretical modelling of the magnetic properties, we have used the SIMPRE computational package,[28] introducing the crystallographic atomic coordinates and the experimental magnetic properties of the compounds as an input. In order to fit the experimental data, we have varied the two parameters (D_r and Z_i) of the REC model for each type of donor atom of the first coordination sphere.[29] The electronic structure of the excited energy multiplets have been determined using the full hamiltonian[30] in the CONDON package.[31] A detailed explanation is provided in the Supporting Material (*Part IV*).

Photophysical Measurements. Photoluminescence (PL) experiments were performed with pulsed laser irradiance at 355 nm wavelength. Finely ground powders were compacted between quartz slides for measurements in standard conditions, or attached to the cold finger of a continuous-flow cryostat (Janis ST-500) for measurements under controlled atmosphere (air, vacuum, N_2), fed with liquid N_2 for low-temperature measurements under vacuum conditions at 77K. For time-resolved measurements of the ligand-centered emissions, samples were excited by optical parametric amplifier (Light Conversion TOPAS-C) emitting ~200-fs-long pulses at the repetition frequency of 1 kHz and detected by a Vis streak camera (Hamamatsu C1091) connected to a single-grating spectrometer (Princeton Instruments Acton SpectraPro2300i). For all other PL experiments, samples were pumped by a passively Q-switched powerchip laser (Teem Photonics PNV-M02510) delivering ~350 ps pulses, centered at 355 nm wavelength, at 1 kHz. The PL signals were analyzed by a single-grating spectrometer (Princeton

Instruments Acton SpectraPro 2300i) and acquired by thermoelectrically cooled detectors, namely, (a) a Vis CCD camera (Andor NewtonEM) for ligand-centered emission spectra, (b) a NIR array detector (Andor iDus InGaAs 1.7μm) for NIR PL spectra, and (c) a photomultiplier (Hamamatsu H10330A-75) connected to a 1 GHz digital oscilloscope (Tektronix TDS 5104) for NIR PL decay transients.

3. Results and Discussion

3.1. Synthesis

By combining $Er(NO_3)_3 \cdot 6H_2O$ with H_2trz_2An, in 1:1 ratio, through hydrothermal method, $[Er_2(trz_2An)_3(H_2O)_4]n \cdot 10H_2O$ (**1a**) and $[Er_2(trz_2An)_3(H_2O)_4]n.7H_2O$ (**1b**) were obtained (**Scheme 4.1**). Two types of crystals are observed in each hydrothermal batch: dark red blocks crystals (**phase a**) and orange prismatic crystals (**phase b**), as reported in **Figure 4.1a**. Due to their difference in density, it was possible to separate both phases by using a CH_2Cl_2/CH_2Br_2 solvent mixture: when the crystals are suspended in a CH_2Cl_2/CH_2Br_2 solution, **phase a** starts floating, while **phase b** lies at the bottom (**Figure 4.1b**). Furthermore, by heating or applying vacuum to **1a** it is possible to remove both water molecules present in the channels and one coordinated water molecule, leading to the formation of a new crystalline phase, **1a_d**.

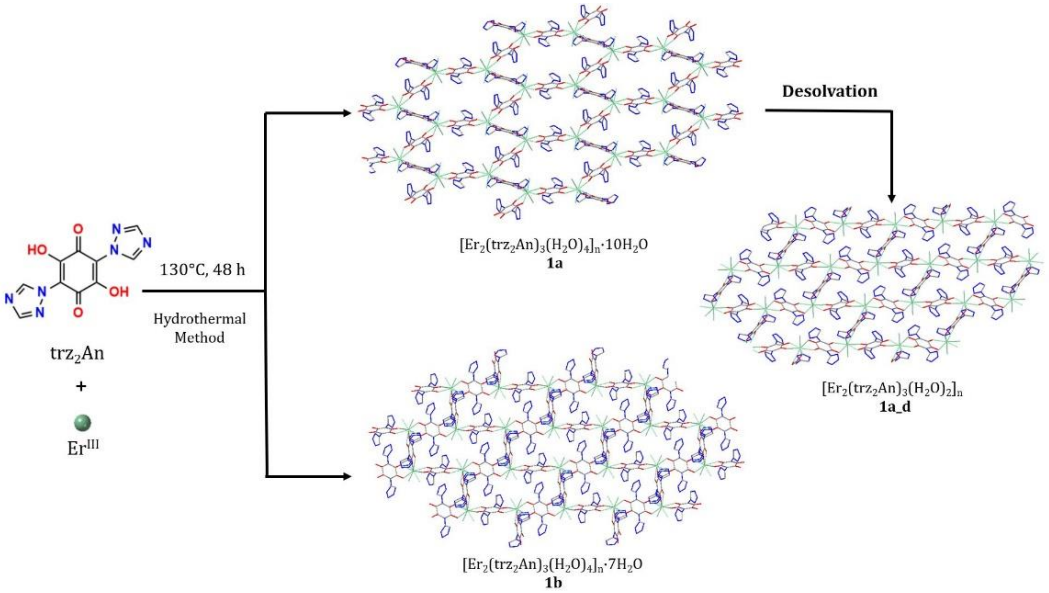

Scheme 4.1. Synthetic strategy for **1a**, **1a_d** and **1b**.

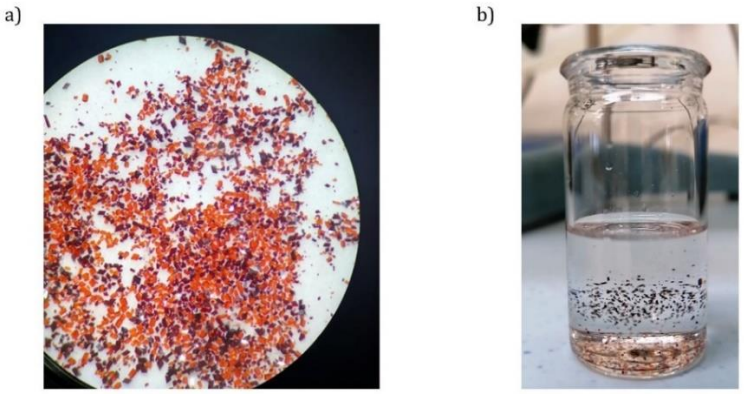

Figure 4.1. a) Optical microscope image of mixture of crystals of phases **a** and **b**; b) crystals separations by using the CH_2Cl_2/CH_2Br_2 solution mix.

3.2. Crystal Structure

1a and **1b** both crystallize in triclinic space group *P-1* and are 3D neutral coordination frameworks of the trz_2An linker bridging the Er^{III} ions. In **1a**, Er^{III} ion is enneacoordinated with a $\{NO_8\}$ coordination sphere arising from two oxygens of three bidentate trz_2An ligands, the N4 atom of one trz_2An ligand and two coordinated water molecules. The geometry of the first coordination sphere is closest to a spherical capped square antiprism (CSAPR-9) according to continuous SHAPE analysis (**Figure 4.2a**).[32] The structure shows layers with (6,3) topology forming six-membered rings with distorted hexagonal cavities along the *bc* plane (**Figure 4.2b**). Each cavity contains two anilato rings almost parallel to the layer (*face-on*) and four anilato rings almost perpendicular to it (*edge-on*). The largest Er-Er-Er angle in the hexagon is 134.4°, while the Er-Er distances in the diagonals of the hexagons are 12.8, 13.4 and 21.9 Å (**Table S4.1**, *Part IV*). These distances and angles are similar to those found in Ln-anilato compounds with distorted hexagonal 2D structures, coordination number 9 and spherical tricapped trigonal prism (TCTPR-9) geometry.[33,34] The C−O and C-C bond lengths across the five-membered chelate ring for trz_2An ligands also present typical values of anilato dianions (see **Table 4.1**, *Part IV*).[33] A remarkable difference with respect to previous Ln^{III} anilato-based 2D compounds is that these 2D layers are interconnected through the N4 atoms of the two 1,2,4-triazole substituted pendant arms of one of the three trz_2An linkers coordinated to each Er^{III} (*face-on* linkers) (**Figure 4.2d**). This leads to a porous 3D framework, where neighboring layers are eclipsed along the *a* axis with hexagonal channels filled with water molecules (**Figure 4.2c**). The remaining N4 atoms of the 1,2,4-triazole substituted pendant arms of the other two trz_2An linkers are hydrogen-bonded to coordinating water molecules.

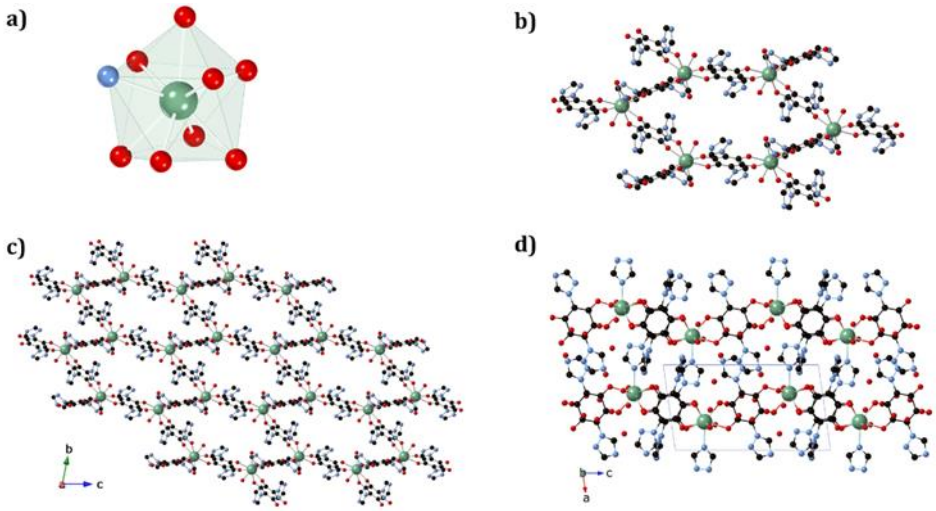

Figure 4.2. a) Spherical capped square antiprismatic coordination geometry of the Er^{III} center. b) View of one hexagonal cavity. c) View of **1a** along the *bc* plane. d) View of **1a** along the *ac* plane. The black, blue,

red, and green spheres represent the C, N, O, and Er^{III} atoms, respectively. Hydrogen atoms and water molecules inside the pores are omitted for clarity.

In **1b,** the Er^{III} ion is enneacoordinated as well, presenting a $\{NO_8\}$ coordination sphere with six oxygens of three bidentate trz_2An linkers, two coordinated water molecules and the N4 atom of one trz_2An ligand. The coordination geometry is nearest to spherical tricapped trigonal prism (TCTPR-9) according to continuous SHAPE analysis[32] (**Figure 4.3a**). The structure shows layers with (6,3) topology in the [101] plane, in which each Er^{III} ion is connected to three other Er^{III} ions through bis-bidentate trz_2An ligands forming rectangular six-membered cavities, which adopt a brick-wall structure where the long axis of all the rectangles are parallel (**Figure 4.3b, 4.3c**). Thus, the two largest Er-Er-Er angles are close to 180° (172.5°) (see **Table 4.3**, *Part IV*). On the other hand, Er^{III} nodes of the same layer are almost coplanar and are connected to Er^{III} nodes of other layers, through the N4 atom of the two pending triazolyl arms of one of the three trz_2An linkers (**Figure 4.3d**), which are placed in the shortest side of the rectangular cavities, leading to a 3D framework. Finally, the C−O and C-C bond lengths across the five-membered anilato ring for trz_2An linkers exhibit, as in **1a**, typical values of anilato dianions (see **Table 4.3**, *Part IV*).[33]

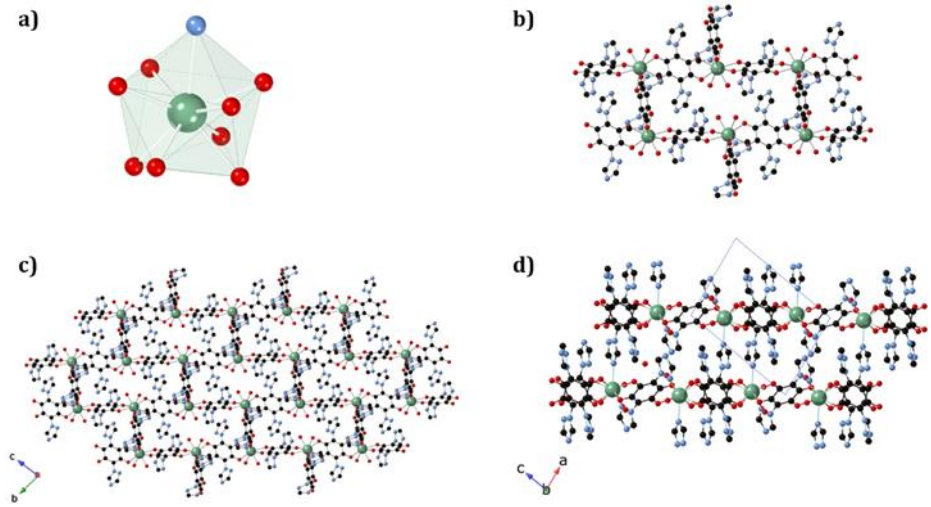

Figure 4.3. a) Spherical tricapped trigonal prismatic coordination geometry of the Er^{III} center. b) View of one distorted hexagonal cavity. c) View along *bc* plane. d) View along *ac* plane of **1b**. The black, blue, red, and green spheres represent the C, N, O, and Er^{III} atoms, respectively. Hydrogen atoms and water molecules inside the pores are omitted for clarity.

Both **1a** and **1b** polycrystalline samples are perfectly consistent with the calculated pattern (**Figure S4.1, S4.2**) confirming the homogeneity and purity of the bulk sample. Furthermore, a polycrystalline sample of **1a** and **1b** was placed under vacuum in a Schlenk

line and then it was sealed in a glove box, in order to study if vacuum could induce changes on the crystal structure. While for **1b** the vacuum treatment led to no changes in the structure (see **Figure S4.3**), a reversible structural change was observed in **1a**, with the formation of a new phase, **1a_d**, owing to loss of water molecules. As reported in **Figure 4.4**, when **1a_d** is left to air for few days, the same powder XRD pattern as **1a** is obtained, proving the complete reversibility of the dehydration/hydration process for powder samples.

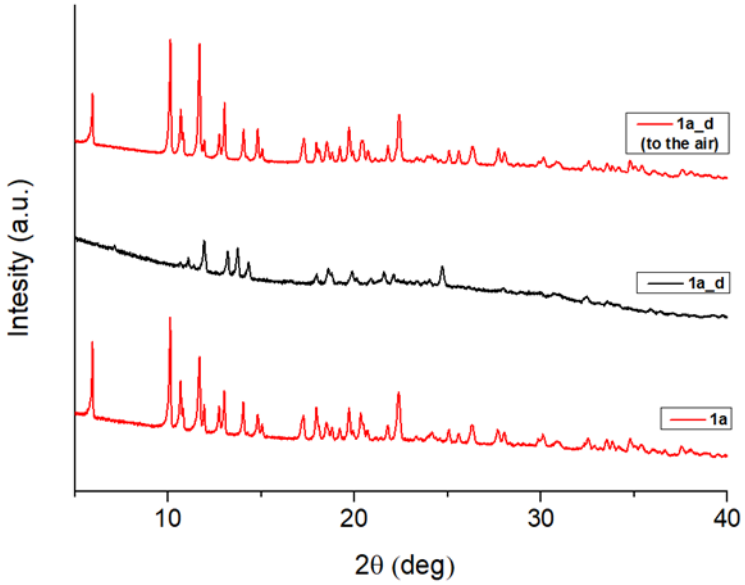

Figure 4.4. PXRD patterns of **1a** (red), **1a_d** (black) and **1a_d** left to air 4 days after vacuum treatment (red top), highlighting the complete reversibility of the structural change induced by dehydration.

Taking into account PXRD and thermogravimetric data (*vide infra*), single crystal X-Ray diffraction was performed on **1a**, to investigate the new desolvated phase, by heating the sample at 360 K in the diffractometer or after vacuum treatment of the sample (similarly to the polycrystalline sample). In **1a_d**, Er^{III} ion shows a $\{NO_7\}$ coordination sphere arising from six oxygens of three bidentate trz_2An linkers, the N4 atom of one trz_2An linker and one coordinated water molecule. The coordination geometry is close to a triangular dodecahedron (TDD-8) (**Figure 4.5a**), according to continuous SHAPE analysis[32] Er–O bond lengths are in the range of 2.266(16)- 2.430(16) Å (**1a_d** vacuum) and 2.28(2)-2.442(13) Å (**1a_d** 360K), while Er-N bond lengths are 2.46(2) Å (**1a_d** vacuum) and 2.464(18) Å (**1a_d** 360K). Again, the C−O and C-C bond lengths across the five-membered anilato ring for trz_2An linkers exhibit typical values of anilato dianions,[33] 1.22(3)-1.26(2) and 1.57(3)-1.60(3) Å for **1a_d** vacuum and 1.22(3)-1.27(2) and 1.52(3)-1.54(3) Å for **1a_d** 360K, respectively (see **Table S4.2**). As in **1a**, the structure shows

layers with (6,3) topology in the *bc* plane but interestingly, they exhibit a drastic change from the distorted hexagonal 2D network found in **1a** to a distorted 3,6-brickwall rectangular structure. Thus, the six-membered rectangular cavities of the layers, showed in **Figure 4.5b**, contain four *face-on* and two *edge-on* anilato rings in **1a_d**, instead of the two *face-on* and four *edge-on* ones found in **1a**. The 3D framework is maintained thanks to the N4 atom of the two pending triazolyl arms of one of the three trz_2An linkers located in the shortest side of the rectangular cavity (*face-on* linker), indicating that the connectivity is the same as the initial solvated MOF (**1a**). Neighbouring layers are eclipsed along the *a* axis defining rectangular channels (**Figure 4.5c**). As shown by pXRD, the phase of **1a_d** is consistent with the calculated one from the CIF (**Figure 4.6**).

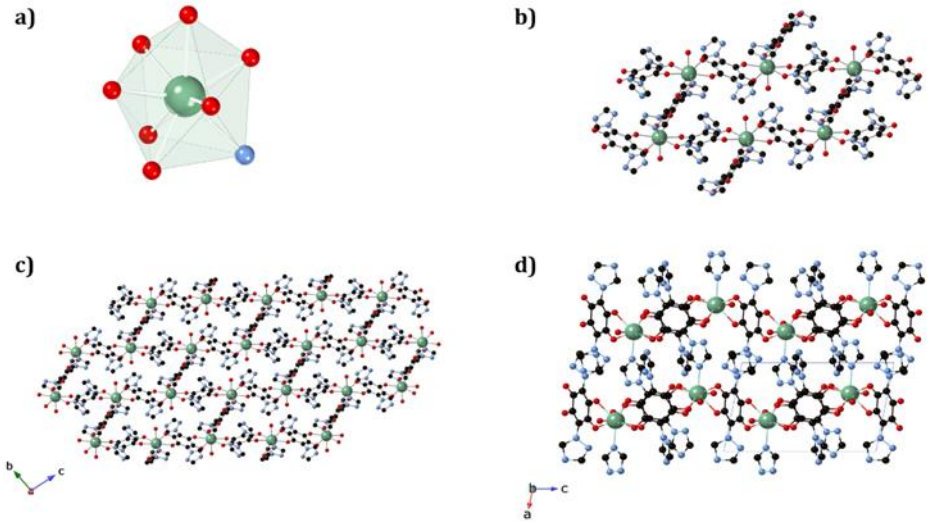

Figure 4.5. a) View along *bc* plane of **1a_d** framework. b) View of one rectangular cavity. c) Triangular dodecahedron coordination geometry of the Er^{III} center. d) View along the *ac* plane of **1a_d**. The black, blue, red, and green spheres represent the C, N, O, and Er^{III} atoms, respectively. Hydrogen atoms are omitted for clarity.

The new phase **1a_d** can be hydrated again to restore the initial framework of **1a**, indicating a reversible structural phase transition between a hexagonal – rectangular cavity, which is observed in flexible MOFs.[35] Interestingly, the flexible structure observed in **1a** enables improvement of luminescent and magnetic properties by reversible dehydration/hydration processes (*vide infra*).

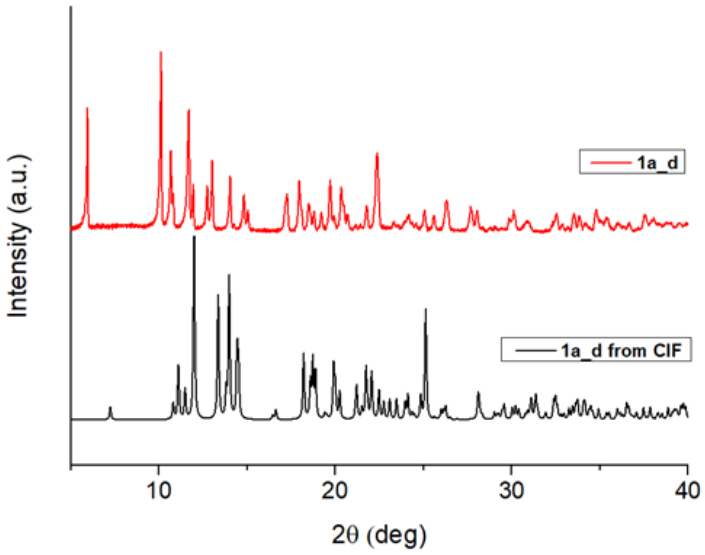

Figure 4.6. Calculated (black) and experimental (red) powder XRD patterns of **1a_d**, in 2θ range of 5-40°.

3.3 Thermogravimetric Analysis

Thermogravimetric analysis (TGA) was performed in order to study the thermal stability of **1a** and to have complementary information about the dehydrated phase **1a_d**.

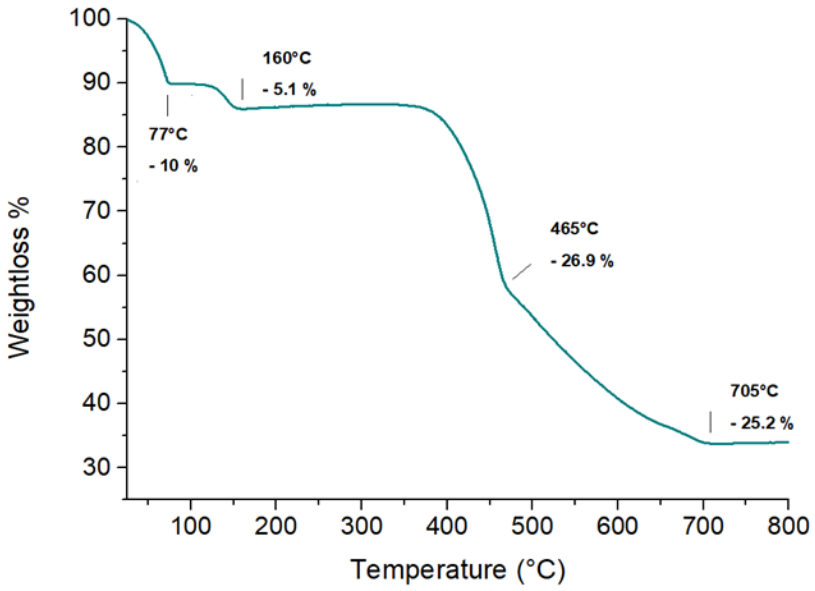

Figure 4.7. Thermogram of **1a** in 25-800°C temperature range. The percentages shown in the graph are referred to the previous weightloss.

1a thermogram shows a continuous weight loss of 10 % from room temperature to 77°C, which is consistent with the expected weight loss of 7.5 water molecules. Then in

the 77-160°C temperature range a second weight loss is present, which is close to the expected weight loss for other 3.5 water molecules. Finally, above 400°C, there is an abrupt weight loss corresponding to the decomposition of the ligands. Taking into account the crystallographic data, the first weight loss is consistent with the transition from the initial compound ($[Er_2(trz_2An)_3(H_2O)_4]_n \cdot 10H_2O$) to $[Er_2(trz_2An)_3(H_2O)_2]_n \cdot 4.5H_2O$. Then the second weight loss is close to the expected loss which lead to the formula $[Er_2(trz_2An)_3(H_2O)_2]_n$, of **1a_d**. Thermogram of **1b** is reported in **Figure S4.4** of the Supplementary Material, *Part IV*.

3.4 Magnetic Properties

Solid state, direct-current (dc) magnetic susceptibility measurements were carried out in the temperature range of 2-300 K under an applied magnetic field of 0.1 T for both phases 1**a** and 1**b**. In the case of **1a**, it was necessary to protect the sample with H_2O since the vacuum of the squid chamber (~2-3 mbar) caused desolvation and the formation of **1a_d**, even in the presence of eicosane. The $\chi_M T$ product at 300 K of **1a**, **1a_d** and **1b** is slightly above the value of 11.475 cm^3 K mol^{-1} expected for each non-interacting Er^{III} ions ($^4I_{15/2}$, S = 3/2, L = 6, J = 15/2, g = 6/5). The $\chi_M T$ product shows a slow and steady decrease upon cooling from 300 K until 50 K, while after that a sharper decrease is observed until 2 K, where it reaches the value of 6.1 and 5.5 cm^{-3} K mol^{-1}, for **1a_d** and **1b**, respectively. The decrease at low temperature is characteristic for the depopulation of the Zeeman split Stark energy levels of the ground multiplet. The field dependence of magnetization was also measured in the 2-8 K temperature range by varying the magnetic field up to 5 T (**Figures S4.6-S4.7**).

To further understand the observed magnetic behaviour of both phases, theoretical calculations were carried out by using the SIMPRE computational package.[28] The static magnetic susceptibility was successfully fitted by using the Radial Effective Charge (REC) model[29] (D_r = 0.98 Å and Z_i = 0.161 for oxygens, and D_r = 1.20 Å and Z_i = 0.05 for nitrogen) (**Figure 4.8**). The predicted magnetization curves are also in good agreement with the experimental data (**Figure S4.6-4.7**). The diagonalization of the crystal field hamiltonian results in a ground state wave function mainly composed by 59% of the |±13/2> microstate in the easy axis direction for **1a** and **1b**, which is congruent with the observed slow relaxation of the magnetization (**Figure 4.8**). The first excited doublet is located at about 32 cm^{-1}, and is mainly composed by |±15/2> and

|±11/2> (63% between both of them). The energy levels are approximately equispaced and the total crystal field splitting reaches 354 cm^{-1}. In the case of the **1a_d**, the loss of a water molecule that reduces the coordination number results in a ground state wave function described by a mixture between |±9/2> (64%), |±11/2> (13%) and |±7/2> (11%) and the first excited energy level is placed at 42 cm^{-1}. Though the ground state is characterized by a lower M_J value than **1a**, most of the wave function is described by higher microstates, thus resulting in a more negligible mixing with lower microstates. This situation is more favourable to reduce quantum tunneling of magnetization at low temperatures. Moreover, the loss of a water molecule erases its molecular vibrations that can couple to spin states and promote magnetic relaxation.[36] The combination of both effects is compatible with the slight increase in the blocking temperature of **1a** after desolvation, as dynamic magnetic measurements indicate.

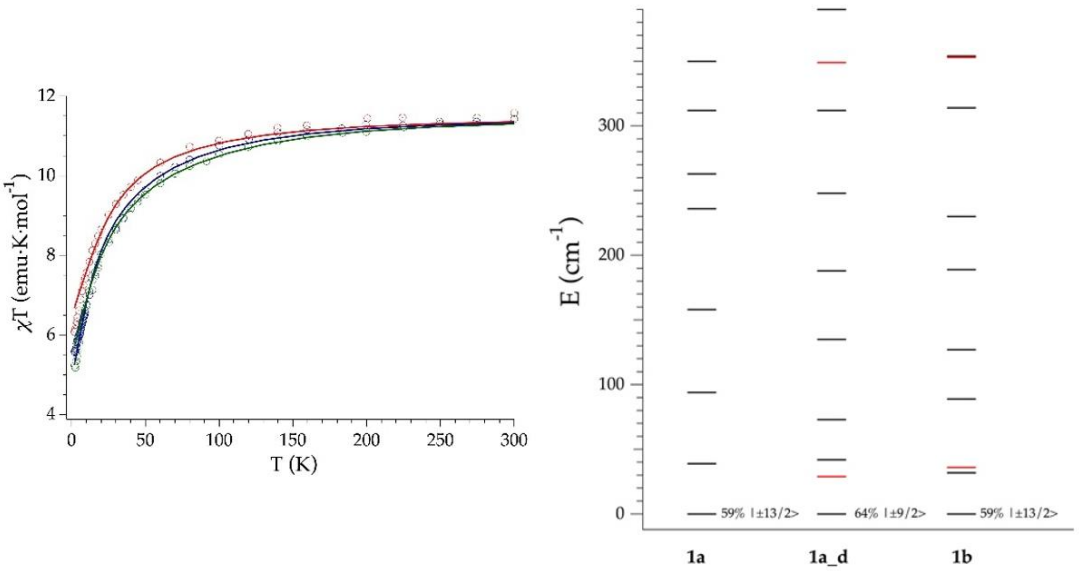

Figure 4.8. (left) Experimental (symbols), fitted (solid line) temperature-dependence of the magnetic susceptibility from 2 to 300 K of **1a** (green), **1a_d (red)** and **1b** (blue); (right) Calculated (black) and experimental (red) ground-*J* multiplet energy levels. Further details are provided in **Table S4.6** and **S4.7**.

The dynamic magnetic properties were studied by susceptibility measurements performed with an alternating magnetic field (AC susceptibility). In the absence of a magnetic field, no signal in the out of phase molar susceptibility (χ") is observed. When magnetic dc fields of 0.09 T for **1a** and 0.1 T for **1b** were applied, strong frequency-dependent peaks in both the in phase molar susceptibility (χ') and χ" appear with clear maxima of χ" below 2.2 K for **1a** and 4.2 K for **1b** (**Figures 4.9** and **4.10**). This is a clear indication that the two compounds present a field-induced slow relaxation of

magnetization. Interestingly, when **1a** is desolvated (**1a_d**) the χ" maxima are shifted to higher temperatures (3.6 K for **1a_d**, 2.2 K for **1a** at 10000 Hz under an applied dc field of 0.09 T, as shown in **Figures 4.9** and **4.11**. When the same desolvated sample is measured again in contact with H_2O, the initial magnetic behavior of **1a** is restored in a reversible way. This result confirms that the structural changes of **1a** after desolvation modify the magnetic properties in agreement with the decrease of the mixing with lower microstates found by theoretical calculation for **1a_d**.

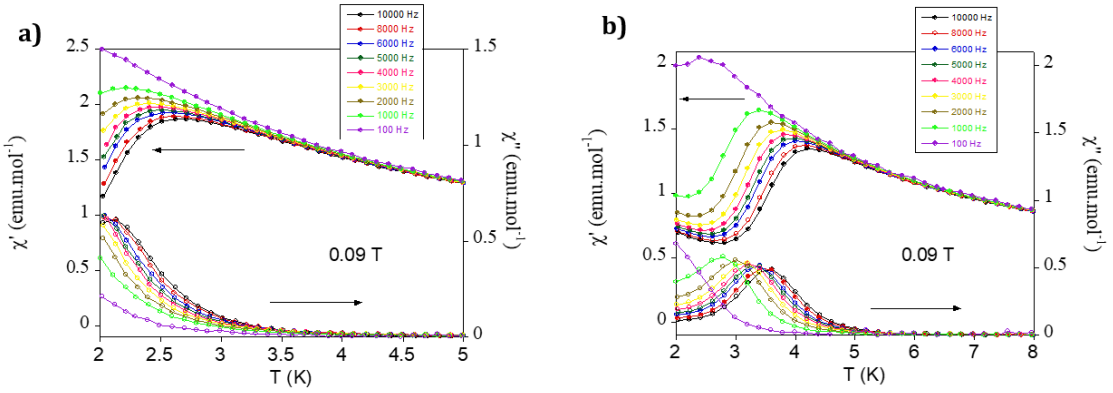

Figure 4.9. Temperature dependence of χ' and χ" of **1a** (a) and **1a_d** (b) in an applied dc field of 0.09 T at frequencies in the range 100 to 10000 Hz.

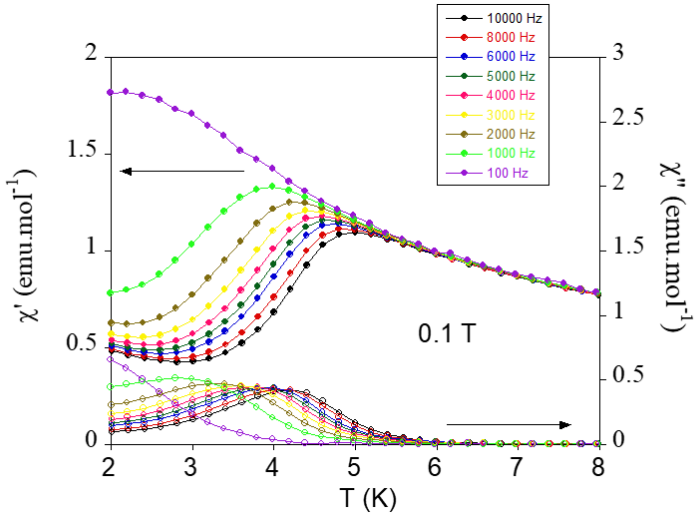

Figure 4.10. Temperature dependence of χ' and χ" of **1b** in an applied dc field of 0.09 T at frequencies in the range 100 to 10000 Hz.

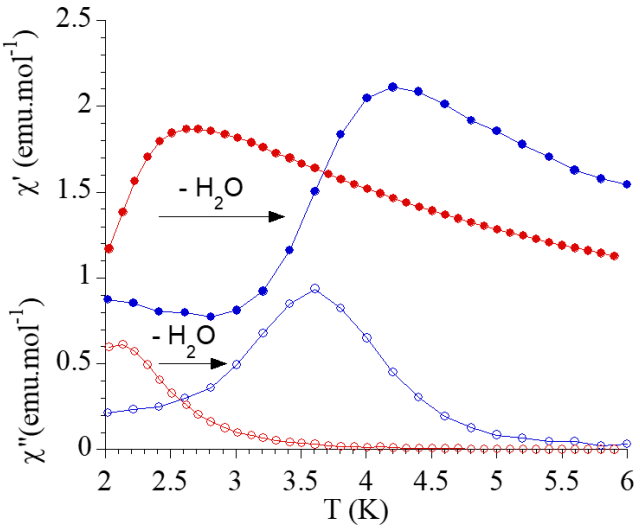

Figure 4.11. Temperature dependence of χ' and χ'' of **1a** (full and empty red circles, respectively) and **1a_d** (full and empty blue circles, respectively)) in an applied dc field of 0.09 T at 10000 Hz.

The relaxation times (τ) of **1a_d** and **1b** were determined from the maximum of χ'' at a given frequency ($\tau = 1/2\pi\nu$). They were fitted to the Arrhenius expression for a thermally activated process (Orbach, $\tau = \tau_0 \exp(U_{eff}/k_B T)$) leading to $\tau_0 = 1.2\times10^{-9}$ s and U_{eff} = 23.5 K at 0.09 T for **1a_d** and $\tau_0 = 1.9\times10^{-8}$ s and U_{eff} = 19.7 K at 0.1 T for **1b**. However, the plots of τ vs. $1/T$ deviate from linearity at low temperatures indicating the coexistence of multiple relaxation pathways as observed in other anilate-based lanthanide complexes. We, therefore, applied the general model where the first, second, third and fourth terms include quantum tunneling, direct, Raman and Orbach relaxation processes, respectively.

$$\tau^{-1} = \tau_{QTM}^{-1} + AH^2T + CT^n + \tau_0^{-1}\exp(-U_{eff}/K_BT)$$

Since the data were obtained at optimal fields of 0.09 (**1a_d**) and 0.1 (**1b**) mT, quantum tunneling and direct terms were excluded. Thus, correct fittings were obtained using Raman and Orbach relaxation processes with values comparable to those found in other anilate-based Ln^{III} compounds with C = 30.4 $s^{-1}K^{-4.3}$, τ_0 = 5.1 10^{-10} s and U_{eff} = 37.2 K for **1a_d** and C = 58.9 $s^{-1}K^{-4.2}$, τ_0 = 6.3 10^{-10} s and U_{eff} = 44.6 K for **1b**.[16,20,37,38] The calculated values of n (4.3 for **1a_d** and 4.2 for **1b**) are smaller than the ideal value of 9 found for Raman processes. This suggests that these Raman-like relaxations are attributed to acoustic and optical vibrations.[39] Finally, temperature dependence of τ values of **1a** was not fitted because only three data points with a maximum of χ'' are observed. The variable-frequency

AC data at different temperatures of **1a_d** and **1b** show a single relaxation with maxima at 5800 Hz (**1a**), 170 Hz (**1a_d**) and 160 Hz (**1b**) at 2 K (see **Figures S4.10, S4.12** and **S4.13**). The Cole–Cole plots (χ" vs. χ') of the two samples confirm the presence of a single relaxation process (see **Figures S4.14**). Thus, at fixed temperatures between 2.0 and 3.5 K for **1a_d** and 2.0 and 4.0 K for **1b**, semi-circular plots were obtained and fitted using a generalized Debye model, yielding α parameter in the range of 0.17-0.40 (**1a_d**) and 0.12-0.21 (**1b**). This indicates narrow distributions of the relaxation processes. In the case of **1a**, only one temperature could be studied due the lower temperature of the maxima in χ". Again, the Cole-Cole plot at this temperature suggests the presence of a single relaxation process (α = 0.31)

3.5 Photoluminescence Properties

Photoluminescence (PL) of **1a**, **1a_d** and **1b** was photoexcited by short laser pulses at a wavelength of 355 nm and analysed both spectrally and temporally. Near UV laser irradiation photoexcites the trz_2An linker dianion in all compounds. Er^{III} emission sensitization then occurs *via* the optical antenna effect through a ligand-to-metal energy relaxation pathway. As clearly seen in **Figure 4.12a**, ligand-centred emission of **1a** and **1b** measured in standard conditions appeared considerably redshifted and quenched with respect to that of the ligand dianion (trz_2An) in the $(Ph_4P)_2trz_2An$ reference compound. This was rationalized as the consequence of strong singlet/triplet intersystem mixing (heavy-atom effect), ensuing a ligand-centred excited state that quickly relaxes toward the lanthanide ion by ligand-to-metal energy transfer.[40] In fact, as deduced by three exponential fitting of the PL decay profile and amplitude averaging of the time constants, the bare excited-state lifetime of trz_2An measured in $(Ph_4P)_2(trz_2An)$ lies in the time scale of hundreds of picoseconds (~460 ps, **Figure 4.12b**), whereas the ligand-centred emission of **1a** and **1b** is nearly resolution-limited (see the impulse response function (IRF) of the detection system, **Figure 4.12b,c**). A monoexponential lifetime of ~30 ps (**Figure 4.12c**) could be inferred for **1b**, hinting to a quantitative ligand-to-metal energy sensitization with nearly unity efficiency in both compounds. At room temperature (295K), **1a** and **1a_d** exhibited different Er^{III}-centred ($J = 13/2 \rightarrow 15/2$) emission spectra, readily interpreted as a consequence of the different coordination environment experienced by Er^{III} in the two compounds (**Figure 4.13a**). Cooling **1a_d** under vacuum conditions down to 77K resulted in higher spectral

definition of the crystal-field-split J = 13/2 → 15/2 optical transitions (**Figure 4.13b**). Up to 13 transitions could be clearly detected and fairly well fitted using a multiple Gaussian fit procedure, thereby demonstrating a non-negligible presence of hot transitions (starting from higher energy states of the J = 13/2 multiplet) still a 77K. A direct comparison between the emission spectra at 295 and 77K allowed for a tentative identification of the zero-line (ZL) transition, which was placed at 1529 nm. In turn, this enabled a direct comparison between the observed transition wavelengths and those inferred from the theoretically calculated energy spectrum of the J = 15/2 multiplet. Despite the strong vibrational quenching of the Er^{III} emission acted by coordinated water molecules, effectively reducing the lanthanide excited-state lifetime from milliseconds to tens of nanoseconds,[41] **1a** and **1a_d** could be quite clearly distinguished on the basis of their decay profiles, being the amplitude-averaged lifetime (extracted from biexponential fits) 55 ns in **1a** and 86 ns in **1a_d** (**Figure 4.13c**). This was ascribed to the different quenching produced by two coordinated water molecules in **1a** and only one water molecule in **1a_d**. Upon cooling at 77K, the PL lifetime of **1a_d** increased by approximately a factor of two possibly due to partial suppression of vibrational quenching. **1b** displayed practically the same room-temperature Er^{III}-centred NIR emission spectrum, both in air and under vacuum (**Figure 4.13d**), in agreement with the results of pXRD measurements and confirming the existence of only one phase. The decay profile of the NIR PL showed a much lower sensitivity to environmental conditions (**Figure 4.13f**), which was in part expected since in **1b** the vacuum does not modify the number of water molecules coordinated to the Er^{III} ions. Comparison of the 295 and 77K emission spectra (**Figure 4.13e**) led to the identification of the emission peak centred at 1524 nm as the most probable ZL transition in **1b**, allowing for comparing experiment and theory just as for **1a_d**.

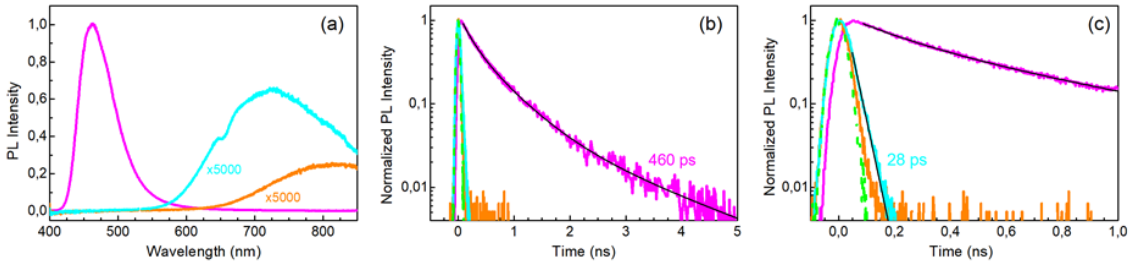

Figure 4.12. Ligand-centered photoluminescence properties of **1a**, **1a_d** and **1b** under 355-nm pulsed laser irradiance. (a) Ligand-centered PL spectra acquired in standard conditions and normalized to the peak of the spectrum of the reference ligand crystal $(Ph_4P)_2trz_2An$. PL intensity of **1a** and **1b** are

multiplied by a factor 5000. (b) Spectrally-integrated ligand-centered PL decay transients. The impulse response function (IRF) of the detection setup is also displayed. The fit of a three exponential decay curve to the $(Ph_4P)_2trz_2An$ decay is shown and the amplitude-average lifetime is indicated. (c) Same as (b) but on a shorter time scale to highlight the ultrafast PL response of **1a** and **1b**. Monoexponential fit of the **1b** decay is shown together with the characteristic time.

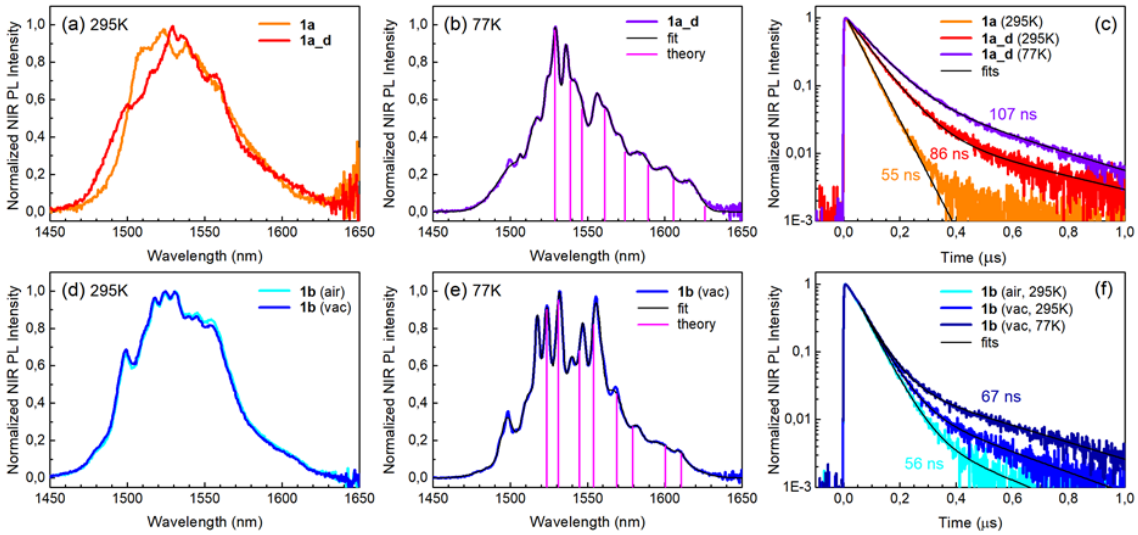

Figure 4.13. Lanthanide-centered photoluminescence properties of **1a**, **1a_d** and **1b**. (a) Er^{III}-centered PL spectra of **1a** and **1a_d** at room temperature. (b) Low-temperature (77K) spectrum of **1a_d** with multiple Gaussian fit. Vertical bars represent the radiative transitions from the J = 13/2 lowest level to the ground (J = 15/2) multiplet levels estimated from theoretical calculations. (c) Er^{III}-centered PL decay transients for **1a** and **1a_d** at room temperature and at 77K. Biexponential fits and amplitude-averaged lifetimes are shown as well. (d) Same as (a) but for **1b**, measured both in air and under vacuum. (e) Same as (b) but for **1b** under vacuum. (f) Same as (c) but for **1b**.

Reversible phase transition from **1a** to **1a_d** was confirmed spectroscopically by performing several air/vacuum (rehydration/dehydration) cycles, where highly reproducible emission spectra and decay transients were obtained (see **Figure S4.15**). Overall, theoretical calculations of the ground (J = 15/2) multiplet spectra turned out to be consistent with the low-temperature emission spectra, as regards both the energy splitting between the first two levels and the whole energy spread within the multiplet. The agreement is quite impressive for **1b**, as clearly seen in **Figure 4.13e**.

4. Conclusions

The H_2trz_2An anilate derivative, bearing a triazole pendant arm at the 3,6 position of the anilato moiety, has been used for the first time in combination with Er^{III} nodes to afford **1a** and **1b** 3D CFs formed by 2D layers with (6,3) topology linked through the anilato ligands. A remarkable difference with respect to previous Ln^{III} anilato-based compounds is that these 2D layers are interconnected through the N4 atoms of the two 1,2,4-triazole substituted pendant arms of trz_2An, leading to formation of 3D frameworks. **1a** and **1b** constitute unique examples of multifunctional CFs as they display NIR emission and field induced slow relaxation of the magnetization. To the best of our knowledge, this is the first report of an anilate-based Er^{III}–MOF that show SIM behaviour. Remarkably, the flexibility and porosity of **1a** MOF, enables drastic structural changes after partial dehydration at very mild conditions (vacuum or heating to 360 K) to a less porous 3D structure in **1a_d**. This partially dehydrated compound shows an increase in the emission intensity and an improvement of the magnetic blocking temperature with respect to the hydrated compound, which are mainly related to the loss of one water coordination molecule. Theoretical calculations evidence that the slight improvement of SIM properties is related to the combination of the decrease of mixing with lower microstates, which reduce quantum tunneling of magnetization at low temperatures, and the loss of a water molecule, which promote magnetic relaxation by erasing its molecular vibrations which can couple to spin states.

Interestingly, the structure, as well as the luminescent and magnetic properties, of **1a** are fully regenerated by simply exposure to air of the crystals of **1a_d**. The present work contribute to the ongoing research on flexible MOFs and shed light on the important role of Luminescence Spectroscopy and Magnetometry as probes for mechanism investigation of flexible Ln-MOFs and to confirm reversibility of the observed phase transition from **1a** to **1a_d**, through several air/vacuum (rehydration/dehydration) cycles, where highly reproducible emission spectra and decay transients were obtained.

References

1 H. C. Zhou, J. R. Long and O. M. Yaghi, *Chem. Rev.*, 2012, **112**, 673–674.

2 H. C. J. Zhou and S. Kitagawa, *Chem. Soc. Rev.*, 2014, 43, 5415–5418.

3 Z. Chang, D. H. Yang, J. Xu, T. L. Hu and X. H. Bu, *Adv. Mater.*, 2015, **27**, 5432–5441.

4 A. Ghoufi, K. Benhamed, L. Boukli-Hacene and G. Maurin, *ACS Cent. Sci.*, 2017, **3**, 394–398.

5 A. Ghoufi, A. Subercaze, Q. Ma, P. G. Yot, Y. Ke, I. Puente-Orench, T. Devic, V. Guillerm, C. Zhong, C. Serre, G. Férey and G. Maurin, *J. Phys. Chem. C*, 2012, **116**, 13289–13295.

6 J. Y. Kim, L. Zhang, R. Balderas-Xicohténcatl, J. Park, M. Hirscher, H. R. Moon and H. Oh, *J. Am. Chem. Soc.*, 2017, **139**, 17743–17746.

7 F. X. Coudert, *Chem. Mater.*, 2015, **27**, 1905–1916.

8 S. M. Hyun, J. H. Lee, G. Y. Jung, Y. K. Kim, T. K. Kim, S. Jeoung, S. K. Kwak, D. Moon and H. R. Moon, *Inorg. Chem.*, 2016, **55**, 1920–1925.

9 S. V. Eliseeva and J. C. G. Bünzli, *Chem. Soc. Rev.*, 2010, **39**, 189–227.

10 L. Sorace, C. Benelli and D. Gatteschi, *Chem. Soc. Rev.*, 2011, **40**, 3092–3104.

11 L. H. G. Kalinke, D. Cangussu, M. Mon, R. Bruno, E. Tiburcio, F. Lloret, D. Armentano, E. Pardo and J. Ferrando-Soria, *Inorg. Chem.*, 2019, **58**, 14498–14506.

12 J. J. Baldoví, E. Coronado, A. Gaita-ariço, C. Gamer, M. Giménez-Marqués and G. Mínguez, *Chem. Eur. J.*, 2014, **20**, 10695–10702.

13 S. Ashoka Sahadevan, N. Monni, A. Abhervé, D. Marongiu, V. Sarritzu, N. Sestu, M. Saba, A. Mura, G. Bongiovanni, C. Cannas, F. Quochi, N. Avarvari and M. L. Mercuri, *Chem. Mater.*, 2018, **30**, 6575–6586.

14 S. Ashoka Sahadevan, N. Monni, M. Oggianu, A. Abhervé;, D. Marongiu, M. Saba, A. Mura, G. Bongiovanni, V. Mameli, C. Cannas, N. Avarvari, F. Quochi and M. L. Mercuri, *ACS Appl. Nano Mater.*, 2020, **3**, 94–104.

15 S. Benmansour, A. Hernández-Paredes, M. Bayona-Andrés and C. J. Gómez-García, *Molecules*, 2021, **26**, 1–21.

16 S. Benmansour, A. Hernández-Paredes, A. Mondal, G. López Martínez, J. Canet-Ferrer, S. Konar and C. J. Gómez-García, *Chem. Commun.*, 2020, **56**, 9862–9865.

17 K. Nakabayashi and S. Ohkoshi, *Inorg. Chem.*, 2009, **48**, 8647–8649.

18 B. F. Abrahams, J. Coleiro, K. Ha, B. F. Hoskins, S. D. Orchard and R. Robson, *J. Chem. Soc. Dalt. Trans.*, 2002, **2**, 1586–1594.

19 K. Bondaruk and C. Hua, *Cryst. Growth Des.*, 2019, **19**, 3338–3347.

20 A. Mondal, S. Roy and S. Konar, *Chem. Eur. J.*, 2020, **26**, 8774–8783.

21 S. Benmansour and C. J. Gómez-García, *Magnetochemistry*, 2020, **6**, 1–44.

22 W. Gauβ, H. Heitzer and S. Petersen, *Justus Liebigs Ann. Chem.*, 1973, **764**, 131–144.

23 C. J. Kingsbury, B. F. Abrahams and R. Robson, *CCDC 1568063 Exp. Cryst. Struct. Determ.*

24 N. N. Monni, E. Andres-Garcia, K. Caamaño, V. García-López, J. M. Clemente Juan, M. Giménez-Marqués, M. M. Oggianu, E. Cadoni, G. Minguez Espallargas, M. Clemente Leon, M. L. Mercuri and E. Coronado, *J. Mater. Chem. A*, 2021, **9**, 25189-25195 .

25 G. M. Sheldrick, *Acta Crystallogr. Sect. A Found. Crystallogr.*, 2015, **71**, 3–8.

26 G. M. Sheldrick, *Acta Crystallogr. Sect. C Struct. Chem.*, 2015, **71**, 3–8.

27 O. V. Dolomanov, L. J. Bourhis, R. J. Gildea, J. A. K. Howard and H. Puschmann, *J. Appl. Crystallogr.*, 2009, **42**, 339–341.

28 J. J. Baldoví, S. Cardona-Serra, J. M. Clemente-Juan, E. Coronado, A. Gaita-Ariño and A. Palii, *J. Comput. Chem.*, 2013, **34**, 1961–1967.

29 J. J. Baldoví, J. J. Borrás-Almenar, J. M. Clemente-Juan, E. Coronado and A. Gaita-Ariño, *Dalt. Trans.*, 2012, **41**, 13705–13710.

30 J. van Leusen, M. Speldrich, H. Schilder and P. Kögerler, *Coord. Chem. Rev.*, 2015, **289**–**290**, 137–148.

31 M. Speldrich, H. Schilder, H. Lueken and P. Kögerler, *Isr. J. Chem.*, 2011, **51**, 215–227.

32 M. Llunell, D. Casanova, J. Cirera, P. Alemany and S. Alvarez, *Univ. Barcelona Barcelona, Spain*.

33 M. P. Van Koeverden, B. F. Abrahams, D. M. D'Alessandro, P. W. Doheny, C. Hua, T. A. Hudson, G. N. L. Jameson, K. S. Murray, W. Phonsri, R. Robson and A. L. Sutton, *Chem. Mater.*, 2020, **32**, 7551–7563.

34 S. Benmansour, I. Pérez-Herráez, C. Cerezo-Navarrete, G. López-Martínez, C. Martínez Hernández and C. J. Gómez-García, *Dalt. Trans.*, 2018, **47**, 6729–6741.

35 M. Souto, J. Romero, J. Calbo, I. J. Vitórica-Yrezábal, J. L. Zafra, J. Casado, E. Ortí, A. Walsh and G. Mínguez Espallargas, *J. Am. Chem. Soc.*, 2018, **140**, 10562–10569.

36 L. Escalera-Moreno, J. J. Baldoví, A. Gaita-Ariño and E. Coronado, *Chem. Sci.*, 2018, **9**, 3265–3275.

37 W. R. Reed, M. A. Dunstan, R. W. Gable, W. Phonsri, K. S. Murray, R. A. Mole and C. Boskovic, *Dalton. Trans.*, 2019, **48**, 15635–15645.

38 P. Zhang, M. Perfetti, M. Kern, P. P. Hallmen, L. Ungur, S. Lenz, M. R. Ringenberg, W. Frey, H. Stoll, G. Rauhut and J. Van Slageren, *Chem. Sci.*, 2018, **9**, 1221–1230.

39 R. Ishikawa, S. Michiwaki, T. Noda, K. Katoh, M. Yamashita and S. Kawata, *Magnetochemistry*, 2019, **5**, 30.

40 F. Quochi, M. Saba, F. Artizzu, M. L. Mercuri, P. Deplano, A. Mura and G. Bongiovanni, *J. Phys. Chem. Lett.*, 2010, **1**, 2733–2737.

41 F. Artizzu, L. Marchiò, M. L. Mercuri, L. Pilia, A. Serpe, F. Quochi, R. Orrù, F. Cordella, M. Saba, A. Mura, G. Bongiovanni and P. Deplano, *Adv. Funct. Mater.*, 2007, **17**, 2365–2376.

Chapter 5

A Novel Family of 3D Ln-CFs based on 3,6-ditriazolyl-2,5-dihydroxybenzoquinone

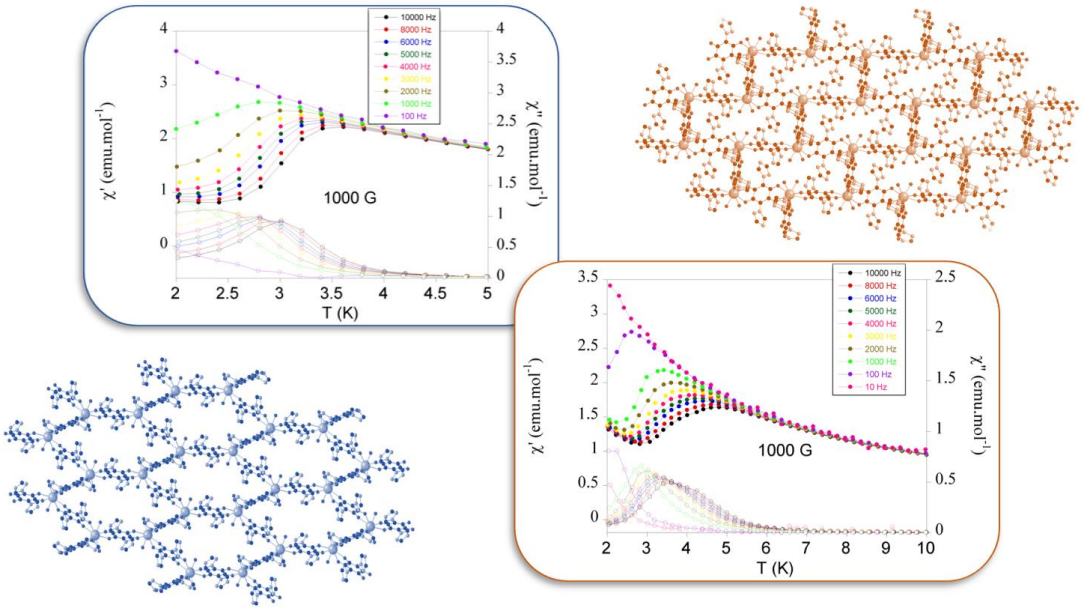

Abstract

The potential of 3,6-ditriazolyl-2,5-dihydroxybenzoquinone (H_2trz_2An) as valuable linker for the most used Ln^{III} ions for SMMs/SIMs (Ln^{III} = Dy, Tb, Ho) has been herein explored. With all aforementioned Ln^{III} ions, two different series of polymorphs, formulated as $[Ln_2(trz_2An)_3(H_2O)_4]_n \cdot 10H_2O$ (Dy^{III}, **1a**; Tb^{III}, **2a**, Ho^{III}, **3a**) and $[Ln_2(trz_2An)_3(H_2O)_4]_n \cdot 7H_2O$ (Dy^{III}, **1b**, Tb^{III}, **2b**, Ho^{III}, **3b**) have been obtained, both isostructural to the previously reported Er^{III}-CFs (see *Chapter 4*). **1-3a** MOFs show reversible structural flexibility as observed in Er^{III}-MOF, involving shrinkage/expansion of the hexagonal-rectangular cavities, upon removal of a coordinated water molecule. In these series only the two Dy^{III}-CFs (**1a** and **1b**) and the phase b of Tb^{III}-CP (**2b**) show a Single Ion Magnet (SIM) behavior, but SIM properties do not be affected by the flexibility of the frameworks. Interestingly, **2b** exhibits the best SIM properties within the series, showing an increase of the blocking temperature respect to **1a**, **1b** and Er^{III}-CFs. Theoretical calculations are still in progress to shed light on their dynamic behavior and to investigate the involved mechanism in the flexibility in order to understand the intriguing results herein presented.

1. Introduction

Since the discovery of the first molecular transition metal coordination compound that could retain for long time its magnetization in the absence of an external magnetic field, at liquid-helium temperatures, a great enthusiasm led researchers to explore such of new materials, defined as Single Molecule Magnets (SMMs).[1] SMMs are usually formed by clusters of transition metal ions (both *3d* and *4f*) linked through organic molecules, but when a SMM only contains one spin center it is defined as Single Ion Magnet (SIM). The fascinating physical behavior of SMMs/SIMs have aroused an huge interest in developing new technological applications.[2–5] Such systems can be defined as the molecular analogues of conventional ferromagnets, thus they can be employed in intriguing applications spanning from storage to processing of digital information. Thanks to their molecular nature, they can in principle open up the possibility to store information with much higher densities, that can processed at unprecedented speeds.[2,6,7] Clearly, one of the most ambitious challenges in this field still remains the design and fabrication of efficient SMMs/SIMs that operate in a temperature range suitable for practical use. There are some parameters that characterize the efficiency of SMMs/SIMs systems. First, the magnetic blocking temperature, T_B, defined as the highest temperature at which a SMM displays hysteresis in magnetization (M) vs magnetic field (H) plots. The T_B is strongly dependent on the sweep rate of the magnetic field and on the characterization technique used for the measurements, thus is not the best parameter for evaluating the quality of a SMM/SIM.[2] The coercive magnetic field, H_C, described as the magnetic field needed to turn to zero the magnetization of a SMM/SIM, after reaching the saturation magnetization, is the second parameter to take into account. The third and most used parameter is the effective energy barrier to turnaround the magnetization (anisotropy barrier), U_{eff}, hence can be defined as the energy required to convert a SMM/SIM into a paramagnet. As said earlier, SMMs/SIMs systems are able to retain their spin orientation and to exhibit a slow relaxation of the magnetization at low temperatures, by following different mechanisms:*(i)* Orbach (O), *(ii)* Raman (R), *(iii)* direct (D) and *(iv)* quantum tunnelling (QT). The O, R and D mechanisms are temperature dependent whereas the D and QT mechanisms are field dependent.[8–10] In most of the cases, different mechanism are involved, therefore the relaxation time is determined by the faster process. QT mechanism is present at low temperatures in absence of DC field, whereas at high temperatures dominates the Orbach mechanism. When a DC field is applied to suppress the fast relaxation through the QT mechanism in order to observe the slow relaxation of the

magnetization, the compounds are called field-induced-SMM of field induced-SIM (FI-SMM or FI-SIM).[11]

As previously defined, SMMs and SIMs are usually clusters or molecular complexes, but since the outstanding growth of the reticular chemistry, CPs and MOFs are also included in this field. Thus, to design a CFs-based SMM/SIM, the choice of the organic linker and metal ion is crucial. In fact, to be a SMM/SIM, a system must have a bistable electronic ground state and magnetic anisotropy must be present. Taking into account these prerequisites, some of the lanthanide ions are the optimal candidates to construct a SMM/SIM since they can have *i)* ground electronic terms, *ii)* large and unquenched orbital contributions to the magnetic moment, and *iii)* ligand field effects in their related complexes that can be regarded as a small-but-significant perturbation.[2] Hence, the most commonly used ions in SMMs/SIMs are Tb^{III}, Dy^{III}, Er^{III} and Ho^{III}. Particularly, Tb^{III} and Dy^{III} are the first choice since their electronic structure possess large anisotropy, due to the strong angular dependence of the *4f* orbitals. Regarding the selection of the organic linker, among the many different class of molecules that can be used to construct such systems, very recently the anilate derivatives (3,6-disubstituted-2,5-dihydroxy-1,4-benzoquinone) have been exploited as molecular building blocks for Ln-based materials since their capability to act as suitable *antennae* towards NIR-emitting lanthanide ions[12,13] and/or to isolate the lanthanide ions magnetically, favoring the formation of SIMs/SMMs due to the prevention of the fast relaxation of magnetization.[11] The first Ln-anilato complexes behaving as SMMs were reported by Boskovic *et al*. in 2017,[14] which present two Dy^{III}-based dimers formulated as $[(Tp)_2Dy_2(Cl_2An)]\cdot 2CH_2Cl_2$ and $[(Tp)_2Dy_2((CH_3)_2An)]\cdot 1.1CH_2Cl_2$ (Tp^-= hydrotris(pyrazolyl)borate). Both compounds show slow relaxation of the magnetization with an Orbach and Raman relaxation mechanisms for $[(Tp)_2Dy_2(Cl_2An)]\cdot 2CH_2Cl_2$ (U_{eff} = 24 K) and a FI-SMM behavior and an Orbach mechanism for $[(Tp)_2Dy_2((CH_3)_2An)]\cdot 1.1CH_2Cl_2$ (U_{eff} = 47 K). After that, different anilato-based SMMs/SIMs have been reported and thoroughly described by Benmansour and Gomez-Garcia.[11]

In this Chapter, we aim to explore the 3,6-ditriazolyl-anilate derivative (H_2trz_2An) as linker with the most used Ln^{III} ions in SMMs/SIMs, particularly Dy^{III}, Tb^{III} and Ho^{III}, as a progress of the previous work with Er^{III}-based CFs (reported in *Chapter 4*). For all Ln^{III} used, two different series were obtained and formulated as $[Ln_2(trz_2An)_3(H_2O)_4]_n\cdot 10H_2O$ (Ln^{III}=Dy (**1a**), Tb (**2a**), Ho (**3a**)) and $[Ln_2(trz_2An)_3(H_2O)_4]_n\cdot 7H_2O$ ((Ln^{III}=Dy (**1b**), Tb (**2b**), Ho (**3b**)). All the compounds were structurally characterized, showing the

previously observed reversible structural flexibility, and magnetically characterized, showing in the case of **1a**, **1b** and **2b** SIM behavior, further investigated with theoretical calculations.

2. Experimental Section

2.1. General Remarks

The lanthanides precursors, NaOH in pellets and the solvents used were purchased from AlfaAesar and Exacta Optech and used without further purification. Synthesis of ligand H_2trz_2An was performed as reported in chapter 1, according with literature.[15] Elemental analyses (C, H, and N) were performed with a CE Instruments EA 1110 CHNS.

2.2. Synthesis

$[Ln_2(trz_2An)_3(H_2O)_4]_n \cdot 10H_2O$ (Ln^{III} = Dy (1a), Tb (2a), Ho (3a)) and $[Ln_2(trz_2An)_3(H_2O)_4]_n \cdot 7H_2O$ (Ln^{III} = Dy (1b), Tb (2b), Ho (3b)). These series were prepared by using the same synthetic procedure for Er^{III}-CFs, reported in *Chapter 4*, with $Ln(NO_3)_3 \cdot 6H_2O$ (0.05 mmol; 17.4 (**1**), 22.6 (**2**), 18.9 (**3**)) H_2trz_2An (0.05 mmol, 13.7 mg) as metal precursors. As for Er^{III}-CFs, two different types of crystals were obtained from the same batch, dark red-block crystals (phase a) and orange prismatic crystals (phase b), both of them suitable for SC-XRD measurements. Their density's difference was exploited to separate them, using CH_2Cl_2/CH_2Br_2 solvent mixture in the ratio 0.925/0.975, for all further measurements.

$[Ln_2(trz_2An)_3(H_2O)_2]_n$ (Ln = Dy (1a_d), Tb (2a_d), Ho (3a_d)). Polycrystalline powders of **1-3a** were placed under vacuum in a vacuum line pump and then sealed in a glove box to obtain the dehydrated phase **a_d**.

Table 5.1. Elemental analysis for all the compounds **1-3a** and **1-3b**.

		Calculated			Found		
		%C	**%H**	**%N**	**%C**	**%H**	**%N**
1a	$C_{30}H_{40}N_{18}O_{26}Dy_2$	25.85	2.89	18.09	25.39	2.80	18.12
1b	$C_{30}H_{34}N_{18}O_{23}Dy_2$	26.90	2.56	18.81	26.54	2.36	17.47
2a	$C_{30}H_{40}N_{18}O_{26}Tb_2$	25.99	2.91	18.18	25.85	2.75	18.23
2b	$C_{30}H_{34}N_{18}O_{23}Tb_2$	27.04	2.57	18.92	25.52	2.27	19.41
3a	$C_{30}H_{40}N_{18}O_{26}Ho_2$	25.76	2.88	18.03	25.79	2.67	18.10
3b	$C_{30}H_{34}N_{18}O_{23}Ho_2$	26.80	2.55	18.75	26.93	2.33	19.11

2.3. Physical Measurements

X-Ray Crystallography. Single crystal X-Ray diffraction was performed on **1-3a** and **1-3b** crystals, which were mounted on a glass fiber using a viscous hydrocarbon oil to coat the single crystal and then transferred directly to the cold nitrogen stream for data collection. X ray data were collected at 120 K for all the samples. Measurements were performed on a Supernova diffractometer equipped with a graphite-monochromated Enhance (Mo) X-ray Source (λ = 0.710 73 Å). The program CrysAlisPro, Oxford Diffraction Ltd., was used for unit cell determinations and data reduction. Empirical absorption correction was performed using spherical harmonics, implemented in the SCALE3 ABSPACK scaling algorithm. The structures were solved with the ShelXT structure solution program[16] and refined with the SHELXL-2013 program,[17] using Olex2.[18] Non-hydrogen atoms were refined anisotropically, and hydrogen atoms were placed in calculated positions refined using idealized geometries (riding model) and assigned fixed isotropic displacement parameters. Crystallographic data of all the compounds are summarized in **Table 5.2** and **Table 5.3**.

All Powder X-ray diffraction patterns were performed using a 0.7 mm glass capillary filled with polycrystalline samples of the compounds and mounted and aligned on an Empyrean PANalytical powder diffractometer, using Cu Kα radiation (λ = 1.541 77 Å). A total of three scans were collected for each compound at room temperature in the 2θ range of 5−40°. Polycrystalline samples of **1-3a** were further placed under vacuum in a vacuum line pump and were then opened in the glove box to be sealed in the 0.7 mm glass capillary.

Table 5.2. Crystallographic data for compounds **1-3a**.

	1a	**2a**	**3a**
Empirical formula	$C_{30}H_{38}N_{18}O_{25}Dy_2$	$C_{30}H_{38}N_{18}O_{25}Tb_2$	$C_{30}H_{38}N_{18}O_{25}Ho_2$
FW	1365.65	1358.50	1370.51
Crystal color	Dark Purple	Dark Purple	Dark Purple
Crystal size (mm^3)	0.22 × 0.16 × 0.13	0.17 × 0.14 × 0.11	0.2 × 0.16 × 0.08
Temperature (K)	120	120	120
Wavelength (Å)	(MoKa) λ = 0.71073	(MoKa) λ = 0.71073	(MoKa) λ = 0.71073
Crystal system	triclinic	triclinic	triclinic
Space group	*P-1*	*P-1*	*P-1*
a (Å)	8.9737 (4)	8.9903(4)	8.9571 (3)
b (Å)	9.4011 (4)	9.4164(4)	9.4084 (3)
c (Å)	15.5290 (6)	15.5861(6)	15.4980 (4)
α (°)	75.273 (4)	75.214(3)	75.173 (2)
β (°)	77.475 (4)	77.435(4)	77.349 (2)
γ (°)	68.042 (4)	68.017(4)	67.977 (3)
V ($Å^3$)	1164.23 (9)	1172.01(9)	1159.35 (7)
ρ_{calc} ($g.cm^{-3}$)	1.962	1.939	1.977
μ(MoKα) (mm^{-1})	3.293	3.100	3.496

2θ range (°)	6.516 to 56.212	6.514 to 55.868	6.626 to 54.962
Index ranges	$-11 \le h \le 11, -12 \le k \le 11, -20 \le l \le 19$	$-11 \le h \le 11, -12 \le k \le 11, -18 \le l \le 20$	$-10 \le h \le 11, -11 \le k \le 12, -20 \le l \le 19$
Reflections collected	17487	15479	16014
Independent reflections	4931 [R_{int} = 0.0259, R_{sigma} = 0.0264]	4908 [R_{int} = 0.0406, R_{sigma} = 0.0517]	4772 [R_{int} = 0.0238, R_{sigma} = 0.0218]
Data/restraints/parameters	4931/0/359	4908/0/384	4772/0/359
Goodness-of-fit on F2	1.070	1.054	1.033
Final R indexes [I>=2σ (I)]	R_1 = 0.0199 wR_2 = 0.0451	R_1 = 0.0290, wR_2 = 0.0562	R_1 = 0.0184 wR_2 = 0.0457
Final R indexes [all data]	R_1 = 0.0213 wR_2 = 0.0459	R_1 = 0.0355, wR_2 = 0.0602	R_1 = 0.0189 wR_2 = 0.0461
Largest diff.peak/hole/e Å^{-3}	0.90/-0.83	1.01/-0.80	0.80/-0.80

Table 5.3. Crystallographic data for compounds **1-3b**.

	1b	**2b**	**3b**
Empirical formula	$C_{30}H_{28}N_{18}O_{20}Dy_2$	$C_{30}H_{28}N_{18}O_{20}Tb_2$	$C_{30}H_{28}N_{18}O_{20}Ho_2$
FW	1285.65	1278.50	1290.51
Crystal color	Orange	Orange	Orange
Crystal size (mm^3)	0.14 × 0.09 × 0.08	0.16 × 0.14 × 0.07	0.29 × 0.13 × 0.09
Temperature (K)	120	120	120
Wavelength (Å)	(MoKa) λ = 0.71073	(MoKa) λ = 0.71073	(MoKa) λ = 0.71073
Crystal system	triclinic	triclinic	triclinic
Space group	*P-1*	*P-1*	*P-1*
a (Å)	8.6480 (4)	8.6577(2)	8.6344 (2)
b (Å)	10.4211 (5)	10.4166(3)	10.4202 (2)
c (Å)	12.0603 (6)	12.0856(4)	12.0281 (3)
α (°)	80.197 (4)	80.206(2)	80.171 (2)
β (°)	79.454 (4)	79.607(2)	79.315 (2)
γ (°)	82.476 (4)	82.473(2)	82.353 (2)
V (Å^3)	1047.33 (9)	1050.75(5)	1042.06 (4)
ρ_{calc} (g.cm^{-3})	2.038	2.021	2.057
μ(MoKα) (mm^{-1})	3.644	3.442	3.874
2θ range (°)	6.564 to 60.882	6.56 to 61.078	6.974 to 60.86
Index ranges	$-12 \le h \le 12, -14 \le k \le 14, -16 \le l \le 16$	$-11 \le h \le 12, -13 \le k \le 14, -16 \le l \le 16$	$-12 \le h \le 12, -14 \le k \le 14, -16 \le l \le 16$
Reflections collected	17270	20971	20633
Independent reflections	5565 [R_{int} = 0.0503, R_{sigma} = 0.0609]	5718 [R_{int} = 0.0316, R_{sigma} = 0.0325]	5678 [R_{int} = 0.0255, R_{sigma} = 0.0247]
Data/restraints/parameters	5565/0/324	5718/0/324	5678/0/324
Goodness-of-fit on F2	1.052	1.065	1.060
Final R indexes [I>=2σ (I)]	R_1 = 0.0312, wR_2 = 0.0550	R_1 = 0.0201, wR_2 = 0.0441	R_1 = 0.0166, wR_2 = 0.0366
Final R indexes [all data]	R_1 = 0.0385, wR_2 = 0.0592	R_1 = 0.0221, wR_2 = 0.0454	R_1 = 0.0175, wR_2 = 0.0370
Largest diff. peak/hole/eÅ^{-3}	0.86/-0.95	0.92/-0.74	0.74/-0.69

Infrared Spectroscopy. FT-IR spectra were collected using a Bruker Equinox 55 spectrometer, on KBr pellets.

Magnetic Measurements. Magnetic measurements were performed with Quantum Design MPMS-XL-5 SQUID and PPMS-9 magnetometers in the 2−300 K temperature range with an applied magnetic field of 0.1 T at a scan rate of 2 K min^{-1}. In the case of **1a**, it was necessary to protect the sample covering it with H_2O since the vacuum of the squid chamber caused desolvation and the formation of **1a_d**.

Theoretical Calculations. SIMPRE computational package[19] was used, by introducing the crystallographic atomic coordinates and the experimental magnetic properties of the compounds as an input. In order to fit the experimental data, two parameters (D_r and Z_i) of the REC model were varied for each type of donor atom of the first coordination sphere.[20] The electronic structure of the excited energy multiplets have been determined by using the full hamiltonian[21] in the CONDON package.[22]

3. Results and Discussion

3.1. Synthesis

Ln-based magnetic CFs (**1-3a** and **1-3b**) were obtained by combining $Ln(NO_3)_3 \cdot xH_2O$ with H_2trz_2An in 1:1 ratio, *via* the hydrothermal method, following the same synthetic strategy reported in Chapter 4 (**Scheme 5.1**). As for Er^{III}, each batch gave two types of crystals which correspond to the two different phases previously reported and formulated as $[Ln_2(trz_2An)_3(H_2O)_4]_n \cdot 10H_2O$ (Ln^{III} = Dy (**1a**), Tb (**2a**), Ho (**3a**)), dark red blocks crystals, and $[Ln_2(trz_2An)_3(H_2O)_4]_n \cdot 7H_2O$ (Ln^{III} = Dy (**1b**), Tb (**2b**), Ho (**3b**)), orange prismatic crystals. As reported in *Chapter 4*, it was possible to use the CH_2Cl_2/CH_2Br_2 solvent mixture in the 0.925/0.975 ratio to separate the crystals of the different phases. Interestingly **1-3a** MOFs show a reversible structural flexibility. With the removal of water solvent from phase **a**, by heating the samples at 80°C or by applying vacuum, the reversible desolvated phase **a_d**, formulated as $[Ln_2(trz_2An)_3(H_2O)_2]_n$ was afforded.

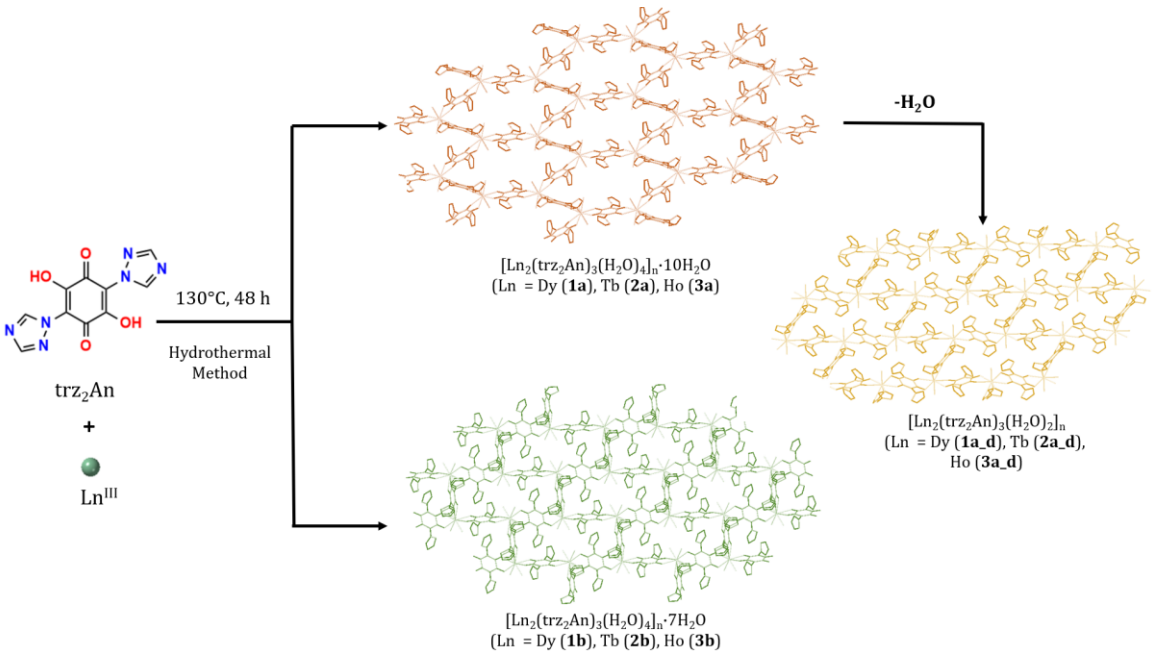

Scheme 5.1. Synthetic strategy for **1-3a, 1-3a_d** and **1-3b**.

3.2. Crystal Structure

Compounds **1-3a** and **1-3b** crystallize in triclinic space group *P-1*, isostructural with Er^{III} based CFs, previously described in *Chapter 4*, and are 3D neutral polymeric frameworks of the trz_2An ligand bridging the Ln^{III} ions, containing water molecules in the pores.

1-3a and **1-3b** polycrystalline samples are pure and homogeneous, proving to be perfectly consistent with the calculated pattern from CIF and isostructural to the corresponding Er^{III}-based CFs (**Figure 5.1**).

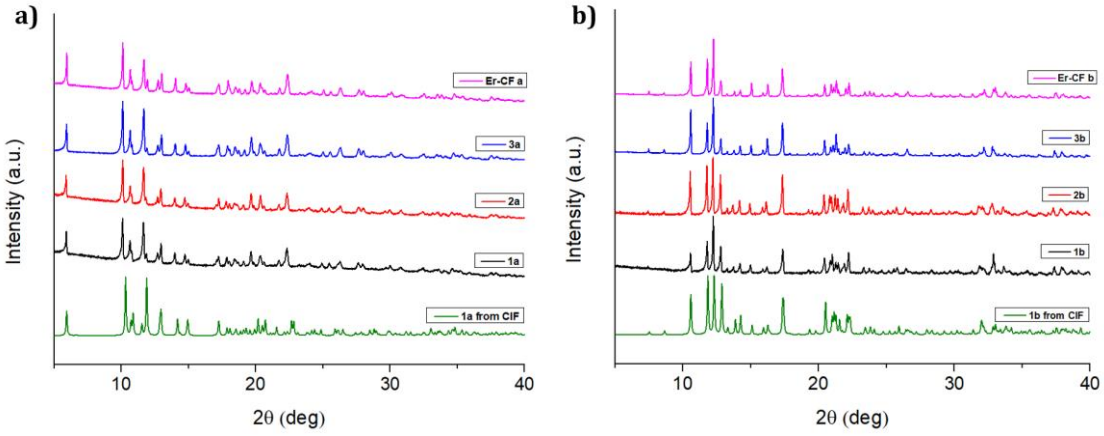

Figure 5.1. Experimental and calculated powder XRD patterns in 2θ range of 5-40° for **1-3a** (a) and for **1-3b** (b), compared with the respective Er^{III}-CFs of phase a and b (magenta lines).

In order to verify the reversible structural flexibility, observed in Er^{III}-CFs, polycrystalline samples of **1-3a** were placed under vacuum, in a vacuum line pump and was then opened in the glove box to be sealed, in order to study possible changes of the crystal structure which could lead to modifications of the magnetic properties of the CFs. As for Er^{III}-MOFs, all series show the same flexible behavior (**Figure 5.2**).

As previously shown, the new phase **a_d** can be rehydrated to restore the initial framework, indicating a reversible structural phase transition between a hexagonal – rectangular cavity, which is already observed in flexible MOFs.[23]

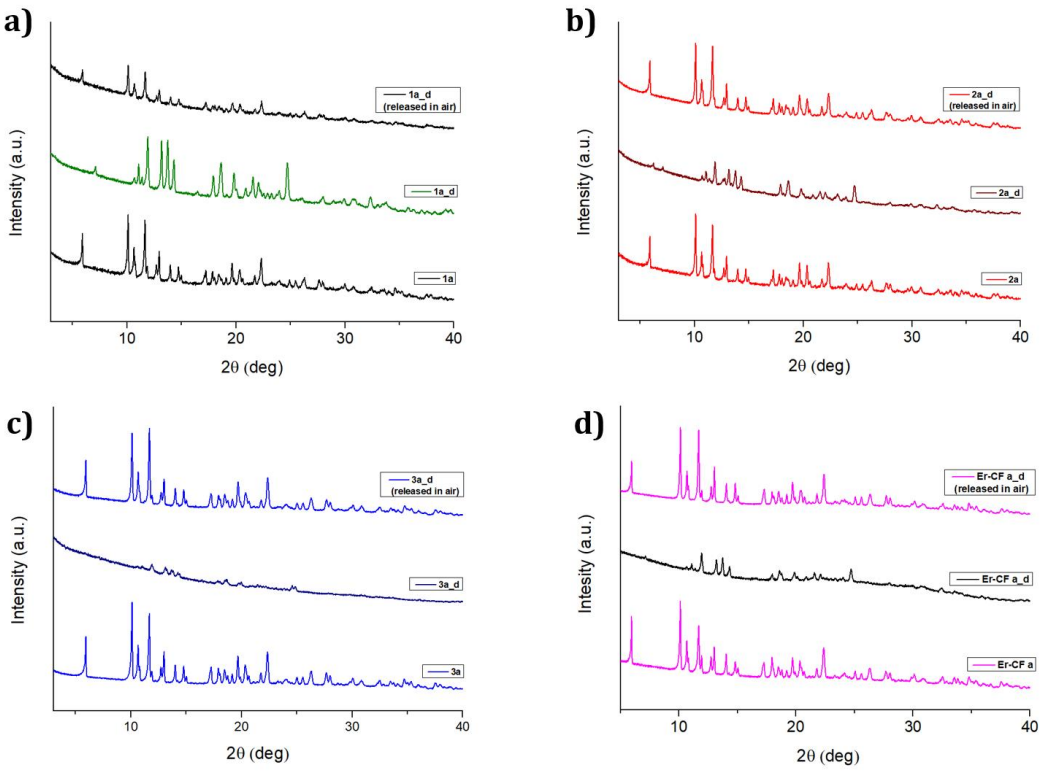

Figure 5.2. PXRD experimental patterns of **1-3a**, **1-3a_d** and **1-3a_d** left in air 4 days after vacuum treatment, highlighting the complete reversibility of the structural change induced by dehydration. Panels *a*, *b* and *c* are respectively for **1a**, **2a** and **3a**, while panel *d* reports on **Er-CFa** and **Er-CFa_d** for comparison.

3.3. FT-IR Spectroscopy

FT-IR spectra of **1-3a** and **1-3b** were performed and compared with H_2trz_2An linker to further confirm the coordination between trz_2An and Ln^{III} ion. Only **1a** and **1b** spectra are reported as representative of the corresponding series, while all the FT-IR spectra are reported in the Supporting Material Section (*Part IV, Chapter 5*). As shown in **Figure 5.3**, the band at 1650 cm^{-1} of nC-O of free ligand disappear and the broad band centered at 1550 cm^{-1} is downshifted, due to the coordination of C-O in the frameworks. Below 460 cm^{-1} the typical bands related to the nLn-O stretching vibrations are present, due to the coordination bonds.

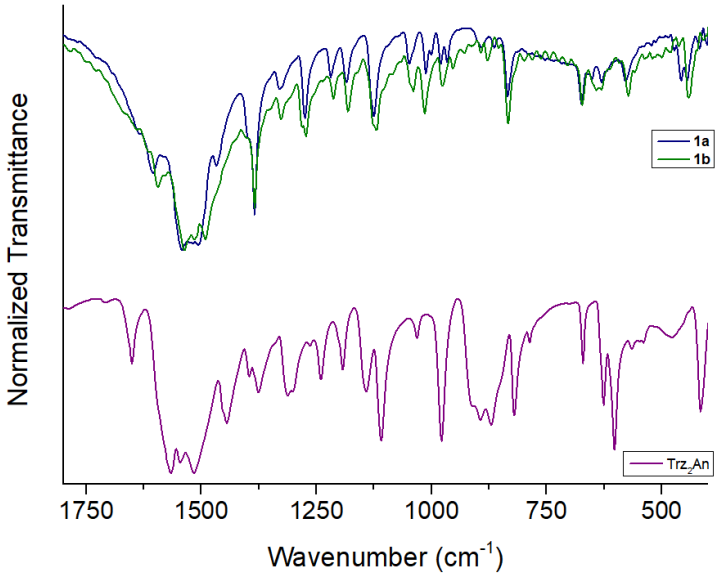

Figure 5.3. FT-IR spectra of H_2trz_2An (purple), **1a** (blue) and **1b** (green) in the 1800-400 cm^{-1} region.

The characteristic FT-IR bands of **1a** and **1b** with their assignments are shown in **Table 5.4**.

Table 5.4. Assignments of characteristic bands for **1a** and **1b**, all the frequencies are in cm^{-1}.[24–27]

	1a	**1b**
ν O-H	3388	3438
ν C=O	1605	1589
ν C=O + ν C=C aromatic	1513 1492	1506 1488
ν aromatic ring	1385	1391 1377
ν C-N	1321 1272	1325 1278 1272
ν N-N	1183	1181
δ C=C	835	835
ν Dy-O	459 446	438

3.4 Magnetic Properties

Solid state, dc magnetic susceptibility measurements were carried out in the temperature range of 2-300 K, under an applied magnetic field of 0.1 T, for **1-3a** and **1-3b**. As in Er^{III}-MOF, phase a, it was necessary to protect the sample with H_2O since the vacuum of the squid chamber (~2-3 mbar) caused desolvation and the formation of **1-3a_d**, even in the presence of eicosane. The magnetic characterization of **1a** and **1a_d** was performed in the case of Dy^{III}, since it is the only one showing a slow relaxation of the magnetization. In Tb^{III} and Ho^{III}, only **2a_d** and **3a_d** samples were characterized. The $\chi_M T$ values at 300 K are 14.0 (**1a**), 13.6 (**1a_d**), 13.7 (**1b**), 11.6 (**2a_d**), 13.8 (**3a_d**), 13.7 (**3b**) emu K mol^{-1}, in agreement with that expected for each non-interacting Ln^{III} ion ($^7F_6$ for Tb^{III}, $^6H_{15/2}$ for Dy^{III} and $^5I_8$ for Ho^{III}), as shown in **Figures 5.4-5.6**. Magnetic measurements of the thermal variation of χ_MT of **2b** is in progress. The field dependence of magnetization was also measured in the 2-8 K temperature range for **1b**, **2a_d**, **3a_d** and **3b**, by varying the magnetic field up to 5 T (**Figures S5.3-S5.6**).

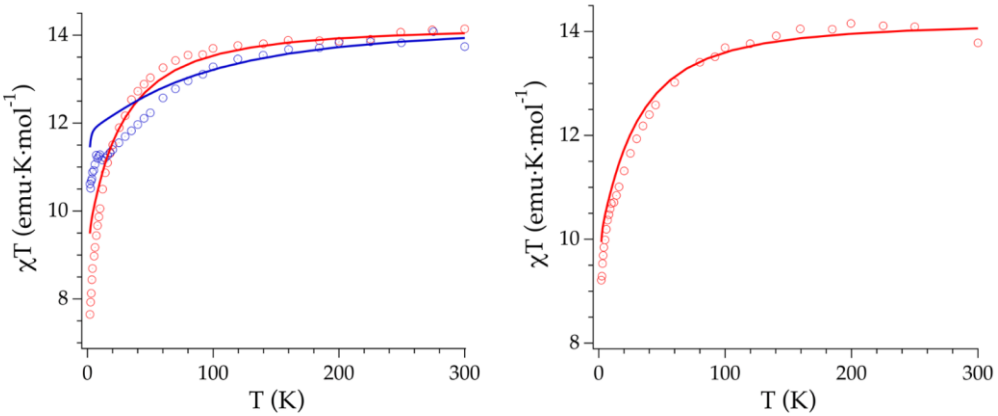

Figure 5.4. Experimental (symbols), predicted (solid line) temperature-dependence of $\chi_M T$ from 2 to 300 K, at 0.1 T of **1a** in red and **1a_d** in blue (left) and **1b** (right).

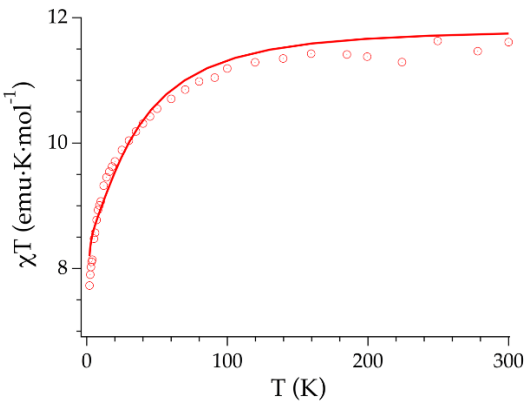

Figure 5.5. Experimental (symbols), predicted (solid line) temperature-dependence of $\chi_M T$ from 2 to 300 K, at 0.1 T of **2a_d**.

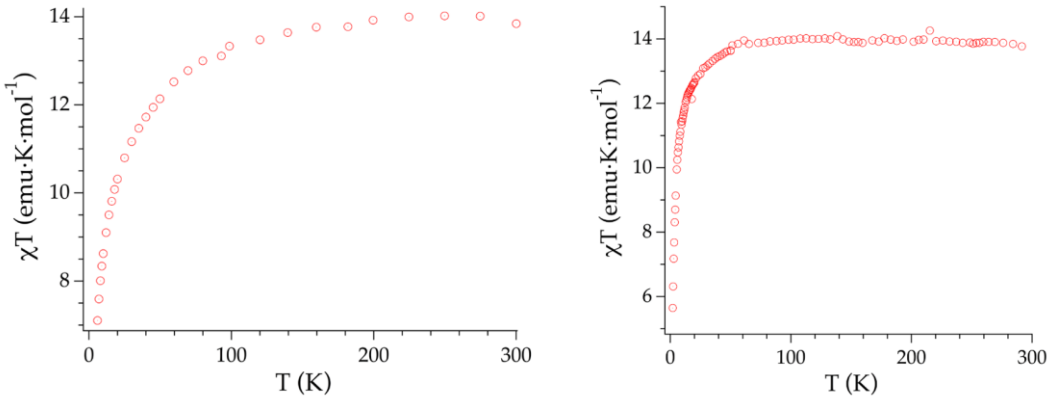

Figure 5.6. Temperature-dependence of $\chi_M T$ from 2 to 300 K, at 0.1 T of **3a_d** (left) and of **3b** (right).

To further understand the observed magnetic behavior, preliminary theoretical calculations were carried out by using the SIMPRE computational package.[19] The static magnetic susceptibility was successfully fitted by using the Radial Effective Charge (REC) model[20] with the same REC parameters obtained for the fitting of the Er^{III}-CFs from *Chapter 4*. All the results are predictions based on the crystallographic structure of the Er^{III} compounds $[Er_2(trz_2An)_3(H_2O)_4]_n \cdot 10H_2O$ (**1a** in *Chapter 4*) and $[Er_2(trz_2An)_3(H_2O)_2]_n$ (**1a_d** in *Chapter 4*) and **1b** (see discussion in paragraph 3.4, *Chapter 4*). This means that these results should be less accurate than the Er^{III} ones. The predicted magnetization curves are also in good agreement with the experimental data (**Figures S5.3 and S5.4**). The diagonalization of the crystal field hamiltonian results in a ground state wave function mainly composed by the |±15/2> microstate in the easy axis direction, with negligible mixing with other Mj microstates for **1a**, **1a_d** and **1b**, which is congruent with the observed slow relaxation of the magnetization (*vide infra*). These results suggest that the loss of a water molecule in **1a_d** should improve the SIM properties. Thus, the ground state is less mixed and the first excited state moves to a higher energy (105 cm^{-1}). However, the measured thermal variation of $\chi_M T$ has an irregular trend that makes difficult to determine if there is an issue with the prediction. In all the cases an axial ligand distribution is found. The reduction of the number of point charges from **1a** to **1a_d** (from 9 to 8) makes the coordination environment a bit more axial, which stabilizes better the largest M_J value due to the oblate shape of the Dy *f*-shell (minimization of repulsion). To explain the relaxation of magnetization, molecular vibrations will also play a key role. The octacoordinated system has less active vibrations due to the loss of a water molecule, however it will depend on the level of resonance of

those molecular vibrations with the electronic energy levels. Theoretical calculations of **2b**, the other sample that shows a slow relaxation of magnetization, will be carried out after the magnetic characterization is finished.

The dynamic magnetic properties were studied by susceptibility measurements performed with an alternating magnetic field (AC susceptibility). In the absence of a magnetic field, no signal in χ" was observed. When magnetic dc fields of 0.1 T were applied, strong frequency-dependent peaks in both the χ' and χ" appeared in **1a, 1a_d**, **1b** and **2b** with clear maxima of χ" below 4 K for **1a** and **1a_d**, at 6 K for **1b** and at 14 K for **2b** (**Figures 5.7-5.9**). This indicates that the four CFs present a field-induced slow relaxation of magnetization.

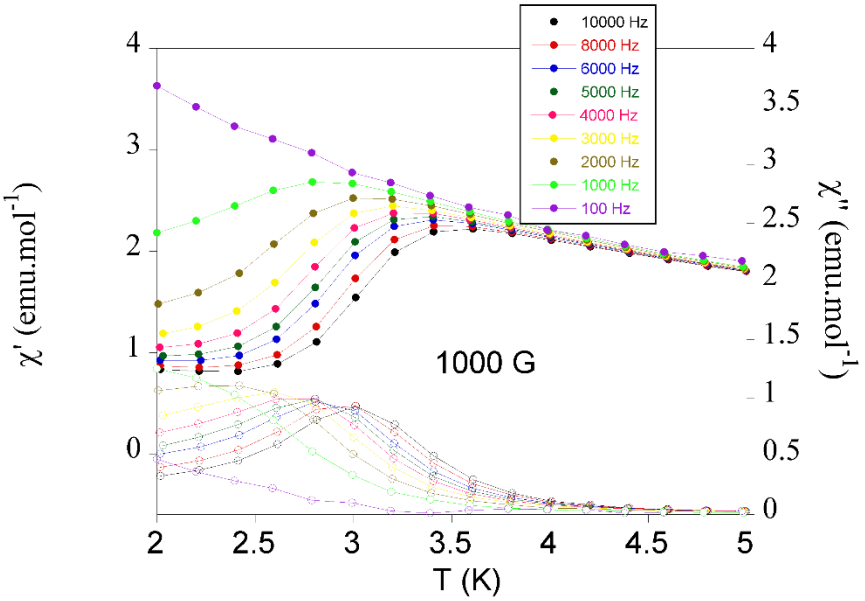

Figure 5.7. Temperature dependence of χ' and χ" of **1a_d** in an applied dc field of 0.1 T at frequencies in the range 100 to 10000 Hz.

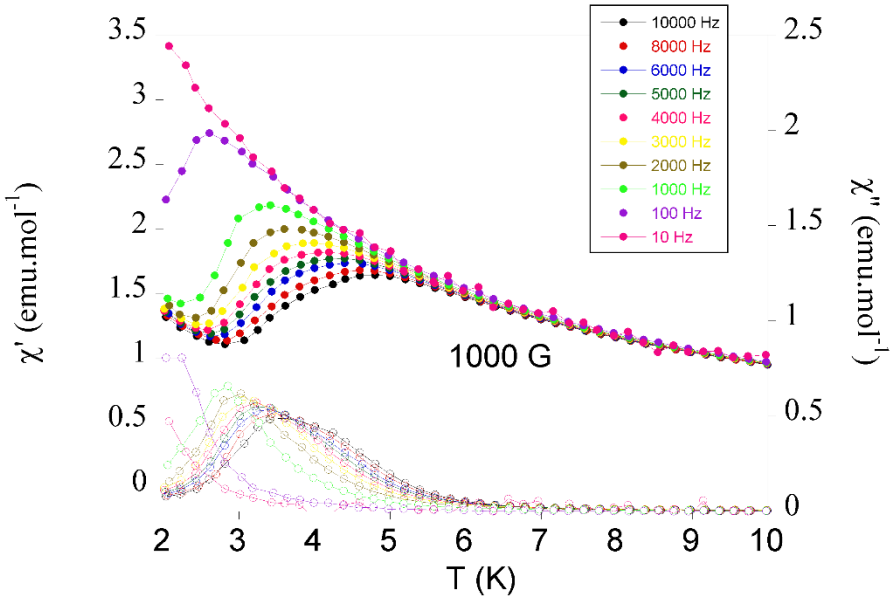

Figure 5.8. Temperature dependence of χ' and χ'' of **1b** in an applied dc field of 0.1 T at frequencies in the range 10 to 10000 Hz.

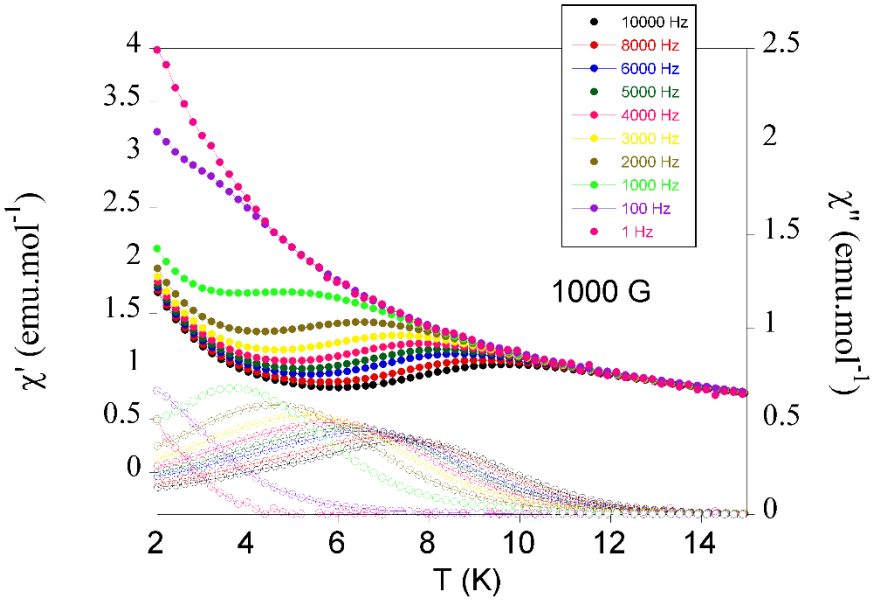

Figure 5.9. Temperature dependence of χ' and χ'' of **2b** in an applied dc field of 0.1 T at frequencies in the range 1 to 10000 Hz.

The χ' and χ'' peaks of **1a** measured in contact with eicosane (**1a_d**) present a small shift to higher temperatures of ca. 0.2 K with respect to those measured in contact with water **1a**. This suggests that the magnetic behavior of **1a** is not as sensitive to desolvation as

that of its correspondent Er^{III}-based MOF (see *Chapter 4*), as shown in **Figure 5.10**, thus the complete AC characterization of **1a_d** is herein performed.

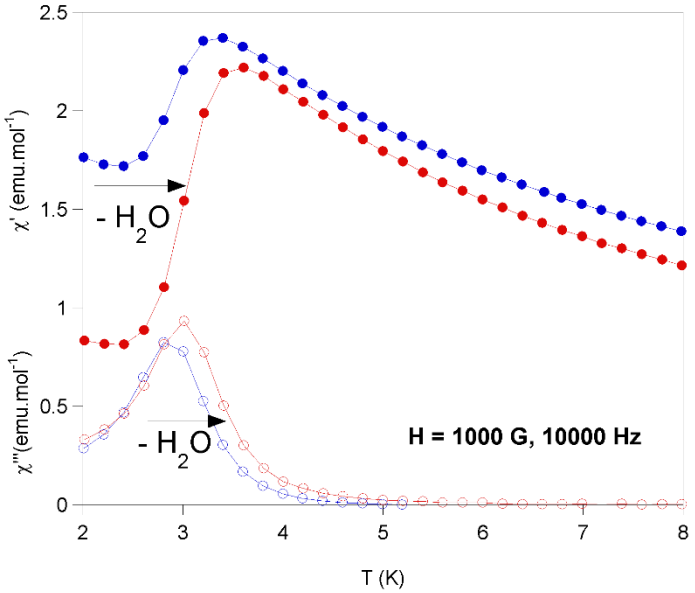

Figure 5.10. Temperature dependence of χ' and χ'' of **1a** (full and empty blue circles, respectively) and **1a_d** (full and empty red circles, respectively)) in an applied dc field of 0.1 T at 10000 Hz.

The relaxation times (τ) of **1a_d**, **1b** and **2b** were determined from the maximum of χ'' at a given frequency ($\tau = 1/2\pi\nu$). They were fitted to the Arrhenius expression for a thermally activated process (Orbach, $\tau = \tau_0 \exp(U_{eff}/k_B T)$) leading to $\tau_0 = 5.4\times10^{-8}$ s and $U_{eff} = 17.5$ K for **1a_d,** $\tau_0 = 1.2\times10^{-8}$ s and $U_{eff} = 25.7$ K for **1b,** and $\tau_0 = 2.0\times10^{-6}$ s and $U_{eff} = 16.4$ K at 0.1 T for **2b**. However, the plots of τ vs. $1/T$ deviate from linearity at low temperatures indicating the coexistence of multiple relaxation pathways as observed in the Er^{III}-CFs from *Chapter 4* and other anilate-based lanthanide complexes (see **Figure S5.8**). The general model where the first, second, third and fourth terms include quantum tunneling, direct, Raman and Orbach relaxation processes, respectively, was applied.

$$\tau^{-1} = \tau_{QTM}^{-1} + AH^2T + CT^n + \tau_0^{-1}\exp(-U_{eff}/K_BT)$$

Correct fittings of **1b** and **2b** were obtained using Raman and Orbach relaxation processes with values comparable to those found in other anilate-based Ln^{III} compounds with $C = 0.9$ $s^{-1}K^{-8.4}$, $\tau_0 = 3.7\ 10^{-9}$ s and $U_{eff} = 33.5$ K for **1b** and $C = 81.7$ $s^{-1}K^{-3.2}$, $\tau_0 = 1.0\ 10^{-6}$ s and $U_{eff} = 30.5$ K for **2b**.[28–31] The calculated values of n (8.4 for **1b** and 3.2 for **1b**) are smaller than the ideal value of 9 found for Raman processes. This suggests that these Raman-like relaxations are attributed to acoustic and optical vibrations.[32] In the case of

1a_d, a reasonable fitting using Raman and Orbach relaxation processes could not be obtained. This was obtained by combining direct and Orbach relaxation processes with $AH^2 = 3061.3\ s^{-1}$, $\tau_0 = 9.1\ 10^{-10}$ s and $U_{eff} = 29.9$ K.

The variable-frequency AC data at different temperatures of **1a_d**, **1b** and **2b** show a single relaxation with maxima at 960 Hz (**1a_d**), 65 Hz (**1b**) and 210 Hz (**2b**) at 2 K (see **Figures 5.11-5.13**). The Cole–Cole plots (χ" vs. χ') of the three samples confirm the presence of a single relaxation process (**Figures 5.14**). Thus, at fixed temperatures between 2.0 and 5.0 K for **1a_d**, 2.0 and 4.0 for **1b** and 2.0 and 7.5 K for **2b**, semi-circular plots were obtained and fitted using a generalized Debye model, yielding α parameter in the range of 0.12-0.42 (**1a_d**), 0.21-0.25 (**1b**) and 0.06-0.33 (**2b**). This indicates narrow distributions of the relaxation processes.

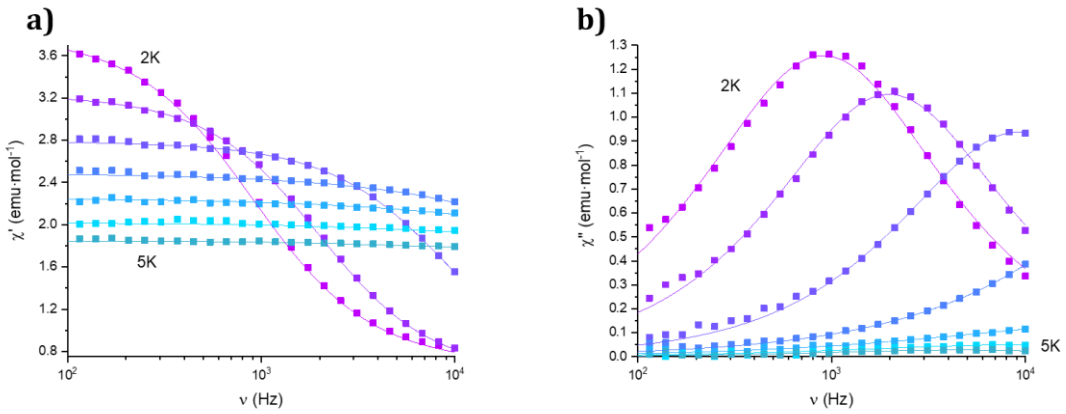

Figure 5.11. AC susceptibility in an applied dc field of 0.1 T of **1a_d** measured as a function of the frequency at the different temperatures (2.0, 2.5, 3.0, 3.5, 4.0, 4.5 and 5.0 K). (a): Real component. (b): Imaginary component. Solid lines represent the best fitting of the experimental data to a Cole-Cole function.

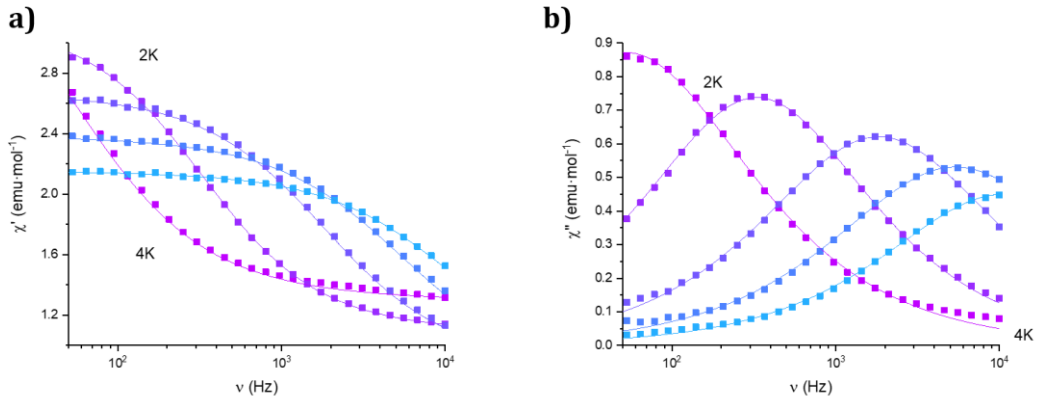

Figure 5.12. AC susceptibility in an applied dc field of 0.1 T of **1b** measured as a function of the frequency at the different temperatures (2.0, 2.5, 3.0, 3.5 and 4.0 K). (a): Real component. (b): Imaginary component. Solid lines represent the best fitting of the experimental data to a Cole-Cole function.

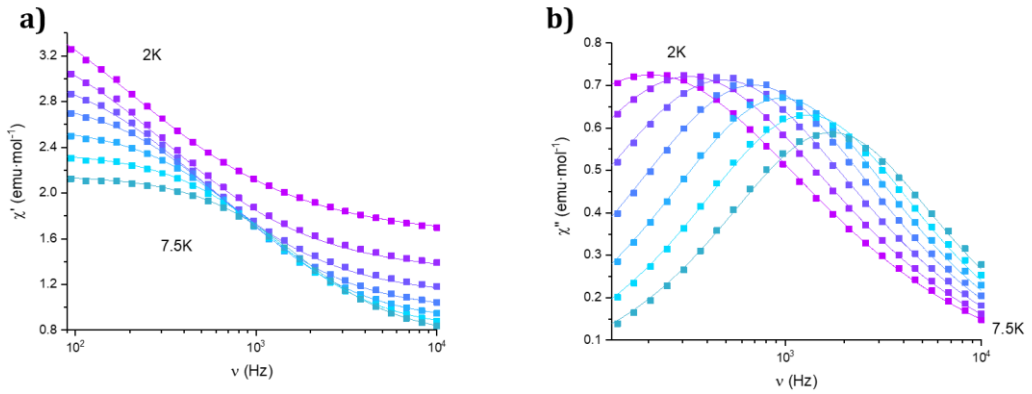

Figure 5.13. AC susceptibility in an applied dc field of 0.1 T **2b** measured as a function of the frequency at the different temperatures (2.0, 2.5, 3.0, 3.5, 4.0, 4.5, 5.0, 5.5, 6.0, 6.5, 7.0 and 7.5 K). (a): Real component. (b): Imaginary component. Solid lines represent the best fitting of the experimental data to a Cole-Cole function.

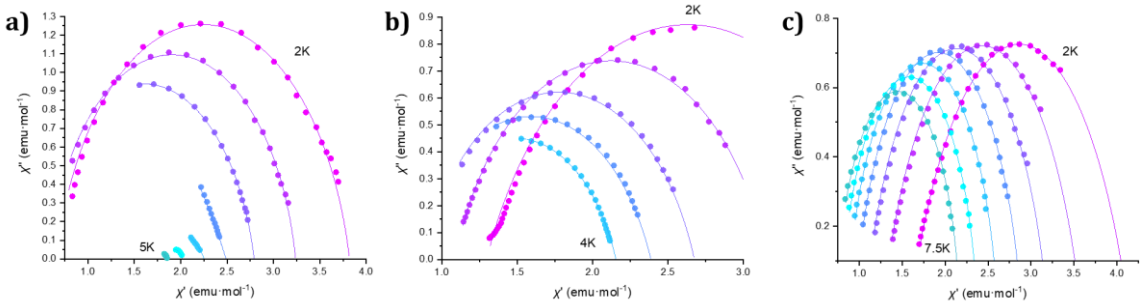

Figure 5.14. Cole-Cole plots of **1a_d** (a) and **1b** (b) and **2b** (c) measured at the same temperatures as **Figures 5.11-5.13** under an applied dc field of 0.1 T. Solid lines represent the best fitting of the experimental data to a Cole-Cole function.

4. Conclusions

The H_2trz_2An anilate derivative, bearing a triazole pendant arm at the 3,6 position of the anilato ring, has been used for the first time in combination with Dy^{III}, Tb^{III} and Ho^{III} nodes to afford **1-3a** and **1-3b** 3D CFs, formed by 2D layers with (6,3) topology linked through the anilato ligands, which are connected through the triazolyl pendant groups. These compounds are isostructural to Er^{III}-CFs reported in *Chapter 4*. Remarkably, **1-3a** MOFs show flexibility and porosity as the Er^{III}-MOF (phase a), with analogous reversible drastic structural changes to a less porous 3D structure, after partial dehydration at very mild conditions (vacuum or heating to 360 K). The use of these three metals enable to optimize the SIM properties. Magnetic characterization reveals a field-induced SIM behaviour for **1a**, **1a_d** and **1b** Dy^{III} CFs and for **2b** Tb^{III} CP, which, to the best of our knowledge, is the first Tb^{III}–anilate-based CP that exhibits SIM behaviour. Interestingly, its blocking temperature is higher than that one of Er^{III} and Dy^{III} CFs, showing the best SIM properties within the series. Conversely, SIM properties of **1a** are much less sensitive to the removal of water molecules than those of the Er^{III}-MOFreported in *Chapter 4.* Preliminary theoretical calculations suggest that SIM properties of the Dy^{III} CFs are related to a ground state wave function mainly composed by the $|\pm 15/2>$ microstate in the easy axis direction, with negligible mixing with other Mj microstates. More detailed magnetic and theoretical studies are required to understand why flexibility slightly affetcs the magnetic behavior of **1a_d** (Dy^{III}-MOF)**,** after partial dehydration and the observed better SIM properties of **2b** (Tb^{III}-CP). Further optimization of SIM properties could be achieved by diluting the paramagnetic Tb^{III} nodes with diamagnetic Eu^{III} ions. With this view, the preparation of isostructural Gd^{III}-CFs, containing an isotropic paramagnetic lanthanide ion, could help to understand if the weak magnetic exchange through the ligand plays a role on the SIM properties of these CFs.

In summary, although significant progress has been made in the area of molecular magnets in general and SMMs/SIMs in particular, the practical applications of these novel compounds is still an ongoing challenge. Important drawbacks need to be overcome, primarily *i)* increase of blocking temperatures; *ii)* retainment of structural and magnetic stability to the micro- and nanoscale; *iii)* ready assembly when anchoring them on surfaces; *iv)* careful selection of surface substrates. Creative responses to the challenges listed will be forthcoming in the next future, but in the meanwhile, it is mandatory a rational design of these systems for exploring their potential in the envisaged

technological applications such as information storage, quantum computing devices and molecular spintronics.

References

1 R. Sessoli, D. Gatteschi, A. Caneschi and M. A. Novakt, *Nature*, 1993, **365**, 141–143.

2 D. N. Woodruff, R. E. P. Winpenny and R. A. Layfield, *Chem. Rev.*, 2013, **113**, 5110–5148.

3 L. Holleis, B. S. Shivaram and P. V. Balachandran, *Appl. Phys. Lett.*, 2019, **114**, 222404.

4 M. Yamashita and K. Katoh, in *Molecular Magnetic Materials: Concepts and Applications*, eds. B. Sieklucka and D. Pinkowicz, Wiley-VCH Verlag GmbH & Co. KGaA, 2017, pp. 79–101.

5 L. Bogani and W. Wernsdorfer, *Nat. Mater.*, 2008, **7**, 179–186.

6 M. N. Leuenberger and D. Loss, *Nature*, 2001, **410**, 789–793.

7 A. Ardavan, O. Rival, J. J. L. Morton, S. J. Blundell, A. M. Tyryshkin, G. A. Timco and R. E. P. Winpenny, *Phys. Rev. Lett.*, 2007, **98**, 1–4.

8 S. T. Liddle and J. Van Slageren, *Chem. Soc. Rev.*, 2015, **44**, 6655–6669.

9 J. L. Liu, Y. C. Chen and M. L. Tong, *Chem. Soc. Rev.*, 2018, **47**, 2431–2453.

10 C. A. P. Goodwin, *Dalton Trans.*, 2020, **49**, 14320–14337.

11 S. Benmansour and C. J. Gómez-García, *Magnetochemistry*, 2020, **6**, 1–44.

12 S. Ashoka Sahadevan, N. Monni, M. Oggianu, A. Abhervé, D. Marongiu, M. Saba, A. Mura, G. Bongiovanni, V. Mameli, C. Cannas, N. Avarvari, F. Quochi and M. L. Mercuri, *ACS Appl. Nano Mater.*,2020, **3**, 1, 94-104

13 S. Ashoka Sahadevan, N. Monni, A. Abhervé, D. Marongiu, V. Sarritzu, N. Sestu, M. Saba, A. Mura, G. Bongiovanni, C. Cannas, F. Quochi, N. Avarvari, M. L. Mercuri, A. Abherve, D. Marongiu, V. Sarritzu, N. Sestu, M. Saba, A. Mura, G. Bongiovanni, C. Cannas, F. Quochi, N. Avarvari and M. L. Mercuri, *Chem. Mater.*, 2018, **30**, 6575–6586.

14 M. A. Dunstan, E. Rousset, M. E. Boulon, R. W. Gable, L. Sorace and C. Boskovic, *Dalt. Trans.*, 2017, **46**, 13756–13767.

15 W. Gauβ, H. Heitzer and S. Petersen, *Justus Liebigs Ann. Chem.*, 1973, **764**, 131–144.

16 G. M. Sheldrick, *Acta Crystallogr. Sect. A Found. Crystallogr.*, 2015, **71**, 3–8.

17 G. M. Sheldrick, *Acta Crystallogr. Sect. C Struct. Chem.*, 2015, **71**, 3–8.

18 O. V. Dolomanov, L. J. Bourhis, R. J. Gildea, J. A. K. Howard and H. Puschmann, *J. Appl. Crystallogr.*, 2009, **42**, 339–341.

19 J. J. Baldoví, S. Cardona-Serra, J. M. Clemente-Juan, E. Coronado, A. Gaita-Ariño and A. Palii, *J. Comput. Chem.*, 2013, **34**, 1961–1967.

20 J. J. Baldoví, J. J. Borrás-Almenar, J. M. Clemente-Juan, E. Coronado and A. Gaita-Ariño, *Dalton Trans.*, 2012, **41**, 13705–13710.

21 J. van Leusen, M. Speldrich, H. Schilder and P. Kögerler, *Coord. Chem. Rev.*, 2015, **289**–**290**, 137–148.

22 M. Speldrich, H. Schilder, H. Lueken and P. Kögerler, *Isr. J. Chem.*, 2011, **51**, 215–227.

23 M. Souto, J. Romero, J. Calbo, I. J. Vitórica-Yrezábal, J. L. Zafra, J. Casado, E. Ortí, A. Walsh and G. Mínguez Espallargas, *J. Am. Chem. Soc.*, 2018, **140**, 10562–10569.

24 F. M. A. Kerim, H. F. Aly and A. El-Agramy, *Proc. Indian Acad. Sci. - Sect. A*, 1977, **85**, 559–566.

25 M. K. Trivedi, R. M. Tallapragada, A. Branton, D. Trivedi, G. Nayak, R. K. Mishra and S. Jana, *J. Mol. Pharm. Org. Process Res.*, 2015, **03**, 1–6.

26 O. Roubeau, B. Agricole, R. Cle and S. Ravaine, *J. Phys. Chem. B*, 2004, **108**, 15110–15116.

27 Q. Deng, C. Tian, Z. Luo, Y. Zhou, B. Gou, H. Liu, Y. Ding and R. Yang, *Chem. Commun.*, 2020, **56**, 12234–12237.

28 W. R. Reed, M. A. Dunstan, R. W. Gable, W. Phonsri, K. S. Murray, R. A. Mole and C. Boskovic, *Dalton Trans.*, 2019, **48**, 15635–15645.

29 P. Zhang, M. Perfetti, M. Kern, P. P. Hallmen, L. Ungur, S. Lenz, M. R. Ringenberg, W. Frey, H. Stoll, G. Rauhut and J. Van Slageren, *Chem. Sci.*, 2018, **9**, 1221–1230.

30 A. Mondal, S. Roy and S. Konar, *Chem. Eur. J.*, 2020, **26**, 8774–8783.

31 S. Benmansour, A. Hernández-Paredes, A. Mondal, G. López Martínez, J. Canet-Ferrer, S. Konar and C. J. Gómez-García, *Chem. Commun.*, 2020, **56**, 9862–9865.

32 R. Ishikawa, S. Michiwaki, T. Noda, K. Katoh, M. Yamashita and S. Kawata, *Magnetochemistry*, 2019, **5**, 30.

Chapter 6

Dual Center Ln'Ln''-CFs NIR Luminescent Ratiometric Thermometers *via* a solvent-free approach

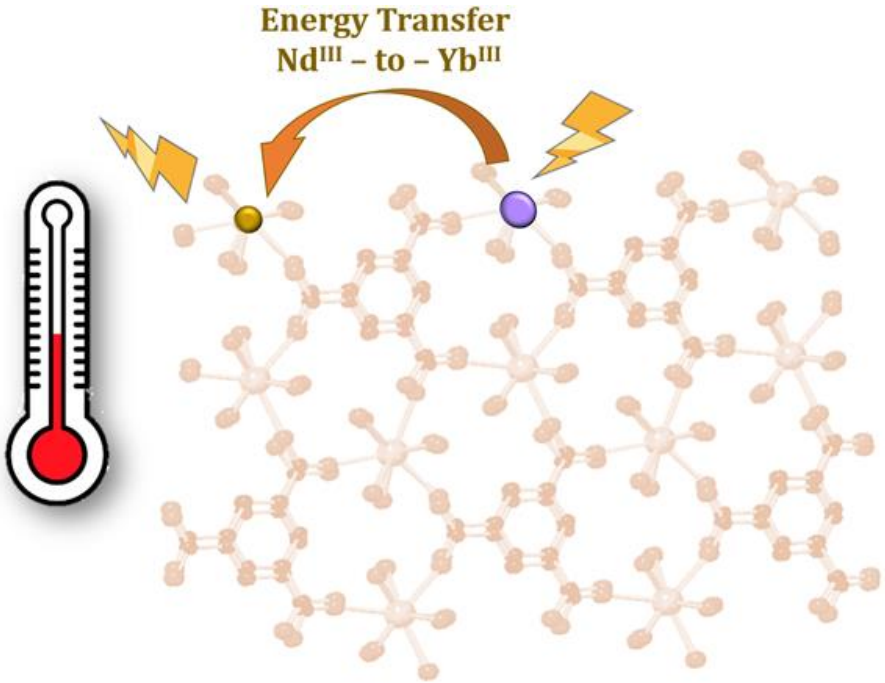

Abstract

NIR luminescent mixed Yb^{III}/Nd^{III} CFs based on 1,3,5-benzentricarboxylic acid (H_3BTC) biofriendly linker are herein reported. A solvent free method was chosen to prepare two different classes of CFs, formulated as $Nd_xYb_{1-x}(BTC)_3(H_2O)_6$ (x = 1 (**1**); x = 0.943 (**2**); x = 0.953 (**3**); x = 0.856 (**4**); x = 0.890 (**5**)) and $Nd_xYb_{1-x}(BTC)_6$ (x = 0.017 (**6**), x = 0 (**7**)), respectively, with different Nd:Yb doping percentage (%) for each class, ranging from 95:5 up to 80:20. Pristine Nd-CFs (**1**) and Yb-CFs (**7**) have been also prepared as reference samples. They crystallize as neutral polymeric frameworks, giving rise to a ribbon-like hydrated structure organized in a 3D network of hydrogen bonding interlinking the different coordination spheres (**1)** and to a 3D framework with no water molecules in the crystal structure, neither adsorbed nor coordinated (**7**). The obtained series has been fully characterized through a multi-technique approach, by using ICP, FT-IR, PXRD, SEM-EDX, TGA and DLS to investigate their structure, morphology, composition and stability. Finally, photophysical studies have been performed with the aim to study *i)* the photophysical processes at the origin of both ligand-centered and NIR metal-centered luminescence emissions, and *ii)* their thermal sensing performances in the 300-10 K range. Among the series, **5** has proven to be the most promising system for thermometry and its thermometer parameters, along with its biocompatibility, will be further explored.

1. Introduction

Temperature (T) is considered one of the most fundamental parameters and T sensors are widely used in daily life and they are expected to reach a 6 billion dollar market by 2023.[1] The recent development of several research areas, from microelectronics to biomedicine, has stimulated the need of monitoring the local T of a given system with a sub-micrometric spatial resolution and high sensitivity,[2] but in contactless mode and, hence, it boosts the growth of luminescent thermometers, which present the advantage of contactless measurement and large-scale imaging. T indeed, determines and affects dynamics and properties of a given biosystem, playing a crucial role, from the influence of cell division rate[3] to the modification of physical properties of fundamental biomolecules such as proteins.[4] In addition, the temperature detection of biosystems is fundamental for early diagnosis and treatment of numerous diseases, including cancer.[5,6]

Among luminescent molecular probes used for T sensing, a novel class of CFs based on Ln'Ln''-CFs (Ln^{III} = Nd-Yb and Yb-Er) are emerging as Dual Center NIR Luminescent Ratiometric Thermometers in the physiological (293–313K) T range. Lanthanide-based CFs, crystalline solids constructed via self-assembly of Lanthanide ions and organic linkers, are excellent candidates as optical sensors due to their ability to show both ligand-centered and metal-centered luminescence. By a valuable choice of the luminescent building blocks, both the lanthanide ions as nodes and the functional organic ligands as linkers, new CFs probes for sensing T, showing different pathways of energy exchange processes between building blocks, can be constructed.[7]

1.1 Thermometer Parameters

To determine the performances of a given thermometer, different parameters should be evaluated.[7] First of all the *sensitivity* (S), indicative of the performance of the sensor, is defined as the change of an experimental observable R as a function of the variation of the temperature (T), as:

$$S = \frac{dR}{dT} \quad (1)$$

While the *relative thermal sensitivity* (S_{rel}) is defined as the relative change of an experimental observable as a function of the variation of the temperature T, usually expressed as percent change per Kelvin [% K^{-1}]:

$$S_{rel} = \frac{1}{S}\frac{dR}{dT} \quad (2)$$

S_{rel} is a standardized quantity which allows for a comparison of different thermometric techniques and evaluation of the performances with literature values. However, S does not include some variables that may be relevant for applications, such as the signal to noise ratio of the experimental observables, affecting the applicability of the sensor. Therefore, it is also necessary to consider the T resolution ΔT_{min}, defined as the minimum variation of T that can actually be resolved. It derives from statistical considerations as the ratio between the standard deviation (σ) of the experimental observable from different measurements at a given T and the thermal sensitivity at that T:

$$\Delta T_{min} = \frac{\sigma}{S} \quad (3)$$

Sensitivity and thermal resolution characterize the performance of the thermometer. Furthermore, other features of the materials should be considered, such as the optimal range of T which is fundamental for the final application, the stability, the reproducibility and the accuracy.

1.2 Mixed-Lanthanide CFs

Trivalent lanthanide (Ln^{III}) doped materials are very promising candidates to develop efficient thermometers based on luminescence, due to their high sensitivity because of the peculiar excited states configuration of Ln^{III} ions.[2,8] Noteworthy the use of mixed-lanthanide CFs, changing the photoluminescence intensity ratio between the two lanthanides (Ln' and Ln'') emissions, as the ratiometric thermometric parameter, makes thermal sensing independent from the concentration and inhomogeneity of luminescence centers, leading to more robust and reliable thermometers.[7] Furthermore fast response, high sensitivity, noninvasive operation and inertness to strong electric or magnetic fields, make these new types of luminescent thermometers more effective than the conventional ones.[9] Most of the work on mixed lanthanide-based CFs thermometers, reported so far, is based on the Eu^{III}-to-Tb^{III} emission ratio,[7,9–11] while only few examples of NIR luminescent mixed Ln-based CFs are reported, of peculiar interest for use in biological tissues, due to their accurate resolution and harmless emission wavelength.[12–15] Among them, a remarkable example was reported by Zhao *et al.*, which prepared a novel thermosensitive

NIR mixed Ln-based CF, formulated as $Nd_{0.866}Yb_{0.134}BTB$ (H_3BTB = 1,3,5-benzenetrisbenzoic acid).[12] This mixed Ln-CF exhibits impressive temperature dependence of the photoluminescence properties in the physiological range, ranging from 303 to 333 K, with a maximum relative sensitivity of 4.755% K^{-1}. This value is one order of magnitude higher than the previously reported for the Nd^{III}/Yb^{III} CFs based on 2,3,5,6-tetrafluoro-1,4-benzenedicarboxylate ($H_2BDC\text{-}F_4$), formulated as $(Nd_{0.577}Yb_{0.423})_2(BDC\text{-}F_4)_3$-(DMF)($H_2O$)xDMF.[15] Furthermore, it shows also low cytotoxicity and good biocompatibility, thus it can be useful for thermal sensing and mapping of biological systems. The rational design of NIR luminescent mixed Ln-based CFs requires a careful choice of organic linkers, since the synthetic methodology plays an important role in avoiding toxic precursors. Even if solvothermal synthesis is the method of choice for preparing these CFs thermometers, the use of solvents as DMF, can lead to CFs containing such toxic solvents in the first inner coordination sphere of Lanthanide ion and/or solvated.[15] Hence, solvent free methods can be an intriguing alternative to afford mixed Ln-based CFs. As reported by Liu and co-workers,[16] by using a solvent-free method, providing firstly mechanical energy through the precursors grinding, followed by a thermal energy by heating the ground mixture above 100°C, a new family of Lanthanide-based MOFs, with 1,3,5-benzentricarboxylic acid (H_3BTC) organic linker, was obtained. Furthermore, within this series, a Dy^{III} and Eu^{III} co-doped Y-MOF, which can be used as ratiometric thermometer since its dual blue/red characteristic emissions are dependent on the temperature, was also prepared.

Hence, to afford biofriendly NIR luminescent mixed Ln-CFs, H_3BTC was selected as organic linker for Yb^{III}/Nd^{III} mixed CFs. The synthesis, *via* solvent free method, of two different classes, formulated as $Nd_xYb_{1-x}(BTC)_3(H_2O)_6$ (x = 1 (**1**); x = 0.943 (**2**); x = 0.953 (**3**); x = 0.856 (**4**); x = 0.890 (**5**)) and $Nd_xYb_{1-x}(BTC)_6$ (x = 0.017 (**6**), x = 0 (**7**)), respectively and for each class different Nd:Yb doping percentage (%) ranging from 95:5 up to 80:20. Nd-CFs and Yb-CFs have been also prepared as reference samples.

The obtained materials have been characterized by ICP, FT-IR, Powder X-Ray Diffractometry. SEM-EDX (Scanning Electron Microscopy - Energy Dispersive X-ray) and Thermal Gravimetric Analysis (TGA) measurements have been carried out in order to study their morphology and thermal stability. Photophysical processes at the origin of both ligand-centered and NIR metal-centered luminescence emissions and their thermal sensing performances have been studied. Photophysical studies have been performed with the aim

to determine the temperature dependence of ion-to-ligand and ion-ion energy transfer processes, in the 300-10 K range and on two representative selected samples $Nd_{0.889}Yb_{0.111}(BTC)_3(H_2O)_6$ and $Nd_{0.017}Yb_{0.983}(BTC)_6$, respectively and on Nd-BTC as reference sample.

2. Experimental Section

2.1. General Remarks

Lanthanides nitrates and 1,3,5-benzenetricarboxylic acid were purchased from Alfa Aesar and Sigma Aldrich, then used without further purification.

2.2. Synthesis

$Nd_xYb_{1-x}(BTC)_3(H_2O)_6$ (x = 1 (1); x = 0.943 (2); x = 0.953 (3); x = 0.856 (4); x = 0.890 (5)) and $Nd_xYb_{1-x}(BTC)_6$ (x = 0.017 (6), x = 0 (7)). All the compounds were prepared according with the previously reported method[16] as follow: 0.5 mmol of Ln^{III} precursor ($Nd(NO_3)_3{\cdot}6H_2O$ for **1** and $Yb(NO_3)_3{\cdot}6H_2O$ for **7**) were mixed with 0.5 mmol of H_3BTC (1,3,5-benzenetricarboxylic acid) and ground in a mortar for 5 min. Then the mixture was transferred into a 25 mL boron-silicate vial and heated at 130°C for 24 h. After cooling to room temperature, the powder was collected and washed with distilled water and with ethanol, two times each, and then dried at 60°C for 3 h. For the synthesis of compounds **2-6** the procedure was exactly the same but mixing the two Ln^{III} nitrates in different stoichiometric ratios (Nd/Yb: 95/5 (**2**), 90/10 (**3**), 85/15 (**4**), 80/20 (**5**), 5/95 (**6**)).

2.3. Physical Measurements

ICP-MS. Inductively coupled plasma spectroscopy (ICP) was performed on a Agilent Technologies ICP-MS 7900 spectrometer.

Powder X-Ray Diffraction (PXRD).

Fingerprinting: PXRD patterns were collected by using a θ–θ Bragg–Brentano focalizing geometry Seifert X 3000 diffraction system equipped with a Cu Kα source (λ = 1.54056 Å), a graphite monochromator on the diffracted beam and a scintillation counter. Step size 0.05°, acquisition time 2 s/step.

Crystal Structure Solution and Refinement: PXRD measurements for structure solution were performed using a Bruker AXS D8 Advance diffractometer in

Bragg-Brentano θ:θ geometry, equipped with a Lynxeye position sensitive detector. DS: 0.5°; Generator setting: 40 kV, 40 mA; Ni-filtered Cu-Kα radiation, λ = 1.5418 Å. Data were collected in the 3–105° 2θ range, sampling at 0.02°, with scan time lasting approximately 16h. XRPD structure solution of compounds **1** and **7** was performed using the TOPAS-R software.[17] Standard peak search methods followed by profile fitting allowed the accurate estimate of the low-angle peak position. These values, through the SVD indexing algorithm,[18] provided a C-centered monoclinic cell for **1** [a = 11.44, b = 17.93, c = 7.25 Å, β = 119.4°, GOF(24) = 64.0] and a rhombohedral one for **7** [a = 8.87, c = 18.73 Å, GOF(20) = 35.9]. Space group determination through the analysis of systematic absences, and the possible isomorphous character of **1** with RAVJUV [catena-((μ$_3$-Benzene-1,3,5-tricarboxylato)-hexa-aqua-gadolinium][19] and of **7** with CETMEU [catena-((μ$_6$-cyclohexane-1,3,5-tricarboxylato)-erbium)],[20] indicated, for the two phases, *Cc* and *R-3c*, respectively, later confirmed by successful structure refinement. The structural models were taken from the isomorphous structures, with the BTC ligand in 1 modeled by a partially flexible rigid body and water molecules bound to Nd geometrically restrained. The final refinements were eventually carried out by the Rietveld method. The background was modelled by a polynomial function of the Chebyshev type, peak profiles were described by the Fundamental Parameters Approach[21] and a common (refinable) isotropic thermal factor was attributed to all atoms. Figure **6.1** contains the final Rietveld refinement plots for **1** and **7**.

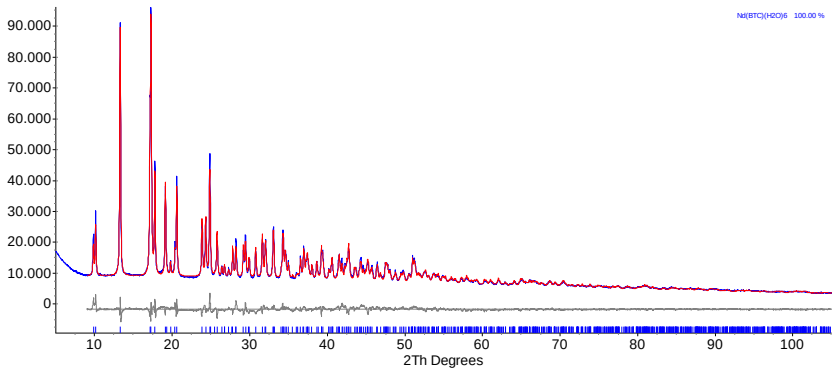

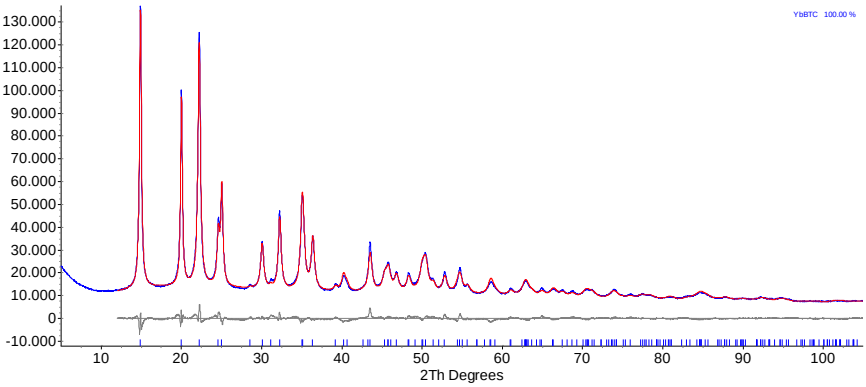

Figure 6.1. Final Rietveld refinement plots for **1** (top) and **7** (bottom), with difference plot and peak markers at the bottom.

Stability Tests. PXRD patterns were collected by using a θ–θ Bragg–Brentano focalizing geometry Seifert X 3000 diffraction system equipped with a Cu Kα source (λ = 1.54056 Å), a graphite monochromator on the diffracted beam and a scintillation counter. Step size 0.05°, acquisition time 2 s/step.

Infrared Spectroscopy. FT-IR spectra were collected using a Bruker Equinox 55 spectrometer, preparing the samples as KBr pellets.

SEM/EDX. SEM images and EDX Microanalysis were performed both on a Hitachi S-4800 and a ESEM:FEI Quanta 200 field emission scanning electron microscopes.

Thermogravimetric Analysis. Thermogravimetric analysis was performed in alumina crucibles with the instrument STA-6000 under nitrogen flux (40 mL/min), in the 25-800°C temperature range at 10°C/min.

Dynamic Light Scattering (DLS). The suspensions of Nd/Yb CPs in water/DMSO were prepared by suspending 2 mg of microcrystalline powder in 2 mL of solvent and ultrasonicated for 15 min. Then were diluted (200 μL of suspension and 800 μL of solvents) to allow DLS performed with Malvern ZETASIZER NANO instrument.

Photophysical Measurements. Continuous-wave (Cw) diffuse reflectance of crystals of coordination compounds was performed with a dual-beam spectrophotometer equipped with an integrating sphere accessory (Agilent Cary 5000 UV−vis−NIR). Lanthanide centered photoluminescence was excited by a passively Q-switched powerchip laser (Teem Photonics PNV-M02510) delivering 310 ps long pulses at a 355 nm wavelength and a 1 kHz repetition rate, wavelength dispersed by a grating spectrometer (Princeton Instruments Acton SpectraPro 2300i), and detected by a NIR array detector (Andor iDus InGaAs 1.7 μm) for spectral measurements and a photomultiplier (Hamamatsu H10330A-75) connected to a 1 GHz digital oscilloscope (Tektronik TDS 5104) for time-resolved

measurements. Emission and excitation spectra were further recorded on a modular double grating excitation spectrofluorimeter with a TRIAX 320 emission monochromator (Fluorolog-3, Horiba Scientific) coupled to a near infrared H9170 Hamamatsu photomultipliers, using the front face acquisition mode. The excitation source was a 450 W Xe arc lamp. The excitation spectra were corrected for the spectral distribution of the lamp intensity using a photodiode reference detector. Time-resolved measurements were carried out with pulsed Xe-Hg lamp excitation, in front face acquisition mode. The low temperature measurements (12 K) were performed using a helium-closed cycle cryostat with vacuum system measuring ca. 5×10^{-6} mbar and a Lakeshore 330 auto-tuning temperature controller with a resistance heater.

3. Results and Discussion

3.1. Synthesis

NIR emitters-based Ln-CFs were synthesized through a solvent free method, showed in **Scheme 6.1**. $Ln(NO_3)_3 \cdot xH_2O$ (Ln = Yb^{III}, Nd^{III}) and 1,3,5-benzenetricarboxylic acid (H_3BTC, trimesic acid) were mixed in 1:1 ratio and grinded for 5 min, then thermal treated at 130°C for 24 hours. The evolution of the solvent free synthesis during the grinding process was monitored by PXRD, selecting Yb-BTC as representative reference sample, as shown in **Figure S6.1** (Supporting Material, *Part IV*, *Chapter 6*). During the grinding process, the peaks of the precursors start to disappear, according with the formation of an amorphous complex Ln-BTC and few amounts of the final product crystal seeds. Then, the thermal treatment induces a rearrangement of the amorphous complex, due to the π···π interactions and the electrostatic repulsive forces between the adjacent charged complex molecules, leading to the formation of the final product.[1] This synthetic methodology also affords bimetallic CFs by adding small percentage of a second Ln^{III} ion to the precursors mixture, to exploit the potential of $Nd^{III} \rightarrow Yb^{III}$ energy transfer, in influencing photoluminescence, by keeping constant the total metal amount:ligand ratio equal to 1:1. After the thermal treatment, by washing all the samples with water and ethanol, compounds formulated as $Nd_xYb_{1-x}(BTC)_3(H_2O)_6$ (x = 1 (**1**); x = 0.943 (**2**); x = 0.953 (**3**); x = 0.856 (**4**); x = 0.890 (**5**)) and $Nd_xYb_{1-x}(BTC)_6$ (x = 0.017 (**6**), x = 0 (**7**)) are obtained in form of microcrystalline powder.

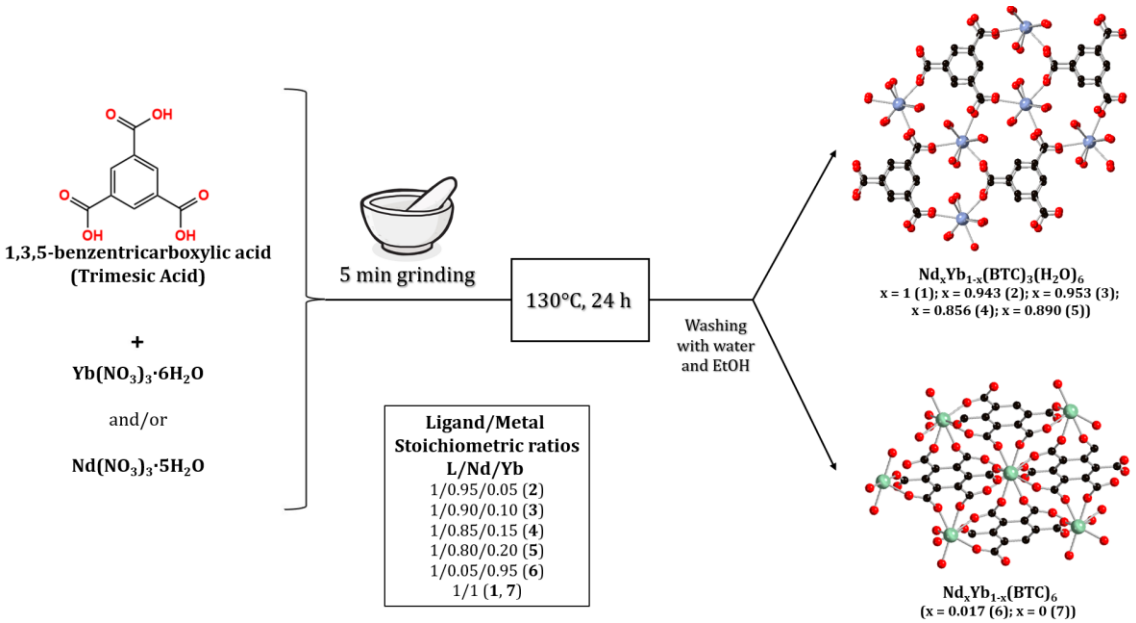

Scheme 6.1. Schematic representation of the solvent free synthesis for **1-7**.

3.2. Crystal Structure

All **1-7** compounds are obtained in form of microcrystalline powder, hence PXRD were performed firstly to **1** and **7** pristine materials to determine their crystal structure.

Compound **1** crystallizes in the monoclinic space group *Cc*, as a neutral polymeric framework, isostructural with a previously reported Gd^{III}-based structure.[18] The asymmetric unit of **1**, showed in **Figure 6.2a**, consists of one Nd^{III} ion, one fully deprotonated BTC unit and six water molecules. Each metal ion is nine coordinated, being surrounded by nine oxygen atoms, three from BTC linkers and six from water molecules, giving rise to the formula $Nd(BTC)_3(H_2O)_6$. The Nd^{III} ions are linked through BTC, forming parallel 1D ribbons running along *b* axis, as reported in **Figure 6.2b**. The ribbons are stacked with each other and interconnected through hydrogen bonds, leading to a 3D framework (**Figure 6.2c**).

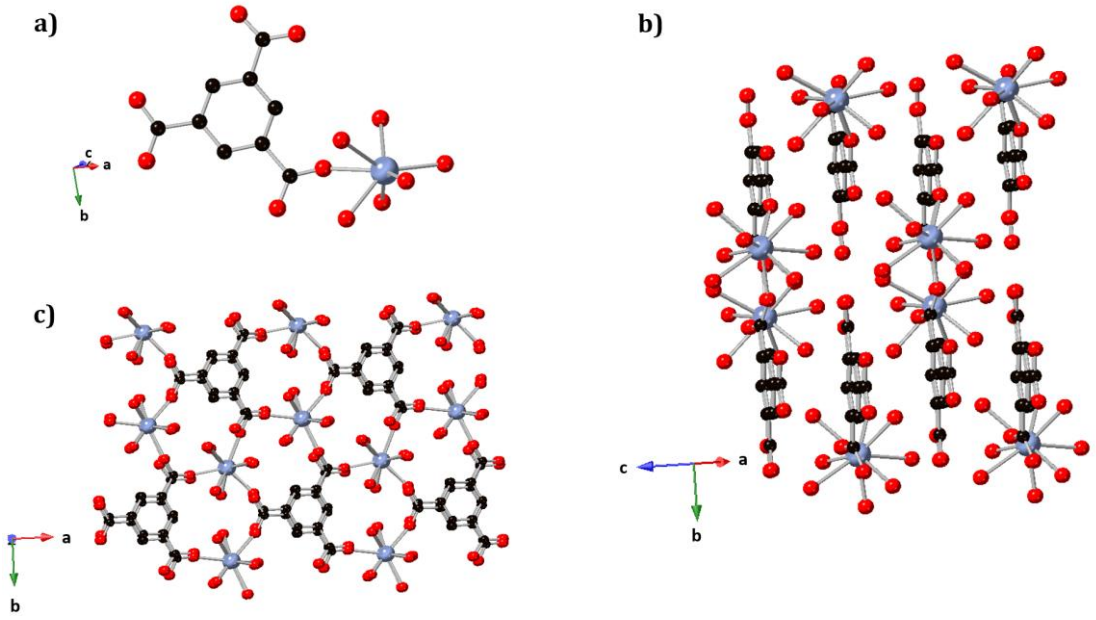

Figure 6.2. View of (a) the asymmetric unit of **1**, (b) parallel 1D ribbons running along *b* axis, (c) stacked ribbons in *ab* plane. The black, red, and pastel blue spheres represent the C, O, and Nd^{III} atoms, respectively, while hydrogen atoms are omitted for clarity.

Figure 6.3 depicts the enneacoordinated Nd atoms as green polyhedral, and dashed red contacts indicate the rich 3D framework of hydrogen bonding interlinking the different coordination spheres:

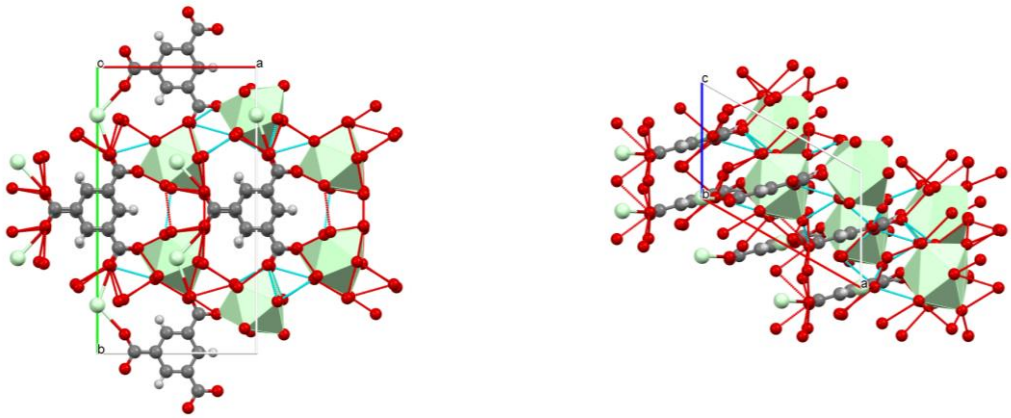

Figure 6.3. Sketch of the rich 3D hydrogen-bond framework (dashed red contacts) viewed down *c* (left) and down *b* (right).

The Nd-O bond distances are all slightly different and are reported in **Table 6.1**. As restraints were introduced in the final Rietveld refinement cycles to stabilize the otherwise untreatable refinement diverging to an unphysical model, the obtained values are mostly mirroring the numerical restriction of the Nd-O distances rather than their true similarity, or their dispersion. The six coordinated water molecules can be removed by heating **1** up to 130°C, as showed by thermogravimetric analysis (*vide infra*), leading to an amorphous phase.

Table 6.1. Nd-O bond distances in **1**.

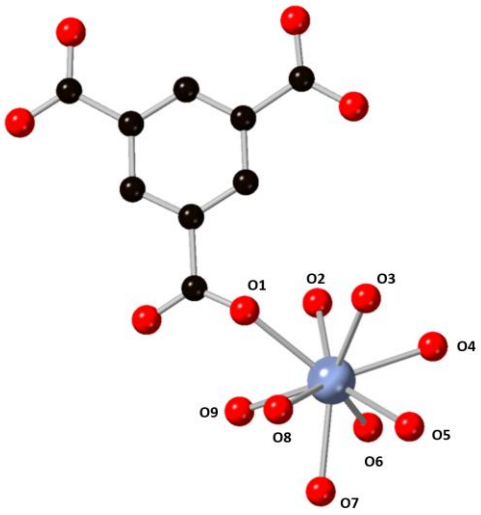

Bond	Distance (Å)
Nd-O1	2.467
Nd-O2	2.448
Nd-O3	2.522
Nd-O4	2.389
Nd-O5	2.479
Nd-O6	2.540
Nd-O7	2.401
Nd-O8	2.538
Nd-O9	2.431

Compound **7** crystallizes, instead, as neutral 3D framework of formula $Yb(BTC)_6$ in the trigonal *R-3c* space group. Its asymmetric unit consists of one Yb^{III} ion and 1/6 of the fully deprotonated BTC. The coordination sphere of each metal ion is composed by six oxygen atoms belonging to six individual BTC linkers (Yb-O bond distance of 2.184 Å), which in turn coordinate three Yb^{III} ions in the bridging coordination mode (**Figure 6.4a**), leading to the formation of a 3D CF, where Yb^{III} and BTC aromatic ring are stacked along *c* axis (**Figure 6.4b**) with a distance Yb^{III}-ring of 4.704 Å. When **7** is observed in *ac* plane, as shown in **Figure 6.4c**, it is evident how all the Yb^{III} ions lay on a different, but parallel, plane than BTC linkers, forming a dense structure with no accessible cavities, with $Yb^{III}\cdots Yb^{III}$ distances of 8.876 Å. Furthermore, **7** is an anhydrous framework with no water molecules, neither coordinated or solvated, present, as confirmed by thermogravimetric analysis (*vide infra*).

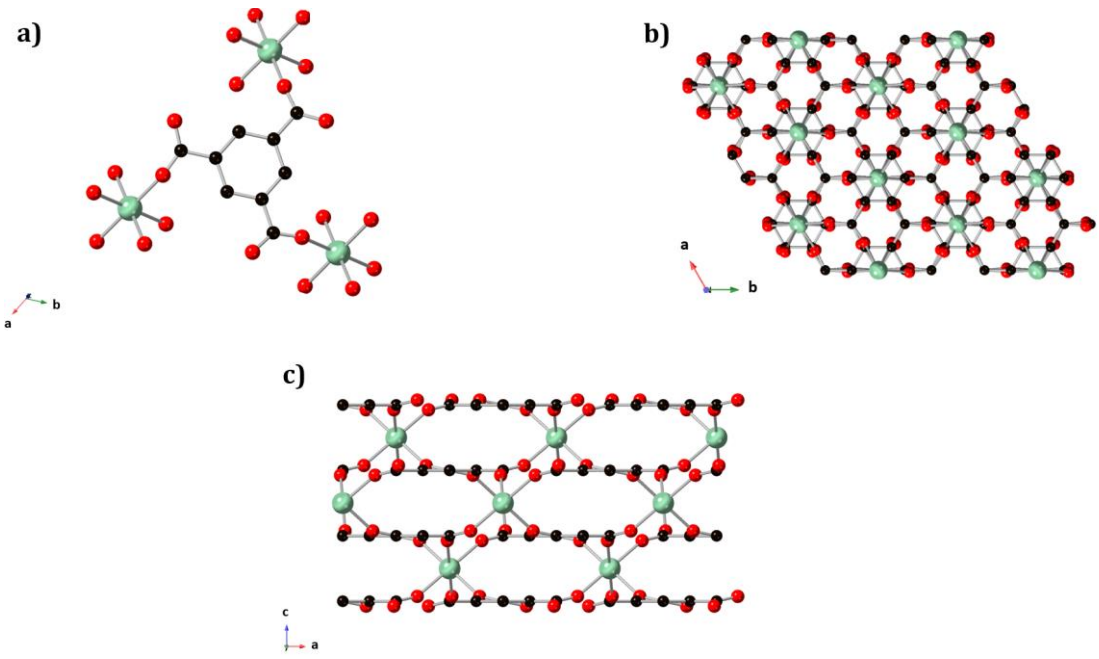

Figure 6.4. View of (a) one BTC linker coordinating three Yb^{III} ions, (b) 3D CF in the *ab* plane, showing Yb^{III} ions stacked along same *c* axis of aromatic BTC ring, (c) 3D CF in the *ac* plane, evidencing Yb^{III} and BTC laying in different planes. The black, red, and light green spheres represent the C, O, and Yb^{III} atoms, respectively, while hydrogen atoms are omitted for clarity.

Both **1** and **7** can be doped with a second metal ion (Yb^{III} and Nd^{III} for **1** and **7**, respectively) using the same synthetic method. Particularly, **1** can be doped with percentage of Yb^{III} up to 20% maintaining the same crystal structure, whereas it is possible to add only a maximum of 5% of Nd^{III} to **7**, since higher percentages lead to the formation of both Yb- and Nd- phases as a mixture of microcrystalline powders. **Figure**

6.5 and **6.6** report the PXRD for all the **1-7** CFs, showing the homogeneity of the doped phases.

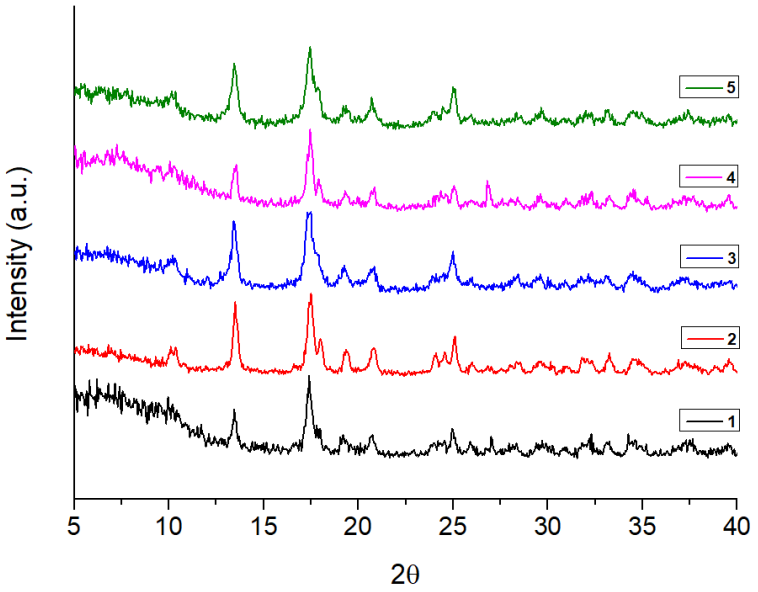

Figure 6.5. PXRD patterns in 5-40° 2θ range of **1-5**.

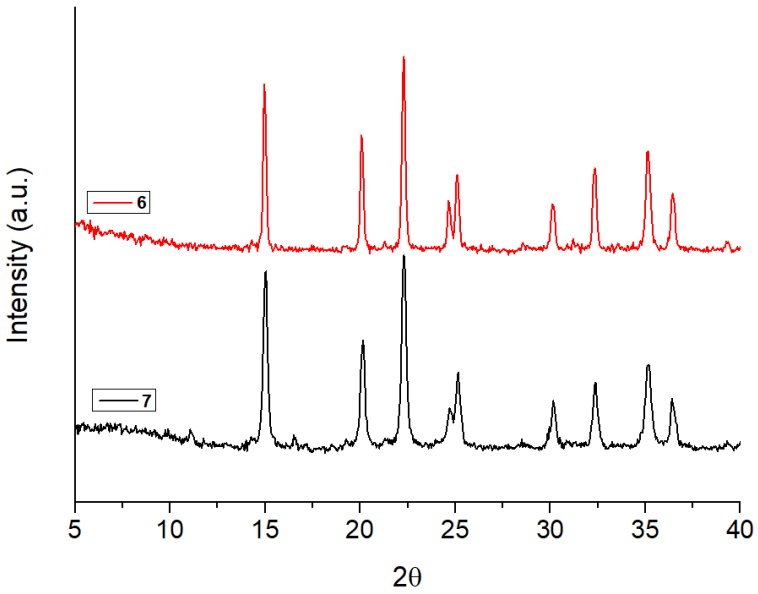

Figure 6.6. PXRD patterns in 5-40° 2θ range of **6** and **7**.

3.3. FT-IR Spectroscopy

Infrared Spectroscopy further confirm the CFs formation, by observing the presence of band attributable to Ln-O vibration and the bands related to carboxylate stretching in a coordination compound. In all spectra of **1-7** CPs, reported in **Figure 6.7** and **6.8**, the typical band at 1700 cm^{-1}, related with the vibrational stretching of carboxylic groups present in trimesic acid,[22] disappear due to the complete deprotonation of COOH groups and to their coordination in CFs.[23] Thus, new bands generated by the antisymmetric and symmetric stretching of carboxylate groups appears in the 1650-1550 and 1450-1350 cm^{-1} region.[23] Since carboxylates can coordinate in different modes (monodentate, bidentate, bridging, *etc.*), a general tendency relationships between their coordination modes and the stretching frequencies has been studied by Deacon and Phillips.[24] In fact, the frequency separation between the carboxylate antisymmetric and symmetric stretching vibrations ($\Delta\nu_{a\text{-}s}$) can be related with the coordination modes. In **1-7**, the $\Delta\nu_{a\text{-}s}$ is in 170-180 cm^{-1} frequencies range, that is attributable to the bridging coordination mode, where one metal ion binds to one of the two oxygens in the carboxylate group and another metal ion to the other oxygen atom.[24,25]

Furthermore, all **1-7** series display the Ln-O bands in the 600-400 cm^{-1} region,[26] and particularly, **6** clearly shows a further band at 412 cm^{-1} compared to **7**, mostly attributable to the presence of Nd^{III}, involved in Nd-O bond.

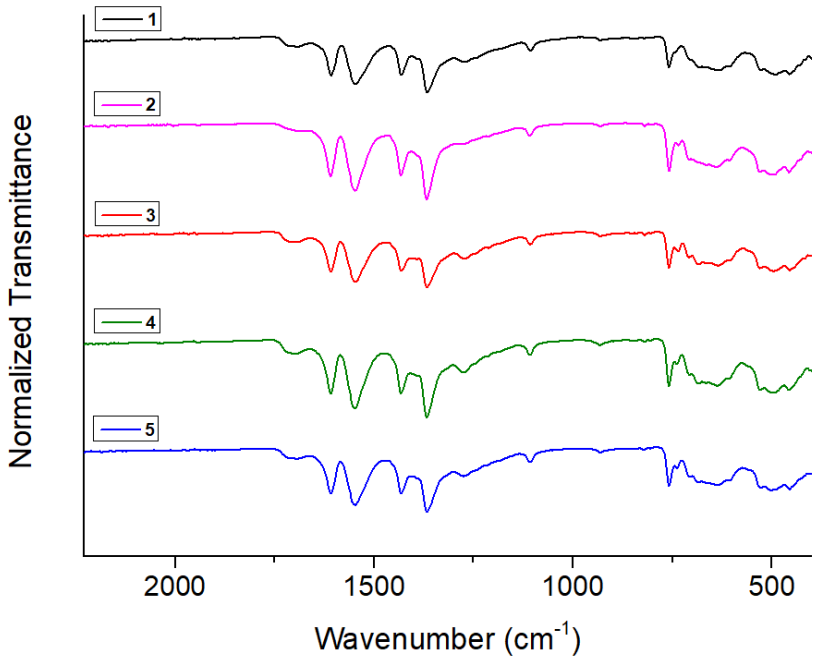

Figure 6.7. FT-IR spectra of **1-5** in 2250-400 cm^{-1} range.

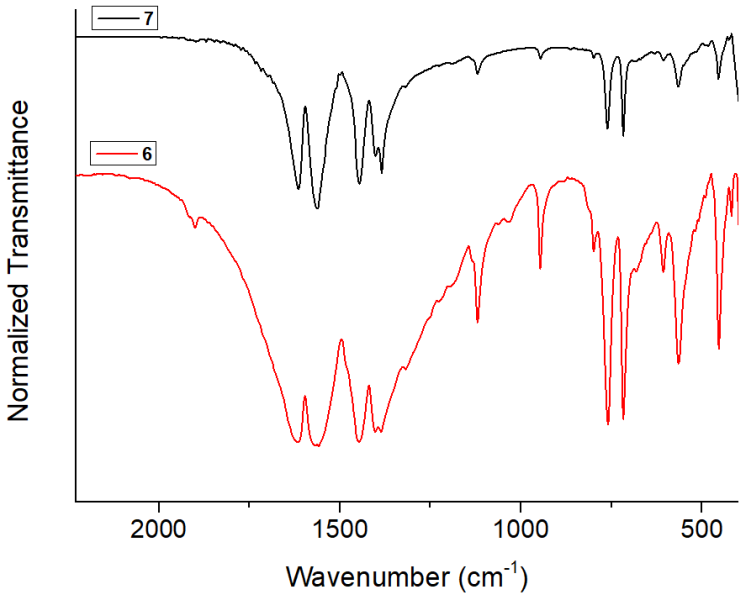

Figure 6.8. FT-IR spectra of **6** and **7** in 2250-400 cm^{-1} range.

3.4. Thermogravimetric Analysis

Thermograms of **1** and **7** were measured to study the thermal stability and water content of the two representative structures. **1** shows a first weightloss of 18.73% at 130°C, consistent with the six coordinated water molecules, and a second 7.65% weightloss at 303°C consistent with a first degradation of the trimesic acid, which degrades completely at 540°C leading to the collapse of the CF (**Figure 6.9**).

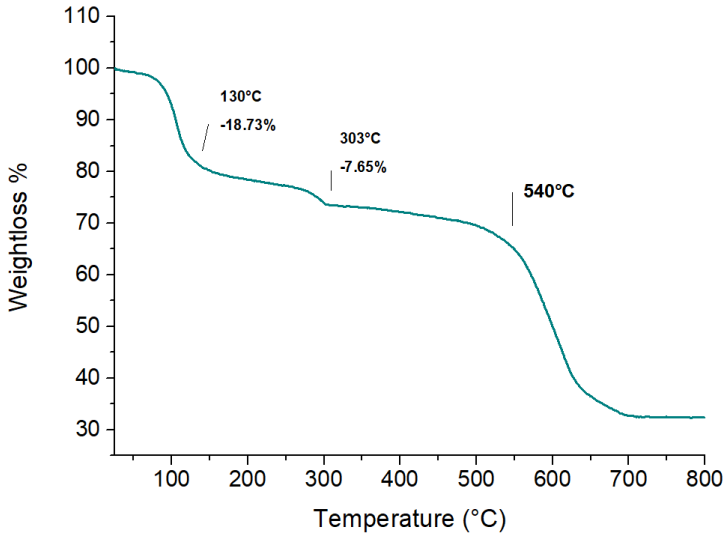

Figure 6.9. Thermogram of **1** in 25-800°C temperature range. The percentages shown in the graph are referred to the previous one weightloss.

Thermogram of **7** confirms the absence of water in the structure, neither absorbed or coordinated, with the first 10% weightloss at 450°C, followed by the degradation of the CFs at 516°C after the complete ligand decomposition, proving and excellent thermal stability (**Figure 6.10**).

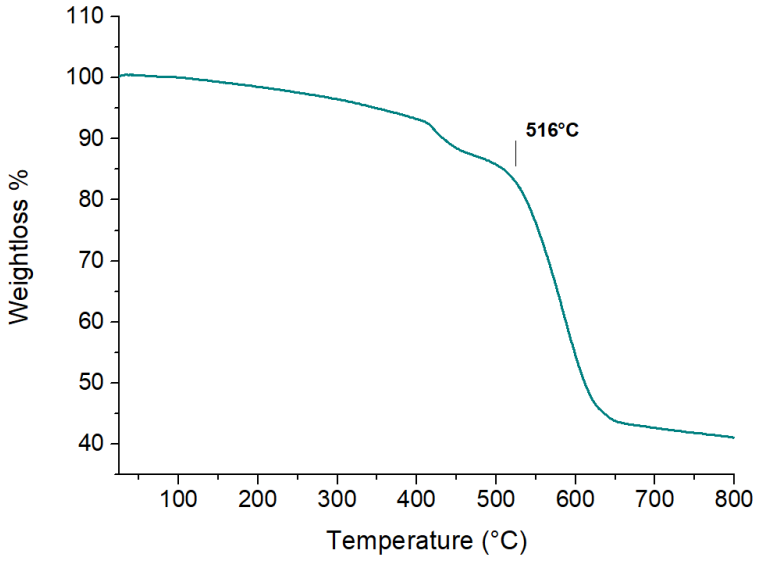

Figure 6.10. Thermogram of **7** in 25-800°C temperature range.

3.5. Morphological Characterization

To verify the morphological homogeneity of the **1-5** and **6-7** doped samples and to have a first insight on the semi-quantitative ratio between Nd/Yb metal ions, Scanning Electron Microscopy (SEM) was performed, while Microanalysis was performed in different areas of each sample, obtaining similar results, as shown in **Table S6.1.**

Compound **1** shows a needle like morphology, consistent with the ribbon crystal structure, and the same morphological aspect was found in all CFs **2-5**, further proving the homogeneity of the Nd-based CPs. Here, SEM images of **1-3** are reported as representative examples in **Figure 6.11** below.

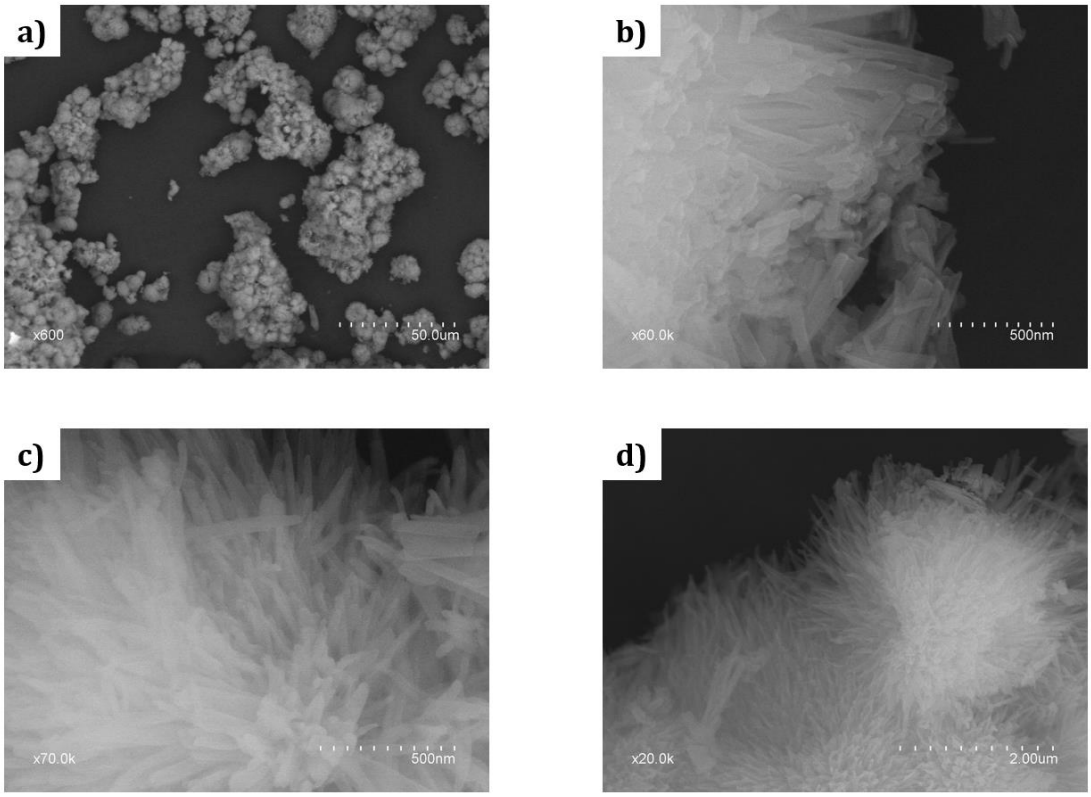

Figure 6.11. SEM images of **1** (a and b), **2** (c) and **3** (d).

7 shows a granular morphology when observed in 50 μm scale, as well as **6**, proving the homogeneity of the two samples (**Figure 6.12**). Due to the instability under the electron beam of **6** and **7,** it was difficult to collect images with a higher magnification.

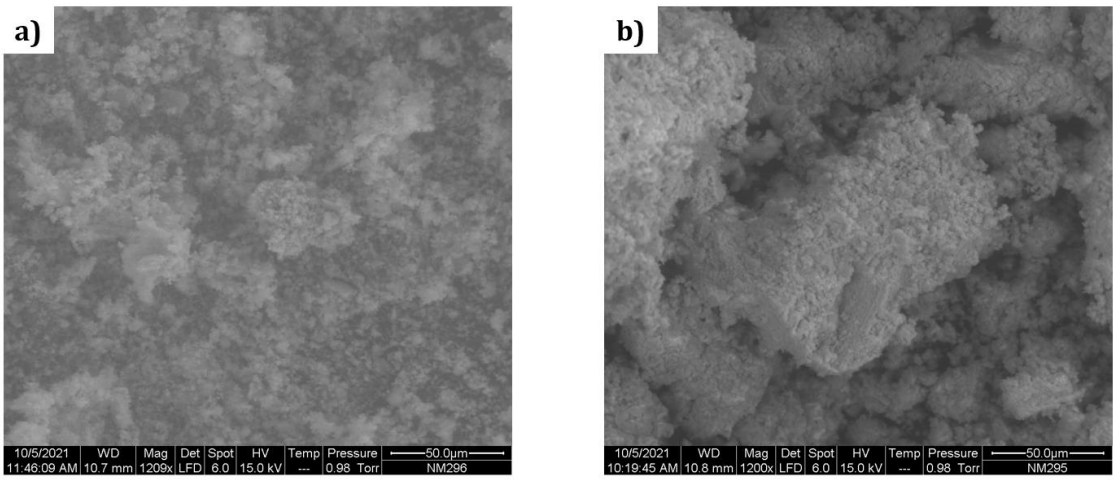

Figure 6.12. SEM images of **7** (a) and **6** (b).

EDX microanalysis confirms the presence of only one Ln^{III} ion both in **1** and **7** and provide a semiquantitative Nd/Yb ratio in **2-6** samples, which is reported in **Table 6.2** below, in comparison with the formula of each sample obtained by ICP-MS.

Table 6.2. Nd/Yb stoichiometric ratio of each sample, along with semiquantitative Nd/Yb ratio obtained by EDX measurements and quantitative Nd/Yb ratio provide by ICP-MS.

Sample	Nd/Yb stoichiometric ratio	Nd/Yb EDX	Nd/Yb formula
1	100% Nd		$Nd(BTC)_3(H_2O)_6$
2	95/5	95.1/4.9	$Nd_{0.943}Yb_{0.057}(BTC)_3(H_2O)_6$
3	90/10	96/4	$Nd_{0.953}Yb_{0.047}(BTC)_3(H_2O)_6$
4	85/15	89.5/10.5	$Nd_{0.856}Yb_{0.144}(BTC)_3(H_2O)_6$
5	80/20	88.4/11.6	$Nd_{0.889}Yb_{0.111}(BTC)_3(H_2O)_6$
6	5/95	1.53/98.4	$Nd_{0.017}Yb_{0.983}(BTC)_6$
7	100% Yb		$Yb(BTC)_6$

3.6. Photophysical Characterization

To further probe the presence of both metals in the same frameworks, Diffuse Reflectance (DR) has been performed in 200-2000 nm wavelength range. DR spectra of **1-7** show absorption bands around 1970, 1660 and 290 nm due to the BTC linker. In **1-5** series (spectra reported in **Figure 6.13**), all the absorption bands of Nd^{III} appear respectively at 872 nm ($^4I_{9/2} \rightarrow {}^4F_{3/2}$), 798 nm ($^4I_{9/2} \rightarrow {}^4F_{5/2}$), 740 nm ($^4I_{9/2} \rightarrow {}^4F_{7/2}$), 680 nm ($^4I_{9/2} \rightarrow {}^4F_{9/2}$), 578 nm ($^4I_{9/2} \rightarrow {}^2G_{7/2}$), 524 nm ($^4I_{9/2} \rightarrow {}^4G_{7/2} + {}^2K_{13/2}$), 513 nm ($^4I_{9/2} \rightarrow {}^4G_{9/2}$) and 355 nm ($^4I_{9/2} \rightarrow {}^4D_{5/2}$).[27] In **2-5**, a further band at 980 nm appears, confirming the presence of Yb^{III} ($^2F_{7/2} \rightarrow {}^2F_{5/2}$) in the CFs.[27] Compound **6** shows as well the absorption bands of both Nd^{III} and Yb^{III} ions, compare to **7** which displays only the Yb^{III} absorption band, as shown in **Figure 6.14**.

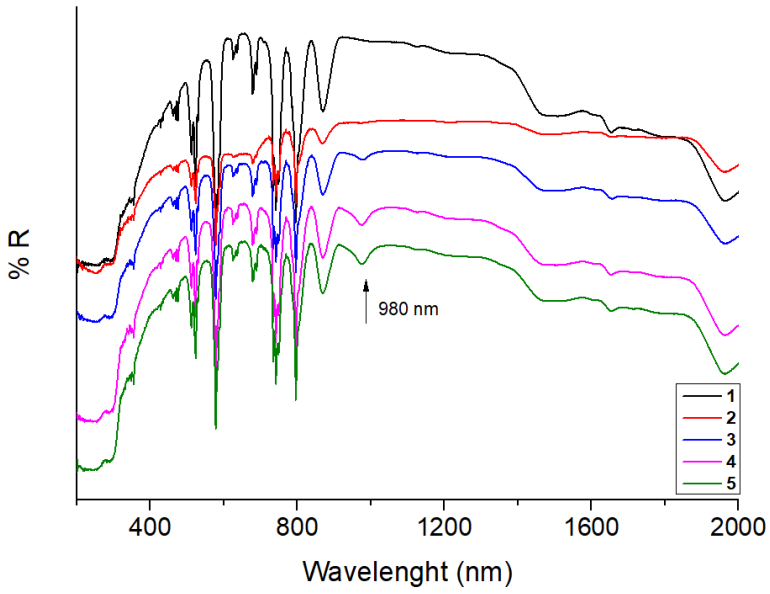

Figure 6.13. DR spectra of **1-5** in 200-2000 nm wavelength range.

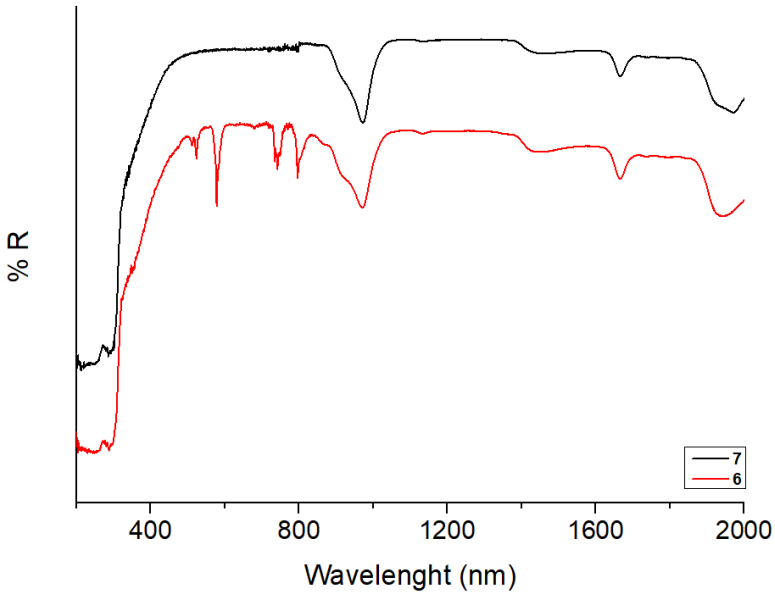

Figure 6.14. DR spectra of **6** and **7** in 200-2000 nm wavelength range.

The photoluminescent (PL) properties of **1-7** were investigated by PL spectra at room temperature, as reported in **Figure 6.15** and **Figures S6.2-S6.3** (*Supporting Material, Part IV*). Upon excitation at 580 nm, all the **1-5** series show the typical Nd^{III} emission bands that are related with the $^4F_{3/2} - {}^4I_J$ (J = 13/2, 11/2, 9/2) transitions in 800 - 1450 nm wavelength range.[28] When Yb^{III} is present in the CFs, its typical emission band correspondent to $^2F_{5/2}–{}^2F_{7/2}$ transition it appears at 980 nm,[28] as shown in **Figure 6.20** and **Figure S6.2**, suggesting the existence of energy transfer from Nd^{III} to Yb^{III}, which

can be also observed by using a NIR laser (808 nm) (**Figure S6.4**). Upon excitation the Nd^{III} ions, which are in their $^4F_{5/2}$ energy state, can either relax to their $^4F_{3/2}$ energy level or transfer the energy to the Yb^{III} ions energy level $^4F_{5/2}$ *via* non-radiation energy transfer. At this point, both the characteristic Yb^{III} emission band related to $^2F_{5/2}$–$^2F_{7/2}$ transition at 980 nm and the Nd^{III} emission bands of $^4F_{3/2}$ – ^4I_J (J = 13/2, 11/2, 9/2) transitions at 890, 1060 and 1350 nm are observed.[28]

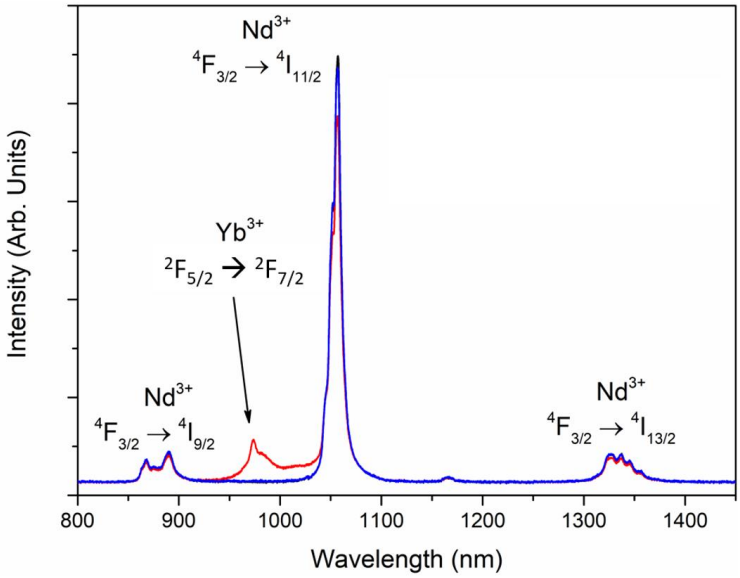

Figure 6.15. Emission spectra of **1** (blue line) and **5** (red line) excited at 580 nm.

Taking into account the thermal dependence of this energy transfer from Nd^{III} to Yb^{III}, such systems can be exploited as ratiometric thermometers. Firstly, emission of **1** was studied at different temperatures, as reported in **Figure 6.16**, showing a relatively weak signal at 1058 nm, assigned to the Nd^{III} $^4F_{9/2}$ → $^4I_{11/2}$ transition, upon 580 nm excitation. The intensity of the signal is weak considering the excitation of the second order around 1160 nm as reference and in this case no significant changes were observed when decreasing the temperature.

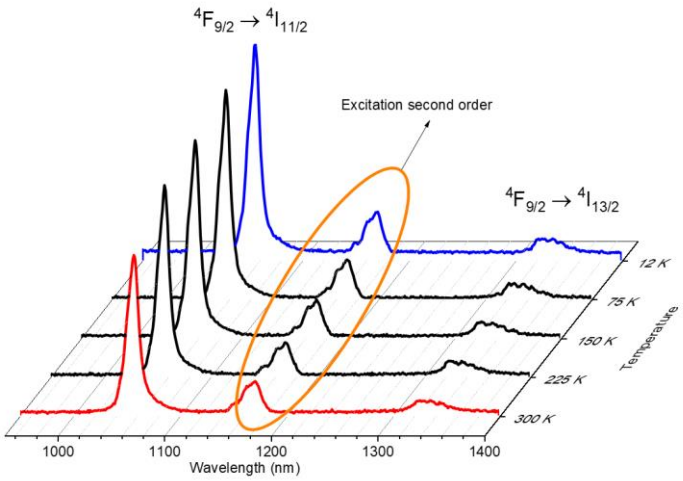

Figure 6.16. Emission spectra of **1** excited at 580 nm, in 5-350 K range temperature.

Among the **2-5** series, **5** was selected as the most promising system for ratiometric temperature sensing because of its high intensity compared to the rest of the samples and the large variation of relative intensities with temperature. Therefore, its temperature-dependent photoluminescent properties were studied both in terms of intensity and lifetime in order to establish its potential as luminescent thermometers (**Figure 6.17**).

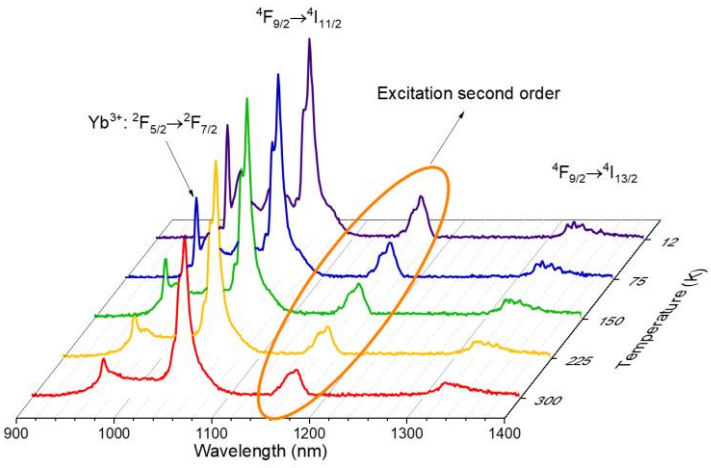

Figure 6.17. Emission spectra of **5** excited at 580 nm, in 5-350 K range temperature.

5 shows two different signals at 980 and 1058 nm, attributed to the Yb^{III} $^2F_{5/2} \rightarrow {}^2F_{7/2}$ and Nd^{III} $^4F_{3/2} \rightarrow {}^4I_{11/2}$ transitions, respectively. The Nd^{III} signal here is slightly more intense than in **1**, because a higher concentration of Nd^{III} ions results in a higher quenching effect. In addition, a weak signal at 1340 nm was observed and assigned to the

$^4F_{3/2} \rightarrow {}^4I_{13/2}$ transition. The relative intensity of Yb^{III} increases when decreasing the temperature and slight changes in the relative intensities between Yb^{III} and Nd^{III} emission bands at 1000 and 1057 nm, respectively, are observed at different temperatures (**Figure 6.18**). Further luminescence measurements at different physiological temperatures as well as biological assays will be further performed on this sample. Additionally, at 300 K, the Yb^{III} and Nd^{III} emission lifetimes in **5** are 6.97±0.32 μs and 56.2±0.2 ns, respectively, as reported in **Figure 6.19**.

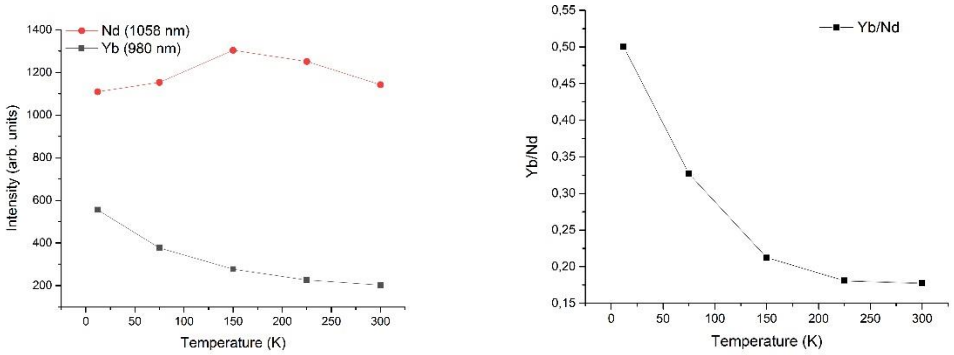

Figure 6.18. Representation of a) Nd and Yb signal intensities and b) Yb/Nd signal ratio at different temperatures.

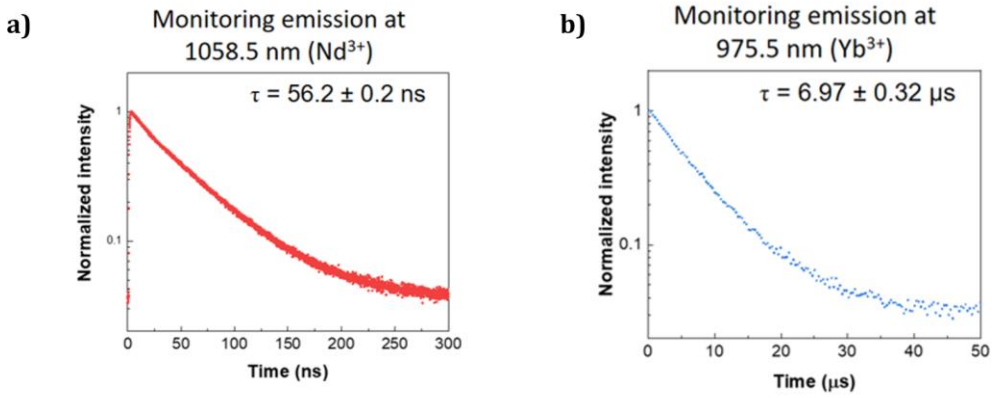

Figure 6.19. $^4I_{11/2}$ and $^2F_{7/2}$ decay curves of **5** monitoring the Nd^{III} (a) and Yb^{III} (b) emissions at 1058.5 and 975.5 nm, respectively, with the excitation fixed at 801 nm.

Considering the inverse ratio of Nd/Yb in **6**, its emission spectra were measured by using different excitation wavelength, in particular λ_{ex} = 355, 580, 808 and 980 nm. Upon excitation at 355 nm, the characteristic emission band at 980 nm ($^2F_{5/2} \rightarrow {}^2F_{7/2}$) of Yb^{III} ions is present, as reported in the **Figure 6.20** and **Figure S6.2**, indicating that

BTC^{3-} linker is able to act as *antenna* sensitizing Yb^{III} ions emission. Additionally, the spectrum of **6** shows a not well-resolved signal at 1070 nm and a very weak signal at 1325 nm due to the $^4F_{3/2} \rightarrow {}^4I_{11/2}$ and $^4F_{3/2} \rightarrow {}^4I_{13/2}$ transitions of Nd^{III} ions, respectively. The emission lifetime of Yb^{III} is 1.5 μs along with a very fast component arising from Nd^{III} ions, at 1070 nm and 1325 nm, is observed (**Figure 6.21**). This fast decay, which lead to emission lifetime values in the nanosecond time scale, could be attributable to the energy transfer from Nd^{III} to Yb^{III}.[29]

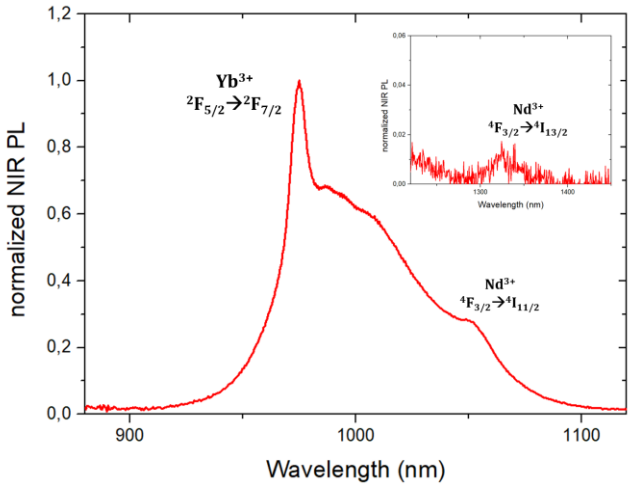

Figure 6.20. Emission spectra of **6** excited at 355 nm (inset: weak signal of Nd^{III} $^4F_{3/2} \rightarrow {}^4I_{13/2}$ transition).

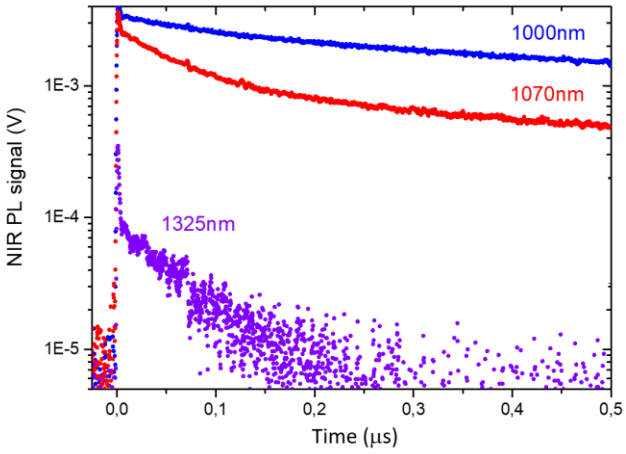

Figure 6.21. Decay curves of **6**, monitoring the Nd^{III} $^4I_{13/2}$ (purple dots) and $^4I_{11/2}$ (red dots) and Yb^{III} $^2F_{7/2}$ (blue dots) emissions at 1325, 1070 and 1000 nm, respectively, with the excitation fixed at 355 nm.

Compound **6** was further studied by directly exciting Nd^{III} ions at 580 nm (**Figure 6.22**) and it shows similar emission bands than **5**, but less intense. Excitation at 808 nm provoke a similar spectrum (**Figure S6.5a**) with a further signal at 1200 nm, which may be assigned to second-order Nd^{III} upconversion red emission ($^4G_{5/2}$), at 600 nm, under

800 nm pumping.[30] Finally, when **6** is excited at 980 nm (**Figure S6.6**) a really weak upconversion signal is observed in 1000-1400 nm wavelength range.

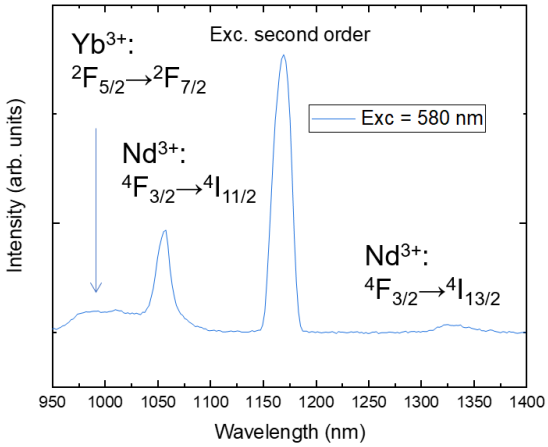

Figure 6.22. Emission spectrum of **6** excited at 580 nm.

Finally, emission spectra of **6** were as well measured at different temperatures upon 580 nm excitation (**Figure 6.23**). Here, despite the second order excitation is higher than the sample signal, it is still possible to observe a slight increase of Yb^{III} emission and thus a temperature dependent change in the intensity ratios of Yb^{III}/Nd^{III} bands. Since the excitation is directly on Nd^{III} ions, the energy transition involved is again Nd^{III} → Yb^{III}, in this case less efficient because Nd^{III}, the sensitizer, is present in a small amount in the sample.

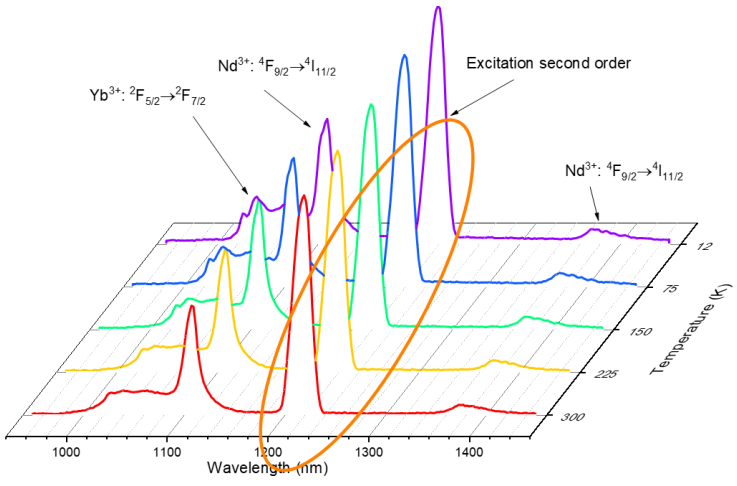

Figure 6.23. Emission spectra of **6** excited at 580 nm, in 5-350 K range temperature.

3.7. Stability Tests

The most interesting samples among these CFs for thermometry applications are **5** and **6**, hence, to study their stability in water or DMSO for further biocompatibility tests, suspensions of **5** and **6** have been prepared and investigated firstly by DLS and then by PXRD measurements.

DLS was performed on **5** and **6** suspended in both water and DMSO. All the four suspensions were milky white and were diluted 1:4 to perform the measurements. **5** shows to be stable in DMSO (**Figure 6.24**) with a size distribution centered at 396 nm, whereas **5** is not stable in the water suspension in which the mean size decreases over a time of few minutes.

On the contrary, **6** shows to be more stable in water suspension (**Figure 6.25**) with a mean diameter of 450 nm, while in DMSO the size decreases over few minutes due to the high instability of the suspension.

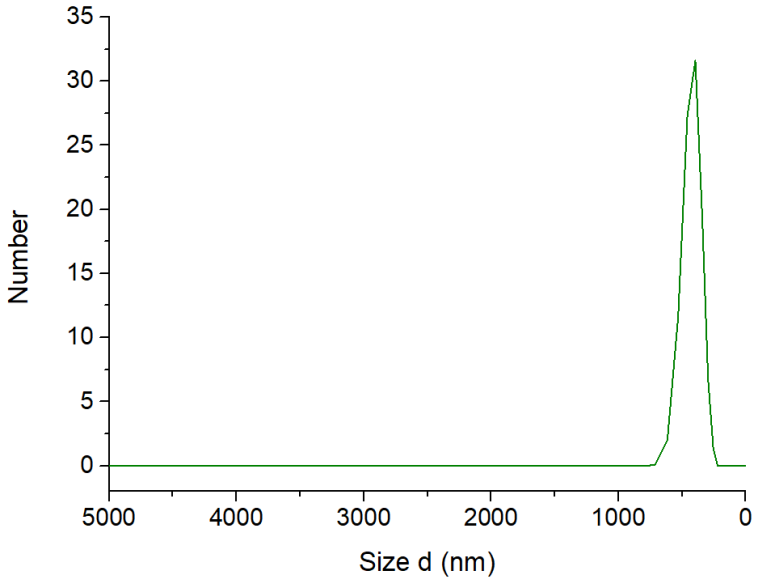

Figure 6.24. Hydrodynamic diameter distribution of suspension of **5** in DMSO mediated between three measurements.

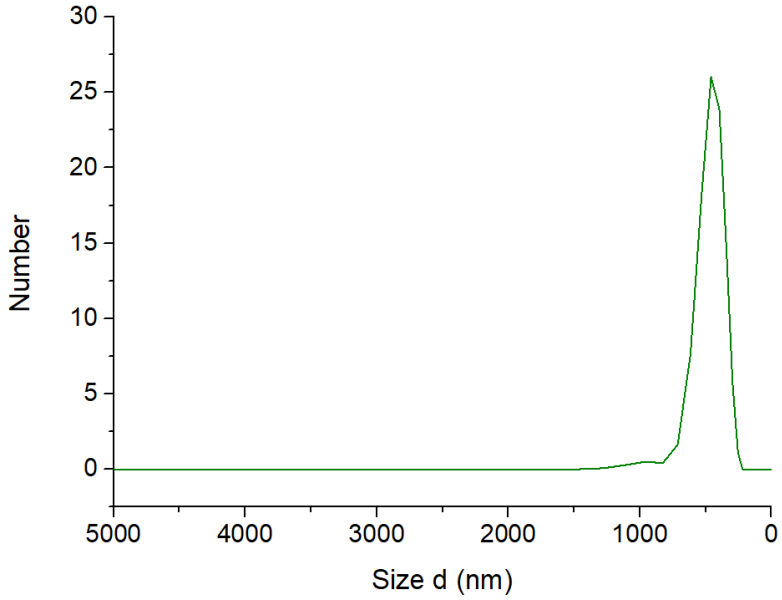

Figure 6.25. Hydrodynamic diameter distribution of suspension of **6** in water mediated between three measurements.

The DMSO and water suspensions of **5** and **6** respectively show stability up to 1-2 hours, after a white precipitate is observed in the vial's bottom.

To verify the crystal structure retainment, PXRD was performed on **5** and **6** respectively soaked in DMSO and water. Each sample was soaked for 2 hours and then deposited on a zerobackground sample holder to be measured. Both samples show excellent stability after soaking, as showed in **Figure 6.26**. In **5**, a small amorphous contribution is observed below 13°, most probably due to the DMSO not completely evaporated, while **6** shows almost the same PRXD pattern after the water soaking.

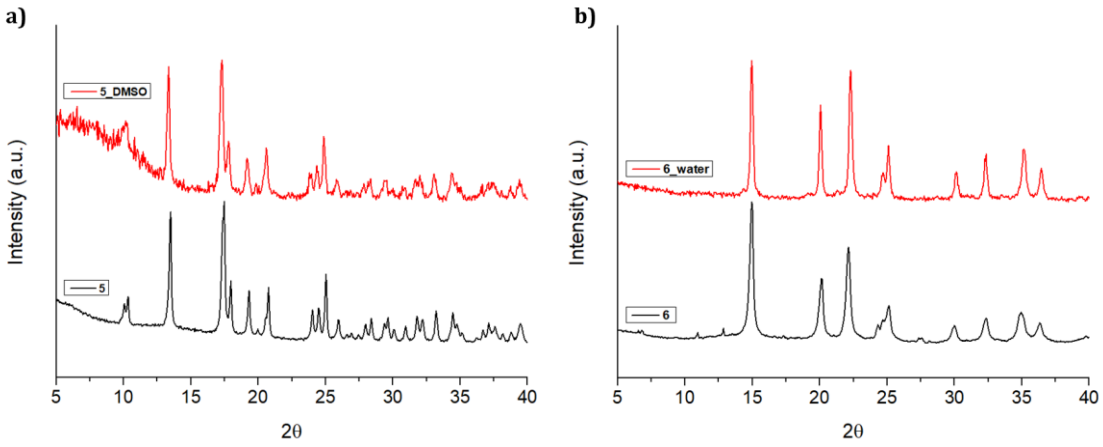

Figure 6.26. PXRD patterns in 5-40° 2θ range of **5** (a) and **6** (b) after soaking in DMSO and water, respectively.

4. Conclusions

A series of NIR luminescent mixed Yb^{III}/Nd^{III} CFs was obtained by using H_3BTC, a biofriendly linker, combined with the Nd^{III} and/or Yb^{III} ions *via* solvent free method. The two different classes of CFs, formulated respectively as $Nd_xYb_{1-x}(BTC)_3(H_2O)_6$ (x = 1 (**1**); x = 0.943 (**2**); x = 0.953 (**3**); x = 0.856 (**4**); x = 0.890 (**5**)) and $Nd_xYb_{1-x}(BTC)_6$ (x = 0.017 (**6**), x = 0 (**7**)), were fully characterized by using a multi-technique approach to investigate their structure and morphology, stability and optical properties. X-Ray Diffraction studies provide information about the two representative pristine samples **1** and **7**, Nd^{III} and Yb^{III}-based respectively. **1** crystallizes as neutral polymeric framework with hydrated ribbon-like structure where a network of hydrogen bonding allows the interlinking of different coordination spheres, affording an organized 3D framework. **7** crystallizes as well in a neutral polymeric framework, which is close-packed, and no coordinated or adsorbed water molecules are present in the structure. Both phases proved high thermal stability (up to 500 °C) and chemical stability, retaining their crystal structure upon soaking in solvent as DMSO or water. Both **1** and **7** could be doped with different percentage of the second Ln^{III} (maximum of 5% of Nd^{III} in **7** and maximum of 20% of Yb in **1**) ion proving to be structurally and morphologically homogenous. The presence of both metals was confirmed by ICP-MS, providing the correct formulae, SEM-EDX and Diffuse Reflectance. Photophysical studies at different conditions evidenced the role of BTC as *antenna* for Yb^{III} ions and the mechanism of energy transfer Nd^{III}-to-Yb^{III}. Particularly, **5** and **6** were selected to perform variable temperature photoluminescence studies in 10-300K range, which revealed a decrease of intensity ratio Yb/Nd with the increase of the temperature. This trend is more evident in **5**, which is the most promising system among the series to be employed as a thermometer. Hence, its performance as thermometer, in terms of relative sensitivity and thermal resolution parameters, will be further explored along with its miniaturization and biocompatibility to be used as a thermometer in biological tissues.

References

1 C. D. S. Brites, S. Balabhadra and L. D. Carlos, *Adv. Opt. Mater.*, 2019, **7**, 1–30.

2 D. Jaque and F. Vetrone, *Nanoscale*, 2012, **4**, 4301–4326.

3 F. Tardieu, M. Reymond, P. Hamard, C. Granier and B. Muller, *J. Exp. Bot.*, 2000, **51**, 1505–1514.

4 G. N. Somero, *Annu. Rev. Physiol.*, 1995, **57**, 43–68.

5 A. M. Stark and S. Way, *Cancer*, 1975, **33**, 1664–1670.

6 T. B. Huff, L. Tong, Y. Zhao, M. N. Hansen, J.-X. Cheng and A. Wei, *Nanomedicine*, 2007, **2**, 125–132.

7 J. Rocha, C. D. S. Brites and L. D. Carlos, *Chem. - A Eur. J.*, 2016, **22**, 14782–14795.

8 M. Quintanilla, I. García, I. De Lázaro, R. García-Alvarez, M. Henriksen-Lacey, S. Vranic, K. Kostarelos and L. M. Liz-Marzán, *Theranostics*, 2019, **9**, 7298–7312.

9 Y. Cui, H. Xu, Y. Yue, Z. Guo, J. Yu, Z. Chen, J. Gao, Y. Yang, G. Qian and B. Chen, *J. Am. Chem. Soc.*, 2012, **134**, 3979–3982.

10 Y. Pan, H. Q. Su, E. L. Zhou, H. Z. Yin, K. Z. Shao and Z. M. Su, *Dalt. Trans.*, 2019, **48**, 3723–3729.

11 D. Ananias, C. D. S. Brites, L. D. Carlos and J. Rocha, *Eur. J. Inorg. Chem.*, 2016, **2016**, 1967–1971.

12 D. Zhao, J. Zhang, D. Yue, X. Lian, Y. Cui, Y. Yang and G. Qian, *Chem. Commun.*, 2016, **52**, 8259–8262.

13 C. Gu, Y. Ding, X. Quan, M. Gong, J. Yu, D. Zhao and C. Li, *J. Rare Earths*, 2021, **39**, 1024–1030.

14 G. E. Gomez, R. Marin, A. N. Carneiro Neto, A. M. P. Botas, J. Ovens, A. A. Kitos, M. C. Bernini, L. D. Carlos, G. J. A. A. Soler-Illia and M. Murugesu, *Chem. Mater.*, 2020, **32**, 7458–7468.

15 X. Lian, D. Zhao, Y. Cui, Y. Yang and G. Qian, *Chem. Commun.*, 2015, **51**, 17676–17679.

16 J. Liu, L. Pei, Z. Xia and Y. Xu, *Cryst. Growth Des.*, 2019, **19**, 6586–6591.

17 TOPAS-R V. 3.0, *Bruker AXS, Karlsruhe, Ger.*

18 A. A. Coelho, *J. Appl. Crystallogr.*, 2003, **36**, 86–95.

19 K. Davies, S. A. Bourne and C. L. Oliver, *Cryst. Growth Des.*, 2012, **12**, 1999–2003.

20 D. T. De Lill and C. L. Cahill, *Chem. Commun.*, 2006, 4946–4948.

21 R. W. Cheary and A. Coelho, *J. Appl. Crystallogr.*, 1992, **25**, 109–121.

22 G. Mahalakshmi and V. Balachandran, *Spectrochim. Acta - Part A Mol. Biomol. Spectrosc.*, 2014, **124**, 535–547.

23 J. Sienkiewicz-Gromiuk, I. Rusinek, Ł. Kurach and Z. Rzączyńska, *J. Therm. Anal. Calorim.*, 2016, **126**, 327–342.

24 G. B. Deacon and R. J. Phillips, *Coord. Chem. Rev.*, 1980, **33**, 227–250.

25 M. Nara and M. Tanokura, *Biochem. Biophys. Res. Commun.*, 2008, **369**, 225–239.

26 F. M. A. Kerim, H. F. Aly and A. El-Agramy, *Proc. Indian Acad. Sci. - Sect. A*, 1977, **85**, 559–566.

27 W. Feng, Y. Zhang, Z. Zhang, P. Su, X. Lü, J. Song, D. Fan, W. K. Wong, R. A. Jones and C. Su, *J. Mater. Chem. C*, 2014, **2**, 1489-1499.

28 D. Yue, J. Zhang, D. Zhao, X. Lian, Y. Cui, Y. Yang and G. Qian, *J. Solid State Chem.*, 2016, **241**, 99–104.

29 F. Artizzu, A. Serpe, L. Marchiò, M. Saba, A. Mura, M. L. Mercuri, G. Bongiovanni, P. Deplano and F. Quochi, *J. Mater. Chem. C*, 2015, **3**, 11524–11530.

30 J. X. Zhang, D. Hou, J. Y. Li, H. Lin, R. Huang, Y. Zhang and J. Hao, *J. Phys. Chem. C*, 2020, **124**, 19774–19780.

PART III

Summary and Outlook

The results therein presented, summarized in the Scheme below, highlight the great versatility of CFs to be potentially employed in various technological applications. To engineer CFs with magnetic and/or luminescent properties, organic linkers, belonging to carboxylate and anilate classes, have been combined with a wide variety of metal ions, through *green* synthetic strategies. 1,3,5-benzentricarboxylic acid, a biofriendly tritopic linker, which possess an aromatic ring as *core unit* and an unexplored anilate tetratopic linker, bearing two triazolyl groups at the 3,6 positions of the benzoquinone *core unit*, have been selected. As metal nodes, *d*-(M^{II}=Co, Cu, Ni, Mn and Fe) and *f*-(Ln^{III}=Nd, Er, Yb, Dy, Tb, Ho) transition metal ions have been used. The structural, morphological and physical characterization of the obtained materials has been performed *via* a Multi-Technique Approach, involving SC-XRD, PXRD, SQUID, PPMS, SEM-EDX, TGA, FT-IR, MicroRaman, CV and PL Spectroscopy.

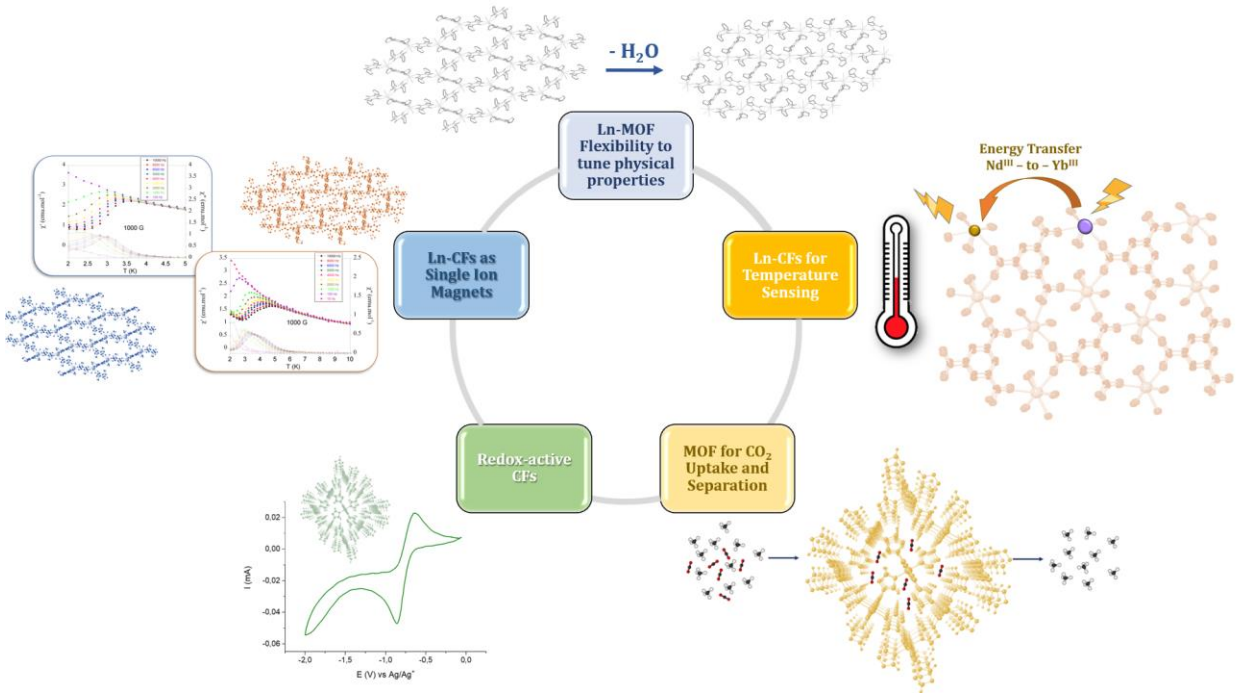

The 3,6-N-ditriazolyl-2,5-dihydroxy-1,4-benzoquinone (H_2trz_2An) along with the new 3,6-N-(dipyrazolyl-4-carboxylic acid)-2,5-dihydroxy-1,4-benzoquinone anilate derivatives, have been prepared and characterized *via* Elemental Analysis, NMR, MS, CV, FT-IR, Raman and Fluorescence Spectroscopies. The potential of H_2trz_2An as molecular building block for the construction of robust 3D CFs has been almost unexplored so far.

When H_2trz_2An is combined with *3d* transition metal ions, particularly M^{II} = Co, Cu, Mn, Ni and Fe, different 3D CFs are afforded thanks to the presence of triazolyl groups at the 3,6 positions of the anilate moiety, which act as a coordinative pendant arms. The materials, formulated as $[M_2(trz_2An)_2]_n3H_2O$ (M^{II} = Co, Cu and Ni), $[Mn(trz_2An)(H_2O)]_n \cdot 2H_2O$ and $[M(trz_2An)]_n \cdot 2H_2O$ (M = Fe^{II}/Fe^{III}, Co^{II}) respectively, have been prepared *via* hydrothermal or one-pot methods and they have been thoroughly characterized, mainly through SC-XRD, SQUID and CV, that evidenced their redox active behavior.

Among the obtained CFs, the 3D $[Co_2(trz_2An)_2]_n3H_2O$ ultramicroporous MOF, has been selected for its potential in CO_2 uptake and separation, due to its structure and the possibility to scale up to 8 times its synthesis. Remarkably, Co^{II}-MOF shows impressive thermal and chemical robustness, high selectivity and adsorption capacity for CO_2 and high regenerability. All these features make this MOF an appealing candidate for industrial applications.

By combining the same linker with *4f* transition metal ions, particularly Ln^{III} = Er, Dy, Tb and Ho, two different 3D CFs polymorphs (phase a and b) differing for the number of uncoordinated water molecules, formulated as $[Ln_2(trz_2An)_3(H_2O)_4]_n \cdot xH_2O$ (Ln = Er, Dy, Tb, Ho; x = 10, phase a; x = 7, phase b), have been obtained. Interestingly, phase a are MOFs while phase b are CPs. The Er^{III}-CFs display NIR emission and field induced slow relaxation of the magnetization being multifunctional materials. Remarkably, the Er^{III}-MOF is flexible, showing a reversible structural change involving shrinkage/expansion of the hexagonal/rectangular cavities upon dehydration/hydration external stimulus, which allow to reversibly tune both SIM and luminescent properties.

CFs containing Dy^{III}, Tb^{III} and Ho^{III} are isostructural to the Er^{III}-CFs, both phases a and b. Phases a (MOFs) show as well structural flexibility upon dehydration/hydration, but intriguingly, in this case, it does not show a marked influence on their magnetic properties. Particularly, only the two Dy^{III}-CFs and phase b of Tb^{III}-CP show a Single Ion Magnet behavior. Interestingly, the single Ion Magnet properties of the phase b of Tb^{III}-CP are improved with respect to those of the Er^{III} and Dy^{III} derivatives. Theoretical calculations are in progress to shed light on their dynamic behavior and to investigate the involved mechanism in the flexibility.

Finally, by combining 1,3,5-benzentricarboxylic acid (H_3BTC) biofriendly linker with NIR-emitting lanthanide ions *via* a solvent free method, NIR luminescent mixed

Yb^{III}/Nd^{III} 3D CFs have been obtained. The two different classes of CFs, formulated as $Nd_xYb_{1-x}(BTC)_3(H_2O)_6$ (x = 1, x = 0.943; x = 0.953; x = 0.856; x = 0.890) and $Nd_xYb_{1-x}(BTC)_6$ (x = 0.017, x = 0), have been fully characterized. Among them, $Nd_{0.890}Yb_{0.110}(BTC)_3(H_2O)_6$ it has proved to be the most promising system as dual-center thermometer, showing a significant decrease of Yb/Nd intensity ratio with the increase of the temperature in the 10-300 K.

In the present work, many challenges are still open, in particular:

1. Optimization of synthetic protocols of $Co^{II}trz_2An$-MOF and $Cu^{II}trz_2An$-MOF, to scale up their production for industrial applications in gas separation and/or catalysis, due to their thermal and chemical robustness. Particularly, the redox activity of Cu^{I}/Cu^{II} couple may be exploit in $Cu^{II}trz_2An$-MOF for catalysis.
2. Development of post-synthetic reduction protocols of $M^{II}trz_2An$-CFs in order to exploit the redox active benzoquinone/semiquinone *core unit* for tuning/switching magnetism and/or conductivity in all obtained CFs. Additionally, in $Co^{II}trz_2An$-MOF, the post synthetic reduction may influence the sorption properties and selectivity towards CO_2 and other industrially challenging gas and gas mixtures.
3. Optimization of $Tb^{III}trz_2An$-CF SIM properties by diluting the paramagnetic Tb^{III} nodes with diamagnetic Eu^{III} ions. Additionally, the preparation of isostructural Gd^{III}-CFs, containing an isotropic paramagnetic lanthanide ion, could help to understand the role of weak magnetic exchange through the ligand on these CFs SIM behaviour.
4. Evaluation of the thermometer performance, *i.e.* thermal sensitivity, of the most promising system, $Nd_{0.890}Yb_{0.110}(BTC)_3(H_2O)_6$, that shows a significant decrease of Yb/Nd intensity ratio with the increase of the temperature (10-300 K range). Furthermore, biocompatibility tests are required for the potential use of such system as valuable thermometer in biological tissues.
5. Investigation of the new anilate derivative, 3,6-N-(dipyrazolyl-4-carboxylic acid)-2,5-dihydroxy-1,4-benzoquinone, reported below, as potential building block for constructing 3D CFs with novel and/or improved physical properties.

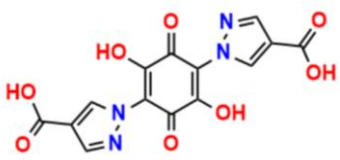

3,6-N-(dipyrazolyl-4-carboxylic acid)-2,5-dihydroxy-1,4-benzoquinone

PART IV

Supporting Material

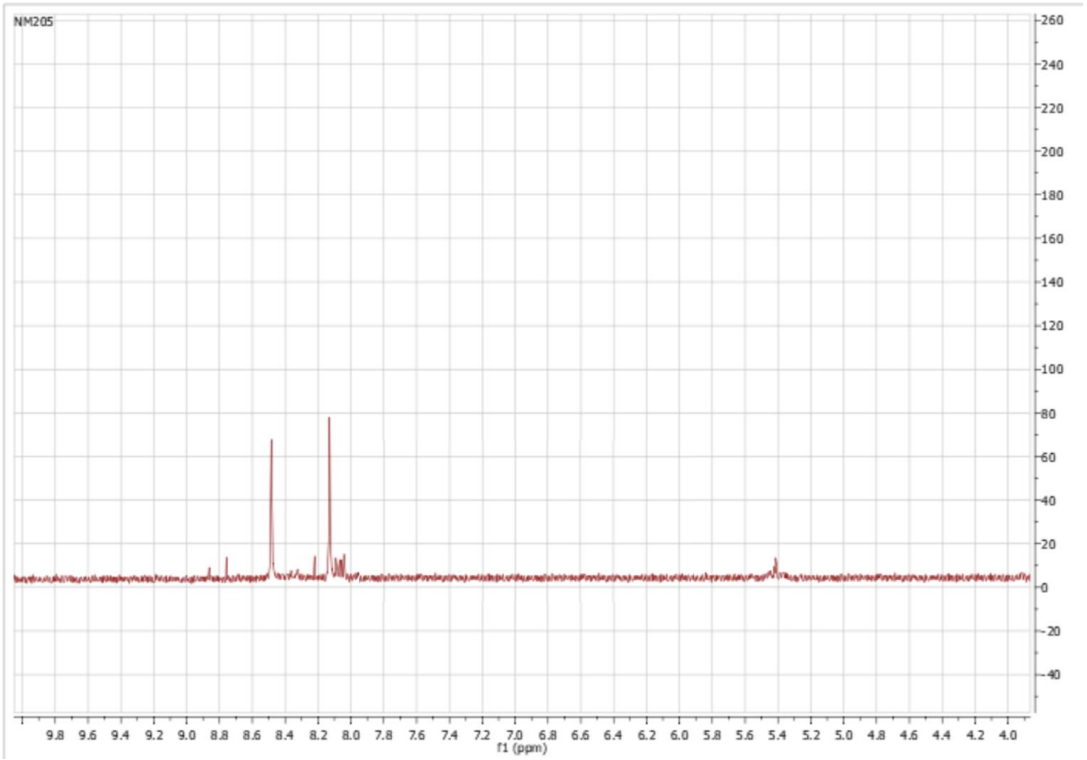

Figure S1.1. ^{1}H NMR spectrum of 3,6-N-ditriazolyl-2,5-dihydroxy-1,4-benzoquinone in DMSO- d_6.

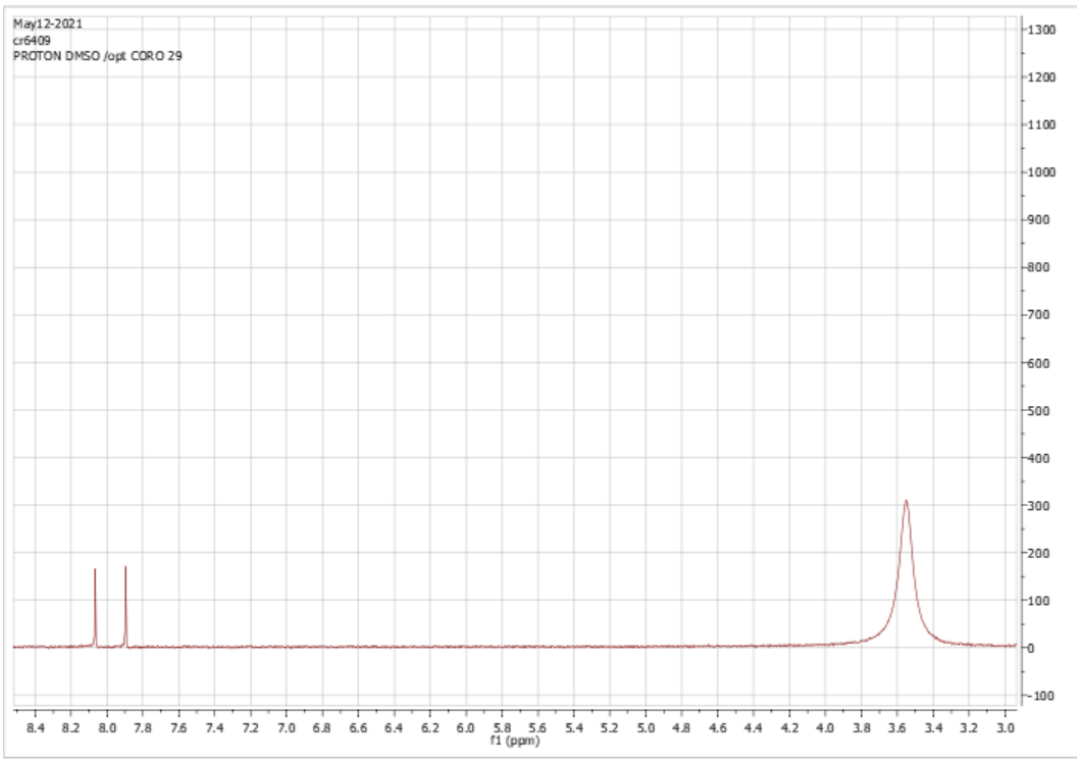

Figure S1.2. ^{1}H NMR spectrum of 3,6-N-(dipyrazolyl-4-carboxylic acid)-2,5-dihydroxy-1,4-benzoquinone in DMSO- d_6

Chapter 2

$[M(trz_2An)]_n \cdot 3H_2O$ (M^{II} = Co, Cu)

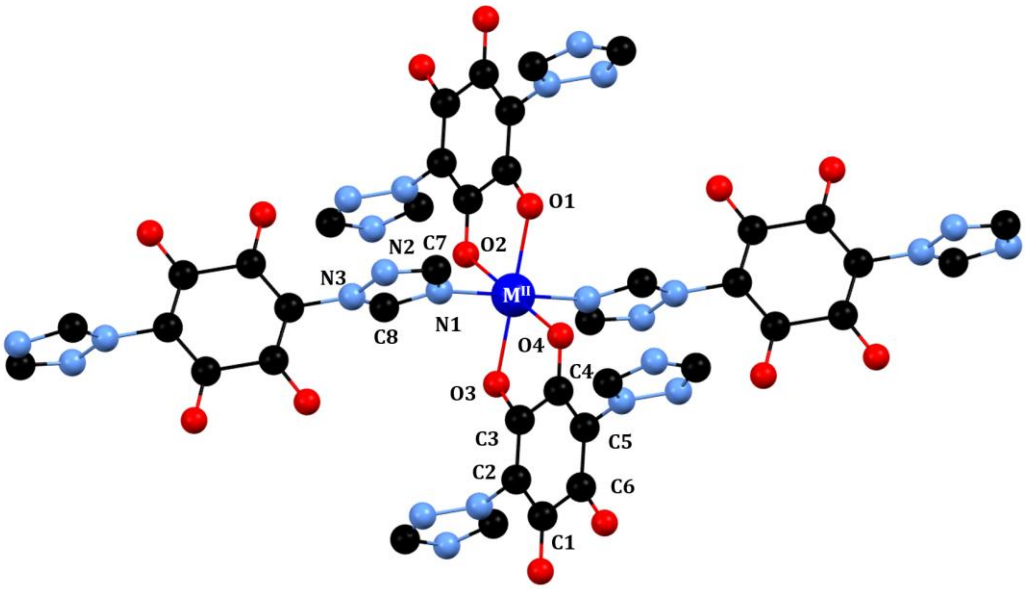

Table S2.1. Selected bond lengths and angles for **$[Co(trz_2An)]_n \cdot 3H_2O$**

Bonds	Å	Angles	°
Co – O1	2.090(6)	O1 – Co – O3	180.0(2)
Co – N1	2.098(9)	O1 – Co – O2	78.4(3)
C1 – O1	1.253(10)	O1 – Co – O4	101.6(3)
C2 – C3	1.358(10)	N1 – Co – O2	89.7(2)
C3 – C4	1.581(17)	N1 – Co – O3	90.3(2)
N1 – C7	1.323(14)	N1 – Co – N1	180.0
N1 – C8	1.329(16)		
N2 – N3	1.324(13		
C8 – N3	1.296(17)		

Table S2.2. Selected bond lengths and angles for **$[Cu(trz_2An)]_n \cdot 3H_2O$**

Bonds	Å	Angles	°
Cu – O1	2.151(6)	O1 – Cu – O3	180.0
Cu – N1	1.972(8)	O1 – Cu – O2	77.3(3)
C1 – O1	1.248(11)	O1 – Cu – O4	102.7(3)
C2 – C3	1.376(11)	N1 – Cu – O2	90.7(2)
C3 – C4	1.575(14)	N1 – Cu – O3	89.3(2)
N1 – C7	1.314(13)	N1 – Cu – N1	180.0

N1 – C8	1.334(15)
N2 – N3	1.357(13)
C8 – N3	1.310(15)

$[Mn(trz_2An)(H_2O)]_n \cdot 3.5H_2O$

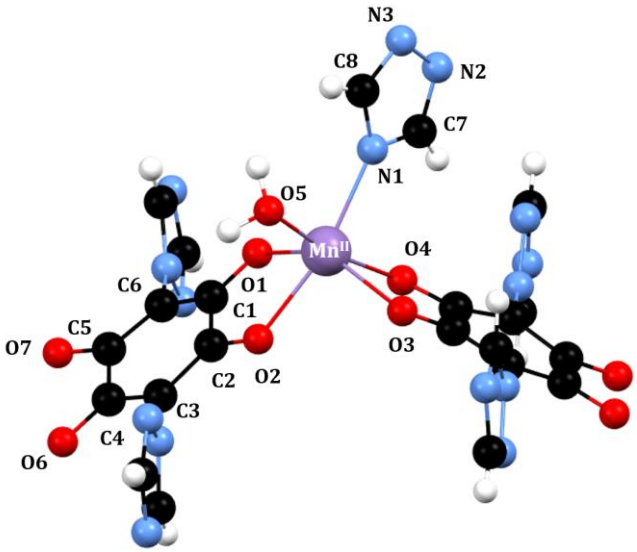

Table S2.3. Selected bond lengths and angles for **$[Mn(trz_2An)(H_2O)]_n \cdot 3.5H_2O$**

Bonds	**Å**	**Bonds**	**Å**	**Angles**	**°**
Mn – O1	2.167(4)			**N1 – Mn – O1**	83.29(18)
Mn – O2	2.236(4)			**N1 – Mn – O2**	105.69(18)
Mn – O3	2.209(4)			**N1 – Mn – O3**	166.57(18)
Mn – O4	2.230(4)			**N1 – Mn – O4**	100.37(17)
Mn – O5	2.159(4)			**N1 – Mn – O5**	88.76(17)
Mn – N1	2.222(5)			**O1 – Mn – O2**	73.28(15)
C1 – O1	1.252(7)			**O1 – Mn – O3**	141.29(15)
C2 – O2	1.263(7)			**O1 – Mn – O4**	86.22(16)
C4 – O6	1.249(7)			**O1 – Mn – O5**	102.80(18)
C1 – C2	1.536(9)			**O2 – Mn – O3**	82.04(15)
C2 – C3	1.377(8)			**O2 – Mn – O4**	106.51(15)
C3 – C4	1.408(8)			**O2 – Mn – O5**	169.70(17)
C4 – C5	1.537(9)			**O3 – Mn – O4**	72.59(16)
C1 – C6	1.402(8)			**O3 – Mn – O5**	82.43(17)
N1 – C7	1.335(8)			**O4 – Mn – O5**	105.92(18)
N1 – C8	1.375(8)				
N1 – N2	1.369(7)				
N2 – C7	1.317(8)				
N3 – C8	1.342(8)				

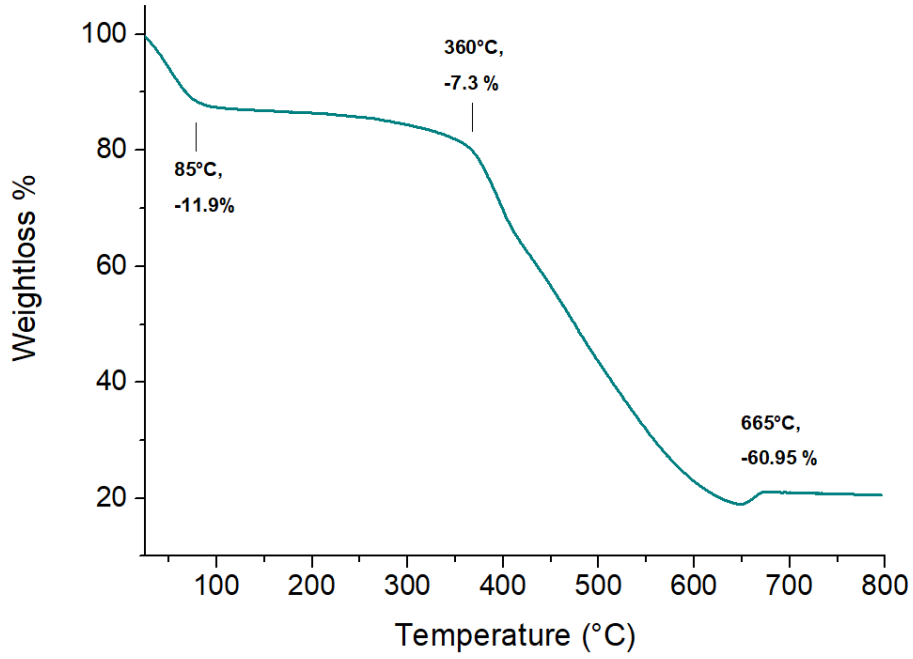

Figure S2.1. Thermogram of **$[Cu_2(trz_2An)_2]_n3H_2O$** in 25-800°C temperature range, showing the weightlosses at different temperatures. The percentages shown in the graph refer to the previous one weightloss.

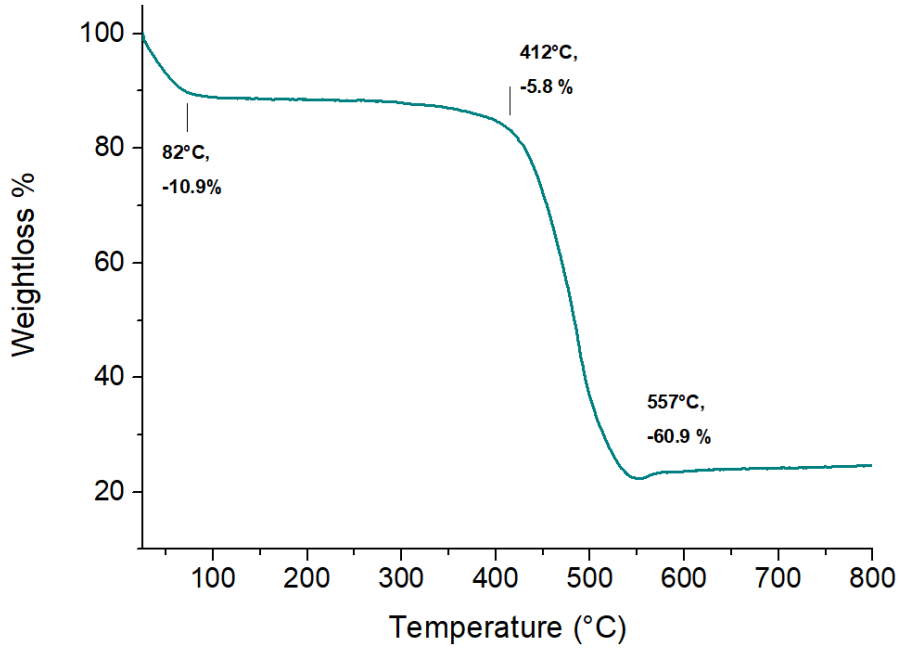

Figure S2.2. Thermogram of **$[Ni_2(trz_2An)_2]_n3H_2O$** in 25-800°C temperature range, showing the weightlosses at different temperatures. The percentages shown in the graph refer to the previous one weightloss.

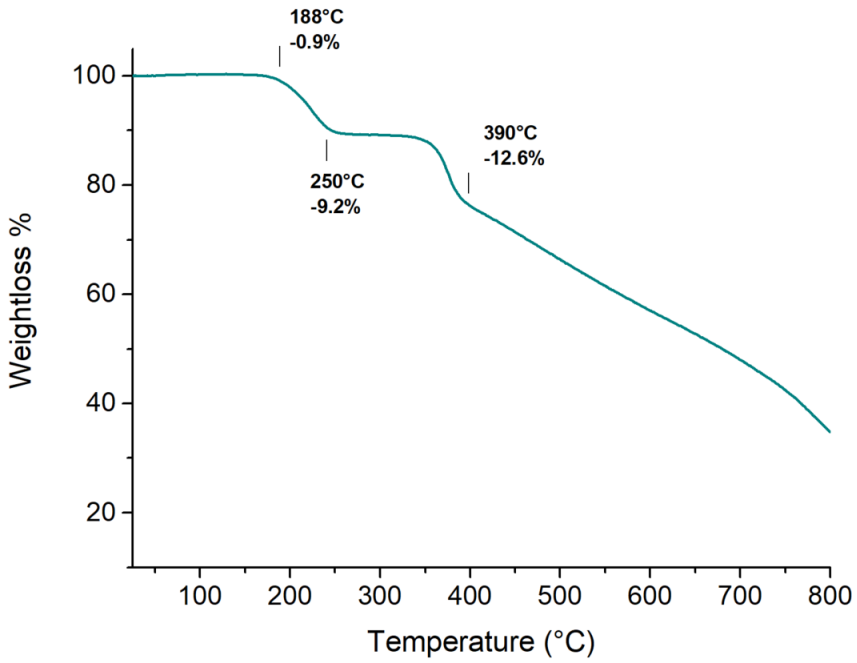

Figure S2.3. Thermogram of [**Mn(trz$_2$An)(H$_2$O)]$_n$·3.5H$_2$O** in 25-800°C temperature range, showing the weightlosses at different temperatures. The percentages shown in the graph refer to the previous one weightloss.

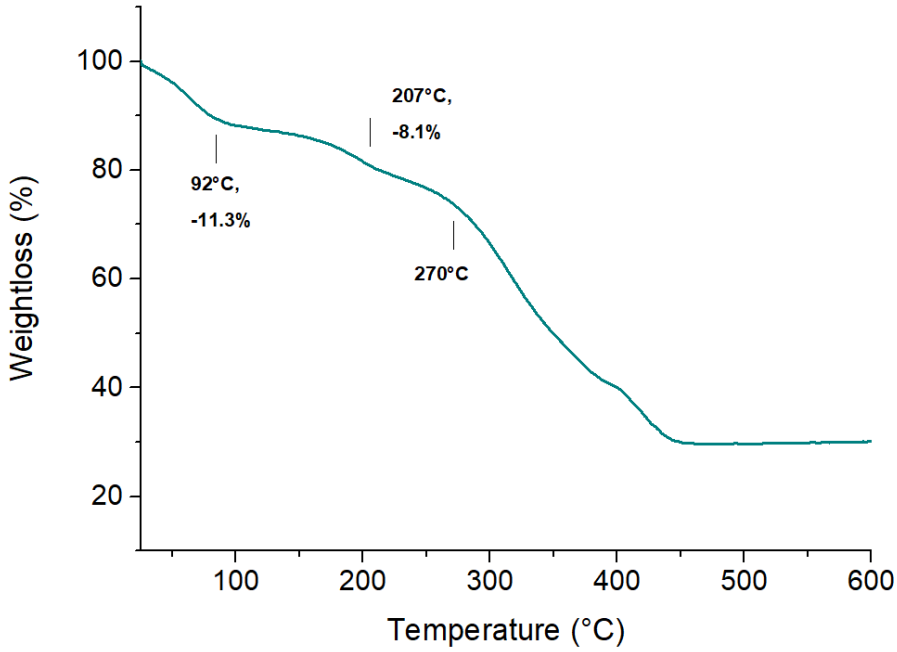

Figure S2.4. Thermogram of [**Fe(trz$_2$An)]$_n$·9H$_2$O** in 25-600°C temperature range, showing the weightlosses at different temperatures. The percentages shown in the graph refer to the previous one weightloss.

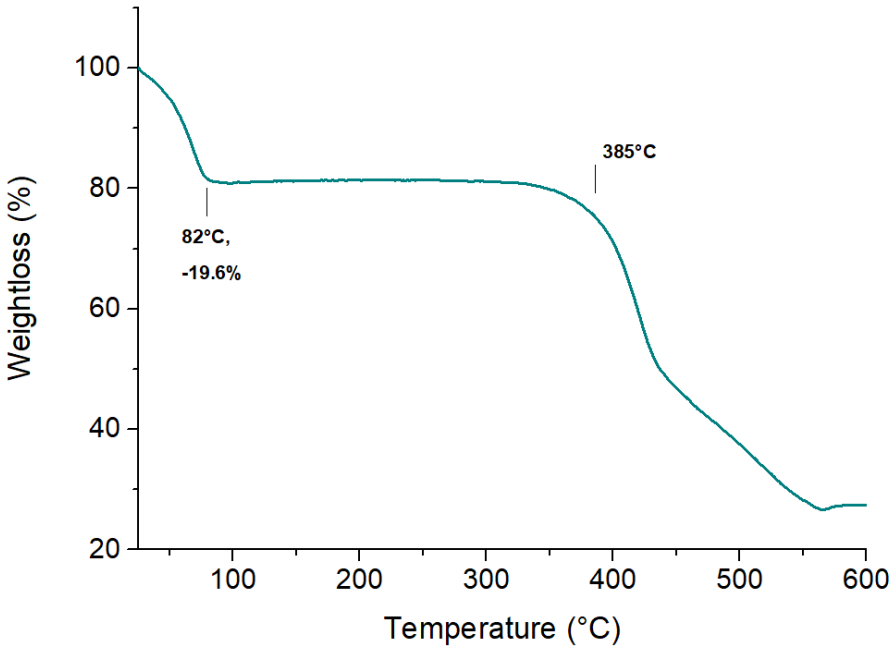

Figure S2.5. Thermogram of [**Co(trz$_2$An)]$_n$·8H$_2$O** in 25-600°C temperature range.

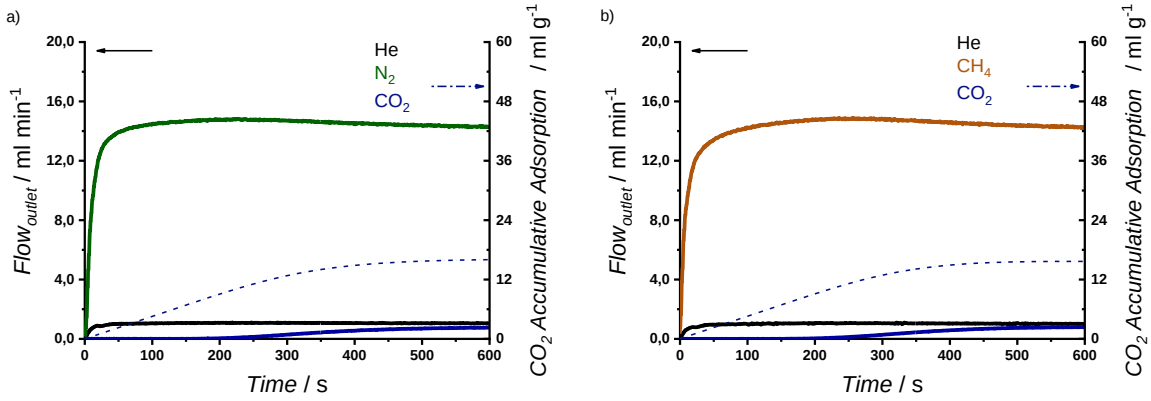

Figure S3.1. Breakthrough exit flowrates (solid line, left axis) and CO_2 accumulative adsorption (dash-dot line, right axis) vs. time at 283 K and 1 bar, on compound **$[Co_2(trz_2An)_2]_n3H_2O$**. Inlet composition corresponds to a 5 % dilution of CO_2: (a) in nitrogen, and (b) in methane. Time zero is set with the first detection of helium (tracer).

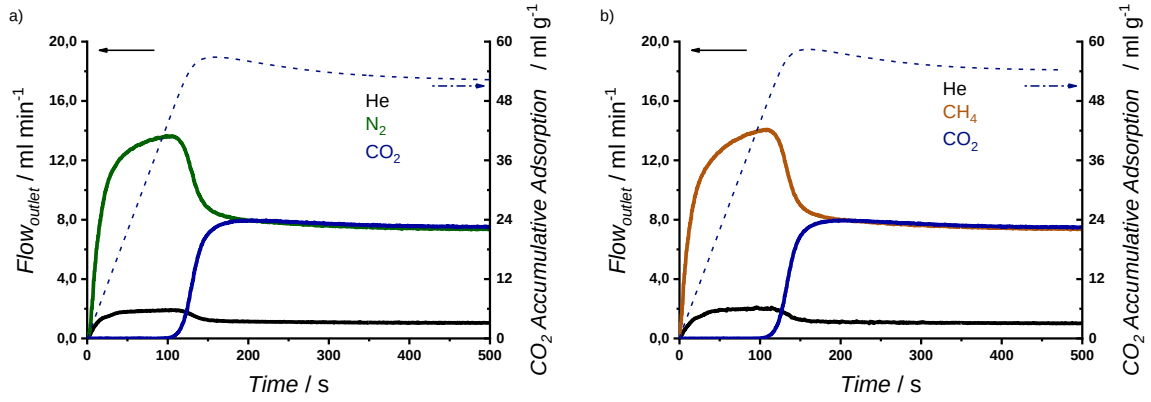

Figure S3.2. Breakthrough exit flowrates (solid line, left axis) and CO_2 accumulative adsorption (dash-dot line, right axis) vs. time at 283 K and 1 bar, on compound **$[Co_2(trz_2An)_2]_n3H_2O$**. Inlet composition corresponds to a 50 % dilution of CO_2: (a) in nitrogen, and (b) in methane. Time zero is set with the first detection of helium (tracer).

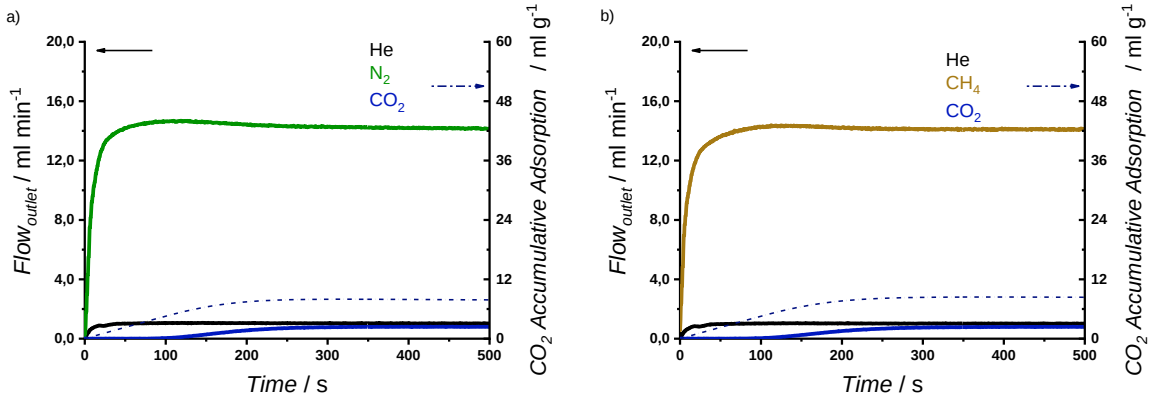

Figure S3.3. Breakthrough exit flowrates (solid line, left axis) and CO_2 accumulative adsorption (dash-dot line, right axis) vs. time at 298 K and 1 bar, on compound **$[Co_2(trz_2An)_2]_n3H_2O$**. Inlet

composition corresponds to a 5 % dilution of CO_2: (a) in nitrogen, and (b) in methane. Time zero is set with the first detection of helium (tracer).

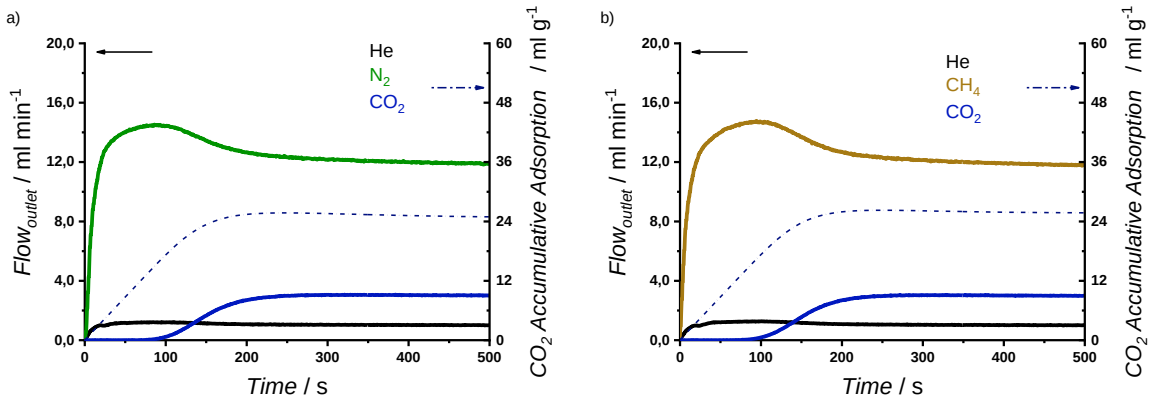

Figure S3.4. Breakthrough exit flowrates (solid line, left axis) and CO_2 accumulative adsorption (dash-dot line, right axis) vs. time at 298 K and 1 bar, on compound **$[Co_2(trz_2An)_2]_n3H_2O$**. Inlet composition corresponds to a 20 % dilution of CO_2: (a) in nitrogen, and (b) in methane. Time zero is set with the first detection of helium (tracer).

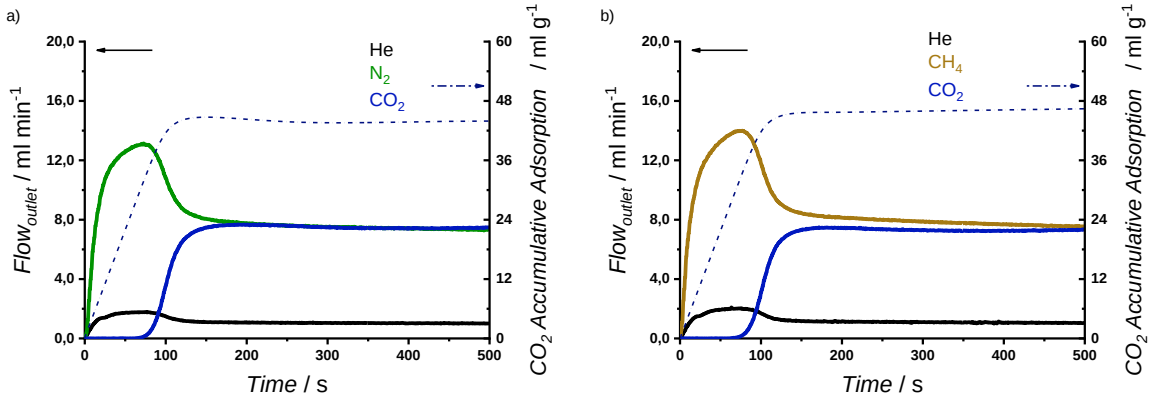

Figure S3.5. Breakthrough exit flowrates (solid line, left axis) and CO_2 accumulative adsorption (dash-dot line, right axis) vs. time at 298 K and 1 bar, on compound **$[Co_2(trz_2An)_2]_n3H_2O$**. Inlet composition corresponds to a 50 % dilution of CO_2: (a) in nitrogen, and (b) in methane. Time zero is set with the first detection of helium (tracer).

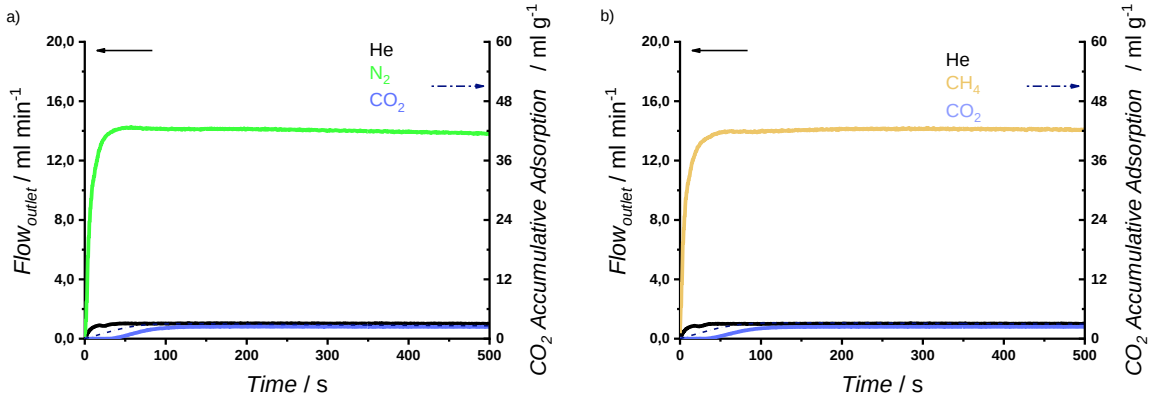

Figure S3.6. Breakthrough exit flowrates (solid line, left axis) and CO_2 accumulative adsorption (dash-dot line, right axis) vs. time at 323 K and 1 bar, on compound **$[Co_2(trz_2An)_2]_n3H_2O$**. Inlet

composition corresponds to a 5 % dilution of CO_2: (a) in nitrogen, and (b) in methane. Time zero is set with the first detection of helium (tracer).

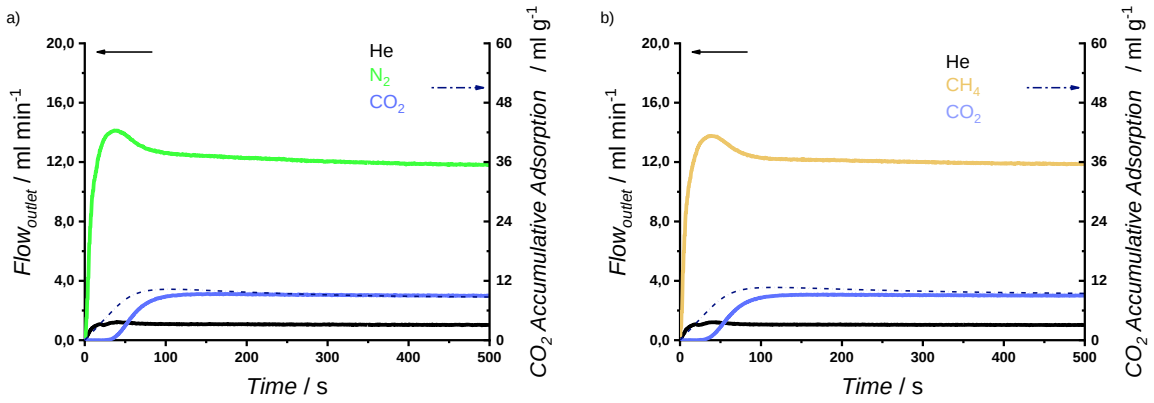

Figure S3.7. Breakthrough exit flowrates (solid line, left axis) and CO_2 accumulative adsorption (dash-dot line, right axis) vs. time at 323 K and 1 bar, on compound **$[Co_2(trz_2An)_2]_n3H_2O$**. Inlet composition corresponds to a 20 % dilution of CO_2: (a) in nitrogen, and (b) in methane. Time zero is set with the first detection of helium (tracer).

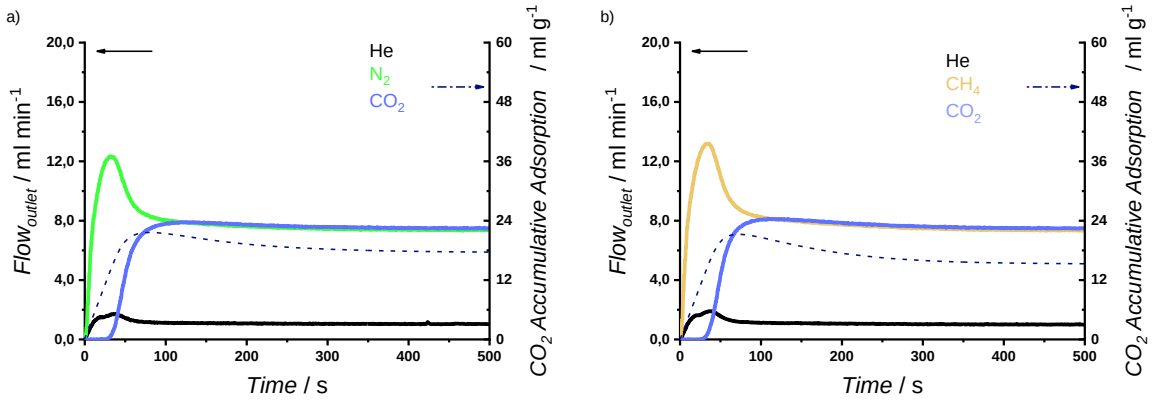

Figure S3.8. Breakthrough exit flowrates (solid line, left axis) and CO_2 accumulative adsorption (dash-dot line, right axis) vs. time at 323 K and 1 bar, on compound **$[Co_2(trz_2An)_2]_n3H_2O$**. Inlet composition corresponds to a 50 % dilution of CO_2: (a) in nitrogen, and (b) in methane. Time zero is set with the first detection of helium (tracer).

Chapter 4

$[Er_2(trz_2An)_3(H_2O)_4]_n \cdot 10H_2O$, Phase A

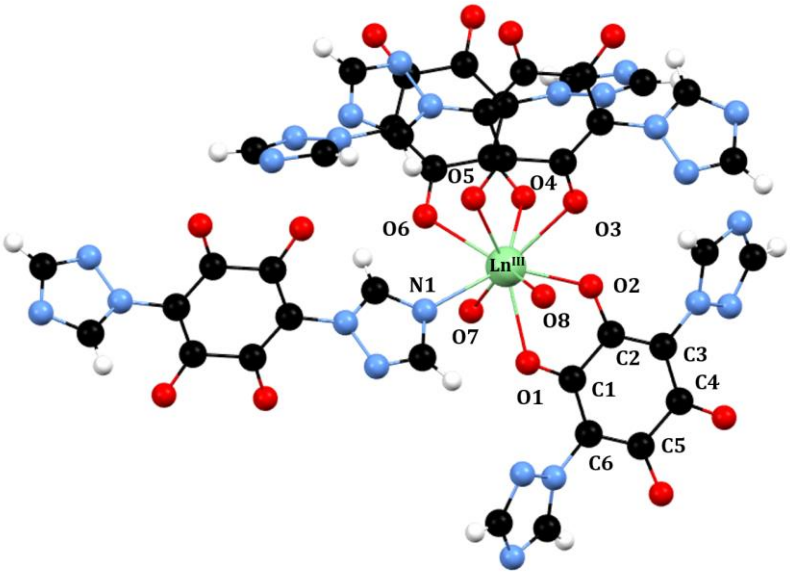

Table S4.1. Selected bond lengths and angles for $[Er_2(trz_2An)_3(H_2O)_4]_n \cdot 10H_2O$

Bonds	Å	Angles	°	Angles	°
Er– O1	2.416(3)	N1 – Er – O1	75.13(12)	O2 – Er – O6	134.50(11)
Er – O2	2.319(3)	N1 – Er– O2	141.28(13)	O2 – Er – O7	87.90(11)
Er – O3	2.409(3)	N1 – Er – O3	135.17(12)	O2 – Er – O8	83.36(11)
Er – O4	2.377(3)	N1 – Er– O4	137.59(12)	O3 – Er – O4	68.53(12)
Er – O5	2.426(3)	N1 – Er – O5	76.69(12)	O3 – Er – O5	65.18(10)
Er – O6	2.433(3)	N1 – Er – O6	72.83(12)	O3 – Er – O6	108.72(12)
Er – O7	2.377(3)	N1 – Er – O7	79.16(12)	O3 – Er – O7	69.60(11)
Er – O8	2.369(3)	N1 – Er – O8	81.06(13)	O3 – Er – O8	143.41(11)
Er– N1	2.461(4)	O1 – Er – O2	66.19(10)	O4 – Er – O5	91.64(12)
C1 – O1	1.250(5)	O1 – Er – O3	118.62(11)	O4 – Er – O6	65.36(11)
C2 – O2	1.247(6)	O1 – Er – O4	130.45(11)	O4 – Er – O7	137.77(11)
C1 – C2	1.545(6)	O1 – Er – O5	137.35(11)	O4 – Er – O8	80.19(12)
C2 – C3	1.396(6)	O1 – Er – O6	132.63(11)	O5 – Er – O6	65.14(12)
C3 – C4	1.385(7)	O1 – Er – O7	68.06(12)	O5 – Er – O7	75.70(12)
		O1 – Er – O8	68.63(12)	O5 – Er – O8	136.39(11)
		O2 – Er – O3	69.95(11)	O6 – Er – O7	135.81(12)
		O2 – Er – O4	72.95(11)	O6 – Er – O8	72.65(12)
		O2 – Er – O5	135.11(11)	O7 – Er – O8	135.63(13)

$[Er_2(trz_2An)_3(H_2O)_2]_n$, Phase A desolvated

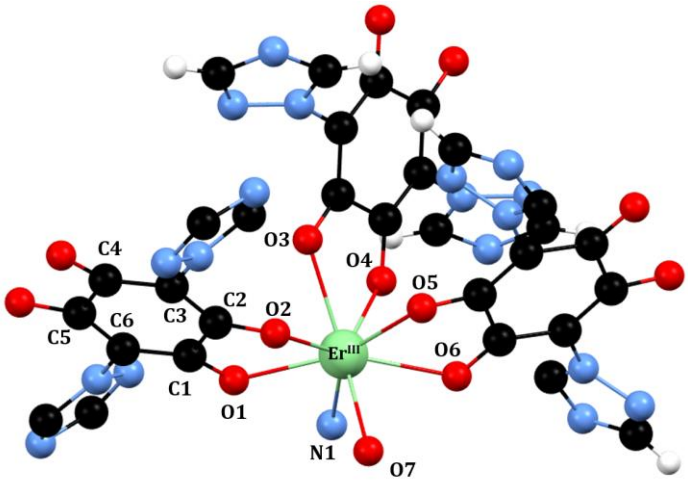

Table S4.2. Selected bond lengths and angles for $[Er_2(trz_2An)_3(H_2O)_2]_n$

Bonds	Å	Angles	°	Angles	°
Er– O1	2.285(16)	**N1 – Er – O1**	69.8(6)	**O2 – Er – O4**	130.6(5)
Er – O2	2.394(17)	**N1 – Er– O2**	134.3(6)	**O2 – Er – O5**	81.7(6)
Er – O3	2.418(17)	**N1 – Er – O3**	84.9(6)	**O2 – Er – O6**	143.9(5)
Er – O4	2.388(14)	**N1 – Er– O4**	78.3(5)	**O2 – Er – O7**	84.5(6)
Er – O5	2.264(17)	**N1 – Er – O5**	141.3(6)	**O3 – Er – O4**	64.2(5)
Er – O6	2.430(16)	**N1 – Er – O6**	75.0(6)	**O3 – Er – O5**	76.8(6)
Er– N1	2.47(2)	**N1 – Er – O7**	125.5(6)	**O3 – Er – O6**	118.3(5)
C1 – O1	1.26(2)	**O1 – Er – O2**	67.1(6)	**O3 – Er – O7**	147.5(6)
C2 – O2	1.24(3)	**O1 – Er – O3**	86.8(6)	**O4 – Er – O5**	87.0(6)
C1 – C2	1.55(3)	**O1 – Er – O4**	109.8(6)	**O4 – Er – O6**	66.3(5)
C2 – C3	1.42(3)	**O1 – Er – O5**	148.5(5)	**O4 – Er – O7**	142.5(6)
		O1 – Er – O6	144.5(6)	**O5 – Er – O6**	66.3(5)
		O1 – Er – O7	95.1(6)	**O5 – Er – O7**	85.5(6)
		O2 – Er – O3	66.4(5)	**O6 – Er – O7**	77.1(5)

$[Er_2(trz_2An)_3(H_2O)_4]_n \cdot 7H_2O$, Phase B

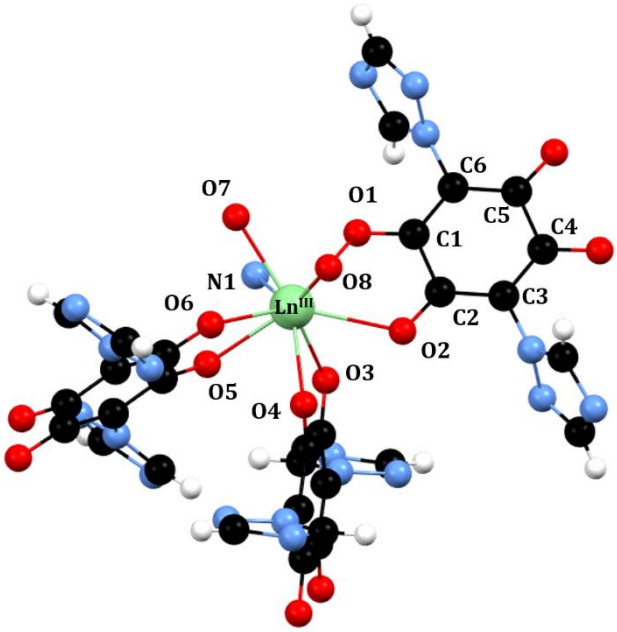

Table S4.3. Selected bond lengths and angles for $[Er_2(trz_2An)_3(H_2O)_4]_n \cdot 7H_2O$

Bonds	Å	Angles	°	Angles	°
Er– O1	2.5060(16)	**N1 – Er – O1**	67.15(6)	**O2 – Er – O6**	126.52(5)
Er – O2	2.3336(15)	**N1 – Er– O2**	117.29(6)	**O2 – Er – O7**	132.66(5)
Er – O3	2.3245(15)	**N1 – Er – O3**	70.96(6)	**O2 – Er – O8**	69.99(5)
Er – O4	2.3423(16)	**N1 – Er– O4**	130.40(6)	**O3 – Er – O4**	67.91(5)
Er – O5	2.3928(15)	**N1 – Er – O6**	115.65(6)	**O3 – Er – O6**	125.26(5)
Er – O6	2.4919(15)	**N1 – Er – O7**	72.67(6)	**O3 – Er – O7**	143.62(5)
Er – O7	2.3648(15)	**N1 – Er – O8**	142.02(6)	**O3 – Er – O8**	136.38(5)
Er – O8	2.3505(15)	**O1 – Er – O2**	133.34(5)	**O4 – Er – O6**	70.45(5)
Er– N1	2.5317(19)	**O1 – Er – O3**	71.19(5)	**O4 – Er – O7**	141.17(6)
C1 – O1	1.254(3)	**O1 – Er – O4**	74.20(5)	**O4 – Er – O8**	87.57(5)
C2 – O2	1.241(3)	**O1 – Er – O6**	64.42(5)	**O5 – Er – O7**	77.04(6)
C1 – C2	1.530(3)	**O1 – Er – O7**	93.86(6)	**O5 – Er – O8**	81.29(6)
C2 – C3	1.400(3)	**O1 – Er – O8**	137.57(6)	**O6 – Er – O7**	71.09(5)
		O2 – Er – O3	67.97(5)	**O6 – Er – O8**	73.46(5)
		O2 – Er – O4	70.33(5)	**O7 – Er – O8**	76.67(6)
		O2 – Er – O5	65.68(5)		

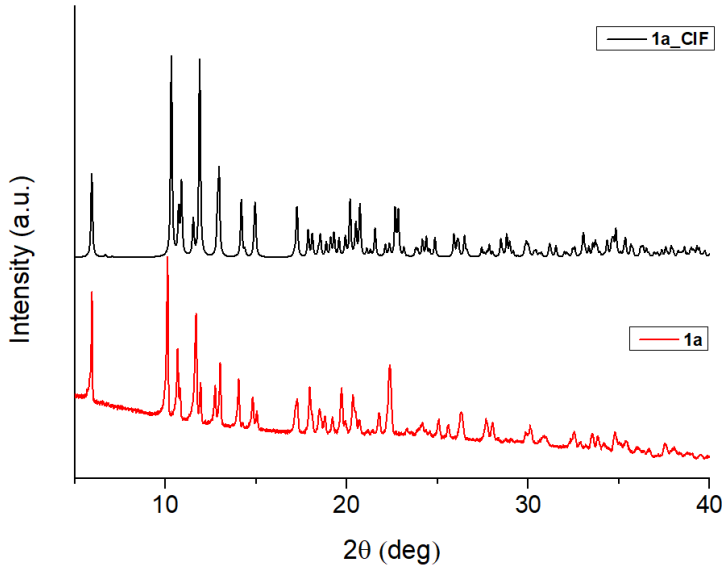

Figure S4.1. Experimental powder XRD pattern (red) and calculated pattern (black) of compound **1a**, in 2θ range of 5-40°.

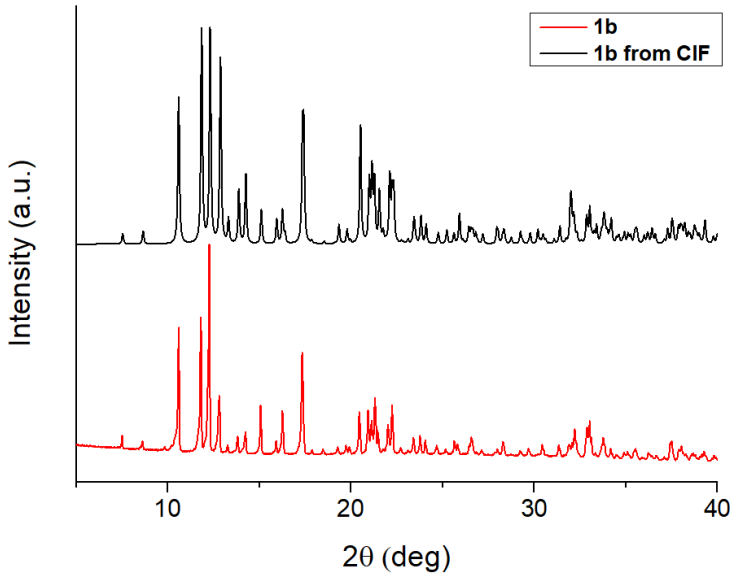

Figure S4.2. Experimental powder XRD pattern (red) and calculated pattern (black) of compound **1b**, in 2θ range of 5-40°.

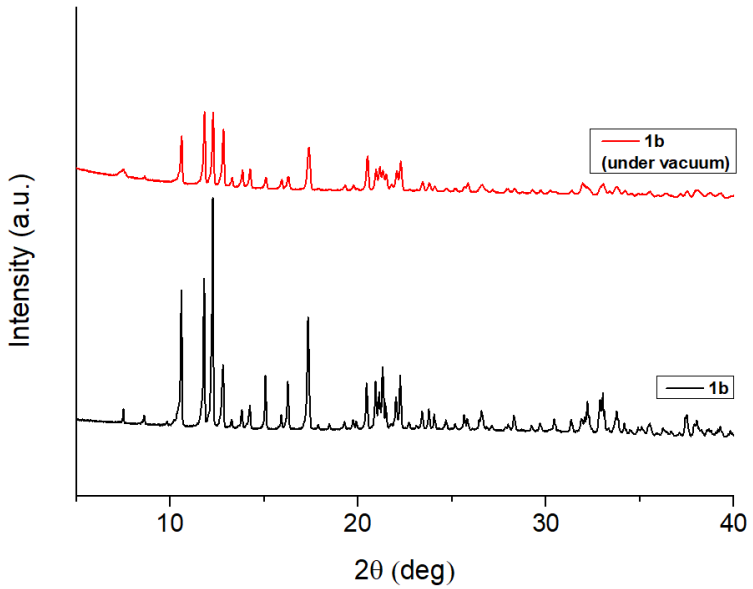

Figure S4.3. PXRD patterns of **1b** (black) and **1b** under vacuum (red) in 2θ range of 5-40°.

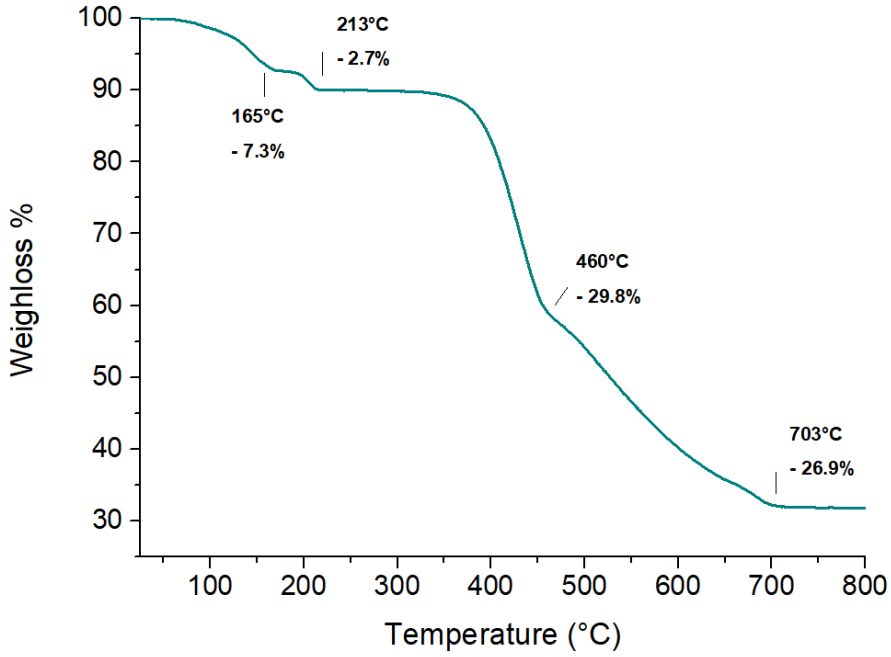

Figure S4.4. Thermogram of **1b** in 25-800°C temperature range, showing the weightlosses at different temperatures. The percentages shown in the graph refer to the previous one weightloss.

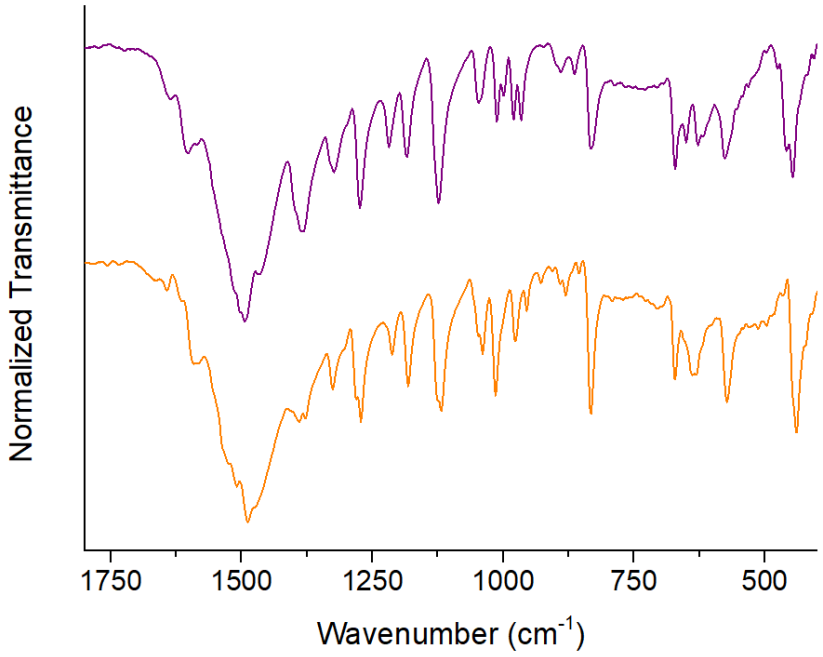

Figure S4.5. FT-IR spectra of **1a** (purple line) and **1b** (orange line) in 1800-400 cm^{-1} range.

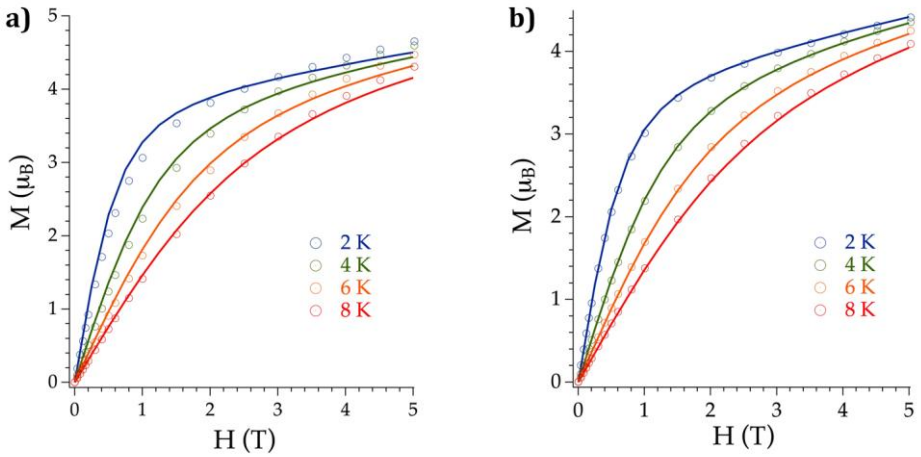

Figure S4.6. Experimental (symbols) and predicted average (lines) of magnetization M versus field H for **1a** (a) and **1a_d** (b) at 2K (blue), 4 K (green), 6 K (orange) and 8 K (red).

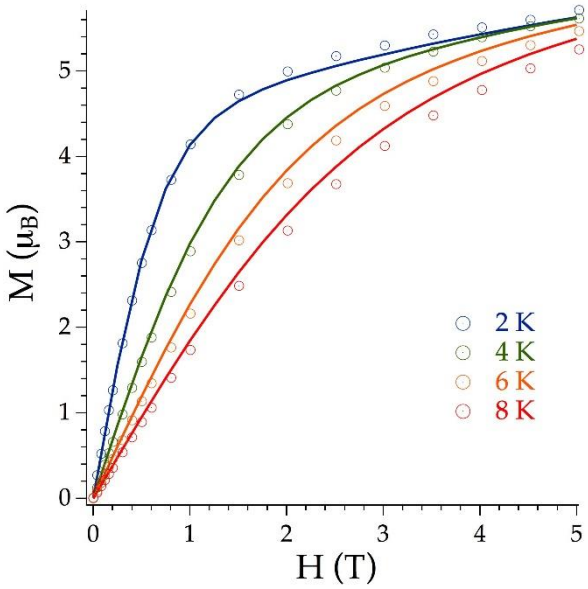

Figure S4.7. Experimental (symbols) and predicted average (lines) of magnetization M versus field H for **1b** at 2K (blue), 4 K (green), 6 K (orange) and 8 K (red).

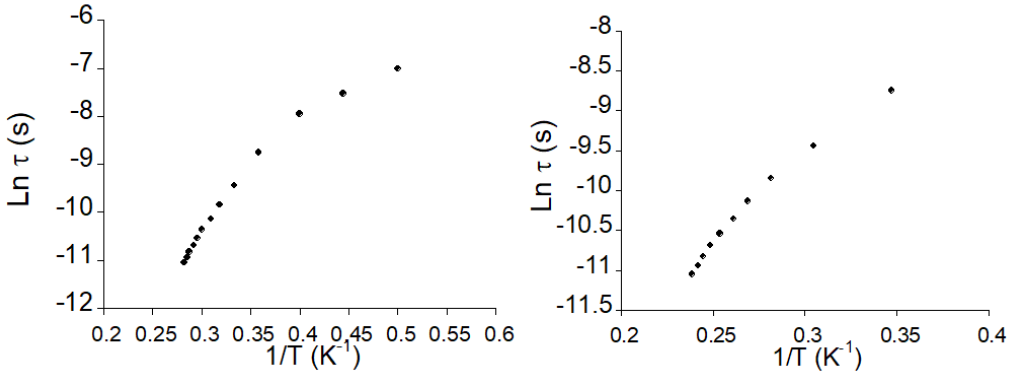

Figure S4.8. Plot of Ln τ versus T^{-1} for **1a_d** (left) and **1b** (right).

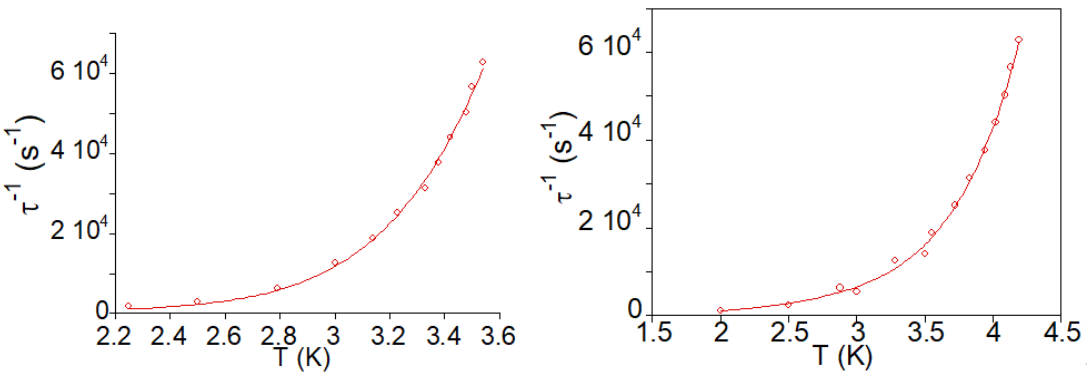

Figure S4.9. Thermal dependence of the relaxation time of **1a_d** (left) and **1b** (right) and best fit from two terms mechanism described in text.

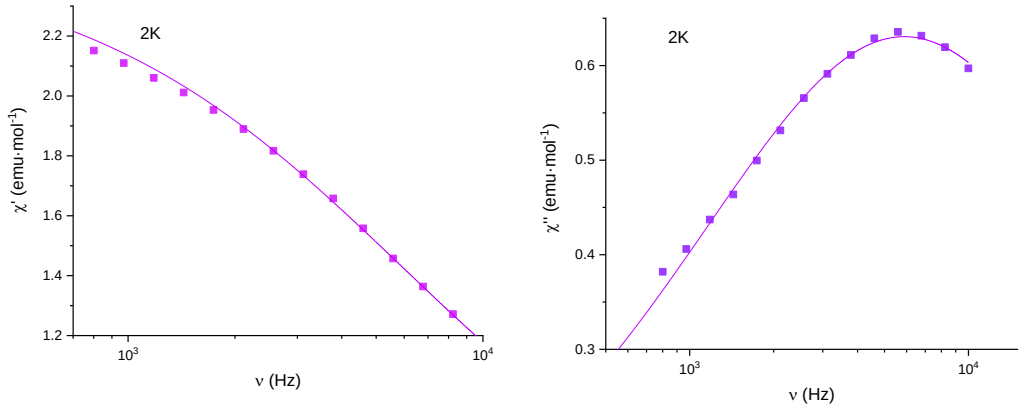

Figure S4.10. ac susceptibility in an applied dc field of 0.09 T of **1a** measured as a function of the frequency at 2 K. Top: Real component. Bottom: Imaginary component. Solid lines represent the best fitting of the experimental data to a Cole-Cole function.

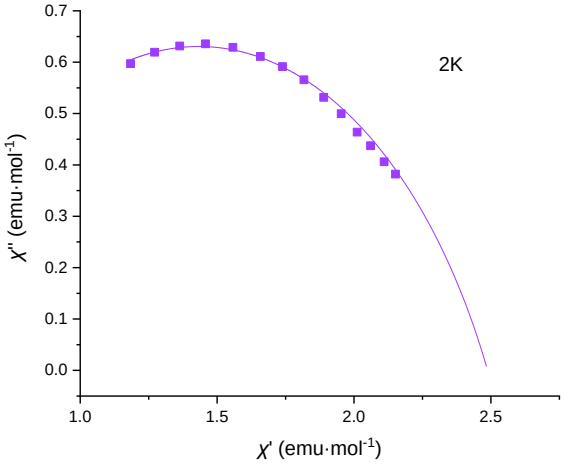

Figure S4.11. Cole-Cole plot of **1a** at 2 K under an applied dc field of 0.09 T. Solid lines represent the best fitting of the experimental data to a Cole-Cole function.

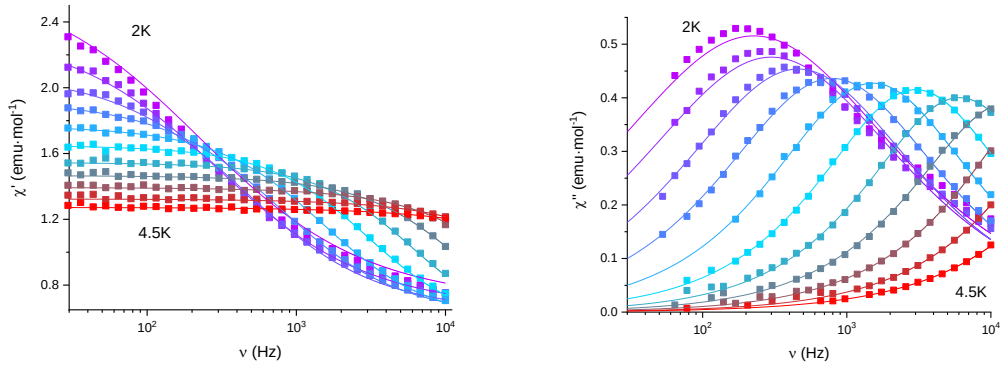

Figure S4.12. ac susceptibility in an applied dc field of 0.09 T of **1a_d** measured as a function of the frequency at the different temperatures (2.0, 2.25, 2.5, 2.75, 3.0, 3.25, 3.5, 3.75, 4.0, 4.25 and 4.5). Left: Real component. Right: Imaginary component. Solid lines represent the best fitting of the experimental data to a Cole-Cole function.

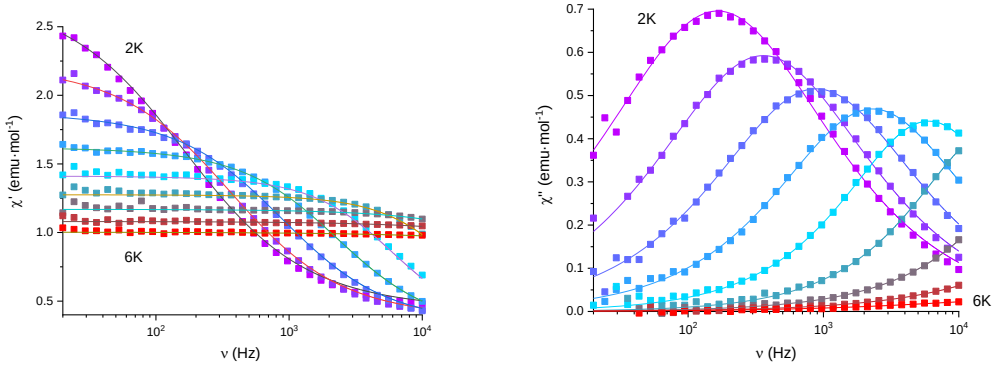

Figure S4.13. ac susceptibility in an applied dc field of 0.09 T of **1b** measured as a function of the frequency at the different temperatures (2.0, 2.5, 3.0, 3.5, 4.0, 4.5, 5.0, 5.5 and 6.0 K). Left: Real component. Right: Imaginary component. Solid lines represent the best fitting of the experimental data to a Cole-Cole function.

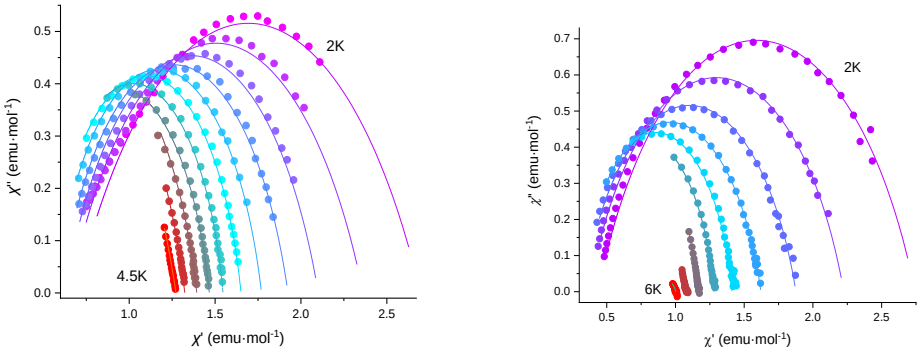

Figure S4.14. Cole-Cole plots of **1a_d** (left) and **1b** (right) measured at the same temperatures as **Figures S4.12-S4.13** under an applied dc field of 0.09 T (**1a_d**) and 0.1 T (**1b**). Solid lines represent the best fitting of the experimental data to a Cole-Cole function.

Theoretical Calculations and Photoluminescence Properties

Radial Effective Charge (REC) model

Our calculations start with the crystallographic/non-idealized atomic coordinates of the first coordination sphere. These are introduced as an input for the portable *fortran77* software code SIMPRE.[5] This code parameterizes the electric field effect produced by the surrounding ligands, acting over the central ion, by using the following Crystal Field Hamiltonian expressed in terms of the Extended Stevens Operators (ESOs):[6,7]

$$\hat{H}_{cf}(J) = \sum_{k=2,4,6} \sum_{q=-k}^{k} B_k^q O_k^q = \sum_{k=2,4,6} \sum_{q=-k}^{k} a_k (1-\sigma_k) A_k^q \langle r^k \rangle O_k^q \qquad (1)$$

where k is the order (also called rank or degree) and q is the operator range, that varies between k and $-k$, of the Stevens operator equivalents O_k^q as defined by Ryabov in terms of the angular momentum operators $J_\pm$ and J_z,[8] where the components $O_k^q(c)$ and $O_k^q(s)$ correspond to the ESOs with $q \geq 0$ and $q < 0$ respectively.[8] Note that all the Stevens CF parameters B_k^q are real, whereas the matrix elements of O_k^q($q < O$) are imaginary. a_k are the α, β and γ Stevens coefficients[9] for $k = 2, 4, 6$, respectively, which are tabulated and depend on the number of f electrons. σ_k are the Sternheimer shielding parameters[10] of the $4f$ electronic shell, and $\langle r^k \rangle$ are the expectation values of the radius.[10]

In SIMPRE, the A_k^q CF parameters are determined by the following relations:

$$A_k^0 = \frac{4\pi}{2k+1} \sum_{i=1}^{N} \frac{Z_i e^2}{R_i^{k+1}} Z_{k0}(\theta_i, \varphi_i) p_{kq} \tag{2.a}$$

$$A_k^q = \frac{4\pi}{2k+1} \sum_{i=1}^{N} \frac{Z_i e^2}{R_i^{k+1}} Z_{kq}^c(\theta_i, \varphi_i) p_{kq} \tag{2.b}$$

$$A_k^q = \frac{4\pi}{2k+1} \sum_{i=1}^{N} \frac{Z_i e^2}{R_i^{k+1}} Z_{k|q|}^s(\theta_i, \varphi_i) p_{k|q|} \tag{2.c}$$

In the REC model[11] the ligand is modeled through an effective point charge situated between the lanthanoid and the coordinated atom at a distance R_i from the magnetic centre, which is smaller than the real metal-ligand distance (r_i). To account for the effect of covalent electron sharing, a radial displacement vector ($\mathbf{D_r}$) is defined, in which the polar coordinate r of each coordinated atom is varied, $R_i = r_i - D_r$. The usual procedure is to obtain the D_r parameter of each kind of donor atom from a collective fit of an observable (e.g. energy levels or magnetic properties) for a family of isostructural lanthanide complexes. At the same time, the charge value (Z_i) is scanned in order to achieve the minimum deviation between calculated and experimental data, whereas θ_i and φ_i remain constant. In this work, we have kept fixed the value of D_r for the oxygen and nitrogen atoms, 0.98 Å and 1.20 Å, which have been taken from the literature and offer a better approximation for the relative relation between $k = 2, 4, 6$, which is one of the main drawbacks of the point-charge electrostatic model. This strategy allows us to restrict the number of free parameters to 2, i.e. the effective charges of the nitrogen and

oxygen atoms, *Zi* (N) = 0.05 and *Zi* (O) = 0.161, which have been obtained by a two-parameter fit of the χT product of both phases. Here it is worth to mention that these phenomenological parameters used by SIMPRE to predict the spin energy levels and wave functions do not pretend to simulate the actual charge distribution. In the fitting procedures, we define the relative error *E* as:

$$E = \frac{1}{n}\sum_{i=1}^{n}\frac{\left[\chi_{theo,i} - \chi_{\exp,i}\right]^2}{\left[\chi_{\exp,i}\right]^2} \quad (4)$$

where χ_{exp} and χ_{theo} are experimental and theoretical magnetic susceptibility, respectively, and *n* is the number of points.

To calculate the magnetic properties, SIMPRE introduces the interaction between the electron spin and an external magnetic field along the z-direction via a Zeeman term $\hat{H}_{ZEE}$:

$$\hat{H}_{ZEE} = g_j \mu_B B_z \cdot \hat{J}_z$$

Where g_j is the Landé *g*-factor for the ground *J*-multiplet, μ_B is the Bohr magneton, B_z is the external magnetic field along the z-direction and $\hat{J}_z$ is the z-component of the total electronic angular momentum operator. Once we have the eigenvalues of the system at different magnetic fields or temperatures, one can evaluate the partition function Z:

$$Z = \sum_n \exp\left(-\frac{E_n}{kT}\right)$$

where E_n are the eigenvalues of the system, *T* is temperature and *k* is the Boltzmann constant. Then, the macroscopic thermodynamic properties, such as magnetization and magnetic susceptibility, are calculated by summing the N microscopic magnetizations weighed by according to the Boltzmann distribution law, via the following fundamental equations:

$$M = NkT\frac{\partial lnZ}{\partial H}$$

Table S4.4. Crystal field parameters ($A_k^q < r^k >$; Stevens notation) in cm^{-1} obtained for **1a**, **1a_d** and **1b**.

k	***q***	**1a**	**1a_d**	**1b**
2	0	-109.47	-4.31	-235.64
2	1	536.28	-174.55	-23.17
2	-1	132.52	97.96	175.22
2	2	-9.96	443.83	-232.21
2	-2	1.21	156.58	47.37
4	0	53.25	177.50	-23.76
4	1	133.83	256.23	58.08
4	-1	126.58	58.57	411.70
4	2	280.14	-351.37	-287.91
4	-2	54.85	319.13	55.10
4	3	260.99	378.95	118.07
4	-3	218.69	36.18	90.32
4	4	-215.45	-114.76	-443.98
4	-4	35.80	302.00	224.24
6	0	19.33	-16.06	24.75
6	1	112.26	116.46	-18.66
6	-1	17.69	18.09	41.02

6	2	1.40	57.54	-81.76
6	-2	10.26	41.34	93.90
6	3	-266.50	-39.74	17.48
6	-3	121.33	292.07	77.70
6	4	-232.96	2.04	111.02
6	-4	103.40	44.61	145.96
6	5	732.41	-346.65	-623.85
6	-5	249.20	431.47	65.11
6	6	167.56	16.77	123.27
6	-6	193.08	10.26	225.20

Table S4.5. Ground multiplet energy level scheme (Kramers doublets in cm^{-1}) and main |MJ> contributions to the wave function calculated for **1a** and **1a_d**.

1a		**1a_d**	
0	59.5% |±13/2> + 14.7% |±5/2>	**0**	63.7% |±9/2> + 13.5% |±11/2> + 10.8% |±7/2>
39	36.6%|±11/2> + 14.0% |±3/2> + 16.3% |±1/2>	**42**	42.3% |±7/2> + 13.0% |±9/2> + 12.9% |±13/2> + 12.9% |±11/2>
94	17.4% |±11/2> + 20.6% |±7/2>	**73**	53.8% |±11/2> + 11.1% |±7/2>
15 8	10.6% |±11/2> + 12.8% |±9/2> + 12.1%	**13 5**	49.4% |±5/2>

	|±7/2> + 12.2% |±3/2> + 13.1% |∓9/2>		
236	12.2% |±13/2> + 14.4% |±9/2> + 16.7% |±3/2> + 23.3% |±1/2>	**188**	44.8% |±13/2> + 14.5% |±3/2>
263	30.0% |±15/2> + 15.1% |±9/2> + 16.9% |±5/2>	**248**	31.9% |±3/2> + 22.7% |±13/2>
312	17.2% |±7/2> + 12.3% |±3/2> + 10.7% |±1/2> + 12.3% |∓3/2>	**312**	79.4% |±15/2>
350	22.0% |±15/2> + 26.8% |±7/2> + 11.2% |±5/2>	**390**	37.8% |±1/2> + 22.8% |∓1/2> + 18.6% |∓3/2>

Table S4.6. Ground multiplet energy level scheme (Kramers doublets in cm^{-1}) and main |MJ> contributions to the wave function calculated for **1a** and **1a_d**. Red numbers in brackets: Main energy values estimated from PL spectrum of **1a_d** at 77K, assuming a zero-line (ZL) transition wavelength of 1529 nm.

1a		**1a_desolv**	
0	59.5% |±13/2> + 14.7% |±5/2>	**0**	63.7% |±9/2> + 13.5% |±11/2> + 10.8% |±7/2>
39	36.6%|±11/2> + 14.0% |±3/2> + 16.3% |±1/2>	**42 (29)**	42.3% |±7/2> + 13.0% |±9/2> + 12.9% |±13/2> + 12.9% |±11/2>
94	17.4% |±11/2> + 20.6% |±7/2>	**73**	53.8% |±11/2> + 11.1% |±7/2>
158	10.6% |±11/2> + 12.8% |±9/2> + 12.1% |±7/2> + 12.2% |±3/2> + 13.1% |∓9/2>	**135**	49.4% |±5/2>
236	12.2% |±13/2> + 14.4% |±9/2> + 16.7% |±3/2> + 23.3% |±1/2>	**188**	44.8% |±13/2> + 14.5% |±3/2>
263	30.0% |±15/2> + 15.1% |±9/2> + 16.9% |±5/2>	**248**	31.9% |±3/2> + 22.7% |±13/2>

312	79.4% |±15/2>		
390 (349)	37.8% |±1/2> + 22.8% |∓1/2> + 18.6% |∓3/2>		

Table S4.7. Ground multiplet energy level scheme (Kramers doublets in cm^{-1}) and main |MJ> contributions to the wave function calculated for **1b**. Red numbers in brackets: Main energy values estimated from the PL spectrum of **1b** at 77K, assuming a zero-line (ZL) transition wavelength of 1524 nm.

1b	
0	59.2% |±13/2>
32 (36)	33.4% |±11/2> + 29.7%|±15/2> + 12.3% |∓13/2> + 10.4% |∓1/2>
89	16.9% |±5/2> + 16.4%|±3/2> + 13.1% |∓3/2> + 11.6% |±1/2>
127	22.5% |±15/2> + 19.7% |±0.50> + 17.4% |∓3/2> + 13.4% |∓1/2>
189	22.0% |±11/2> + 16.7% |±9/2> + 12.0% |±5/2> + 11.6% |±7/2> + 11.3% |±15/2>
230	22.3% |±9/2> + 10.8% |±7/2> + 12.2% |∓15/2>
314	24.8% |±9/2> + 12.0% |∓7/2> + 10.7% |∓5/2> + 10.6% |±3/2>
354 (353)	33.6% |±7/2> + 27.8% |∓5/2> + 10.2% |±3/2>

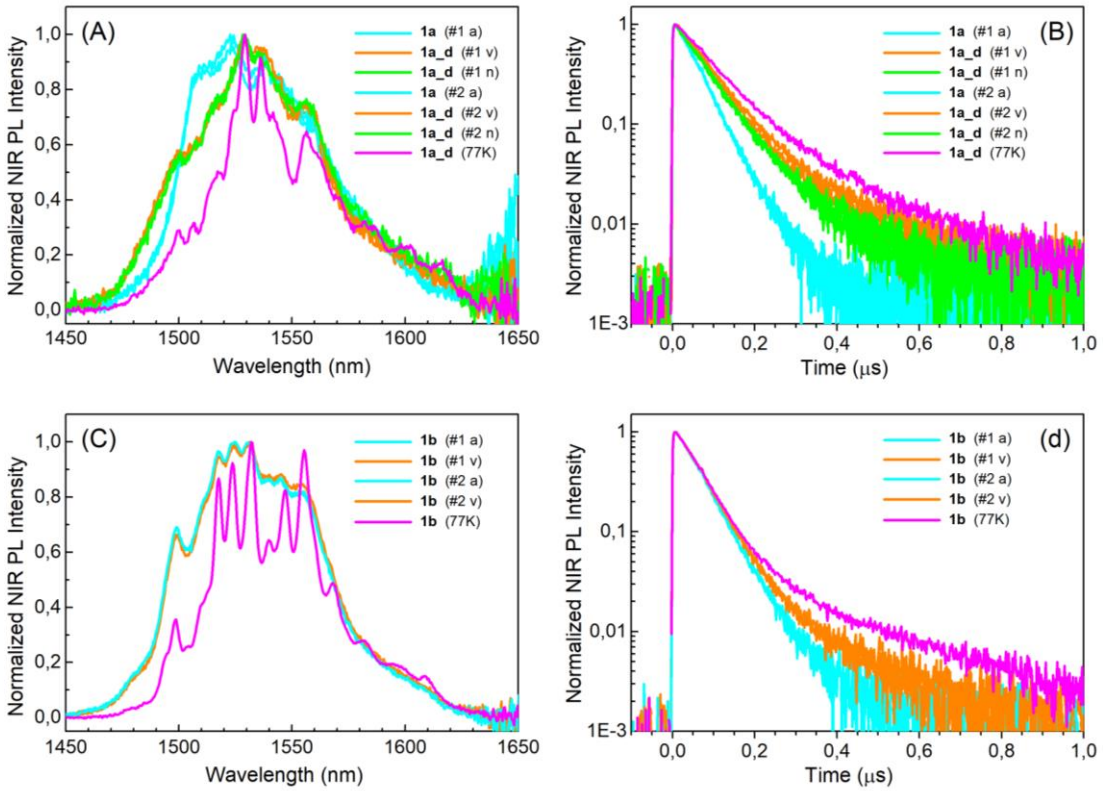

Figure S4.15. Demonstration of reversible PL emission properties in hydration/dehydration cycles. #1(2): First(second) measurement in air (a), under vacuum (v) and N_2 atmosphere (n). (A) PL spectra of phase **1a** (in air) and **1a_d** (under vacuum and N_2). (B) Corresponding PL decay transients. (C,D) Same as (A,B) but for **1b**. All spectra and decay transient where normalized to their peak values for better clarity. Absolute PL intensities were reproduced within 5-10% after each cycle. At room temperature, all phased displayed the same integrated PL intensity within 10%. Cooling to 77K produced less than a factor of two increase in integrated PL intensity in both **1a_d** and **1b**.

Chapter 5

$[Ln_2(trz_2An)_3(H_2O)_4]_n \cdot 10H_2O$ (Ln^{III} = Dy, Tb, Ho), Phase A

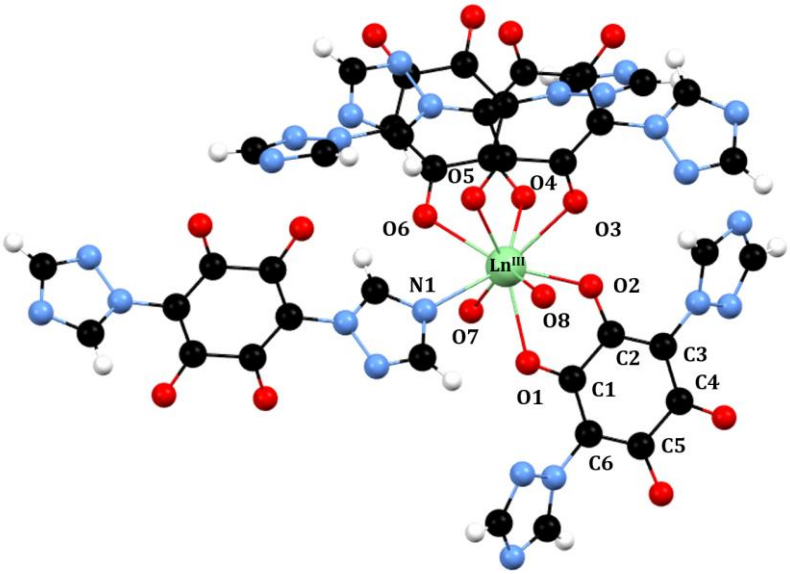

Table S5.1. Selected bond lengths and angles for $[Dy_2(trz_2An)_3(H_2O)_4]_n$ $10H_2O$

Bonds	Å	Angles	°	Angles	°
Dy– O1	2.4253(16)	N1 – Dy – O1	75.82(6)	O2 – Dy – O6	134.38(6)
Dy – O2	2.3449(16)	N1 – Dy – O2	141.57(6)	O2 – Dy – O7	84.32(6)
Dy – O3	2.4303(17)	N1 – Dy – O3	134.56(6)	O2 – Dy – O8	87.99(6)
Dy – O4	2.4007(18)	N1 – Dy – O4	137.20(7)	O3 – Dy – O4	68.95(6)
Dy – O5	2.4511(17)	N1 – Dy – O5	76.46(6)	O3 – Dy – O5	64.82(6)
Dy – O6	2.4516(17)	N1 – Dy – O6	72.86(6)	O3 – Dy – O6	108.60(6)
Dy – O7	2.3924(19)	N1 – Dy – O7	80.64(7)	O3 – Dy – O7	144.32(6)
Dy – O8	2.3976(18)	N1 – Dy – O8	78.72(7)	O3 – Dy – O8	69.86(6)
Dy – N1	2.491(2)	O1 – Dy – O2	65.77(6)	O4 – Dy – O5	91.41(6)
C1 – O1	1.253(3)	O1 – Dy – O3	118.56(6)	O4 – Dy – O6	64.88(6)
C2 – O2	1.256(3)	O1 – Dy – O4	130.16(6)	O4 – Dy – O7	80.24(6)
C1 – C2	1.534(3)	O1 – Dy – O5	137.86(6)	O4 – Dy – O8	138.45(6)
C2 – C3	1.394(3)	O1 – Dy – O6	132.79(6)	O5 – Dy – O6	65.21(6)
		O1 – Dy – O7	68.92(6)	O5 – Dy – O7	135.53(6)
		O1 – Dy – O8	67.97(6)	O5 – Dy – O8	75.94(6)
		O2 – Dy – O3	70.20(6)	O6 – Dy – O7	71.83(6)
		O2 – Dy – O4	73.27(6)	O6 – Dy – O8	135.93(6)
		O2 – Dy – O5	135.01(6)	O7 – Dy – O8	135.48(6)

Table S5.2. Selected bond lengths and angles for **$[Tb_2(trz_2An)_3(H_2O)_4]_n$ $10H_2O$**

Bonds	Å	Angles	°	Angles	°
Tb– O1	2.439(2)	**N1 – Tb – O1**	76.03(8)	**O2 – Tb – O6**	134.42(8)
Tb – O2	2.353(2)	**N1 – Tb – O2**	141.50(8)	**O2 – Tb – O7**	84.47(9)
Tb – O3	2.413(2)	**N1 – Tb – O3**	137.00(9)	**O2 – Tb – O8**	87.96(8)
Tb – O4	2.438(2)	**N1 – Tb – O4**	134.35(9)	**O3 – Tb – O4**	69.02(8)
Tb – O5	2.468(2)	**N1 – Tb – O5**	76.51(8)	**O3 – Tb – O5**	91.21(8)
Tb – O6	2.459(2)	**N1 – Tb – O6**	72.97(9)	**O3 – Tb – O6**	64.53(8)
Tb – O7	2.406(3)	**N1 – Tb – O7**	80.31(9)	**O3 – Tb – O7**	72.08(9)
Tb – O8	2.415(2)	**N1 – Tb – O8**	78.46(9)	**O3 – Tb – O8**	138.75(8)
Tb – N1	2.504(3)	**O1 – Tb – O2**	65.49(7)	**O4 – Tb – O5**	64.48(8)
C1 – O1	1.251(4)	**O1 – Tb – O3**	130.27(8)	**O4 – Tb – O6**	108.47(8)
C2 – O2	1.253(4)	**O1 – Tb – O4**	118.54(8)	**O4 – Tb – O7**	144.88(8)
C1 – C2	1.545(4)	**O1 – Tb – O5**	137.91(8)	**O4 – Tb – O8**	70.07(8)
C2 – C3	1.393(4)	**O1 – Tb – O6**	132.93(8)	**O5 – Tb – O6**	65.47(9)
C3 – C4	1.392(5)	**O1 – Tb – O7**	68.45(8)	**O5 – Tb – O7**	135.89(8)
		O1 – Tb – O8	67.85(8)	**O5 – Tb – O8**	75.85(8)
		O2 – Tb – O3	73.69(8)	**O6 – Tb – O7**	80.86(8)
		O2 – Tb – O4	70.36(8)	**O6 – Tb – O8**	135.98(8)
		O2 – Tb – O5	134.82(8)	**O7 – Tb – O8**	134.76(8)

Table S5.3. Selected bond lengths and angles for **$[Ho_2(trz_2An)_3(H_2O)_4]_n$ $10H_2O$**

Bonds	Å	Angles	°	Angles	°
Ho – O1	2.4205(16)	**N1 – Ho – O1**	75.50(6)	**O2 – Ho – O6**	134.38(6)
Ho – O2	2.4440(17)	**N1 – Ho – O2**	141.45(6)	**O2 – Ho – O7**	83.76(6)
Ho – O3	2.3303(16)	**N1 – Ho – O3**	134.80(6)	**O2 – Ho – O8**	88.07(6)
Ho – O4	2.4211(16)	**N1 – Ho – O4**	137.23(6)	**O3 – Ho – O4**	68.85(6)
Ho – O5	2.3882(17)	**N1 – Ho – O5**	76.48(6)	**O3 – Ho – O5**	64.99(5)
Ho – O6	2.4434(17)	**N1 – Ho – O6**	72.79(6)	**O3 – Ho – O6**	108.76(6)
Ho – O7	2.3887(17)	**N1 – Ho – O7**	80.92(6)	**O3 – Ho – O7**	143.85(6)
Ho – O8	2.3838(18)	**N1 – Ho – O8**	78.81(6)	**O3 – Ho – O8**	69.82(6)
Ho – N1	2.471(2)	**O1 – Ho – O2**	65.98(5)	**O4 – Ho – O5**	91.54(6)
C1 – O1	1.247(3)	**O1 – Ho – O3**	118.68(5)	**O4 – Ho – O6**	64.99(6)
C2 – O2	1.253(3)	**O1 – Ho – O4**	130.34(6)	**O4 – Ho – O7**	80.12(6)
C1 – C2	1.539(3)	**O1 – Ho – O5**	137.59(6)	**O4 – Ho – O8**	138.33(6)
C2 – C3	1.395(3)	**O1 – Ho – O6**	132.51(6)	**O5 – Ho – O6**	65.34(6)
		O1 – Ho – O7	68.70(6)	**O5 – Ho – O7**	136.00(6)
		O1 – Ho – O8	68.07(6)	**O5 – Ho – O8**	75.74(6)
		O2 – Ho – O3	70.15(6)	**O6 – Ho – O7**	135.88(6)
		O2 – Ho – O4	73.24(6)	**O6 – Ho – O8**	72.12(6)
		O2 – Ho – O5	135.11(6)	**O7 – Ho – O8**	135.53(6)

$[Ln_2(trz_2An)_3(H_2O)_4]_n \cdot 7H_2O$ (Ln^{III} = Dy, Tb, Ho), Phase B

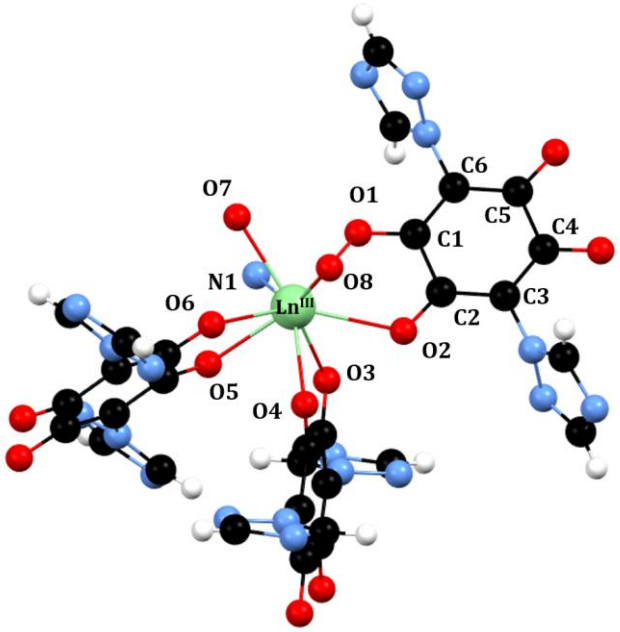

Table S5.4. Selected bond lengths and angles for $[Dy_2(trz_2An)_3(H_2O)_4]_n$ $7H_2O$

Bonds	Å	Angles	°	Angles	°
Dy– O1	2.358(2)	**N1 – Dy – O1**	70.81(8)	**O2 – Dy – O6**	127.08(7)
Dy – O2	2.503(2)	**N1 – Dy – O2**	116.94(8)	**O2 – Dy – O7**	131.99(8)
Dy – O3	2.417(2)	**N1 – Dy – O3**	70.98(8)	**O2 – Dy – O8**	70.28(8)
Dy – O4	2.378(2)	**N1 – Dy – O4**	129.79(8)	**O3 – Dy – O4**	67.26(7)
Dy – O5	2.417(2)	**N1 – Dy – O5**	67.10(8)	**O3 – Dy – O5**	70.84(8)
Dy – O6	2.517(2)	**N1 – Dy – O6**	115.39(8)	**O3 – Dy – O6**	124.65(7)
Dy – O7	2.369(2)	**N1 – Dy – O7**	142.35(9)	**O3 – Dy – O7**	136.44(8)
Dy – O8	2.359(2)	**N1 – Dy – O8**	72.99(8)	**O3 – Dy – O8**	143.96(8)
Dy – N1	2.551(3)	**O1 – Dy – O2**	65.16(7)	**O4 – Dy – O5**	73.74(8)
C1 – O1	1.252(4)	**O1 – Dy – O3**	92.00(8)	**O4 – Dy – O6**	70.54(8)
C2 – O2	1.246(4)	**O1 – Dy – O4**	135.71(8)	**O4 – Dy – O7**	87.85(8)
C1 – C2	1.531(4)	**O1 – Dy – O5**	137.71(8)	**O4 – Dy – O8**	141.65(8)
C2 – C3	1.408(4)	**O1 – Dy – O6**	143.25(8)	**O5 – Dy – O6**	64.10(7)
		O1 – Dy – O7	81.40(8)	**O5 – Dy – O7**	94.58(8)
		O1 – Dy – O8	76.74(8)	**O5 – Dy – O8**	137.36(8)
		O2 – Dy – O3	67.97(8)	**O6 – Dy – O7**	71.52(8)
		O2 – Dy – O4	70.74(7)	**O6 – Dy – O8**	73.61(8)
		O2 – Dy – O5	133.26(8)	**O7 – Dy – O8**	76.33(8)

Table S5.5. Selected bond lengths and angles for **$[Tb_2(trz_2An)_3(H_2O)_4]_n$ $7H_2O$**

Bonds	Å	Angles	°	Angles	°
Tb– O1	2.4014(14)	**N1 – Tb – O1**	67.11(5)	**O2 – Tb – O6**	143.30(5)
Tb – O2	2.5260(15)	**N1 – Tb – O2**	115.20(5)	**O2 – Tb – O7**	71.85(5)
Tb – O3	2.4279(15)	**N1 – Tb – O3**	70.98(6)	**O2 – Tb – O8**	74.63(5)
Tb – O4	2.3900(15)	**N1 – Tb – O4**	129.57(5)	**O3 – Tb – O4**	66.92(5)
Tb – O5	2.5086(15)	**N1 – Tb – O5**	116.84(5)	**O3 – Tb – O5**	68.19(5)
Tb – O6	2.3707(15)	**N1 – Tb – O6**	70.75(5)	**O3 – Tb – O6**	92.42(5)
Tb – O7	2.3817(17)	**N1 – Tb – O7**	72.79(6)	**O3 – Tb – O7**	143.77(5)
Tb – O8	2.3672(15)	**N1 – Tb – O8**	141.80(6)	**O3 – Tb – O8**	136.43(5)
Tb – N1	2.5664(18)	**O1 – Tb – O2**	63.86(5)	**O4 – Tb – O5**	70.91(5)
C1 – O1	1.255(2)	**O1 – Tb – O3**	70.52(5)	**O4 – Tb – O6**	135.91(5)
C2 – O2	1.246(2)	**O1 – Tb – O4**	73.56(5)	**O4 – Tb – O7**	142.03(5)
C1 – C2	1.531(3)	**O1 – Tb – O5**	133.27(5)	**O4 – Tb – O8**	88.62(5)
C2 – C3	1.402(3)	**O1 – Tb – O6**	137.67(5)	**O5 – Tb – O6**	65.20(5)
		O1 – Tb – O7	94.69(6)	**O5 – Tb – O7**	131.83(5)
		O1 – Tb – O8	138.18(5)	**O5 – Tb – O8**	69.92(5)
		O2 – Tb – O3	124.15(5)	**O6 – Tb – O7**	76.34(5)
		O2 – Tb – O4	70.58(5)	**O6 – Tb – O8**	80.57(5)
		O2 – Tb – O5	127.34(5)	**O7 – Tb – O8**	76.36(6)

Table S5.6. Selected bond lengths and angles for **$[Ho_2(trz_2An)_3(H_2O)_4]_n \cdot 7H_2O$**

Bonds	Å	Angles	°	Angles	°
Ho – O1	2.3793(13)	**N1 – Ho – O1**	67.20(5)	**O2 – Ho – O6**	142.96(4)
Ho – O2	2.5081(13)	**N1 – Ho – O2**	115.55(5)	**O2 – Ho – O7**	71.39(5)
Ho – O3	2.4052(13)	**N1 – Ho – O3**	70.99(5)	**O2 – Ho – O8**	74.02(5)
Ho – O4	2.3647(13)	**N1 – Ho – O4**	130.15(5)	**O3 – Ho – O4**	67.57(4)
Ho – O5	2.4956(13)	**N1 – Ho – O5**	117.06(5)	**O3 – Ho – O5**	68.01(4)
Ho – O6	2.3487(13)	**N1 – Ho – O6**	70.49(5)	**O3 – Ho – O6**	91.99(4)
Ho – O7	2.3547(13)	**N1 – Ho – O7**	72.84(5)	**O3 – Ho – O7**	143.82(5)
Ho – O8	2.3405(13)	**N1 – Ho – O8**	141.78(5)	**O3 – Ho – O8**	136.32(5)
Ho – N1	2.5396(16)	**O1 – Ho – O2**	64.27(4)	**O4 – Ho – O5**	70.57(4)
C1 – O1	1.252(2)	**O1 – Ho – O3**	70.97(4)	**O4 – Ho – O6**	135.94(4)
C2 – O2	1.246(2)	**O1 – Ho – O4**	73.96(5)	**O4 – Ho – O7**	141.50(5)
C1 – C2	1.529(3)	**O1 – Ho – O5**	133.31(4)	**O4 – Ho – O8**	88.05(5)
C2 – C3	1.404(2)	**O1 – Ho – O6**	137.51(5)	**O5 – Ho – O6**	65.56(4)
		O1 – Ho – O7	94.38(5)	**O5 – Ho – O7**	132.15(5)
		O1 – Ho – O8	137.98(5)	**O5 – Ho – O8**	69.87(5)
		O2 – Ho – O3	124.94(4)	**O6 – Ho – O7**	76.59(5)
		O2 – Ho – O4	70.51(4)	**O6 – Ho – O8**	80.86(5)
		O2 – Ho – O5	126.83(4)	**O7 – Ho – O8**	76.37(5)

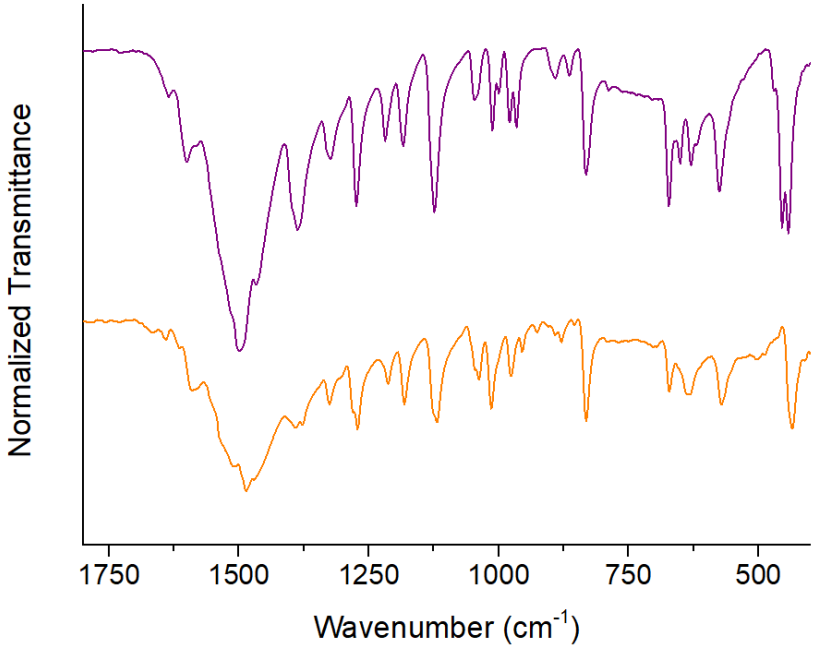

Figure S5.1. FT-IR spectra of **2a** (purple line) and **2b** (orange line) in 1800-400 cm^{-1} range.

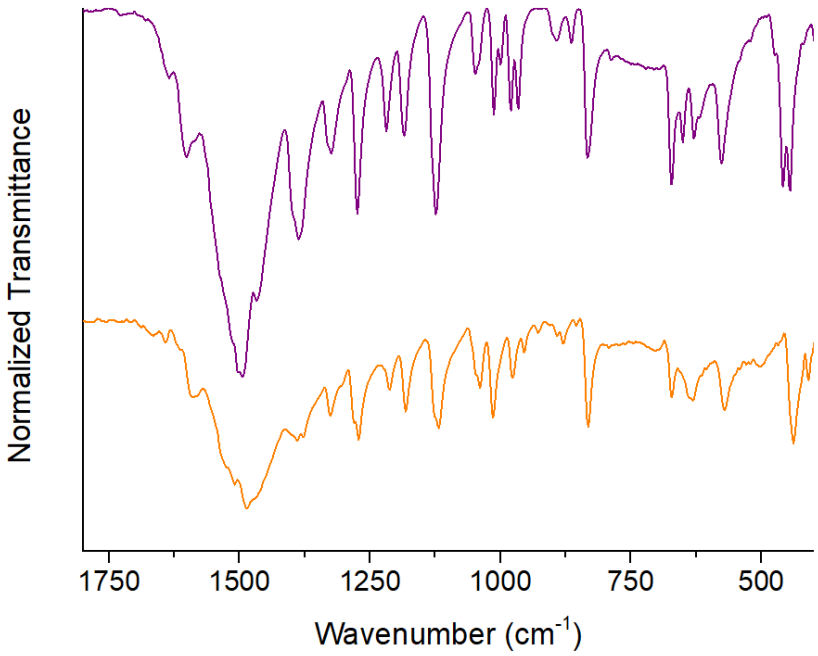

Figure S5.2. FT-IR spectra of **3a** (purple line) and **3b** (orange line) in 1800-400 cm^{-1} range.

Table S5.7. Crystal field parameters ($A_k^q < r^k >$; Stevens notation) in cm^{-1} obtained for **1a**, **1a_d** and **1b**.

k	***q***	**1a**	**1a_d**	**1b**
2	0	109.34	315.81	124.80
2	1	530.12	130.58	-527.09
2	-1	-115.07	331.45	103.14
2	2	207.04	-0.81	413.37
2	-2	-348.97	-155.33	96.40
4	0	60.64	36.88	58.33
4	1	-69.41	-340.05	13.08
4	-1	-145.91	117.08	-163.76
4	2	-199.48	-121.80	-289.69
4	-2	221.64	197.15	-12.19
4	3	-403.38	-539.24	1328.81
4	-3	1321.14	1444.07	59.62
4	4	-168.25	-231.10	-251.28
4	-4	284.27	578.32	188.66
6	0	-18.61	-10.65	-19.87
6	1	150.06	-203.92	-210.50
6	-1	-183.58	329.01	-114.94
6	2	80.99	-70.10	19.15
6	-2	50.44	10.32	-82.00
6	3	2.87	-249.92	-187.08
6	-3	-184.67	-266.96	-27.98
6	4	130.11	72.76	-301.11
6	-4	279.56	126.46	-101.03
6	5	-171.53	23.38	211.41
6	-5	311.20	-110.35	-268.02
6	6	33.91	-118.35	-26.67
6	-6	-16.76	126.18	-42.90

Table S5.8. Ground multiplet energy level scheme (Kramers doublets in cm^{-1}) and main |MJ> contributions to the wave function calculated for **1a** and **1a_d**.

1a		**1a_d**	
0	77.5% |±15/2>	**0**	94.0|±15/2>
32	12.8% |±5/2> + 17.4% |±3/2> + 12.6% |±1/2> + 15.5% |∓1/2>	**105**	60.2 |±13/2> + 24.0 |±11/2>
87	15.8% |±13/2> + 22.0% |±7/2> + 18.1% |±5/2> + 11.6% |±3/2>	**164**	17.3 |±11/2> + 22.8 |±7/2> + 13.0 |±5/2> + 14.2 |±3/2> + 11.5 |∓1/2>
113	19.3% |±13/2> + 30.7% |±11/2> + 24.6% |±9/2>	**215**	12.5 |±13/2> + 31.2 |±9/2> + 14.3 |±3/2>
139	23.3% |±13/2> + 10.5% |±5/2> + 14.0% |±1/2> + 10.4% |∓3/2> + 10.5% |∓5/2>	**327**	15.2 |±13/2> + 17.1 |±11/2> + 19.6 |±7/2> + 13.3 |±5/2>
258	17.0% |±13/2> + 20.7% |±9/2> + 12.6% |±7/2> + 10.8% |∓11/2>	**392**	21.7 |±11/2> + 22.7 |±9/2> + 11.0 |±3/2>
339	14.1% |±13/2> + 33.1% |±11/2> + 11.6% |±9/2> + 13.1% |∓7/2>	**427**	13.6 |±9/2> + 15.1 |±7/2> + 14.5 |±5/2> + 12.3 |∓1/2>
451	19.3% |±5/2> + 19.9% |±1/2> + 15.2% |∓3/2>	**536**	16.2 |±5/2> + 14.6 |±3/2> + 15.6 |±1/2> + 15.4 | 1/2> + 15.9 |∓3/2>

Table S5.9. Ground multiplet energy level scheme (Kramers doublets in cm-1) and main |MJ> contributions to the wave function calculated for **1b**.

1b	
0	81.0% |±15/2>
38	11.5% |±5/2> + 17.2% |±3/2> + 10.5% |±1/2> + 16.9% |∓1/2>
92	15.1% |±13/2> + 11.9%|±9/2> + 19.4% |±7/2> + 12.4% |±5/2>
120	24.4% |±13/2> + 27.5% |±11/2> + 18.0% |±9/2> + 11.9% |±7/2>
150	19.5% |±13/2> + 16.7% |±9/2> + 13.8% |±5/2> + 13.7% |±1/2> + 11.7% |∓3/2>
265	16.3% |±13/2> + 20.5% |±9/2> + 13.8% |±7/2> + 11.7% |∓11/2>
344	13.3% |±13/2> + 32.5% |±11/2> + 12.0% |±9/2> + 10.6% |±3/2> + 13.1% |∓7/2>
464	33.6% |±7/2> + 18.8% |±5/2> + 10.6% |±3/2> + 19.9% |±1/2> + 14.7% |∓3/2>

Table S5.10. Crystal field parameters ($A_k^q < r^k >$; Stevens notation) in cm^{-1} obtained for **2a_d** and **2b**.

k	***q***	**2a_d**	**2b**
2	0	-89.06	-291.18
2	1	-3.06	-137.21
2	-1	596.39	138.47
2	2	232.51	48.950
2	-2	-69.59	-266.39
4	0	-90.12	-51.01
4	1	93.33	109.53
4	-1	-80.71	-69.50
4	2	57.46	60.03
4	-2	83.06	-362.35
4	3	-7.28	-370.46
4	-3	-717.37	-558.41
4	4	194.85	425.68
4	-4	-36.20	278.18
6	0	-27.60	25.20
6	1	-1.23	-19.52
6	-1	104.52	-210.49
6	2	86.57	72.77
6	-2	-78.03	-51.10
6	3	0.859	-199.24
6	-3	-135.67	-12.31
6	4	-113.14	-106.75
6	-4	78.64	-193.58
6	5	590.14	-224.14
6	-5	556.41	335.86
6	6	-386.18	357.17
6	-6	348.25	-87.88

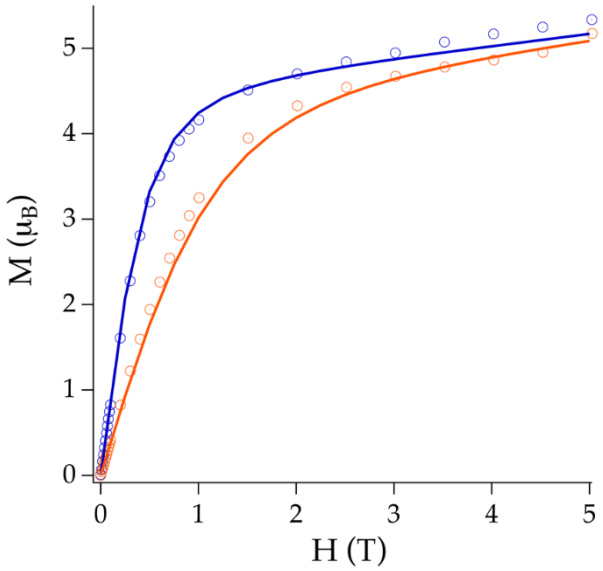

Figure S5.3. Experimental (symbols) and predicted average (lines) magnetization M versus field H of **1b** at 2K (blue) and 5 K (orange).

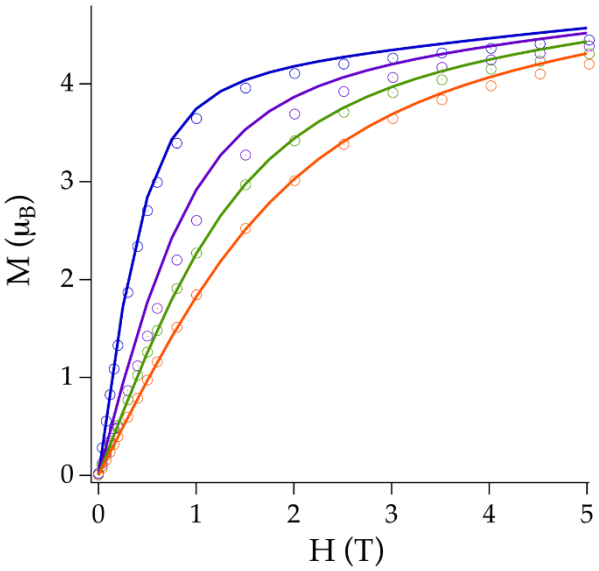

Figure S5.4. Experimental (symbols) and predicted average (lines) magnetization M versus field H of **2a_d** at 2K (blue), 4 K (violet), 6 K (green) and 8 K (red).

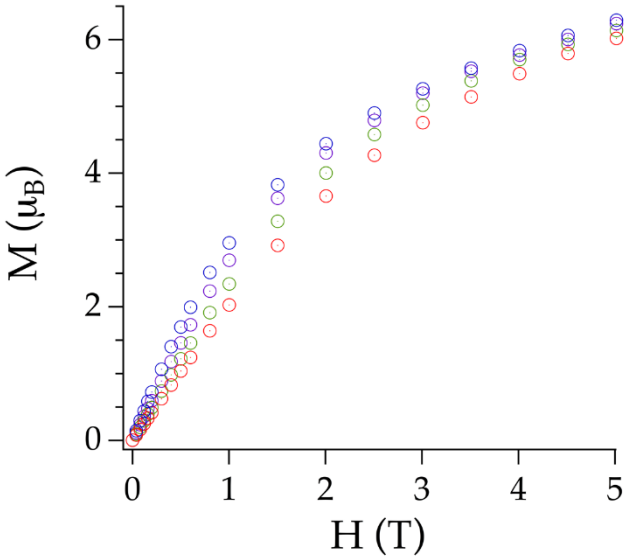

Figure S5.5. M versus field H of **3a_d** at 2K (blue), 4 K (violet), 6 K (green) and 8 K (red).

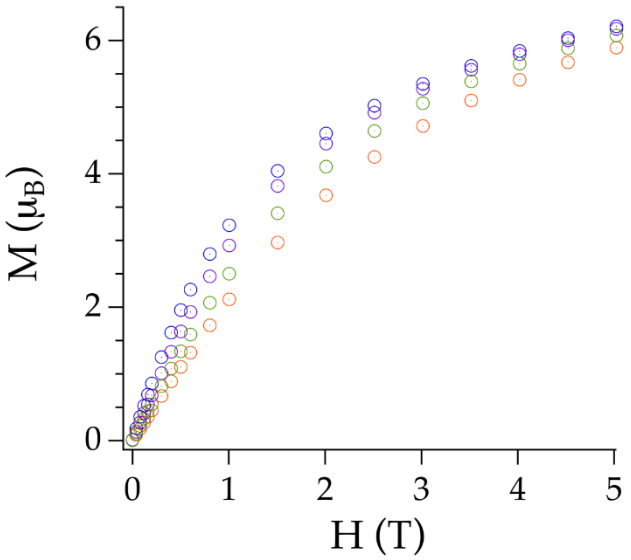

Figure S5.6. M versus field H of 3**b** at 2K (blue), 4 K (violet), 6 K (green) and 8 K (red).

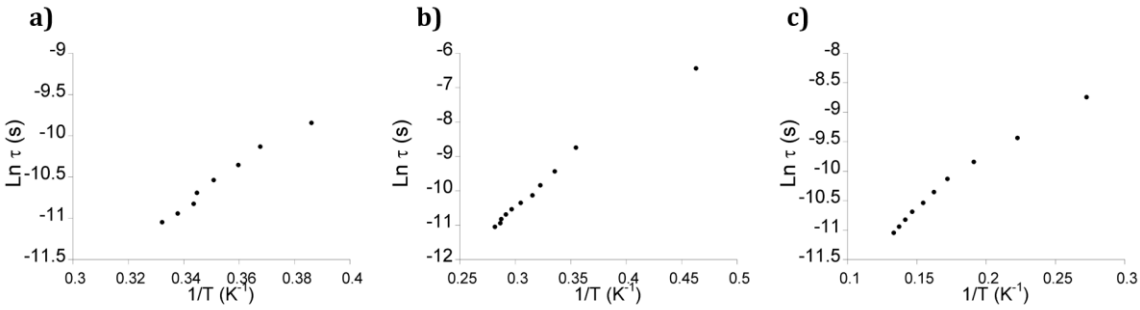

Figure S5.7. Plot of Ln τ versus T^{-1} for **1a_d** (a), **1b** (b) and **2b** (c).

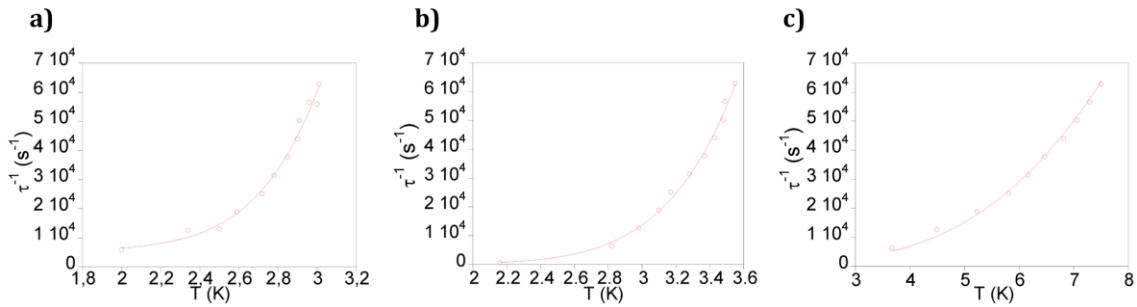

Figure S5.8. Thermal dependence of the relaxation time of **1a_d** (a), **1b** (b) and **2b** (c) and best fit from two terms mechanism described in text.

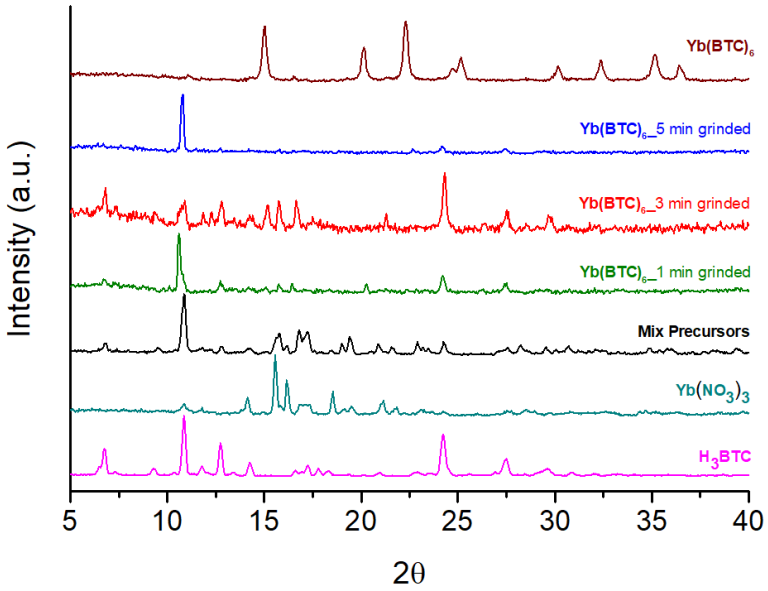

Figure S6.1. PXRD pattern recorded to follow the synthesis of **Yb(BTC)$_6$**, comparing precursors, their mix at different time of grinding and after the thermal treatment.

Table S6.1. Microanalysis of **2-6** samples showing the Nd/Yb atomic ratio.

Sample	Nd (at %)	Yb (at %)
2	93.21	6.79
	96.06	3.94
	96.17	3.83
3	94.99	5.01
	96.49	3.51
	96.49	3.51
4	89.03	10.97
	89.03	10.97
	90.40	9.60
5	87.56	12.44
	87.94	12.06
	89.78	10.22
6	0.20	99.80
	0.11	99.89
	1.5	98.5

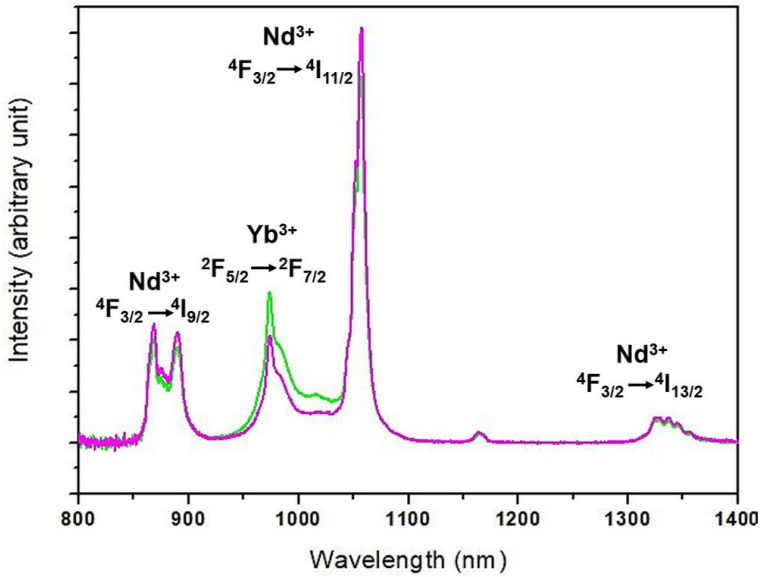

Figure S6.2. Emission spectra of $Nd_{0.943}Yb_{0.057}(BTC)_3(H_2O)_6$ (magenta line) and $Nd_{0.856}Yb_{0.144}(BTC)_3(H_2O)_6$ (green line) excited at 580 nm.

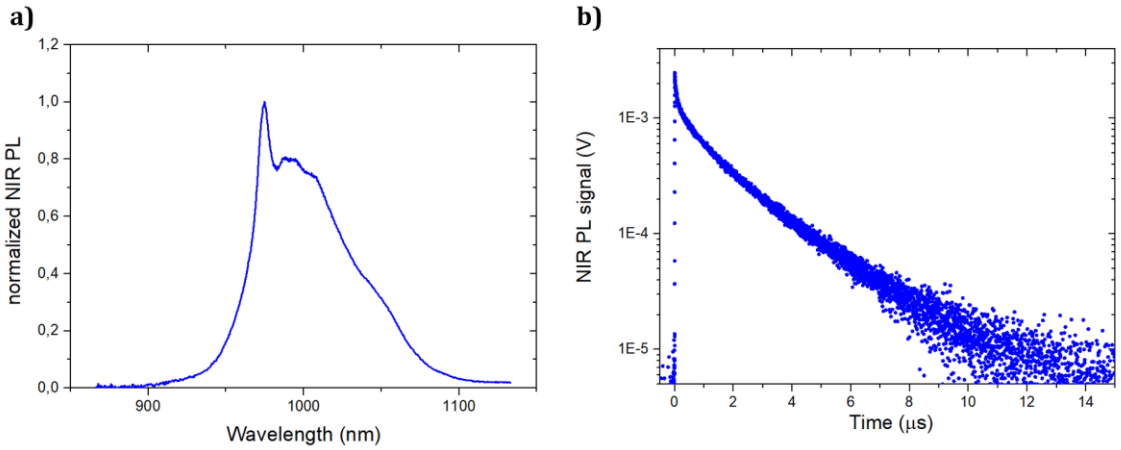

Figure S6.3. (a) Emission spectra of **Yb(BTC)$_6$** excited at 355 nm. (b) Decay curves of **Yb(BTC)$_6$**, monitoring the Yb^{III} $^2F_{7/2}$ emission at 1000 nm, with the excitation fixed at 355 nm (emission lifetime 2.6 μs).

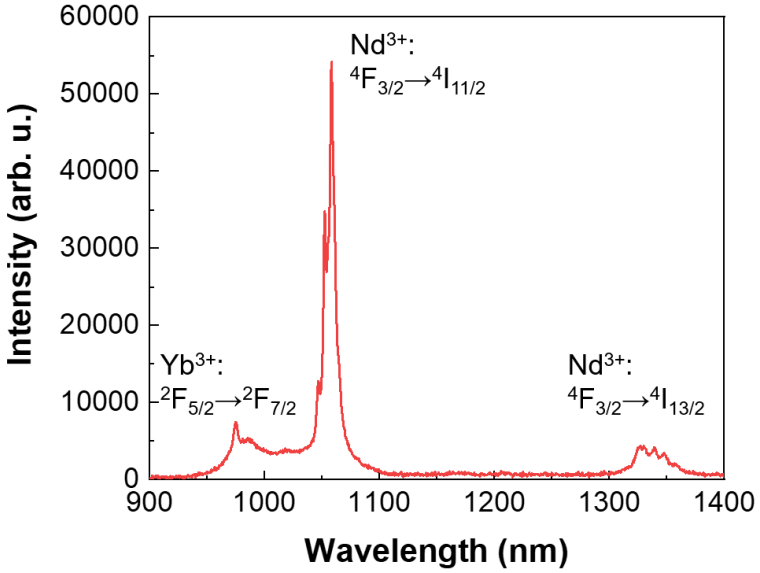

Figure S6.4. Emission spectra of $Nd_{0.889}Yb_{0.111}(BTC)_3(H_2O)_6$ excited at 808 nm.

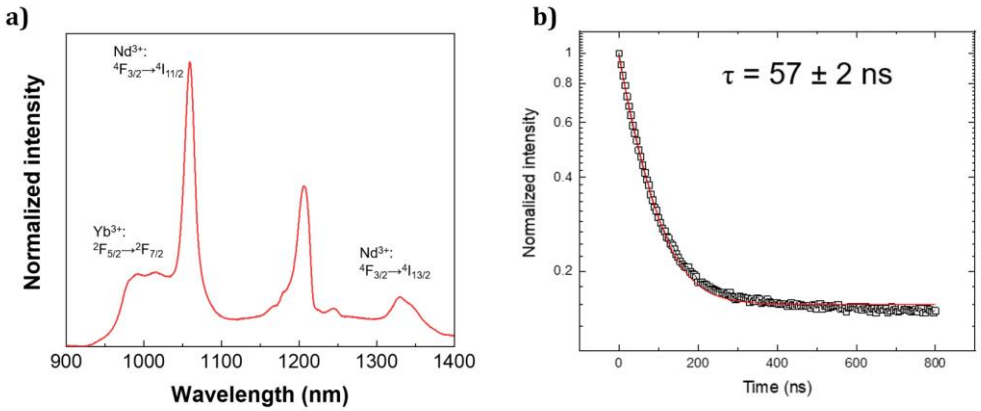

Figure S6.5. (a) Emission spectra of $Nd_{0.017}Yb_{0.983}(BTC)_6$ excited at 808 nm. (b) $^4I_{11/2}$ decay curve of $Nd_{0.017}Yb_{0.983}(BTC)_6$ monitoring the Nd^{III} emission at 1058.5 nm with the excitation fixed at 801 nm.

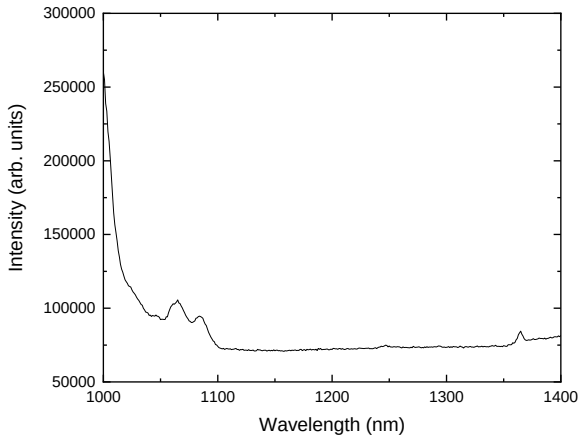

Figure S6.6. Emission spectra of $Nd_{0.017}Yb_{0.983}(BTC)_6$ excited at 980 nm.

Publication List (during the PhD period: 2018-2021)

1. "*Redox-Active Benzoquinones as Powerful "non-innocent" Linkers to Construct 2D Frameworks and Nanostructures with tunable Physical Properties"* N. Monni, M. Sanna Angotzi, M. Oggianu, S.A. Sahadevan*, M. L. Mercuri*. *Journal of Mater Chem C.* **2021**, (accepted with Minor Revisions).

2. "*A thermally/chemically robust and easily regenerable anilato-based ultramicroporous 3D MOF for CO_2 uptake and separation*" N. Monni, E. Andres-Garcia, K. Caamaño, V. García-López, J. M. Clemente-Juan, M. Giménez-Marqués, M. Oggianu, E. Cadoni, G. Mínguez Espallargas*, M. Clemente-León*, M. L. Mercuri* and E. Coronado. *Journal of Mater Chem A*, **2021**, 9, 25189-25195. doi: https://doi.org/10.1039/D1TA07436A

3. *"Redox Activity as a Powerful Strategy to Tune Magnetic and/or Conducting Properties in Benzoquinone-Based Metal-Organic Frameworks"* N. Monni,* M. Oggianu, S. Ashoka Sahadevan, M.L Mercuri* *Magnetochemistry*, **2021**, *7*, 109. **Invited as Perspective to "Special Issue: Perspectives on Molecular Materials – A Tribute to professor Peter Day"**. doi: https://doi.org/10.3390/magnetochemistry7080109

4. "*A Combined Experimental/Theoretical Study on the Luminescent Properties of Homoleptic/Heteroleptic Er^{III}/anilate-based 2D Coordination Polymers*" S. A. Sahadevan, F. Manna, A. Abhervé, M. Oggianu, N. Monni, V. Mameli, D. Marongiu, F. Quochi, F. Gendron, B. Le Guennic, N. Avarvari*, M. L. Mercuri*. Inorg Chem. **2021**, just accepted, doi: https://doi.org/10.1021/acs.inorgchem.1c02386

5. *"Nanoscaled Metal-Organic Frameworks (NanoMOFs): Challenges towards Biomedical Applications*" M. Oggianu, V. Mameli, N. Monni, S. A. Sahadevan, M. Sanna-Angotzi, C. Cannas, M. L. Mercuri*, Journal of Nanoscience and Nanotechnology, **2021**, 21, 1-8. doi:10.1166/jnn.2021.19043 (no WOS/SCOPUS indexing)

6. *"Radical Cation Salts of Tetramethyltetrathiafulvalene (TM-TTF) and Tetramethyltetraselenafulvalene (TM-TSF) with Chlorocyananilate-Based Anions"* S.A. Sahadevan, A. Abhervè, N. Monni, P. Auban-Senzier, H. Cui, R. Kato, M.L. Mercuri*, N. Avarvari*, Crystal Growth and Design, **2020**, *20(10)*, 6777-6786. ***Article selected for the Cover of the Issue***. doi: 10.1021/acs.cgd.0c00873.

7. *"Designing Magnetic NanoMOFs for Biomedicine: Current Trends and Applications"*, Oggianu, M.; Monni, N.; Ashoka Sahadevan, S*.; Mameli, V.; Cannas, C.; Mercuri, M.L.*, Magnetochemistry, **2020**, *6*, 39. **Invited as Perspective to "Special Issue: Feature Papers in Magnetochemistry"**. doi:10.3390/magnetochemistry6030039

8. *"Heteroleptic NIR-Emitting YbIII/Anilate-Based Neutral Coordination Polymer Nanosheets for Solvent Sensing"* S.A. Sahadevan, N. Monni, M. Oggianu, A. Abhervè, D. Marongiu, M. Saba, A. Mura, G. Bongiovanni, V. Mameli, C. Cannas, N. Avarvari*, F. Quochi*, M.L. Mercuri*, ACS Appl. NanoMater. **2020**, 3, 94−104. doi: 10.1021/acsanm.9b01740

9. *"Magnetic Molecular Conductors Based on Bis(ethylenedithio)tetrathiafulvalene (BEDT-TTF) and the Tris(chlorocyananilato)ferrate(III) Complex"* S.A. Sahadevan, A. Abherve, N. Monni, P. Auban-Senzier, J. Cano, F. Lloret, M. Julve, H. Cui, R. Kato, E. Canadell, M.L. Mercuri*, N. Avarvari*, Inorg. Chem. **2019**, 58, 15359−15370. doi: 10.1021/acs.inorgchem.9b02404.

10. *"Dysprosium Chlorocyanoanilate-Based 2D-Layered Coordination Polymers*" S.A. Sahadevan, N. Monni, A. Abherve, G. Cosquer, M. Oggianu, G. Ennas, M. Yamashita, N. Avarvari*, M.L. Mercuri*, Inorg. Chem. **2019**, 58, 13988−13998. DOI: 10.1021/acs.inorgchem.9b01968. doi: 10.1021/acs.inorgchem.9b01968.

Manuscripts in Preparation:

"Reversible Tuning of Luminescent and SIM properties in a 3D Anilato-based Er-MOF through Structural Flexibility" N. Monni, J. J. Baldoví, V. Garcia Lopez, M. Oggianu, E. Cadoni, F. Quochi, M. Clemente-León,* M. L. Mercuri* and E. Coronado

"Dual Center Ln'Ln''-CFs NIR Luminescent Ratiometric Thermometers via a solvent-free approach" N. Monni, M. Rodriguez, M. Souto, C. Brites, V. Mameli, C. Cannas, M. Oggianu, F. Quochi, E. Cadoni, M. Clemente-León, N. Masciocchi and M. L. Mercuri*